

**MOLECULAR IMAGING
OF MESOTHELIN EXPRESSING CANCERS**

by

Ripen Misri

B.Pharm.Sci., University of Mumbai, 2000

M.Pharm.Sci., University of Mumbai, 2002

A THESIS SUBMITTED IN PARTIAL FULFILLMENT OF THE
REQUIREMENTS FOR THE DEGREE OF

DOCTOR OF PHILOSOPHY

in

THE FACULTY OF GRADUATE STUDIES

(PHARMACEUTICAL SCIENCES)

THE UNIVERSITY OF BRITISH COLUMBIA

(Vancouver)

December 2010

© Ripen Misri, 2010

ABSTRACT

Mesothelin is a cell surface glycoprotein highly expressed in mesothelioma, ovarian cancer, pancreatic cancer and some other malignancies. It is a promising candidate for tumour specific therapy and diagnosis, given its limited expression in normal tissues. The purpose of the work presented in this dissertation is to develop and characterize a molecular imaging bioprobe that targets mesothelin.

We radiolabelled fab and f(ab')₂ fragments of the anti-mesothelin antibody mAbK1 with ^{99m}Tc-tricarbonyl core using a histidine-modified tridentate ligand, while whole mAbK1 was radiolabelled with ^{99m}Tc using a direct labelling approach. *In vivo* evaluation of these ^{99m}Tc labelled radioimmunoconjugates in mesothelin expressing NCI-H226 tumour model, revealed low mesothelin specific tumour uptake. These findings were attributed to low expression of mesothelin on NCI-H226 cells as well as to the low affinity of mAbK1. An anti-mesothelin antibody mAbMB, with higher mesothelin affinity than mAbK1 was labelled with ¹¹¹In and evaluated in A431K5 tumour model which expresses clinically relevant levels of mesothelin. Biodistribution studies and SPECT imaging revealed specific localization of ¹¹¹In-mAbMB in mesothelin expressing A431K5 tumours. An interesting finding with ¹¹¹In-mAbMB was its preferential localization in spleen, which suggests a role of circulating mesothelin antigen in forming immune complexes with ¹¹¹In-mAbMB. In comparison, control studies with ¹¹¹In-mAbK1 revealed low specific uptake into A431K5 tumours. These studies provided evidence that ¹¹¹In-mAbMB is a better choice than ¹¹¹In-mAbK1 for imaging mesothelin expression in tumours. A dual-modality SPECT/MR imaging bioprobe was further developed by conjugating ¹¹¹In-mAbMB with SPIONs (superparamagnetic iron oxide nanoparticles) which demonstrated specific targeting and MR imaging capability in A431K5 tumour bearing mice.

The work in this dissertation for the first time demonstrates successful SPECT imaging of mesothelin expressing cancers using radiolabelled antibodies. The radiopharmaceutical ^{111}In -mAbMB developed in this work holds promise for clinical use as a radioactive imaging bioprobe. Additionally, bioconjugates of ^{111}In -mAbMB and SPIONs are promising as dual-modality SPECT/MRI imaging bioprobes, which may be beneficial in improving the imaging outcomes of these difficult to treat tumours. In conclusion, our studies demonstrate that molecular imaging agents targeting mesothelin have a role to play for the detection and monitoring of mesothelin expressing cancers.

PREFACE

Ripen Misri designed, performed and interpreted the experiments described in this dissertation and is the principal author of all chapters presented in this dissertation. **Dr. Urs Häfeli** is the principal investigator and supervisor of Ripen Misri. The contributions of other individuals to this dissertation are explained below:

Chapter 2

Dr. Katayoun Saatchi synthesized the ligand for radiolabelling of antibody fragments. **Dr. Sylvia Ng** provided the technical expertise for tumour model development and tail vein injections in mice. A version of this chapter has been submitted for publication and is under review.

Chapter 3

Dr. Katayoun Saatchi provided technical assistance in optimizing the chelation chemistry. **Dr. Sylvia Ng** provided the technical expertise for tumour model development and tail vein injections in mice. **Dr. Ujendra Kumar** contributed to the design of western blot experiments. A version of chapter 3 has been submitted for publication and is under review.

Chapter 4

Dr. Dominik Meier provided technical expertise in MR image analysis. **Andrew Yung** and **Dr. Piotr Kozlowski** from UBC MRI Center provided MR imaging support. A version of this chapter will be submitted for publication.

All research work involving the use of animals, clinical samples and biological hazards was conducted in accordance with the University of British Columbia Policies and Procedures, after obtaining study approval certificates from the respective committees as listed below:

Animal Care Certificate # A-06-0349 (UBC Animal Care Committee)

Biohazard Approval Certificate # B10-0031 (UBC Biosafety Committee)

Research Ethics Approval Certificate # H07-02225 (UBC Clinical Research Ethics Board)

TABLE OF CONTENTS

ABSTRACT	ii
PREFACE.....	iv
TABLE OF CONTENTS	vi
LIST OF TABLES.....	x
LIST OF FIGURES	xi
LIST OF ABBREVIATIONS	xvi
ACKNOWLEDGEMENTS.....	xxi
DEDICATION.....	xxiii
Chapter 1: Introduction.....	1
1.1. Introduction to Imaging with Molecular Bioprobes	2
1.2. Mesothelin Expressing Cancers.....	4
1.3. Molecular Imaging.....	9
1.4. Mesothelin: A Target for Molecular Imaging.....	12
1.5. Mesothelin Expression in Human Cancers	15
1.6. Mesothelin Shedding From Tumour Cells	17
1.7. Mesothelin Targeted Immunotherapy.....	17
1.8. Antibodies Against Mesothelin	20
1.9. Radiolabelled Antibodies in Diagnosis and Therapy of Cancer.....	23
1.10. Factors to be Considered for Selection of a Radionuclide for Imaging.....	24
1.11. Factors Affecting Accumulation of Antibody Conjugated Imaging Bioprobes in Tumours.....	25
1.12. Dual Modality Imaging with SPECT/MRI.....	28
1.13. Contrast Agents Used in MRI.....	29
1.14. Dissertation Overview	32
1.15. Research Objectives.....	33
1.16. Impact of Research	33
Chapter 2: Evaluation of Technetium-99m Labelled Anti-mesothelin Antibody mAbK1 and its fab and f(ab') ₂ Fragments in a Mesothelin Expressing Cell Modelpen	35
2.1. Introduction.....	36
2.1.1. ^{99m} Tc Labelled Anti-mesothelin Antibody mAbK1	36
2.1.2. Improving Tumour Penetration with Antibody Fragments.....	38

2.1.3.	Current Study Outline	38
2.2.	Materials	41
2.3.	Methods	42
2.2.1.	^{99m} Tc Labelling of mAbK1 Antibody	42
2.2.2.	Synthesis of N-(<i>o</i> -phenol)-Histidine Chelator	43
2.2.3.	Preparation and Radiolabelling of fab and f(ab') ₂ Fragments	44
2.2.4.	Stability Studies: Cysteine Challenge	45
2.2.5.	Cell Culture and Immunofluorescence / Immunocytochemistry Studies	45
2.2.6.	Determination of Immunoreactivity.....	46
2.2.7.	Saturation Binding - K _d and B _{max} Determination	47
2.2.8.	Tumour Uptake and Biodistribution	47
2.2.9.	Western Blotting	48
2.3.	Results.....	50
2.3.1.	^{99m} Tc Labelling and Stability of mAbK1 Antibody and its fab and f(ab') ₂ Fragments.....	50
2.3.2.	Immunoreactivity of ^{99m} Tc Labelled Antibodies and Fragments	55
2.3.3.	K _d and B _{max} of Radioimmunoconjugates	56
2.3.4.	Biodistribution and Tumour Uptake of ^{99m} Tc Labelled mAbK1 and its fab/ f(ab') ₂ Fragments.....	57
2.4.	Discussion.....	63
2.5.	Conclusion	69
Chapter 3: SPECT/CT Imaging of Mesothelin Expressing Tumours with ¹¹¹ In-Labelled Antibodies.....		71
3.1.	Introduction.....	72
3.1.1.	Imaging Mesothelin Expression with ¹¹¹ In Labelled mAbMB Antibody.....	72
3.1.2.	Current Study Outline	73
3.2.	Materials	75
3.3.	Methods	76
3.3.1.	Radiolabelling.....	76
3.3.2.	Cell Culture	76
3.3.3.	Determination of Immunoreactivity.....	77
3.3.4.	Saturation Binding - K _d and B _{max} Determination	77
3.3.5.	Internalization of ¹¹¹ In-labelled Antibodies by A431K5 Cells	78

3.3.6.	Tumour Uptake and Biodistribution	78
3.3.7.	MicroSPECT/CT Imaging	79
3.3.8.	Mesothelin Expression in Tumours	80
3.4.	Results.....	82
3.4.1.	Radiolabelling	82
3.4.2.	Immunoreactivity and Saturation Cell Binding Studies	82
3.4.3.	Internalization by A431K5 cells	83
3.4.4.	Biodistribution Studies.....	85
3.4.5.	MicroSPECT/CT Imaging	95
3.4.6.	Mesothelin Expression in Tumours	98
3.5.	Discussion.....	99
3.6.	Conclusion	104
Chapter 4: Development and Evaluation of Dual-Modality (MRI/SPECT) Molecular Imaging Bioprobe for Mesothelin Expressing Cancers		105
4.1.	Introduction.....	106
4.1.1.	Dual Modality Imaging of Mesothelin Expressing Cancers	106
4.1.2.	Iron Oxide Nanoparticles for MR Imaging.....	107
4.1.3.	Current Study Outline	108
4.2.	Materials	111
4.3.	Methods	112
4.3.1.	Particle Characterization by TEM and Zetasizer	112
4.3.2.	Conjugation of ¹¹¹ In-mAbMB Antibody with SPIONs	112
4.3.3.	<i>In Vitro</i> Cell Binding and Specificity	113
4.3.4.	Relaxivity Measurement and <i>In Vitro</i> MR Imaging	114
4.3.5.	Tumour Uptake and Biodistribution	115
4.3.6.	Prussian Blue Staining of Tissue Specimens	116
4.3.7.	<i>In Vivo</i> MRI Studies.....	116
4.3.8.	Autoradiography	117
4.3.9.	Cellular Toxicity Determination by MTT Assay	117
4.4.	Results.....	119
4.4.1.	Particle Characterization and Antibody Conjugation	119
4.4.2.	<i>In Vitro</i> Cell Binding and Specificity	123

4.4.3.	Relaxivity Measurement and <i>In Vitro</i> MR Imaging	127
4.4.4.	Tumour Uptake and Biodistribution	129
4.4.5.	Prussian Blue Staining	133
4.4.6.	<i>In Vivo</i> MRI Studies.....	133
4.4.7.	MTT Assay	138
4.5.	Discussion.....	140
4.6.	Conclusion.....	145
Chapter 5: Summary and Conclusion.....		147
5.1.	Research Rationale	148
5.2.	Assessing Suitability of ^{99m} Tc Labelled mAbK1 Antibody and its Fragments in NCI-H226 Tumour Model	150
5.3.	Designing Mesothelin Targeted SPECT Imaging Probes with ¹¹¹ In Labelled mAbMB Antibody and Comparison of its Properties with ¹¹¹ In Labelled mAbK1	152
5.4.	Designing Dual-Modality MRI/SPECT Imaging Probes with ¹¹¹ In Labelled mAbMB and SPIONs	157
5.5.	Conclusions.....	159
BIBLIOGRAPHY		162
APPENDIX		191

LIST OF TABLES

Table 1.1. Clinical and pre-clinical immunotherapeutic agents designed to target mesothelin antigen.	19
Table 1.2. Antibodies against mesothelin.....	22
Table 2.1. Organ to blood ratios of ^{99m} Tc labelled mAbK1 and its fab and f(ab') ₂ fragments in SCID mice (n=5) bearing NCI-H226 (mesothelin positive) and LCC6-HER2 (mesothelin negative).	61
Table 3.1. Immunoreactivity of ¹¹¹ In-mAbMB and ¹¹¹ In-mAbK1 determined by a cell-binding assay using A431K5 cells. Total binding of ¹¹¹ In-mAbMB and ¹¹¹ In-mAbK1 to A431K5 cells was used to calculate K _d . Data is presented as mean±SD.	82
Table 3.2. Organ to blood ratios of ¹¹¹ In-mAbMB (740 kBq), injected in SCID mice (n=5) bearing A431K5 (mesothelin positive) and A431 (mesothelin negative) subcutaneous xenografts. Biodistribution was determined after 24, 48, 72 and 96 hours. Data is presented as mean±SD. .	88
Table 3.3. Organ to blood ratios of ¹¹¹ In-mAbMB (7.4 to 10.1 MBq), injected in SCID mice (n=3) bearing A431K5 and A431 subcutaneous xenografts. Biodistribution was determined after 48 and 72 hours. Data is presented as mean±SD.	90
Table 3.4. Organ to blood ratios of ¹¹¹ In-mAbK1 (740 kBq) in SCID mice (n=3) bearing A431K5 (mesothelin positive) and A431 (mesothelin negative) subcutaneous xenografts. Biodistribution were determined after 24 and 72 hours. Data is presented as mean±SD.	94
Table 4.1. Organ to blood ratios determined from biodistribution of ¹¹¹ In-mAbMB-SPIONs (15 mg/kg body weight Fe), injected in SCID mice (n=3) bearing A431K5 and A431 subcutaneous xenografts. Organ to blood ratios were determined after 24 and 72 hours. Data is presented as mean±SD.	131

LIST OF FIGURES

Figure 1.1. Schematic representation of the molecular bioprobes for imaging of mesothelin expressing cancers, developed in the current work.	3
Figure 1.2. A comparison of imaging sensitivities and resolution of commonly used molecular imaging modalities. Adapted from Zhou et al. [96].	12
Figure 1.3. Schematic representation of the maturation of mesothelin protein, its proposed role and mechanisms involved.....	14
Figure 1.4. Representative fluorescent microscopy image of a positive case (L) of mesothelioma patient tumour sample from the post-mortem histology study. The cell nuclei were stained blue with DAPI. The picture (L4) shows the mesothelin receptors stained red after staining with primary anti-mesothelin antibody and texas-red conjugated secondary antibody.....	15
Figure 2.1. Schematic picture of A) mAbK1, B) f(ab') ₂ fragment and C) fab fragment.	39
Figure 2.2. Experimental overview of chapter 2.	40
Figure 2.3. Representative autoradiographic images of ITLC strips used for the determination of the radiolabelling yield of ^{99m} Tc labelled mAbK1. ^{99m} Tc was conjugated to the antibody by a direct labelling method. Radiochemical purity was determined by ITLC using three different solvent systems to separate hydrolysed ^{99m} Tc colloid, and free ^{99m} Tc-pertechnetate. System I (ITLC-SG plates in saline): R _f ([^{99m} Tc]pertechnetate) = 1, R _f (^{99m} Tc- mAbK1 and ^{99m} Tc-colloid) = 0 (A), System II (Whatman 3 MM chromatography strips in acetone): R _f ([^{99m} Tc]pertechnetate) = 1, R _f (^{99m} Tc- mAbK1, ^{99m} Tc-colloid) =0 (B), System III (ITLC-SG strips / 5 mg/ml HSA in ethanol: ammonium hydroxide: water = 2:1:5): R _f (^{99m} Tc-colloid)=0, R _f (^{99m} Tc-mAbK1 and [^{99m} Tc]pertechnetate)=1(C). The radiochemical yield obtained was 92.6±1.6%.	51
Figure 2.4. Western blot showing the molecular weights of fab and f(ab') ₂ fragments of mAbK1. A non-reducing western blot was carried out for fab and f(ab') ₂ fragments obtained after digestion with ficin. The western blot confirm the formation of 50 kDa fab and 100 kDa f(ab') ₂ fragments.	52
Figure 2.5. Representative autoradiographic images of ITLC strips used for determination of radiolabelling yield for ^{99m} Tc labelled fabK1 and f(ab') ₂ K1 fragments. ^{99m} Tc from the precursor, [^{99m} Tc (CO) ₃] ⁺ was conjugated to the antibody by means of a bifunctional tridentate ligand. The activity at R _f = 0 corresponds to ^{99m} Tc-fabK1 (A and C) or ^{99m} Tc-f(ab') ₂ K1 (B). The peak at R _f = 0.6 – 1 corresponds to unbound ^{99m} Tc impurities. The radiochemical yield obtained was 91.6±9.1% and 80.7±8.5% for ^{99m} Tc-fabK1 and ^{99m} Tc-f(ab') ₂ K1, respectively. Control experiments (C) carried out to directly label fab fragments with [^{99m} Tc(CO) ₃] ⁺ yielded <20% radiochemical purity.	53
Figure 2.6. Stability of ^{99m} Tc labelled mAbK1, fabK1, f(ab') ₂ K1 in 1 mM cysteine after incubation for 1 hour and 24 hours at 37°C. After 1 hour, 95.1±0.9% of radioactivity was bound to mAbK1, while after 24 hours, 85.1±0.7% of the radioactivity was present on the antibody. For the fabK1 fragment, 79.5±1.7% of radioactivity was antibody-bound after 1 hour, which decreased to 66.7±4.9% after 24 hours. For f(ab') ₂ K1 72.5±2.8% of radioactivity was antibody-bound after 1 hour, which decreased to 63.4±0.5% after 24 hours. Control studies carried out in 0.9% saline for 1 hour and 24 hours at 37°C, indicated that the antibody and fragments retained >90% of the radiolabel for 24 hours.	54

Figure 2.7. Representative photomicrographs illustrating immunohistochemical staining of mesothelin in NCI-H226 cells with (A) the unlabelled mAbK1 antibody and (B) the ^{99m}Tc-radiolabelled antibody. (C) is a control without the primary antibody. Arrows point to the cell surface expression of mesothelin..... 55

Figure 2.8. Representative total binding curves for (A) ^{99m}Tc-mAbK1, (B) ^{99m}Tc-fabK1, (C) ^{99m}Tc-f(ab')₂K1. Adherent NCI-H226 cells were incubated in serum-free culture media with increasing concentrations (0–80 nM) of ^{99m}Tc-mAbK1, ^{99m}Tc-fabK1 and ^{99m}Tc-f(ab')₂K1 for 3 hours at 4°C. After removal of unbound radioactivity, the cells bound activity, was determined and. Prism® Version 5.0 software used calculate the K_d and B_{max} values. The K_d values obtained from saturation binding experiments were 21.5±2.8 nM, 22.7±6.4 nM and 25.0±1.3 nM for ^{99m}Tc-mAbK1, ^{99m}Tc-fabK1 and ^{99m}Tc-f(ab')₂K1, respectively. The number of mesothelin receptors on NCI-H226 cells, calculated from the B_{max} values were 9.1×10⁴ ± 1.0×10⁴ / cell.... 56

Figure 2.9. Biodistribution of ^{99m}Tc-mAbK1 (10-18 MBq), injected in SCID mice (n=5) bearing NCI-H226 (mesothelin positive) and LCC6-HER2 (mesothelin negative) subcutaneous xenografts. Percentage of the injected dose/gram (Activity %ID/g) was determined in the tumours and all major organs after 8, 24 and 48 hours, post-injection. ^{99m}Tc-mAbK1 showed fast blood clearance and peak uptake into NCI-H226 tumours was 0.80±0.39% ID/g at 8 hours. Data is presented as mean±SD. 59

Figure 2.10. Biodistribution of ^{99m}Tc-labelled f(ab')₂ and fab fragments of mAbK1. Biodistribution was determined after injecting 10-18 MBq of ^{99m}Tc-f(ab')₂ (A) and ^{99m}Tc-fab (B), in SCID mice (n=5) bearing NCI-H226 (mesothelin positive) and (mesothelin negative) subcutaneous xenografts. Percentage of the injected dose/gram (Activity %ID/g) was determined in the tumours and all major organs after 4, 8, 24 hours, post-injection. Both ^{99m}Tc-f(ab')₂K1 and ^{99m}Tc-fabK1 showed significantly higher uptake into NCI-H226 tumours than LCC6-HER2 tumours at 8 hours. Data is presented as mean±SD..... 60

Figure 2.11. Western blot of mesothelin positive NCI-H226 (H1-H6) and mesothelin negative LCC6-HER2 (L1-L6) tumour lysates. *In vivo* expression of 40 kDa mesothelin was confirmed in NCI-H226 tumours, while LCC6-HER2 tumours did not express mesothelin. The cell lysate from NCI-H226 was used as a positive control, while beta actin was used as a loading control. 61

Figure 2.12. Synthetic scheme for preparing ^{99m}Tc labelled antibody fragments starting from L-histidine. The tridentate ligand L1 is obtained by reductive amination and binds to Ab through a stable amide bond. Ab in the figure represents f(ab')₂ fragment or fab fragment..... 62

Figure 3.1. Experimental overview of chapter 3. 74

Figure 3.2. Time and temperature dependent cellular internalization of ¹¹¹In-mAbMB and ¹¹¹In-mAbK1 by A431K5 cells. ¹¹¹In-mAbMB has greater cellular internalization than ¹¹¹In-mAbK1 throughout the time course of the study, with significantly higher values (P<0.05) achieved at 18 hours. Data is presented as mean±SD..... 84

Figure 3.3. Biodistribution of ¹¹¹In-mAbMB (740 kBq) injected into SCID mice (n=5) bearing A431K5 (mesothelin positive) and A431 (mesothelin negative) subcutaneous xenografts. Percentage of the injected dose/gram (Activity % ID/g) was determined in the tumours and all major organs after 24, 48, 72 and 96 hours. Data is presented as mean±SD. 87

Figure 3.4. Biodistribution of ¹¹¹In-mAbMB (7.4 to 10.1 MBq), injected in SCID mice (n=3) bearing A431K5 (mesothelin positive) and A431 (mesothelin negative) subcutaneous xenografts.

Percentage of the injected dose/gram (Activity %ID/g) was determined in the tumours and all major organs after 48 and 72 hours. Data is presented as mean±SD.	89
Figure 3.5. Biodistribution of ¹¹¹ In-mAbMB in SCID mice (n=3) without tumours. Percentage of the injected dose/gram (Activity %ID/g) was determined in all major organs after 24 hours. Data is presented as mean±SD.	91
Figure 3.6. A comparison of spleen activity uptake and spleen weights at 48 and 72 hours after injection of ¹¹¹ In-mAbMB at low dose (4 µg) or high dose (50 µg). The spleen activity in terms of %ID/organ (A) decreases at the higher dose accompanied by decrease in the spleen weights (B), which results in an increased activity on per weight basis (%ID/g) in spleen (C). Data is presented as mean±SD.	92
Figure 3.7. Biodistribution of ¹¹¹ In-mAbK1 (740 kBq), injected in SCID mice (n=5) bearing A431K5 (mesothelin positive) and A431 (mesothelin negative) subcutaneous xenografts. Percentage of the injected dose/gram (Activity %ID/g) was determined in the tumours and all major organs after 24 and 72 hours. Data is presented as mean±SD.	93
Figure 3.8. MicroSPECT/CT images of SCID mice bearing A431K5 (mesothelin positive) and A431 (mesothelin negative) tumours. SCID mice were injected with 7.4 to 10.1 MBq of (A) ¹¹¹ In-mAbMB and (B) ¹¹¹ In-mAbK1 and images were acquired after 24, 48 and 72 hours (h). .	96
Figure 3.9. Target to Non-Target (T/NT) ratios calculated from ROI analysis of microSPECT/CT images of SCID mice bearing A431K5 and A431 subcutaneous xenografts. Images were acquired (A) at 24 (n=6), 48 (n=6) and 72 (n=3) hours after injection with 7.4 to 10.1 MBq of ¹¹¹ In-mAbMB and (B) at 24, 48 and 72 hours of mice (n=2) injected with 7.4 to 10.1 MBq of ¹¹¹ In-mAbK1. Data is presented as mean±SD.	97
Figure 3.10. Western blot confirming the mesothelin expression in A431K5 (K1-K5) tumours. The spleen (S) and A431 (A1-A5) tumours showed no expression of mesothelin. The cell lysate from A431K5 (KC) was used as a positive control, while beta actin was used as a loading control.	98
Figure 4.1. Schematic of the proposed dual modality MRI/SPECT imaging bioprobe.	108
Figure 4.2. Experimental overview of chapter 4.	110
Figure 4.3. Characterization of SPIONs. (A) Schematic of the carboxy methyl dextran coated SPIONs. (B) TEM micrograph of the SPIONs. (C) Frequency distribution (n=50) of the magnetic core size of SPIONs obtained from TEM. Scale bar is 20 µm.	120
Figure 4.4. Particle size of SPIONs before and after antibody conjugation. Frequency distribution of the hydrodynamic diameter of SPIONs (A) and ¹¹¹ In-mAbMB-SPIONs (B) obtained from DLS method.	121
Figure 4.5. Overview of antibody conjugation to SPIONs by carbodiimide coupling reaction. EDC reacts with the carboxylic acid groups on the particle surface to form an active ester intermediate (O-acylisourea). In the presence of an antibody, a peptide bond is formed, releasing in an isourea byproduct.	122
Figure 4.6. Cellular uptake of ¹¹¹ In-mAbMB-SPIONs by A431K5 and A431 cells. The cells were incubated with 0.05 mg/ml Fe equivalent of ¹¹¹ In-mAbMB-SPIONs at 37°C and cellular uptake determined after 3 hours, 6 hours and 24 hours. Significantly higher uptake was observed in A431K5 cells compared to A431 cells. Data is presented as mean±SD.	124

- Figure 4.7. Competitive binding assay of ^{111}In -mAbMB-SPIONs to A431K5 cells. A431K5 cells were incubated with 0.05 mg/ml Fe equivalent of ^{111}In -mAbMB-SPIONs at 37°C and cellular uptake determined after 24 hours. About 4.5 times higher uptake of ^{111}In -mAbMB-SPIONs was observed in A431K5 cells compared to that observed in presence of excess unlabelled mAbMB. Data is presented as mean \pm SD. 125
- Figure 4.8. Confocal microscopy images of cellular uptake of ^{111}In -mAbMB-SPIONs and SPIONs by A431K5 cells. A431K5 cells were incubated for 3 hours with 0.05 mg/ml Fe equivalent of ^{111}In -mAbMB-SPIONs at 4°C showed binding to the cell membrane while cellular internalization was inhibited (A) and at 37°C , ^{111}In -mAbMB-SPIONs was mainly internalized by the cells (B). When A431K5 cells were incubated with 0.05 mg/ml Fe equivalent of SPIONs, decreased binding and internalization was observed (C). Arrows in the figure point to the ^{111}In -mAbMB-SPIONs and SPIONs, respectively. 126
- Figure 4.9. Signal intensity weighted MR image of phantom agar gel at different Fe concentrations for SPIONs and ^{111}In -mAbMB-SPIONs. 127
- Figure 4.10. Relaxivity determination of SPIONs and ^{111}In -mAbMB-SPIONs using T_1 and T_2 weighted MR image. Phantoms containing different Fe concentration of SPIONs and ^{111}In -mAbMB-SPIONs were made in agar gel. T_1 and T_2 weighted images were obtained by using inversion recovery pulse and CPMG sequence, respectively. Signal intensity was used to obtain fitted T_1 (A) and T_2 (B) time constants, which were plotted against the respective concentrations. Relaxivity values r_1 and r_2 were obtained from slopes of linear fits of experimental data. 128
- Figure 4.11. Biodistribution of ^{111}In -mAbMB-SPIONs injected into SCID mice (n=5) bearing A431K5 (mesothelin positive) and A431 (mesothelin negative) subcutaneous xenografts. Percentage of the injected dose/gram (Activity %ID/g) was determined in the tumours and all major organs after 24 and 72 hours. Data is presented as mean \pm SD. 130
- Figure 4.12. A representative autoradiographic image of excised organs. At 72 hours post-injection of ^{111}In -mAbMB-SPIONs major organs were excised and ex-vivo autoradiography of major organs was carried out by exposing a $20\times 25\text{ cm}^2$ phosphor screen to the excised organs followed by visualization using a phosphor imager. High activity uptake can be visualized mainly in liver, spleen, kidney and A431K5 tumour. 132
- Figure 4.13. Iron oxide staining of tissue specimens of A431 tumour (A), A431K5 tumour (B) and spleen (C), by Prussian blue staining method. While spleen shows the highest presence of iron oxide, the presence of iron oxide in A431K5 tumour is greater than A431 tumour. The insets provide a 3 times magnified view of the tissue. 133
- Figure 4.14. T_2 weighted coronal gradient echo MR images of SCID mice bearing xenograft tumours, injected intravenously with 15 mg/kg body weight Fe equivalent of ^{111}In -mAbMB-SPIONs. Images A1, A2 and A3 represent A431K5 tumour at pre-injection and 24 hours and 72 hours post-injection time points, respectively, while images B1, B2 and B3 are corresponding images for the A431 tumour from the same mouse. The mice were imaged using a 7 T MRI Bruker scanner. The yellow arrows in the images point to the regions in the tumours, where a change in MR signal can be observed. The insets to the right are a representation of the coronal view of the mouse with green arrows indicating the locations of tumours (neck- A431K5, lower back A431). 135
- Figure 4.15. T_2 weighted axial gradient echo MR images and tumour volume maps for A431K5 tumours of SCID mice bearing xenograft tumours, injected intravenously with 15 mg/kg body

weight Fe equivalent of ^{111}In -mAbMB-SPIONs. Image analysis was performed using the 3D Slicer program. Images A1, A2 and A3 represent A431K5 tumour volumes obtained at pre-injection and 24 and 72 post-injection time points, respectively. Images B1, B2 and B3 are the MR images of A431K5 tumour at pre-injection and 24 and 72 hours post-injection time points, respectively. The inset in image B3 represents the autoradiographic image of a 20 μm tumour section obtained from the corresponding tumour. The region of MR signal change observed in the B3 image correlates with the region of activity uptake as observed in the autoradiographic image. The mice were imaged using a 7 T MRI Bruker scanner. 136

Figure 4.16. ROI intensity histograms for T2 weighted axial gradient echo MR images of A431K5 tumours. SCID mice bearing A431K5 tumours were, injected intravenously with 15 mg/kg body weight Fe equivalent of ^{111}In -mAbMB-SPIONs. The suppression of the signal intensity is mainly observed for the 24 hours image, represented by a shift in the green curve towards lower intensity region on the x-axis. 137

Figure 4.17. T₂ weighted axial gradient echo MR images for A431 tumours of SCID mice bearing xenograft tumours, injected intravenously with 15 mg/kg body weight Fe equivalent of ^{111}In -mAbMB-SPIONs at pre-injection (A), 24 hours (B) and 72 hours (C) post-injection. 138

Figure 4.18. MTT assay on A431 cells. Cell viability of the ^{111}In -mAbMB-SPIONs (MA) was determined by the MTT assay, 24 hours after incubation with A431 cells and compared with SPIONs (M) and Feridex IV (F) at the equivalent concentration of 0.1, 0.5 [Fe] mg/ml, respectively ($n = 8$). Untreated cells were used as control to determine 100% cell viability. 139

Figure 5.1. Overview of research findings. 149

Figure A.1. Representative fluorescent microscopy images of two positive cases of mesothelioma patient tumour samples from our post-mortem histology study. The cell nuclei were stained blue with DAPI. The control images were obtained without primary and secondary antibody (F1, J1), without primary antibody but with secondary antibody (F2, J2) and with primary antibody but no secondary antibody (F3, J3). The final picture (F4, J4) was stained with both primary anti-mesothelin antibody and secondary antibody and shows the mesothelin receptors stained red. 194

Figure A.2. Representative fluorescent microscopy images of two negative cases of mesothelioma patient tumour samples from our post-mortem histology study. The cell nuclei were stained blue with DAPI. The control images were obtained without primary and secondary antibody (D1, I1), without primary antibody but with secondary antibody (D2, I2) and with primary antibody but no secondary antibody (D3, I3). The final picture (D4, I4) was stained with both primary anti-mesothelin antibody and secondary antibody, however very low mesothelin staining was observed. 195

Figure A.3. Representative fluorescent microscopy images of a reactive fibrous pleurisy patient sample from our post-mortem histology study. The cell nuclei were stained blue with DAPI. The control images were obtained without primary and secondary antibody (P1), without primary antibody but with secondary antibody (P2) and with primary antibody but no secondary antibody (P3). The final picture (P4) was stained with both primary anti-mesothelin antibody and secondary antibody, however very low mesothelin staining was observed. 196

LIST OF ABBREVIATIONS

ADCC	Antibody dependent cell toxicity
APD	Avalanche photo diodes
^{211}At	Astatine-211
^{213}Bi	Bismuth-213
B_{max}	Saturation receptor concentration
BSA	Bovine serum albumin
^{11}C	Carbon-11
CA125	Cancer antigen 125
CD4	Cluster of differentiation 4
CD8	Cluster of differentiation 8
CEA	Carcinoembryonic antigen
cm	Centimeter
CPMG	Carr-Purcell-Meiboom-Gill
CRlg	Complement receptor of immunoglobulins
CT	Computed tomography
^{64}Cu	Copper-64
CZT	Cadmium zinc telluride
DCE-MRI	Dynamic contrast enhanced-magnetic resonance imaging
DLS	Dynamic light scattering
DMSO	Dimethyl sulfoxide
DOTA	Tetra azacyclododecanetetra acetic acid
DTPA	Diethylene triamine pentaacetic acid

EDC	1-Ethyl-3-(3-dimethylaminopropyl)-carbodiimide
EDTA	Ethylene diamine tetra acetic acid
EGTA	Ethylene glycol tetraacetic acid
ELISA	Enzyme-linked immunosorbent assay
EPR	Enhanced permeation and retention
Her-2/neu	Human epidermal growth factor receptor 2
ESI	Electrospray ionization
FDA	Food and drug administration
FDG	Fluorodeoxyglucose - ^{18}F
Fe	Iron
Fe_2O_3	Hematite
Fe_3O_4	Magnetite
FeCo	Iron cobalt
FOV	Field of view
Gd	Gadolinium
GPI	Glycosyl phosphatidyl inositol
HCl	Hydrochloric acid
HER-2	Human epidermal growth factor receptor 2
^{123}I	Iodine-123
^{131}I	Iodine-131
IC_{50}	Half maximal inhibitory concentration
ID/g	Injected dose/gram
IgG	Immunoglobulin G
^{111}In	Indium-111

ITLC	Instant thin layer chromatography
ITLC-SG	Instant thin layer chromatography-silica gel
kBq	Kilo Becquerel
K_d	Dissociation constant
kDa	Kilo daltons
keV	Kilo electron volt
Kg	Kilogram
L1	N-(<i>o</i> -phenol)-histidine
LSO	Lutetium oxyorthosilicate
m/z	Mass-to-charge ratio
mAb	Monoclonal antibody
MBq	Mega Becquerel
MES	2-(N-morpholino) ethanesulfonic acid
Mg	Milligram
M-H ⁻	Deprotonated molecular ions
MHz	Megahertz
MIONS	Monocrystalline iron oxide nanoparticles
MM	Malignant mesothelioma
mM	Millimolar
Mm	Millimeter
Mn ²⁺	Manganese
MnFe ₂ O ₄	Manganese ferrite
MPF	Megakaryocyte potentiating factor
MPM	Malignant pleural mesothelioma

MRI	Magnetic resonance imaging
MTT	3-[4,5-dimethylthiazol-2yl]-2,5-diphenyltetrazolium bromide
^{13}N	Nitrogen-13
NaBH_4	Sodium borohydride
NaOH	Sodium hydroxide
$\text{Na}^{99\text{m}}\text{Tc}$ pertechnetate	Sodium pertechnetate
NHS	N-hydroxysuccinimide
NK	Natural killer
nM	Nano molar
NMR	Nuclear magnetic resonance
^{15}O	Oxygen-15
PBS	Phosphate buffered saline, pH 7.4
PET	Positron emission tomography
pM	Pico molar
p-SCN-bn-DTPA	2-(4-Isothiocyanatobenzyl)-diethylenetriamine pentaacetic acid
r_1	Longitudinal relaxivity
r_2	Transverse relaxivity
RARE	Rapid acquisition with refocused echoes
RECIST	Response evaluation criteria in solid tumours
R_f	Retention factor
RIPA	Radioimmunoprecipitation assay buffer
ROI	Region of interest
ROR	Radius of rotation
scFv	Single chain fragment

SCID	Severe combined immunodeficient
SDS	Sodium dodecyl sulphate
SMRP	Serum mesothelin related protein
SnCl ₂	Tin chloride
SPECT	Single photon emission computed tomography
S-S	Disulfide group
SUV	Standard uptake value
T	Tesla
T/N	Tumour to non-tumour ratio
T ₁	Longitudinal relaxation time
T ₂	Transverse relaxation time
TAA	Tumour associated antigen
TBST	Tris-buffered saline with tween-20
^{99m} Tc	Technetium-99m
[^{99m} Tc(CO) ₃] ⁺	^{99m} Tc(I) tricarbonyl core
TE	Echo time
TEM	Transmission electron microscopy
TNM	Tumour node metastasis
TR	Repetition time
μm	Micrometer
μg	Microgram
UV	Ultraviolet
v/v	Volume/volume
⁹⁰ Y	Yttrium-90

ACKNOWLEDGEMENTS

I wish to express my deep sense of gratitude to my Ph.D. supervisor, Dr. Urs Häfeli, for his excellent guidance, critical advice and mentorship throughout the course of this research work. I would also like to thank him for providing all the necessary resources and facilitating collaborations for successful completion of this work. I am also grateful to my supervisory committee members: Drs. Philip Cohen, Sylvia Ng, Judy Wong and Peter Soja for their invaluable advice and suggestions. My special thanks to Dr. Sylvia Ng for being very gracious in helping me with her technical expertise.

I am also thankful to Dr. Kathy Saatchi for her valuable advice and help during the course of this work. I am grateful to Dr. John English, UBC Pathology, for providing the patient tissue specimens. I would also like to thank Leo Dai for his help in carrying out immunostaining and Peter Soema for his help with confocal microscopy. In addition, my special thanks to all my current and past lab colleagues for fostering a stimulating and cheerful work environment.

I would like to express my gratitude to Dr. Ujendra Kumar and his lab group for allowing me the use of their cell culture facilities and providing useful suggestions. I am also grateful to Dr. Helen Burt's lab for allowing me the use of their lab facilities and instruments.

My special thanks to UBC hospital for providing the sodium pertechnetate used in my experiments. I am grateful to Chemicell, Germany for providing the magnetic nanoparticles for my research. In addition, I would like to acknowledge the support from UBC Bioimaging facility in carrying out TEM experiments. It is my pleasure to thank Chantal Saab, Dr. Troy Farncombe, and Rod Rhem at McMaster's Centre for Preclinical and Translational Imaging (Hamilton, Ontario, Canada) for excellent SPECT/CT imaging support. My special thanks to Andrew Yung and Dr. Piotr Kozlowski for their support in carrying out MR imaging studies. I am grateful to

Dr. Dominik Meier, Harvard Medical School for his prompt help in MR image analysis. I would like to express my thanks to Dr. Ira Pastan, National Cancer Institute for generously providing the A431K5 cell line. Additionally, my sincere gratitude to Drs. Wan Lam, Don Yapp and Marcel Bally for providing the other cell lines used in my research.

I wish to thank my friend Ganesh for supporting and encouraging me. I am forever indebted to my parents for their blessings, love and support. My heartfelt thanks to my wife Pooja, for her patience, understanding and love.

Finally, I would also like to acknowledge the financial support received from the University of British Columbia in the form of University Graduate Fellowship, Douglas Jean and Bailey Scholarship, Graduate Entrance Scholarship and Ph.D. Tuition Scholarship. My special thanks to the Society of Nuclear Medicine and IEEE Magnetics Society for providing research travel awards.

DEDICATION

I dedicate this work to my family for their unconditional love and support and to the Almighty for giving me patience, strength and belief to complete this work.

Anybody who has been seriously engaged in scientific work of any kind realizes that over the entrance to the gates of the temple of science are written the words: 'Ye must have faith.'

-Max Planck

Chapter 1: Introduction

1.1. Introduction to Imaging with Molecular Bioprobes

Designing molecules that bind to deregulated targets in cancer cells is an important strategy for both therapeutic and diagnostic drug design. Monoclonal antibodies (mAbs) are valuable targeting molecules, while radionuclides have great value as diagnostic tracers or therapeutic agents. mAbs against tumour associated antigens can be applied to deliver radionuclides to tumour sites for imaging or therapy [1-3]. This approach is highly significant to the early detection and management of cancer as some of the most difficult to treat cancers are best treated when diagnosed as early as possible. In addition, nanoparticles coupled with cancer specific targeting ligands can be used to image tumours and detect peripheral metastases [4,5]. The use of therapeutic and diagnostic agents for tumour targeting with specific antibodies has become an established science in the last 15 years. The most significant achievements in this area have been in the treatment of lymphomas [6] as well as in the diagnosis of colorectal [7] and prostate cancers [8]. Studies have also shown that a highly specific and powerful contrast agent can be prepared by coating magnetite (Fe_3O_4) particles with monoclonal antibodies directed against a tumour antigen [9]. Such a preparation retains both the immunoreactivity of the monoclonal antibody and the full relaxing capability of the magnetite particle [9]. Superparamagnetic iron oxide nanoparticles with covalently bound antibodies against Her-2/neu (an antigen overexpressed in some breast cancers) have also shown promise for simultaneous imaging and therapeutic targeting of breast cancers *in vivo* [10].

The purpose of the work presented in this dissertation is to develop and characterize a molecular imaging bioprobe that targets a cell surface antigen known as 'mesothelin' over-expressed mainly by mesotheliomas, pancreatic and ovarian cancers (**Figure 1.1**) [11-16]. A tumour specific bioprobe was developed based on the ability of radiolabelled mAbs to detect molecular expression of mesothelin by radioimmunoimaging using single photon emission computed

tomography (SPECT). Further, the radiolabelled mAb was conjugated to dextran coated superparamagnetic iron oxide nanoparticles (SPION), to develop a molecular imaging bioprobe for dual modality imaging using SPECT and MRI, thus making it capable of both functional and anatomical imaging with high signal sensitivity and good contrast.

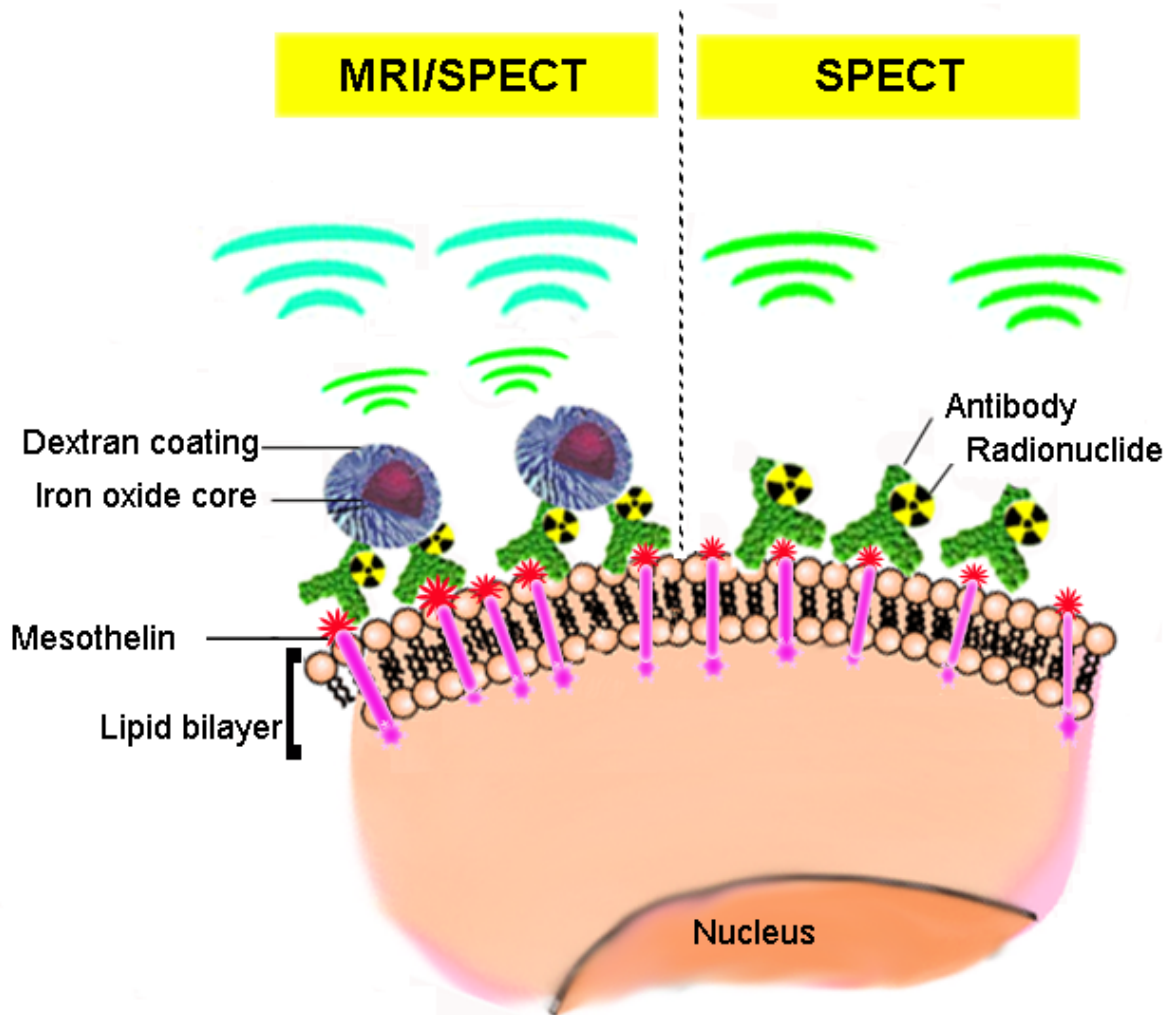


Figure 1.1. Schematic representation of the molecular bioprobes for imaging of mesothelin expressing cancers, developed in the current work.

1.2. Mesothelin Expressing Cancers

Mesothelin is expressed mainly by mesotheliomas, pancreatic and ovarian cancers [11,17,18]. These cancers are characterized by low patient survival rates primarily due to late diagnosis. Therefore, specific targeting of mesothelin expression for early diagnosis as well as treatment monitoring of these cancers represents a potentially important strategy towards improving therapeutic outcomes. Malignant mesothelioma (MM) is an aggressive tumour of serosal surfaces such as the pleura, pericardium, and peritoneum [19]. Exposure to asbestos fibers, which cause progressive scratching of the pleural surface, is the most common cause of MM [20]. It is estimated that the number of patients with MM will continue to increase and reach a peak between 2015 and 2020 [21]. It has been estimated that about 10 million lives may be lost to MM before asbestos is completely banned worldwide [22]. Annually, about 15,000 cases of MM are diagnosed worldwide and the United States alone accounts for about 2200 of these cases. The number of Canadians per year who receive an MM diagnosis has been steadily increasing over the past 20 years [23]. In 2003 (the last year for which data is available), 344 Canadian men and 78 Canadian women were diagnosed with MM. In that same year, 343 Canadians died of the disease [24]. About 50-65% of these mesotheliomas overexpress mesothelin [11,12]. Due to the long latent periods between carcinogen exposure and disease development, and the nonspecific nature of the symptoms preceding diagnosis, a sensitive and specific screening test is pivotal to the early diagnosis of MM [25]. Better imaging of the tumour sites will also permit more accurate, targeted drug or radiation delivery for subsequent management of the disease [26,27]. This approach is also invaluable in tumour-node-metastasis (TNM) staging by assisting thoracic oncologic surgeons to identify the resectability of the tumours prior to surgery [28].

The biological behaviour of MM is very different from that of lung cancer and many difficulties remain in its diagnosis [29]. The diagnosis of MM is hampered by the nonspecific nature and gradual onset of its symptoms [29,30]. As a result, it is usually not diagnosed before the disease has progressed to Stage III or IV [19]. Although cytological diagnosis can be made quickly, MM is usually not diagnosed until 2-3 months after the onset of symptoms [19,30]. Malignant pleural mesothelioma (MPM) is the most common form of MM. Cytologic testing of the pleural fluid has limited value in diagnosing malignant pleural mesothelioma, due to low sensitivity (30-50%) of the test [30,31]. X-rays, computed tomography (CT) scans, MRI, and needle biopsies have limited value in the diagnosis of MPM [19]. Thoracoscopy is considered to be the most accurate for MPM diagnosis, and is the procedure of choice because it affords the pathologist a larger tissue sample [32]. However, it needs to be done in a hospital under general anesthesia. Local radiation may also need to be used because of the possibility of tumour seeding. Advances that have been made in understanding the pathogenesis, diagnosis, and staging of MM have yet to be translated into improved patient survival [33,34]. New approaches incorporating better imaging techniques are urgently needed for more accurate assessment of disease burden and evaluation of treatment response, as well as for better matching of patient population and treatment strategy in clinical trials [25].

Considerable focus has been given to evaluating the best imaging modality for MM [35-37]. CT is the most commonly used imaging modality for the diagnosis, staging, and monitoring of therapeutic response in MM [38]. However, CT has the limitation of underestimating early chest wall invasion and peritoneal involvement [38]. CT also has low sensitivity and specificity in the evaluation of mediastinal lymph node metastasis [39]. MRI is superior to CT in revealing invasion of chest wall and diaphragm [38]. Assessment of the total tumour burden by CT and MRI during the course of treatment is useful in evaluating the therapy [38]. However, this

assessment is based only on anatomical identification of the residual viable tumour, which can often lead to ambiguity in distinguishing active tumour tissue from reparative changes or scars [38]. In case of solid tumours, FDG (fluoro-2-deoxy-d-glucose) accumulation measured by standard uptake value (SUV) using positron emission tomography (PET) can be used for evaluating response to anticancer drugs [38]. In comparison, for a diffuse tumour disease such as MM, the use of SUV alone for monitoring the response to therapy is limited because it is only based on a single pixel and therefore does not take the whole tumour volume into account [38]. This lack of whole tumour volume information can lead to underestimation of spread of the disease. FDG PET still has some prognostic value though it is believed to be an unreliable diagnostic tool for MM [40]. An imaging modality with the potential to distinguish accurately between benign and malignant lesions and to define the extent of disease would be invaluable in the management of MM [38]. Single photon emission computed tomography (SPECT) combined with MRI can potentially overcome these problems.

Pancreatic cancer is the second most common gastrointestinal malignancy and the fourth leading cause of cancer deaths in North America, where 43,000 new cases are diagnosed every year [41]. In Canada alone it is estimated that 4000 new cases of pancreatic cancer will be diagnosed in 2010 (Canadian Cancer Society). About 80% of these cases are diagnosed in the advanced stages of the disease [42]. Surgery remains the sole curative therapeutic option, yet less than 15% of pancreatic tumours are operable due to the propensity for early metastasis [43]. Early detection would allow us to find more tumours when they are still confined to the pancreas and amenable to surgical removal or other therapeutic approaches [44]. Over 90% of malignant pancreatic tumours are adenocarcinomas derived from the ductal epithelium of the exocrine pancreas. Although improved imaging methods are needed to assist detection and treatment, few agents have been designed to image molecular targets expressed by pancreatic adenocarcinomas. Many

molecularly targeted peptides (e.g., secretin, bombesin, CCK) employed in radioactive form as pancreatic tumour imaging agents have limited utility because of the expression of these receptors on cells of the non-cancerous pancreas [45-47]. The ultimate aim of imaging in pancreatic adenocarcinomas has been to determine the resectability of a patient's tumour. It has been suggested that both PET and CT are poor at nodal staging of disease. In detecting metastatic disease, the lack of anatomical definition and poor spatial resolution of PET limit local staging of the disease [48]. MRI has considerable potential in characterizing pancreatic masses by adding anatomic imaging information, especially when using magnetic bioprobes that function as contrast agents to provide high signal sensitivity and good contrast [49].

Ovarian cancer has the highest mortality amongst all gynecologic cancers and is the fifth leading cancer in cancer-related deaths in women in the United States. In the United States, it is estimated that 21,880 (3% of total) of new cancer cases and 13,85000 (5% of total) of cancer-related deaths in 2010 will be caused by ovarian cancers [41]. In Canada, it is estimated that 2600 new cases of ovarian cancer will be diagnosed in 2010 (Canadian Cancer Society). When diagnosed early, the survival rate of patients with ovarian cancer can be higher than 90% [50], but unfortunately 70% of the ovarian cancers are diagnosed only at the advanced stages of the disease [51-53]. The tumour stage at the time of diagnosis has a direct relationship with 5-year survival rates, as seen from the reported 5-year survival rates of 93%, 70%, 37% and 25% for the stages I, II, III and IV [54]. In this context, role of imaging is pivotal for diagnosis, staging and subsequent management of ovarian cancer. Currently, CT is the imaging modality of choice for diagnosis and staging of ovarian cancer, but CT can detect tumours only after they are anatomically differentiated [55]. Additionally, the role of CT is limited in detection and characterization of small-size peritoneal metastases, bowel surface, mesenteric, or peritoneal tumour implants smaller than 5 mm, especially in the absence of ascites [56-58]. The role of

FDG-PET in the primary diagnosis and tissue characterization of ovarian cancer is yet to be completely established due to low specificity and sensitivity as well as due to false-negative results seen with borderline tumours, early carcinomas, and adenocarcinomas [59]. An imaging technique based on detection of molecular markers expressed in ovarian cancers has thus the potential in identifying tumours early, much before the anatomical changes can be detected by CT.

1.3. Molecular Imaging

Molecular imaging allows non-invasive and direct visualization and characterization of cellular processes at a molecular or genetic level *in vivo* [60,61], which are of high relevance to diagnosis and treatment of a disease. According to the American College of Radiology, molecular imaging may be defined as the “spatially localized and/or temporally resolved sensing of molecular and cellular processes *in vivo*” [62]. Although the field of molecular imaging has only seen rapid progress in the last decade or so, molecular imaging has been in clinical practice since the first use of Iodine-131 to test for thyroid cancer [63]. Another example of a molecular imaging technique used in clinical practice today is Fluorine-18-labelled fluorodeoxyglucose positron emission tomography (FDG-PET). FDG-PET is based on the quantification of phosphorylation of 2-deoxyglucose by hexokinase within malignant tissue, for assessment for mediastinal lymphadenopathy [64].

Molecular imaging allows evaluation of specific parameters such as molecular abnormalities [65], growth kinetics [66], angiogenesis [67], tumour cell markers [68] and provides potential for earlier detection, characterization of disease and evaluation of treatment. Currently, the assessment of tumour response to therapy is primarily based on uni-dimensional and bi-dimensional measurements of tumour size according to the Response Evaluation Criteria in Solid Tumours (RECIST) classification [69]. In comparison, molecular imaging offers a major advantage by assessing therapeutic effectiveness at a molecular level, long before phenotypic changes occur. However, *in vivo* molecular imaging is challenging as several criteria for development of molecular imaging bioprobes must be met. The probes must be biocompatible and have an ability to overcome biological delivery barriers (vascular, interstitial, cell membrane) to bind specific receptors with high-affinity [70]. An imaging probe must clear from the blood pool as well as other irrelevant sites within the time frame compatible with the half-life

of the radionuclide. Also signal amplification strategies must be considered based on the probes' signal motif (nuclear, magnetic, optical) (**Figure 1.2**) [70]. Additionally imaging techniques must be sensitive, fast and capable of achieving high-resolution [70].

Nuclear medicine based molecular imaging techniques have the ability to detect and monitor a variety of molecular processes using tracer quantities of radiolabelled probes. Both SPECT and PET modalities have wide ranging applications including oncologic imaging, cardiovascular imaging and imaging of movement disorders [71-74]. Positron emitting radionuclides include isotopes of carbon (^{11}C), nitrogen (^{13}N) and oxygen (^{15}O), which allow radiolabelling of biological compounds of interest [75], while SPECT relies more frequently on the use of radiolabelled analogues with radioisotopes such as ^{111}In and $^{99\text{m}}\text{Tc}$. Examples of molecular imaging applications in nuclear medicine include the detection of specific peptide receptor expression [76,77], angiogenesis [78], multi drug resistance [79,80], hypoxia [81], and glucose metabolism [82]. The major advantage of nuclear medicine methods is that only picomolar concentrations of radiotracers are required to provide a measurable signal without interfering with the process under investigation. In comparison, MR imaging is several magnitudes less sensitive (millimolar rather than picomolar), due to low quantum energy involved and therefore requires signal amplification. However, MR imaging has higher spatial resolution than nuclear imaging methods (micrometer rather than several millimeter) (**Figure 1.2**) [83]. MR image contrast depends on certain fundamental parameters like spin-lattice relaxation time (T_1) and spin-spin relaxation time (T_2), which are a function of the local chemical structure of the molecules being imaged. These parameters can be exploited to reflect the molecular content of the tissue being imaged, therefore making MRI particularly useful for molecular imaging [84]. More recent developments in the field of MRI have facilitated imaging of tissues, cells and molecules. For example, the measurement of transendothelial transport of the MRI contrast agent

by dynamic contrast-enhanced MRI (DCE-MRI) has been used as a marker for angiogenesis in tumours [85]. Cells labelled with MR contrast agents like superparamagnetic iron oxide nanoparticles have been developed [86] which can potentially be used for efficient *in vivo* tracking of stem cells, progenitor cells, or cell lines expressing transgenes, even at the single-cell level [87].

Optical imaging is another imaging modality that is increasingly being used for molecular imaging applications [88,89]. Current optical imaging techniques mainly use fluorescence or bioluminescence as a source of contrast. Molecular optical probes have been studied to image receptor expression of cancer markers, angiogenesis, individual membrane proteins, cellular signaling pathways, atherosclerosis [90-93] and a variety of other cellular and sub-cellular targets *in vivo*. Despite the promise, optical imaging techniques have limited clinical applicability because of substantial attenuation of optical signals. Newer approaches such as near infrared imaging with a potential penetration depth of 10 cm in tissue may ultimately lead to the development of optical tomographic imaging systems in the near-infrared spectrum [94]. However, it is anticipated that clinical approval of optical probes will be more difficult as milligram concentrations of probes are often required for imaging, whereas molecular imaging with radioactive probes (for PET and SPECT) generally requires only nanogram levels of molecular imaging agents.

By combining two or more detection techniques using multi-modal probes it is possible to combine the advantages of one imaging modality with another, and at the same time to reduce the disadvantages of both. This synergistic combination of imaging modalities ensures enhanced visualisation of biological targets thereby providing information on all aspects of structure and function which is difficult to obtain by a single imaging modality [95].

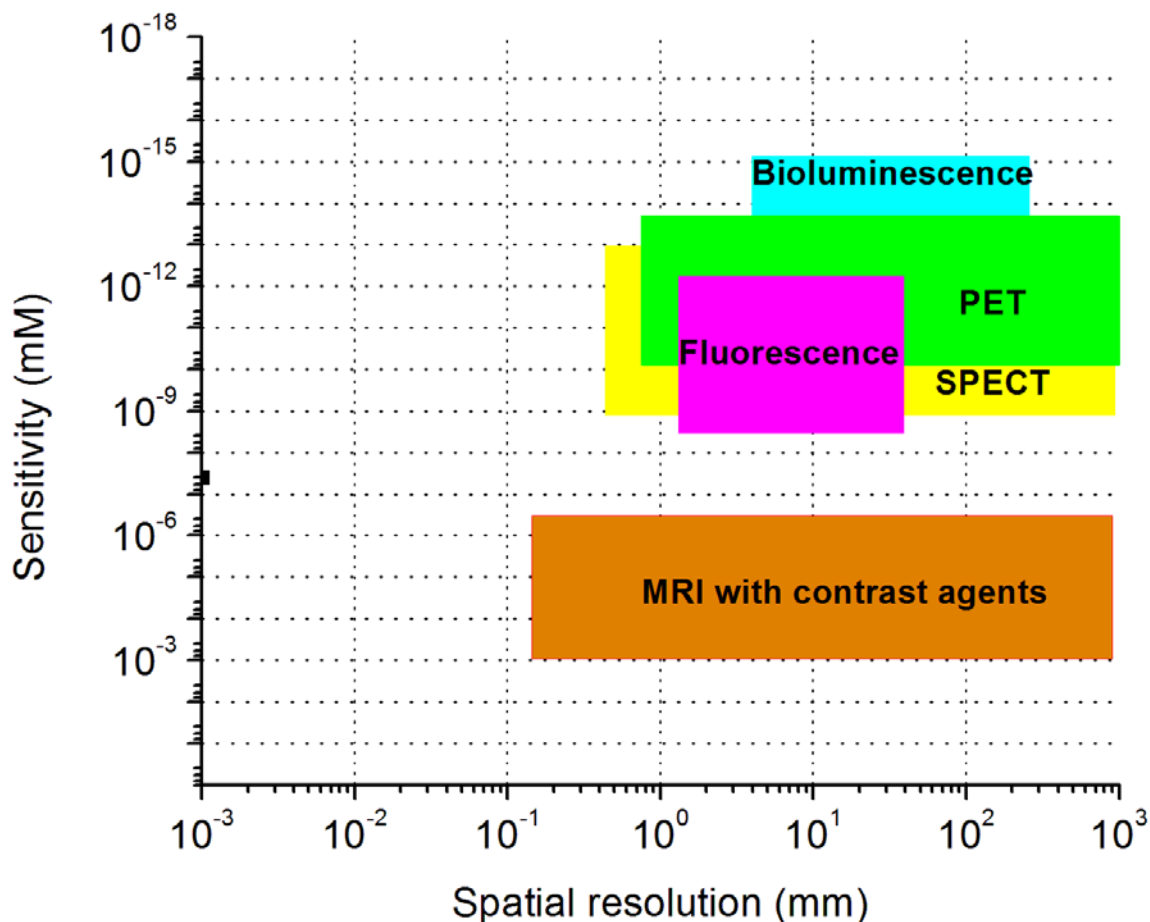


Figure 1.2. A comparison of imaging sensitivities and resolution of commonly used molecular imaging modalities. Adapted from Zhou et al. [96].

1.4. Mesothelin: A Target for Molecular Imaging

Mesothelin is a cell surface glycoprotein present at low levels on normal cells. It is highly expressed in MM, ovarian cancer, pancreatic cancer and some other malignancies [97]. It is a promising candidate for tumour specific therapy and diagnosis, given its limited expression in normal tissues and high expression in mesothelial tumours [98]. The mesothelin gene encodes a 71-kDa precursor protein that undergoes glycosylation to yield a 40-kDa membrane-bound protein termed mesothelin and a 31-kDa shed fragment called megakaryocyte-potentiating factor (MPF) (**Figure 1.3 A**) [98]. Serum MPF has been shown to be a useful marker for the presence

of mesothelioma [99]. Many previous studies have commented on the existence of different mesothelin variants (at least three) [100-103]. It has been commonly agreed that there is only one variant which is predominantly present in human cell lines and tissues, and the remaining variants could be a result of abnormal splicing [12,98,103,104]. It has also been recognized that, there is only a minor difference (about 5%) in the amino acid sequences of the reported mesothelin variants and therefore its impact for applications such as mesothelin-targeted therapy and imaging is minimal [12,97,103]. Our experiments and the discussion throughout this dissertation refers to this predominant mesothelin variant, which corresponds to GenBank accession no. NM_005823.

The biological role of mesothelin is yet to be completely established. For example, Bera *et al.* saw no phenotypical changes in mesothelin-deficient mice [105]. Some studies suggested that mesothelin might have a role in cell adhesion; Rump *et al.* reported that mesothelin interaction with CA125 (cancer antigen 125) mediates cell adhesion leading to the metastatic spread of ovarian cancer [97,106]. Using a cell adhesion assay, Scholler *et al.* further confirmed that over-expression of mesothelin and its interaction with CA125 is associated with increased proliferation, migration, and tumour volume, that is mediated by its role in cell adhesion (**Figure 1.3 B**) [107]. Kaneko *et al.* and Gubbels *et al.* determined that CA125 primarily binds with the N-terminal portion of cell surface mesothelin [108,109]. Additionally, the authors suggested that blocking of this interaction can inhibit cancer cell adhesion and may have a role in prevention of metastatic spread (**Figure 1.3 C**) of mesothelin expressing cancers. In a phase I clinical trial with therapeutic anti mesothelin antibody MORAb-009, Hassan *et al.* reported increased serum levels of CA125, which decreased rapidly after stopping MORAb-009 therapy [110]. The authors further suggested that inhibition of the mesothelin-CA125 interaction could be a useful strategy to prevent tumour metastasis in mesotheliomas and ovarian cancers. Studies by Cheng *et al.*

provide evidence that mesothelin expression is associated with chemoresistance and with shorter disease-free survival and worse overall survival of patients with epithelial ovarian carcinoma [111]. Bharadwaj *et al.* recently reported that mesothelin induces cell proliferation in pancreatic cancer by altering cyclin E via activation of signal transducer and activator of transcription protein 3 (**Figure 1.3 E**) [112]. A role of mesothelin in resistance of tumours to apoptosis mediated by P13K pathway [113] as well as by extracellular signal-regulated kinase signalling pathway (anoiksis, a subtype of apoptosis), has also been reported recently (**Figure 1.3 F**) [114].

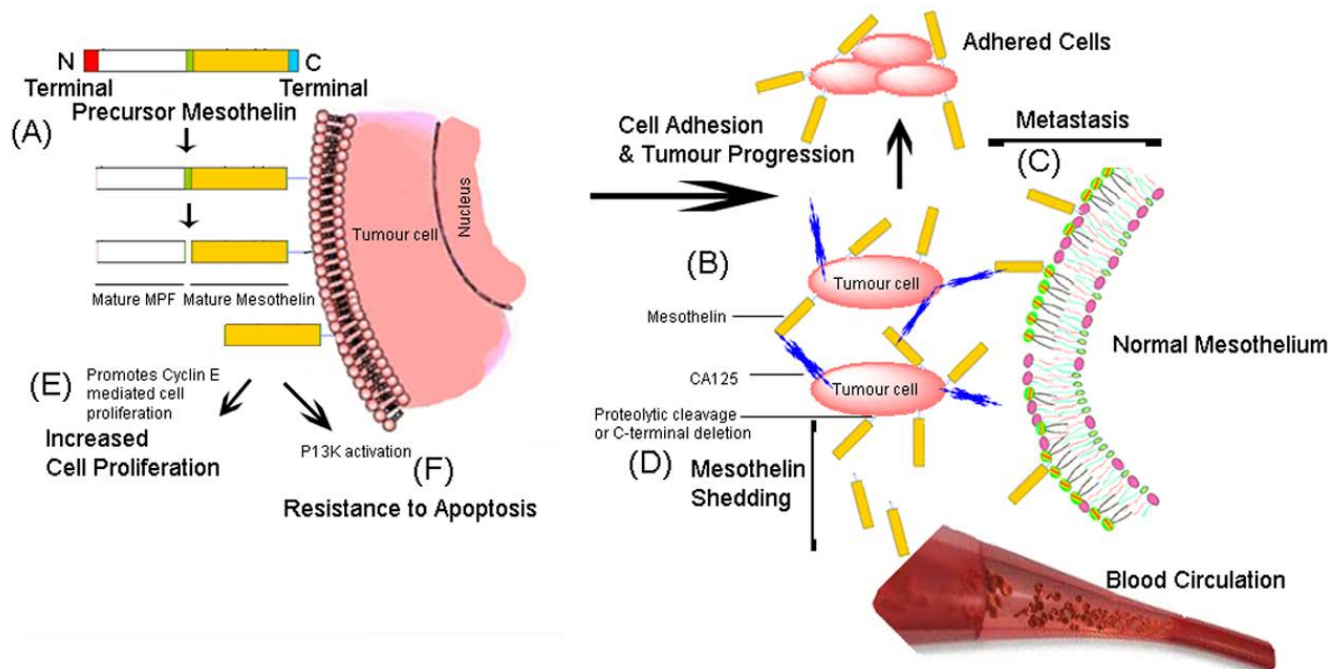


Figure 1.3. Schematic representation of the maturation of mesothelin protein, its proposed role and mechanisms involved.

Mesothelin precursor (71 kDa) undergoes translocation into the endoplasmic reticulum of the cell resulting in removal of N-terminal signal peptide (red) and the C-terminal glycosylphosphatidylinositol (GPI) anchor addition signal (blue region). The latter is replaced with a GPI anchor attached to the cell membrane. Cleavage at the furin site (green region) generates membrane-bound 40 kDa mature mesothelin (yellow) and the 31 kDa secretory protein megakaryocyte-potentiating factor (MPF-white) (A). Interaction of mesothelin with CA125 promotes tumour progression (B) and metastasis (C). Proteolytic cleavage or C-terminal deletion causes mesothelin shedding into blood circulation (D). Mesothelin promotes cyclin E mediated increase in cell proliferation (E) and activates P13K pathway leading to resistance to apoptosis (F). Figure adapted from Hassan *et al.* [98,102].

1.5. Mesothelin Expression in Human Cancers

Mesothelin is mainly expressed in epithelioid mesotheliomas, pancreatic adenocarcinomas and epithelial ovarian cancers. About 50-70% of mesothelioma cancers are of the epithelioid type [115]. In a study by Ordonez *et al.*, it was found that all (100%) of the 44 epithelioid mesotheliomas investigated expressed mesothelin [17]. Another group reported mesothelin expression in 25 of 28 (89%) epithelioid mesotheliomas [116]. Onda *et al.* demonstrated that epithelioid mesotheliomas, as well as the epithelioid component of biphasic mesotheliomas, strongly express mesothelin, whereas sarcomatoid mesotheliomas were invariably negative for this glycoprotein [17]. Recently Yaziji *et al.* showed that reactivity of antibodies towards mesothelin can be used to distinguish epithelioid mesotheliomas for adenocarcinomas [117]. In our own lab we have identified mesothelin expression in 15 out of the 17 epithelioid mesothelioma cases that were tested by immunostaining (**Figure 1.4**). A detailed explanation of these studies has been provided in **Appendix A**. Similar studies by many other authors have reinforced the value of mesothelin for mesothelioma diagnosis [118].

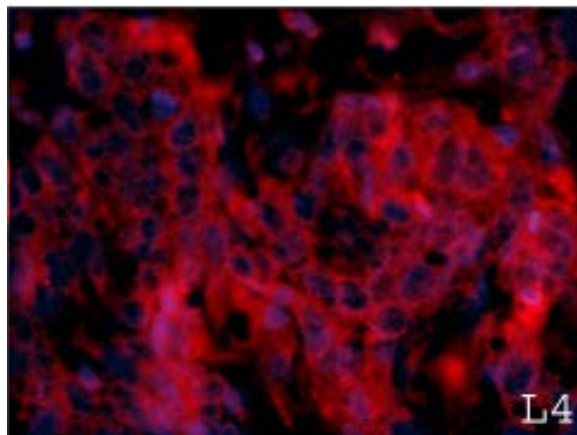


Figure 1.4. Representative fluorescent microscopy image of a positive case (L) of mesothelioma patient tumour sample from the post-mortem histology study. The cell nuclei were stained blue with DAPI. The picture (L4) shows the mesothelin receptors stained red after staining with primary anti-mesothelin antibody and texas-red conjugated secondary antibody.

Argani *et al.* reported the presence of the mesothelin mRNA transcript by *in situ* hybridization and RT-PCR, and verified expression of mesothelin by immunohistochemical analysis in all 60 surgically resected ductal pancreatic adenocarcinomas that were tested [11]. In another study, Hassan *et al.* demonstrated that only pancreatic adenocarcinomas but not the adjacent normal pancreas show mesothelin expression [16]. Furthermore, no expression of mesothelin was detected in normal pancreatic tissues and chronic pancreatitis. Many other studies have reported the over-expression of mesothelin in pancreatic cancers, thereby showing its potential as a diagnostic biomarker and molecular target for imaging and therapy [119-123].

A study that used oligonucleotide microarrays to profile the expression of the mesothelin gene for 150 carcinomas of different anatomic locations showed that serous carcinomas of the ovary and pancreatic adenocarcinomas have the highest average expression of mesothelin. In the same study, tissue microarrays containing 621 carcinomas from the same and additional sites as those profiled by gene expression showed that mesothelin immunoreactivity was highest in cancers of the ovary and pancreas [124]. In studies by Hassan *et al.*, mesothelin expression was noted in 27 of 33 (82%) of serous ovarian cancers [18]. Chang *et al.* used anti-mesothelin monoclonal antibody K1 (mAbK1) to demonstrate mesothelin expression in 10 out of 15 non-mucinous epithelial ovarian carcinomas, but mesothelin expression was absent in all 4 mucinous ovarian cancers examined [125]. Ordonez *et al.* further observed mesothelin expression in 14 of 14 serous, 3 of 3 endometrioid, 6 of 8 clear cell and 3 of 6 mucinous ovarian carcinomas using anti-mesothelin antibody 5B2 [126]. These findings indicate the presence of mesothelin expression in most serous ovarian cancers, which constitute the majority of epithelial ovarian cancers and to a lesser degree in other subtypes of ovarian cancer. Several other authors have further provided evidence about the over-expression of mesothelin in ovarian cancers [12,127,128].

In addition to the above, mesothelin is also commonly expressed in a large number of lung cancers [116] as well as in squamous cell carcinomas found at different sites (cervix, lung and head and neck carcinomas; endometrial adenocarcinomas) [126,129].

1.6. Mesothelin Shedding From Tumour Cells

Mesothelin is expressed at the surface of cells and released into body fluids through deletion at its carboxyl terminus or by proteolytical cleavage from its membrane bound form (**Figure 1.3 D**) [130]. This form of mesothelin is termed soluble mesothelin-related protein (SMRP) and has been suggested as a serum biomarker for the diagnosis of mesothelioma, pancreatic and ovarian cancers [119,131-138]. An ELISA based kit, Mesomark[®], is commercially available for the diagnosis and monitoring of mesothelioma. The kit detects SMRP in the serum of patients [139]. SMRP has also been suggested as a prognostic marker for monitoring therapy of mesothelin expressing cancers [136,140]. In a clinical study, SMRP levels of patients with ovarian tumours were lower than patients with benign tumours. SMRP levels increased significantly with disease progression from early to advanced stage and were also characterized by poorer overall survival [127]. Tajima *et al.* further showed that following chemotherapy the serum levels of SMRP were significantly lower in patients showing partial response to therapy than in patients with stable or progressive disease [141]. These results suggest that serum mesothelin can be used as a marker for chemotherapeutic response in mesothelioma patients.

1.7. Mesothelin Targeted Immunotherapy

Due to its over-expression in many human cancers mesothelin is an attractive candidate for cancer immunotherapy. Several groups have developed mesothelin targeted immunotherapeutic agents (**Table 1.1**). Most notably, a recombinant immunotoxin SS1P (CAT-5001), a chimeric

therapeutic antibody (MORAb-009) and *Listeria monocytogene*-mesothelin vaccine (CRS-207) have all reached the clinical stage of development [110,142-144]. A phase I clinical study among 33 patients (with mesothelioma, ovarian, and pancreatic cancers) treated with recombinant immunotoxin SS1P, showed complete resolution of ascites in at least 2 patients, while 50% of the patients had stable disease [142]. In a separate preclinical study, the authors also reported synergistic anti-tumour activity of immunotoxin SS1P and the chemotherapeutic drug Taxol[®] in tumour bearing mice [145,146]. The authors now plan to conduct another clinical study using a combination of chemotherapy with immunotoxin SS1P [102]. In another clinical study, pancreatic cancer patients vaccinated with autologous tumour cells have shown increased mesothelin-specific CD8⁺ T-cell response, including CD8⁺ T cells that are able to lyse mesothelin-expressing tumour cells [147]. Many other preclinical studies with mesothelin specific DNA vaccines have shown promise in inhibiting tumour growth in mice [123,148-150]. Brockstedt *et al.* demonstrated in preclinical studies that *Listeria monocytogene*-mesothelin vaccine elicits human mesothelin-specific CD4⁺/CD8⁺ immunity in both mice and cynomolgus monkeys, while exhibiting therapeutic efficacy in tumour bearing mice [144]. Based on these findings, a Phase I clinical study was initialized. The results are still awaited. A study evaluating mesothelin targeted adenoviral gene therapy demonstrated increased transduction rates resulting in increased transgene expression in established ovarian cancer cell lines. The authors also tested adenoviruses containing the mesothelin promoter in ovarian cancer cells and demonstrated that mesothelin promoter is transcriptionally active in ovarian cancer cells, but has significantly reduced activity in normal control cells. This study provides evidence that mesothelin could be a potentially useful candidate for combined transductional and transcriptional targeting [151]. In addition to above, several therapeutic antibodies (**Table 1.2**) have shown promise for immunotherapy for mesothelin expressing cancers and have been discussed in section **1.7**.

Table 1.1. Clinical and pre-clinical immunotherapeutic agents designed to target mesothelin antigen.

Agent	Class of Drug	Development Stage	Comments
HN1	Humanized antibody	Pre-clinical	Kills mesothelin expressing cells by antibody dependent cell-mediated toxicity (ADCC) [152].
MORAb-009	Chimeric antibody	Phase II Clinical Trial	ADCC. Enhances anti tumour effects of chemotherapy (Taxol [®] /MORAb-009) [110,143]
22A31	Mouse mAb	Pre-clinical	ADCC [153]
CRS-207	<i>Listeria monocytogene</i> -mesothelin vaccine	Phase I Clinical Trial	Elicits human mesothelin-specific CD4 ⁺ /CD8 ⁺ immunity [144].
DT-A encoding DNA	Nanoparticles with of DNA encoding a diphtheria toxin suicide protein (DT-A)	Pre-clinical	Gene therapy [123,148]
m912	Humanized mAb	Pre-clinical	ADCC [154]
pcDNA3-Hmeso	DNA vaccine encoding human mesothelin	Pre-clinical	CD4 ⁺ and CD8 ⁺ T-cell immune responses as well as the humoral immune responses leading to antitumour effects [150].
pcDNA3-Hmeso540-beta2m-A2	DNA vaccines employing single-chain trimers (SCT)	Pre-clinical	Antigenic peptide-specific CD8 ⁺ T cell immune responses and anti tumour effects [149].
SS1P	Recombinant anti-mesothelin immunotoxin	Phase I Clinical Trial	Kills cells by arrest of protein synthesis and initiation of programmed cell death after binding and internalization to mesothelin expressing cells [142,155-157].
⁹⁰Y labelled SS1scFvSA	Single-chain Fv-streptavidin fusion protein (SS1scFvSA)	Pre-clinical	Radioimmunotherapy [158].
Adenovirus	Advector containing mesothelin promoter gene	Pre-clinical	Gene therapy [151].
K1-LysPE38QQR	Recombinant anti-mesothelin immunotoxin	Pre-clinical	Kills cells by arrest of protein synthesis and initiation of programmed cell death [159].

1.8. Antibodies Against Mesothelin

Amongst all the antibodies against mesothelin (**Table 1.2**), mAbK1 has been most extensively studied for diagnostic as well as therapeutic purposes [18,160-162]. The anti-mesothelin mAbK1 has also been converted to a single-chain Fv (scFv) that is fused to a truncated form of Pseudomonas exotoxin A (PE), resulting in a fusion protein (immunotoxin) SS1P [163]. In another study, mAbK1 was chemically conjugated with LysPE38QQR to form immunotoxin K1-LysPE38QQR. This construct was highly toxic to A431K5 cells (a human epidermoid carcinoma cell line transfected with a mesothelin expression plasmid) with an IC_{50} of 3-6 ng/ml. The immunotoxin had negligible activity against A431 cells that do not express mesothelin (IC_{50} >100 ng/ml). This immunotoxin also caused complete regression of tumours in nude mice bearing mesothelin-positive human carcinoma xenografts [159]. Hassan *et al.* studied mAbK1 labelled with ^{111}In in athymic nude mice bearing one mesothelin-positive and one mesothelin-negative subcutaneous tumour. The biodistribution study showed that the uptake in antigen-positive tumours was higher than blood levels at all time points, and the tumours contained a high level of the radiolabelled mAb even at 7 days [164].

In 2005, two new antibodies, mAbMB and mAbMN were reported by Onda *et al.* which have since become commercially available from Rockland Immunochemicals. Both these antibodies are mouse antibodies which bind to mesothelin with high affinity (**Table 1.2**). The antibody 5B2 has been used for immunostaining of mesothelin expression in mesothelioma, pancreatic cancers and ovarian cancers [16,17,126], but its utility for targeting mesothelin *in vivo* has not been established. Recently, Yoshida *et al.* investigated the biodistribution of ^{111}In labelled anti-mesothelin IgG antibodies and performed PET imaging with ^{64}Cu labelled fab fragments in

tumour bearing mice. The authors' reported preferential uptake of the imaging agents in mesothelin positive tumours, and were also able to visualize the tumours by PET imaging.

In the past 3 years, a lot of progress has been seen in the development of therapeutic anti-mesothelin antibodies. Hassan *et al.* reported a human-mouse chimeric antibody MORAb-009, which exhibits ADCC after internalization by mesothelin expressing cells of mesothelioma, ovarian and pancreatic cancer. The authors further reported that a combination of Taxol[®] and MORAb-009 results in synergistic effects, which caused complete tumour regression in 4 out of 7 mice treated with this combination, compared to none in the control groups [143]. A clinical trial is currently in progress for MORAb-009, and the first results from the trial suggest a role of MORAb-009 in inhibition of the mesothelin-CA125 interaction, which could be a useful strategy to prevent tumour metastasis in mesotheliomas and ovarian cancers [110]. Ho *et al.* developed a fully humanized antibody HN1 from a single chain Fv fragment (scFv) specific to mesothelin. This IgG antibody kills mesothelin expressing cells via ADCC and also prevents the interaction between mesothelin-CA125 [152]. Another humanized antibody, m912, was developed by Feng *et al.* in fab, scFv, and IgG formats, and was shown to be able to specifically recognize and bind cell surface-associated mesothelin with high affinity in all three formats. Further, the authors also reported that in the presence of peripheral blood mononuclear cells, the IgG₁ form of m912 specifically lysed mesothelin-positive cells likely by ADCC but did not affect mesothelin-negative cells [154]. In another study, Inami *et al.* developed a mouse anti-mesothelin antibody, 22A31 which induced NK (natural killer) cell-mediated ADCC resulting in antitumour activity *in vivo* [153].

Table 1.2. Antibodies against mesothelin.

Anti-mesothelin antibody	Type	Isotype / Format	Kinetic dissociation constant K_d	Cell toxicity	Availability	Reference
mAbK1	Mouse	IgG ₁	12 nM	NA	AbCAM	[160]
MB	Mouse	IgG _{2a}	0.6 nM	NA	Rockland Immunochemicals	[165]
MN	Mouse	IgG _{2a}	1 nM	NA	Rockland Immunochemicals	[160]
5B2	Mouse	IgG ₁	Unknown	NA	Novacastra Labs	[160]
Anti-mesothelin IgG	Mouse	IgG ₁ , Fab	4 to 8 nM	NA	Unknown	[166]
MORAb-009	Mouse-human chimeric	IgG ₁	1.5 nM	ADCC	Morphotek	[110,143]
HN1	Human	IgG ₁	3 nM	ADCC	Unknown	[152]
m912	Human	IgG ₁ , Fab	1.5 nM	ADCC	Unknown	[154]
22A31	Mouse	IgG	Unknown	ADCC	Unknown	[153]

1.9. Radiolabelled Antibodies in Diagnosis and Therapy of Cancer

The use of antibodies as radioactive tracers was pioneered by Pressman *et al.* in 1948, who radiolabelled anti-mouse kidney anti sera and polyclonal antibody with ^{131}I [167]. Subsequently, the authors also obtained radioautographs of kidney tissue to demonstrate localization of activity in kidneys [168]. Pressman *et al.* were also the first to demonstrate localization of ^{131}I labelled anti-osteogenic sarcoma polyclonal antibodies in osteogenic tumours in mice for the purpose of radioimmunodetection [169]. Further, in 1974, Mach *et al.* and Goldenberg *et al.*, reported localization of radioiodinated anti-CEA polyclonal antibodies CEA expressing tumour xenografts in nude mice and in a Syrian hamster model, respectively [170,171]. Thereafter, many other studies reported the use of radiolabelled polyclonal antibodies, but the non-specificity and cross-reactivity due to their polyclonal nature limited their usefulness as radiotracers for clinical use [172-174]. In 1975, Nobel laureates Kohler and Milstein developed the hybridoma technology facilitating the manufacture of monoclonal antibodies with ability to specifically bind antigens [175]. Monoclonal antibodies can be made against virtually any biomolecule; therefore there is an opportunity to develop specific radiotracers that target many physiological and pathophysiological processes of importance to cancer biology, diagnosis, and therapy. This approach has led to advances in both diagnosis (radioimmunoimaging) and therapy (radioimmunotherapy). ^{90}Y -ibritumomab tiuxetan (Zevalin; IDEC Pharmaceuticals Corporation) and ^{131}I -tositumomab (Bexxar; Corixa and GlaxoSmithKline Corporations) are FDA approved radiolabelled antibodies for the treatment of cancer [6]. Both work by directing an antibody to the CD20 antigen that is abundantly present on normal and malignant B cells of follicular non-Hodgkin's lymphoma. Radioimmunoscintigraphy using radiolabelled antibodies has also been used for the diagnosis of various human solid tumours [176] and lymphomas [177]. The commercial product arcitumomab (CEAscan) is a $^{99\text{m}}\text{Tc}$ -labelled fab fragment directed against

CEA (carcinoembryonic antigen). Clinical trials with arcitumomab have been successful in detecting colorectal cancer [7], including occult colorectal cancer when conventional imaging methods, such as CT, are negative [178]. These tumours are difficult to diagnose and may be missed by FDG-PET if well differentiated [179]. Capromab pendetide (ProstaScint) is an IgG1 murine mAb (7E11-C5.3) labelled with ^{111}In via linker-chelator, glycyl-tyrosyl-lysyl-diethylenetriamine pentaacetic acid. Capromab pendetide reacts with an intracellular epitope of prostate-specific membrane antigen, and has been shown to be advantageous primarily for the detection of soft tissue lesions, especially lymph node metastases [180,181]. The imaging technique is difficult to perform, and fusion imaging of capromab pendetide using SPECT with CT or MRI is a highly valuable adjunct [180]. $^{99\text{m}}\text{Tc}$ labelled fab fragment of the pancarcinoma murine antibody NR-LU-10 (Nofetumomab merpentan - Verluma) has also been used as a diagnostic imaging agent in staging patients with lung cancer [182].

1.10. Factors to be Considered for Selection of a Radionuclide for Imaging

Various selection criteria need to be considered when choosing a radionuclide for radioimmunoimaging [183]:

- a) The physical half life should be between 6 and 200 hours, which is sufficiently long to allow imaging at the time when target to non-target ratio (T/N) reaches a maximum.
- b) The gamma energy range (100-300 keV) matches with most of the clinically available scanners in nuclear medicine.
- c) Single energy gamma abundance per decay and a high photon density is desired for obtaining high resolution.
- d) It does not emit low abundance or low energy particulate radiation, so that the secondary radiation dose to the patient is minimized.

- e) The daughter product of the radionuclide is stable, and thus prevents an exposure to additional radiation dose from the daughter nuclei.
- f) It can be produced in the carrier free form, so as to yield a radiolabelled product with high specific activity.
- g) It is easily available and has a reasonable cost.

Based on the above listed criteria, ^{99m}Tc with a physical half life of 6 hours is widely recognized as the radionuclide of choice for most nuclear medicine studies, preventing excessive radiation dose to the patient [184] and allowing for optimal imaging due to its major gamma line at 140 keV [183]. Other advantages of ^{99m}Tc include easy availability, and the fact that its decay product has a very long half life which does not deliver any additional dose to the patients and also does not obscure the image. In addition to ^{99m}Tc , ^{111}In is another isotope commonly used in nuclear medicine. ^{111}In has a half life of 68 hours and major gamma energy lines at 171 and 245 keV, with no beta emission. ^{111}In is especially suitable for imaging with antibodies due to ease of radiolabelling via metal chelators as well as due to its sufficiently long half life that allows imaging after a time period during which antibodies have cleared from the circulation, thus reducing the background. ^{123}I and ^{131}I are other radionuclides of choice for γ -scintigraphy. However, their clinical applications are limited due to the high cost, poor availability and relatively low *in vivo* stability [183,185].

1.11. Factors Affecting Accumulation of Antibody Conjugated Imaging Agents in Tumours

1. Antibody affinity

Binding of antibodies to tumour associated antigens (TAA's) depends on their affinity for the antigen. The antibodies with higher affinity (low dissociation constant, K_d for the antigen) usually lead to higher tumour uptake and better images. A K_d value between 10 pM to 10 nM is

usually considered ideal for imaging. An antibody with very high affinity ($K_d < 10$ pM), could mean that its pharmacokinetics are heavily dependent on flow or permeability, while for a low affinity antibody ($K_d > 10$ nM), it may be difficult to achieve sufficient specific binding to allow targeted imaging [186].

2. Antigen concentration

A high concentration of TAA's means higher availability of receptors for binding to antibody molecules. As a result the tumours can take up a greater number of antibodies before being saturated, which results in a higher concentration of specifically targeted molecular imaging bioprobes in the tumours.

3. Blood flow

Blood flow to the tumour cells is essential for maintaining a supply of imaging bioprobes for binding to the cells. This helps in achieving a concentration gradient between the blood and the tumour, which is the driving force for diffusion of imaging agents from the vascular compartment into the tumour. Higher and longer presence (long circulation time) of the imaging agents in the blood will lead to higher accumulation of the imaging bioprobes in the tumours. Blood flow to the tumours is affected by tumour size, so as the tumour enlarges with rapidly dividing cancer cells outgrowing the blood supply, a necrotic tumour core is formed resulting in lower activity uptake per weight of tumour tissue [183].

4. Permeability

Tumour permeability depends on the hydrostatic pressure inside the tumours as well as the size of the molecular bioprobes. In general, a low hydrostatic pressure and low molecular weight (e.g., antibody fragments) of the bioprobes will lead to higher tumour permeability, resulting in increased concentration of the imaging bioprobes inside the tumours.

5. Non-specific binding

Fc receptor mediated binding to cell membranes in liver, spleen, and blood accounts for a large non-specific uptake of the antibody based molecular bioprobes, thus resulting in a decreased amount of bioprobes available for specific targeting.

6. Distribution, metabolism and excretion

Biodistribution and metabolism of the molecular bioprobes is based on many factors. For example, antibody fragments are mainly taken up and metabolized in kidneys whereas the whole antibodies are metabolized in the liver [187,188]. Also the number of chelator molecules attached to the antibody alters its biodistribution as an antibody with a higher number of attached chelator molecules undergoes rapid removal by the liver [183]. The isoelectric point of the antibody also impacts its biodistribution [189,190]. Chelator labelled antibody probes undergo slower elimination compared to directly labelled probes. Whole antibodies undergo slower elimination compared to lower molecular weight antibody fragments (fab and f(ab')₂). The presence of shed antigen in the circulation also alters the pharmacokinetics of the antibody by forming immune complexes with the molecular bioprobes, which are then removed from the blood circulation by spleen and liver. This results in lower uptake of the radiolabelled bioprobes by the tumour.

7. Antibody Dose

At low doses large proportion of the bioprobes can be taken up by the liver and spleen, resulting in decreased availability for tumour localization [191].

1.12. Dual Modality Imaging with SPECT/MRI

Nuclear medicine imaging techniques, such as SPECT, allow non-invasive determination of *in vivo* biodistribution of radiotracers at picomolar concentrations. By using specific radiolabelled probes, functional information about molecular processes can be obtained using SPECT. However, due to lack of anatomical references, SPECT images need to be co-registered with anatomic images obtained by CT or MRI. MRI is advantageous to CT due to lack of ionizing radiation, high soft-tissue contrast, and sensitivity to tissue alterations. Further, imaging with contrast agents such as gadolinium and iron oxide extends MR into the domain of molecular imaging, thus offering an excellent capability of examining soft tissues. Therefore, dual modality imaging with SPECT and MRI not only provides anatomical references in an image but also acts synergistically to combine the high spatial resolution associated with MR with the high sensitivity of SPECT [192]. Dual modality imaging bioprobes would allow simultaneous SPECT/MRI imaging, thus making possible the dynamic imaging with radiotracers and MRI contrast agents. This would facilitate non invasive monitoring of treatment as well as study of pharmacokinetics and metabolism of drugs. Additionally, simultaneous dual modality imaging with MRI and SPECT can reduce the overall scan time, avoid multiple anesthesia sessions and the errors associated with co-registration.

Despite the promise, simultaneous SPECT/MRI dual modality imaging technology is still in its infancy, due to the technological challenges in operating a SPECT scanner within an MR

instrument. PET and SPECT detectors based on scintillators coupled to photomultiplier tubes and associated electronics commonly are highly sensitive to magnetic fields. SPECT instrumentation also consists conducting and radiofrequency radiating components which can potentially interfere with the MRI system. In addition, effects such as the induction of eddy currents, the introduction of susceptibility artifacts, and an increase in temperature or vibrations induced by the running of MRI sequences also create interferences with the nuclear detectors [193]. With the development of gamma ray detectors based on avalanche photodiodes (APD's) as well as availability of fast scintillation materials like lutetium oxyorthosilicate (LSO), it has become possible to incorporate fully magnetic-field-insensitive high-performance PET detectors within PET/MRI scanners [193-195]. An initial study using a similar hybrid PET/MRI system has demonstrated the feasibility of structural, functional, and molecular imaging of brain tumours in patients [196]. Similar design principles apply to the development of SPECT/MRI scanners, where semiconductor detectors (cadmium–zinc–telluride [CZT]) used in small-animal SPECT were shown to be insensitive to magnetic fields up to 7 T, leading to the development of a prototype for simultaneous SPECT/MRI systems [197]. Further, Hamamura *et al.* have recently demonstrated that simultaneous SPECT and MRI data acquisition is feasible, justifying the further development of SPECT/MRI for small-animal and whole-body human imaging. The research in this dissertation focuses on developing SPECT/MRI imaging agents for use with such dual modality scanners.

1.13. Contrast Agents Used in MRI

There are essentially two types of agents used in MRI classified as T_1 and T_2 contrast agents. Although all contrast agents produce both T_1 (longitudinal) and T_2 (transverse) relaxation, the type of relaxation produced to a greater extent defines how we classify them. The ability of MR contrast agents to produce relaxation is expressed in terms of relaxivity. The relaxivity value is a

parameter that describes the enhancement of the water proton relaxation rate ($1/T_1$ or $1/T_2$) in solutions containing 1 mM of the magnetic solute. Due to low concentration of biological targets, contrast agents with high sensitivity are required for molecular imaging. This is a challenge, as most contrast agents are not very sensitive. Considerable research has thus focused on the design of metal complexes with high relaxivity values. Paramagnetic complexes of metal ions with symmetric electronic ground states, such as gadolinium (Gd(III)) and Manganese (Mn(II)), produce T_1 contrast due to an ability to catalyze the relaxation process of surrounding water protons, commonly expressed in terms of the longitudinal relaxivity (r_1). The paramagnetic metal complexes produce hyperintensity (bright contrast) in T_1 -weighted MR images as a consequence of predominantly longitudinal relaxation process, whereas T_2 contrast agents produce a hypointense (dark) contrast due to higher transverse relaxation.

Superparamagnetic iron oxide nanoparticles (SPIONs) are able to efficiently shorten T_2 , and particularly T_2^* (contribution of both transverse relaxation and local magnetic field non-uniformities), of water protons and therefore have been utilized as MR imaging probes for molecular imaging experiments [198]. T_2 shortening is a result of increase in transverse relaxation characterized by change in relaxation rate of protons in the surrounding water [199].

SPIONs typically consist of a crystal core of magnetite (Fe_3O_4) and maghemite (Fe_2O_3) coated with a suitable material with an overall diameter between approximately 60 and 250 nm [200,201]. Size characteristics play an important role in determining the pharmacological and magnetic properties of SPIONs. Particles with monodisperse population of crystal cores and high degree of crystallinity are important to achieve good relaxivity characteristics required to obtain imaging probes with high sensitivity. SPIONs in the size range of 20–50 nm are typically characterized by a higher r_2 value. For *in vivo* applications, the particle needs to be coated with a

suitable biocompatible material to prevent aggregation and sedimentation and to improve stability. In addition, the surface coating is also critical for defining the pharmacokinetic behavior of the particle, since the nanoparticles, when introduced into the body are recognized as foreign and undergo phagocytic uptake into the macrophage-rich organs like spleen and liver. Coatings such as PEG (poly ethylene glycol) reduce the ability of serum proteins to recognize the particle and thus prolong circulation times in the blood pool [202]. In addition to PEG, materials such as dextran, starch, and silica are frequently utilized as coating materials for SPIONs [203-205].

Targeted imaging with iron oxide particles is often pursued because the particles have sensitivity in the nanomolar range. The clinical use of SPIONs is primarily in the detection of liver and lymph node lesions [206,207]. Recently, it has been shown that antibodies conjugated with SPIONs can non-invasively image HER-2 expressing cells or tissues both *in vitro* and *in vivo* by MRI [208]. In another study, ⁶⁴Cu labelled-SPION probes produced strong MR and PET signals and were stable in mouse serum for 24 hours at 37°C making them attractive for the development of dual modality PET/MRI bioprobes. The good sensitivity and the ability to be efficiently taken up by cells, either by passive or active means, are specific advantages associated with SPIONs for MR imaging. However, the uptake of SPIONs by phagocytic cells make it necessary to use specific target approaches for their delivery into tumours or other cells of interest (e.g., cardiac myocytes, endothelial cells [209-211]). In addition to iron oxide based nanoparticles, other nanosystems utilizing bimetallic cores, e.g., iron cobalt (FeCo) or manganese ferrite (MnFe₂O₄), have shown promise for developing T₂ contrast agents with higher relaxivity [212-214]. Such nanoparticles are still at the preclinical stage of development and their clinical translation will require a careful assessment of their toxicity.

1.14. Dissertation Overview

The work in this dissertation is aimed towards the development of molecular mesothelin imaging bioprobes. The work is based on the premise of using anti-mesothelin monoclonal antibodies as specific targeting ligands for the delivery of radionuclides and magnetic nanoparticles as motifs for SPECT and MR imaging, respectively. The development of a molecular imaging bioprobes will provide a powerful diagnostic tool for early diagnosis and monitoring of mesothelioma, pancreatic and ovarian tumours, which are all cancers that express mesothelin.

In chapter 2 of this dissertation, studies using ^{99m}Tc labelled mAbK1 antibody and its fab and f(ab)_2 fragments are described. Both direct and indirect labelling methods were investigated for the development of the radiolabelled probes. The *in vitro* properties of the radiolabelled probes were determined using mesothelin expressing NCI-H226 cells. Biodistribution and tumour uptake of ^{99m}Tc labelled, mAbK1, and its fab and f(ab)_2 fragments were evaluated in tumour-bearing mice.

In chapter 3, the characteristics of ^{111}In labelled mAbMB were investigated and compared to ^{111}In labelled mAbK1. *In vitro* and *in vivo* studies were performed using mesothelin transfected A431K5 cells. Biodistribution and SPECT/CT imaging studies were performed in tumour bearing mice to determine the suitability of the radiolabelled probes for imaging mesothelin expressing tumours.

In chapter 4, conjugates of ^{111}In labelled mAbMB with SPIONs were developed and further examined using *in vitro* and *in vivo* studies. The relaxometric properties and cellular uptake of the conjugates were investigated in order to determine whether the conjugates are adequate

SPECT/MRI dual modality molecular imaging bioprobes. Biodistribution and MR imaging properties of the dual modality probes were evaluated in tumour bearing mice.

1.15. Research Objectives

This work addresses the need for molecular imaging bioprobes so that tumours expressing mesothelin antigen can be imaged. The main objectives of the work described in this dissertation are:

1. To radiolabel the anti-mesothelin antibody mAbK1 and its fab and f(ab')₂ fragments with ^{99m}Tc, and evaluate biodistribution and tumour uptake in tumour bearing mice.
2. To develop molecular bioprobes by radiolabelling the anti-mesothelin antibody mAbMB with ¹¹¹In and evaluate its potential for imaging mesothelin expressing tumours in mice.
3. To develop dual modality SPECT/MRI imaging bioprobes by conjugating the ¹¹¹In-labelled mAbMB antibody to magnetic nanoparticles and test their biodistribution and MR imaging properties in tumour bearing mice.

1.16. Impact of Research

Molecular imaging will have a tremendous impact in the development of innovative diagnostic tools for early diagnoses and therapeutic treatment monitoring. The design of molecular imaging agents that probe molecular processes is central to molecular imaging. For mesothelioma, ovarian and pancreatic cancers, which all over-express mesothelin, molecular imaging is expected to play a pivotal role in improving patient survival by detecting the cancers early, staging them more exactly, and monitoring therapy success.

The work in this dissertation provides direct evidence of the potential of mesothelin directed molecular imaging of cancers. The data from chapter 3, for the first time demonstrates successful SPECT/CT imaging of mesothelin expressing tumours. The results show that an ^{111}In labelled antibody mAbMB has the potential to being translated into clinical use. Such radiolabelled imaging bioprobes would be useful in the early detection of tumours, as well as the assessment of patient response to therapy.

Data from chapter 4 is highly relevant for the development and validation of multimodality probes, especially for SPECT/MRI imaging. With the recent progress in the development of SPECT/MRI scanners, such probes will be required to take advantage of the synergism between the two imaging modalities. The development of multimodal probes is especially important for cancers of pancreas, ovaries and mesothelioma, for which better imaging techniques are direly needed for early detection as well as successful therapy.

The findings of chapter 2 shed light on the need for appropriate cell models and antibodies for the development of mesothelin targeted imaging as well as therapeutic agents and therefore is of high significance to the related pre-clinical research. The $^{99\text{m}}\text{Tc}$ labelling method developed for radiolabelling of fab and f(ab')_2 fragments, provides a new bioconjugation method for labelling biomolecules via histidine-modified tridentate ligand.

Chapter 2: Evaluation of Technetium-99m Labelled Anti-mesothelin Antibody mAbK1 and its fab and f(ab')₂ Fragments in a Mesothelin Expressing Cell Model.

2.1. Introduction

2.1.1. ^{99m}Tc Labelled Anti-mesothelin Antibody mAbK1

Specific molecular bioprobes in the form of anti-mesothelin radiolabelled antibodies have enormous potential to be used for mesothelin directed imaging of mesotheliomas, pancreatic and ovarian cancers. The first anti-mesothelin antibody, mAbK1 was reported by Chang *et al.* in 1992. They isolated mAbK1 from the spleen lymphocytes of mice immunized with periodate-treated human ovarian carcinoma (OVCAR-3) cells [125]. Other commercially available mouse monoclonal anti-mesothelin antibodies are mAb5B2, mAbMN and mAbMB. While none of the above antibodies has cytotoxic effects, two cytotoxic antibodies MORAb-009 and m912 have recently been reported. MORAb-009, a chimeric antibody is currently being investigated in a clinical trial for the treatment of mesothelin expressing mesothelioma, pancreatic, non-small cell lung and ovarian cancers [143]. M912 is a fully humanized antibody which is promising for therapy of mesothelin expressing cancers [154].

Among several available anti-mesothelin antibodies, mAbK1 has been the most extensively studied [18,160-162] and was considered the most appropriate candidate for our experiments because of promising results reported in many previous studies [142,155,159,163,164]. Hassan *et al.* studied mAbK1 labelled with ¹¹¹In in athymic nude mice bearing one mesothelin-positive and one mesothelin-negative subcutaneous tumour. The biodistribution study showed that the uptake in antigen-positive tumours was higher than blood levels at all time points, and the tumours contained a high level of the radiolabelled mAb even at 7 days [164]. These studies show that the mAbK1 efficiently recognizes and targets the mesothelin expressing cells and is promising for diagnostic as well as therapeutic purposes.

^{99m}Tc with a physical half life of 6 hours is widely recognized as the radionuclide of choice for most nuclear medicine studies, preventing excessive radiation dose to the patient [184] and allowing for optimal imaging due to its gamma energy of 140 keV [183]. The ability to successfully incorporate ^{99m}Tc into targeting molecules is the foremost consideration in developing ^{99m}Tc based diagnostic radiopharmaceuticals. ^{99m}Tc labelling of antibodies and their fragments has been a subject of considerable research and both direct and indirect labelling methods have been explored by researchers in the past [215-217]. Direct methods rely on covalently linking ^{99m}Tc with the endogenous thiols of the antibody produced after reduction of its inter-chain and intra-chain disulfide bridges. Indirect methods work by incorporating a bifunctional chelator between the biomolecule and ^{99m}Tc , which acts as a strong chemical tether to hold ^{99m}Tc within the radiopharmaceutical complex. Alberto *et al.* described an indirect method for ^{99m}Tc labelling using the $^{99m}\text{Tc(I)}$ tricarbonyl ($[\text{}^{99m}\text{Tc}(\text{CO})_3]^+$) core, which has been commonly employed in recent years [218]. The $[\text{}^{99m}\text{Tc}(\text{CO})_3]^+$ core is advantageous as it provides an ideal geometry for the labelling of chelators with high specific activity, while also being small, kinetically inert and stable to oxidation. Bioconjugates incorporating the $[\text{}^{99m}\text{Tc}(\text{CO})_3]^+$ core have been developed for various biomolecules including carbohydrates [219,220], peptides [221,222], recombinant proteins [223] and nucleotides [224]. Until now, the labelling of targeted biomolecules such as scFv's [225], nanobodies [226], minibodies [227] and affibodies [228] with the tricarbonyl core has typically been accomplished via histidine tags produced by protein engineering techniques. To our knowledge, for antibodies and antibody fragments that are not genetically engineered to express histidine tags, bifunctional chelator mediated labelling with $[\text{}^{99m}\text{Tc}(\text{CO})_3]^+$ core has not been reported yet.

2.1.2. Improving Tumour Penetration with Antibody Fragments

For imaging, it is critical to achieve high tumour uptake of the antibody as well as high tumour to blood ratio. The elevated interstitial pressure in tumours arising from inadequate lymphatic function often slows or impedes tumour penetration of the whole IgG molecule [229]. It is therefore important to consider strategies to prevent low uptake due to fast clearance or tissue binding of mAbK1. Promising in this regard is the use of antibody fragments that still contain the antibody binding sites such as fab (~50 kDa) or f(ab')₂ (~100 kDa). To select the most optimal form of the targeting molecule, we decided to evaluate both fab and f(ab')₂ fragments along with the whole mAbK1 for their suitability as an imaging probe to target mesothelin.

2.1.3. Current Study Outline

The aim of this study was to evaluate the potential of the anti-mesothelin antibody mAbK1 and its fragments fab and f(ab')₂ (**Figure 2.1 A, B & C**) to selectively accumulate at the tumour site and allow diagnostic radioimmunoimaging. The experiments presented in this chapter are outlined in the schematic shown in **Figure 2.2**. For the *in vitro* characterization and *in vivo* biodistribution studies, we chose NCI-H226 cells, which have shown highest mesothelin expression amongst the established cell lines as reported by Fan *et al.* [157]. Antibody mAbK1 (whole IgG) was radiolabelled with ^{99m}Tc using a direct labelling approach. ^{99m}Tc labelling of fab and f(ab')₂ fragments was accomplished using a N-(*o*-phenol)-histidine chelator. ^{99m}Tc labelled mAbK1 (^{99m}Tc-mAbK1), fabK1 (^{99m}Tc-fabK1) and f(ab')₂K1 (^{99m}Tc-f(ab')₂K1) radioimmunoconjugates were characterized *in vitro* for stability and immunoreactivity. Finally, SCID mice bearing NCI-H226 tumours (mesothelin positive) and LCC6-HER2 tumours (mesothelin negative), were intravenously injected with different ^{99m}Tc labelled radioimmunoconjugates and biodistribution was determined at different time intervals post-

injection. Mesothelin expression of excised NCI-H226 tumours was verified by Western blot studies.

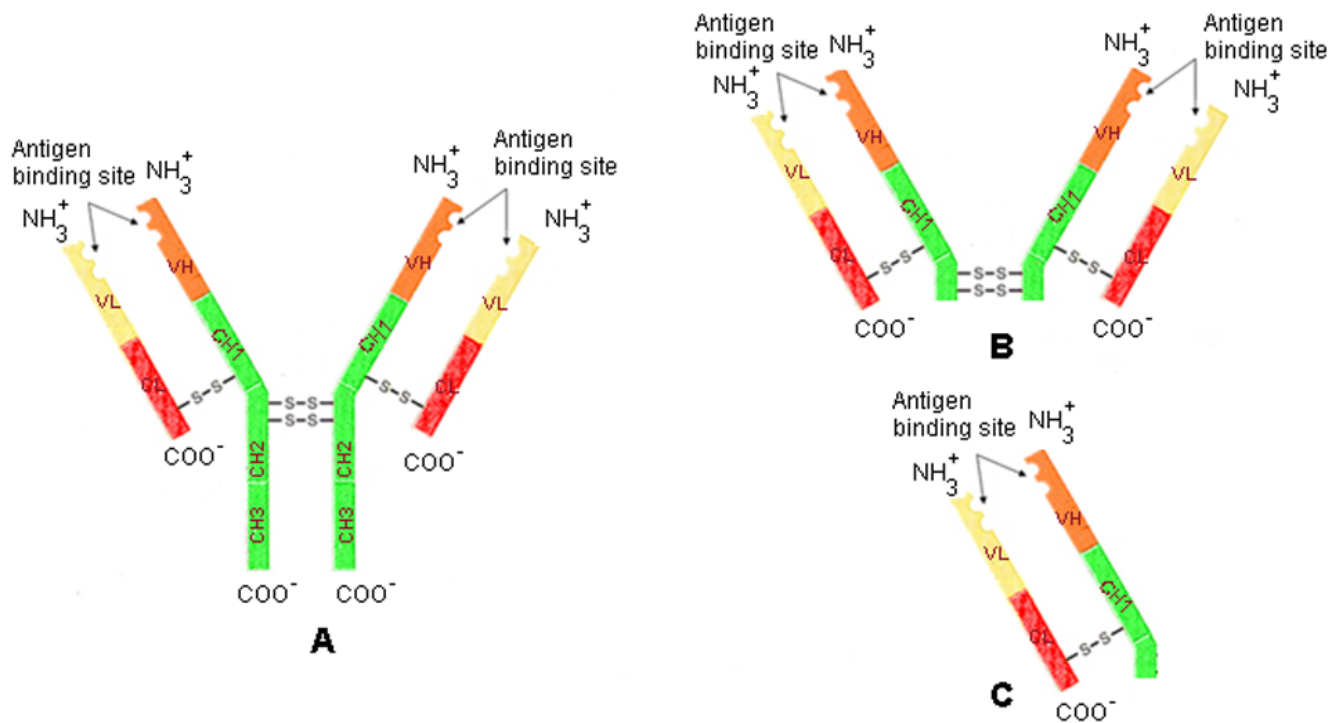


Figure 2.1. Schematic picture of A) mAbK1, B) f(ab)₂ fragment and C) fab fragment.

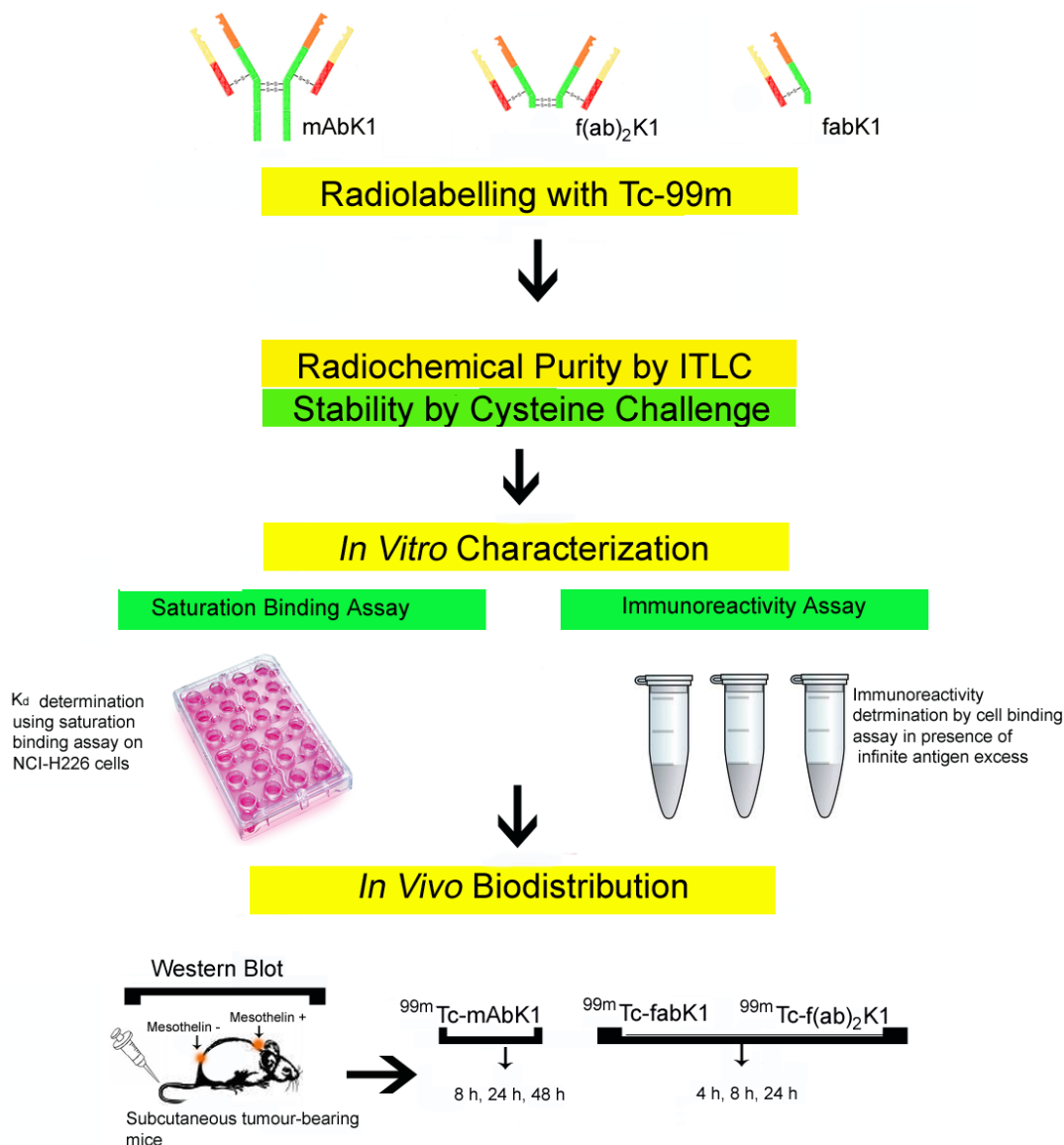


Figure 2.2. Experimental overview of chapter 2.

mAbK1 and its fab and f(ab)₂ fragments were radiolabelled with ^{99m}Tc. Radiochemical purity was determined by ITLC followed by stability studies using cysteine challenge. A saturation binding assay on mesothelin expressing NCI-H226 cells was used to determine the binding affinity (K_d-dissociation constant) of ^{99m}Tc-mAbK1, ^{99m}Tc-fabK1 and ^{99m}Tc-f(ab)₂K1. Immunoreactivity of the radioimmunoconjugates was determined in presence of infinite antigen excess, by a cell binding assay. Biodistribution studies were carried out in SCID mice bearing subcutaneous xenografts of NCI-H226 (mesothelin positive; neck) and LCC6-HER2 (mesothelin negative; lower back). Radioimmunoconjugates were injected through the tail vein and biodistribution determined at 8 hours, 24 hours and 48 hours for ^{99m}Tc-mAbK1 and at 4 hours, 8 hours and 24 hours for ^{99m}Tc-fabK1 and ^{99m}Tc-f(ab)₂K1. Mesothelin expression of excised tumours was verified by Western blot.

2.2. Materials

All chemicals and reagents were purchased from Sigma, Aldrich (Oakville, Ontario, Canada). The mAbK1 antibody was purchased from Abcam (Cambridge, Massachusetts, U.S.A.), ITLC strips were obtained from Biodex (Cat# 150-005; Biodex, Shirley, New York, U.S.A.), mouse IgG1 fab and f(ab')₂ preparation kit was purchased from Thermo Scientific (Rockford, Illinois, U.S.A.). The Isolink kits were received as a generous gift from Mallinkrodt (now Covidien, St. Louis, Missouri, U.S.A.) and [^{99m}Tc(H₂O)₃(CO)₃]⁺ was prepared according to the manufacturer's instructions. Sodium pertechnetate was obtained from Vancouver General Hospital (Vancouver, Canada). The cell culture media and supplements were obtained from Invitrogen (Burlington, Ontario, Canada). The mesothelioma cell line NCI-H226 (mesothelin positive) and the breast cancer cell line LCC6-HER2 (mesothelin negative) were generously provided by Drs. Wan Lam and Donald Yapp, respectively, from the British Columbia Cancer Research Centre (Vancouver, Canada). Ultracel-YM30 (30 kDa cut off) and YM100 (100 kDa cut off) microconcentrators were purchased from Millipore Corporation (Billerica, Massachusetts, U.S.A.). Reagents for electrophoresis were purchased from BIO-RAD Laboratories (Mississauga, Ontario, Canada). The radioactive TLCs were autoradiographed using a phosphor imager (Cyclone storage phosphor imager with 20×25 cm² phosphor screen; Perkin-Elmer, Waltham, Massachusetts, U.S.A.) and analyzed using OptiQuant software. Activity measurements were carried out using a Packard Cobra II gamma counter (Perkin-Elmer, Waltham, Massachusetts, U.S.A.).

2.3. Methods

2.2.1. ^{99m}Tc Labelling of mAbK1 Antibody

The full size mAbK1 antibody was radiolabelled with ^{99m}Tc by the direct labelling method known as ‘pretinning method’ [230]. In this method, the disulfide groups of the antibody are reduced to generate thiol residues (SH) which can then directly bind ^{99m}Tc [231,232]. Briefly, a freshly prepared 0.5 M SnCl_2 (50 μl) solution in concentrated HCl was added to a 5 ml solution of 40 mM potassium phthalate/10 mM potassium sodium tartrate. The pH was adjusted to about 5 with NaOH (10 N). From this solution, 13.3 μl was aliquoted and incubated with 20 μg of the IgG antibody (purified previously using 100 kDa microconcentrators) for 21 hours at room temperature under N_2 . The reduced antibody was then incubated with 9 MBq of $\text{Na}^{99m}\text{TcO}_4$ for 1 hour at RT. The radiochemical yield was determined by Instant Thin Layer Chromatography (ITLC). ITLC measurements were carried out three separate systems to quantify ^{99m}Tc -mAbK1, free [^{99m}Tc] pertechnetate and ^{99m}Tc -colloid [233].

1. System I (ITLC-SG plates in saline): R_f [^{99m}Tc] pertechnetate)=1, R_f (^{99m}Tc - mAbK1 and ^{99m}Tc -colloid) = 0
2. System II (Whatman 3 MM chromatography strips in acetone): R_f (^{99m}Tc]pertechnetate) =1, R_f (^{99m}Tc - mAbK1, ^{99m}Tc -colloid) = 0
3. System III (ITLC-SG strips / 5 mg/ml HSA in ethanol: ammonium hydroxide: water = 2:1:5): R_f (^{99m}Tc -colloid) = 0, R_f (^{99m}Tc -mAbK1 and [^{99m}Tc]pertechnetate) = 1

The radioactive TLC strips were visualized using a phosphor imager (Cyclone storage phosphor imager with $20 \times 25 \text{ cm}^2$ phosphor screen, Perkin-Elmer, Waltham, MA, USA) and analyzed using Optiquant software.

Ellman's Assay

The number of reduced thiol groups per mAbK1 antibody was determined using Ellman's assay. Both a 2 mM stock solution of cysteine and a 4 mg/ml solution of Ellman's reagent (5-5'-dithiobis (2-nitrobenzoic acid)) were prepared freshly in 0.1 M sodium phosphate (pH 8.0) buffer. A standard curve was generated using various dilutions of the cysteine stock solution mixed with 0.5 ml of Ellman's reagent solution followed by incubation at room temperature for 2 hours. The test solutions of reduced antibody, non-reduced antibody, and reagent blank were prepared similarly. The absorbance was read at 413 nm in a UV-visible spectrophotometer. The absorbance values obtained from the standard curve of known thiol concentrations were correlated with the values obtained for the test solutions for determination of the number of thiol groups.

2.2.2. Synthesis of N-(*o*-phenol)-Histidine Chelator

N-(*o*-phenol)-histidine (**L1**) was synthesized by adding salicylaldehyde (0.79 g, 6.5 mmol) in 15 mL of EtOH, to a solution of L-histidine (1 g, 6.5 mmol) in 15 mL of H₂O and stirred for 3 hours at room temperature. NaBH(OAc)₃ (2.5 g) was added in small portions and mixture stirred overnight at room temperature. The white solid was filtered off, washed with EtOH and dried under vacuum (**Figure 2.12**). ¹H NMR (DMSO, HCl; 300 MHz) δ 3.24 – 3.45 (m, 5H), 6.81 (t, 1H), 6.89 (d, 1H), 7.22 (t, 1H), 7.31 (d, 1H), 7.34 (s, 1H), 8.91 (s, 1H); Anal. Calcd. (Found) for

$C_{13}H_{15}N_3O_3$: hours 5.79 (5.88), C 59.74 (59.22), N 16.09 (15.97); ESI⁺ m/z 262 [M + H], 284 [M + Na]; ESI⁻ m/z 260 [M – H].

2.2.3. Preparation and Radiolabelling of fab and f(ab')₂ Fragments

The antibody fragments of mAbK1 were prepared using the mouse IgG1 fab and f(ab')₂ preparation kit that utilizes immobilized ficin (Pierce Biotechnology, IL, USA). Ficin generates fab fragments in the presence of 10 mM cysteine when incubated for 5 hours, and f(ab')₂ fragments in the presence of 1 mM cysteine when incubated for 15-20 hours. Different fractions containing fab or f(ab')₂ were collected, pooled, and concentrated using microconcentrators with 30 kDa and 100 kDa cut-off to yield the fab and f(ab')₂ fractions, respectively. Bradford's assay (Sigma) was carried out to determine the protein concentrations of the fab and f(ab')₂ fractions and a non-reducing western blot (method similar to 2.3.9 in non-reducing conditions) was carried out to confirm the molecular weight of fragments. Radiolabelling of fab and f(ab')₂ was performed using the bifunctional chelate approach. The carboxylate group of **L1** was reacted with the free amines of the antibody fragments by carbodiimide coupling. A 25 µl solution of freshly prepared 1-ethyl-3-(3-dimethylaminopropyl) carbodiimide (EDC) (3 mg EDC + 6 mg NHS (N-hydroxysuccinimide in 0.5 ml of 2-(N-morpholino) ethanesulfonic acid (MES) buffer pH 4.5) was added to 50 µl of **L1** solution (6 mg in 1 ml MES buffer, pH 8.0). From this solution, 22.5 µl was added to 10 µg of antibody solution (fab or f(ab')₂) in 10 µl MES buffer (pH 4.5). The reaction mixture was adjusted to pH 7.0 and incubated for 20 hours at room temperature. The antibody-ligand solution was then buffer exchanged into MES buffer, pH 9.0 using microconcentrators with 30 kDa cut off. [^{99m}Tc(H₂O)₃(CO)₃]⁺ (9 MBq) was then added to the antibody-**L1** solution and incubated at 60°C on an Eppendorf thermomixer at 1000 RPM for 30 min to complete the ^{99m}Tc-labelling step. The radiochemical yield was determined by ITLC using 0.9% saline as the mobile phase. The radioactive TLC strips were analysed using

autoradiography (phosphor imaging) using Optiquant software. Rapid purification of radioimmunoconjugates with centrifugal filters was carried out to separate the impurities in the form of ^{99m}Tc colloid and pertechnetate. A control experiment was also carried out to label fabK1 fragments with $[\text{}^{99m}\text{Tc}(\text{CO})_3]^+$, in the absence of the chelator.

2.2.4. Stability Studies: Cysteine Challenge

^{99m}Tc -mAbK1, ^{99m}Tc -fabK1 and ^{99m}Tc -f(ab')₂K1 were incubated with 1 mM cysteine solution (20,000-fold molar excess over antibody concentration) at 37°C and aliquots were taken at 1 hour and 24 hours. Radiochemical yield measurements were done to determine the stability of ^{99m}Tc -mAbK1 to transchelation by cysteine. Control measurements of the respective samples were carried out by incubation with 0.9% saline. The percentage of ^{99m}Tc displaced by cysteine was determined by ITLC using 0.9% saline as mobile phase.

2.2.5. Cell Culture and Immunofluorescence / Immunocytochemistry Studies

NCI-H226 and LCC6-HER2 cells were cultured in RPMI-1640 medium and Dulbecco's Modified Eagle medium supplemented with 10% fetal bovine serum, respectively, at 37°C in a humidified atmosphere in the presence of 5% CO₂.

Immunohistochemical staining was carried out on non-permeabilized NCI-H226 cells. ^{99m}Tc labelled mAbK1 was used as a primary antibody for the study. The cells were cultured on glass cover slips in a 12-well plate and grown to >70% confluency and processed for mesothelin immunocytochemistry. Briefly, cells were washed with PBS and fixed with 4% paraformaldehyde for 20 min on ice. Subsequently, the cells were incubated with 5% normal goat serum for 1 hour at room temperature to block non-specific binding of antibodies. ^{99m}Tc

labelled mAbK1 solution was prepared in 1% normal goat serum (1: 400) and the cells were incubated at 4°C overnight. On the next day, the cells were washed with PBS and incubated with a Texas red-conjugated goat anti-mouse secondary antibody (1:1000; Jackson ImmunoResearch, West Grove, Pennsylvania, U.S.A.) for 1 hour at room temperature. Following subsequent washes with the cover slips were mounted onto slides. Slides were also prepared in the absence of primary antibody to confirm its specificity. Images were captured on a Leica DMLB microscope (Leica Microsystems Inc, Bannockburn, Illinois, U.S.A.) with attached Retiga 2000R camera and processed using Image J software [234].

2.2.6. Determination of Immunoreactivity

The immunoreactivity of mAbK1 and its fab and f(ab')₂ fragments labelled with ^{99m}Tc were determined by a cell binding assay described by Lindmo *et al.* [235]. Varying concentrations (1×10⁶ cells/ml to 5×10⁶ cells/ml) of mesothelin expressing NCI-H226 cells were incubated with 200 ng of ^{99m}Tc-mAbK1 or 100 ng of the ^{99m}Tc-fabK1 or ^{99m}Tc-f(ab')₂K1 fragments on a rocker at 4°C for 2 hours. Following centrifugation, the supernatant was removed and the cells were washed with the binding buffer (PBS with 1% BSA) and counted in a γ-counter. This represents the total binding of ^{99m}Tc- mAbK1 (or fabK1 and f(ab')₂K1) to NCI-H226 cells. To determine non-specific binding, a second set of experiments was done exactly as described above except that an excess of unlabelled mAbK1 (10 μg) was added to the Eppendorf tubes containing different concentrations of cells prior to the addition of ^{99m}Tc-mAbK1 (or fabK1 and f(ab')₂K1). The difference between total and non-specific binding is the specific NCI-H226 cell binding [164]. The immunoreactivities were calculated from the Y-intercept of the double reciprocal plot of fraction of the radioactivity specifically bound *vs.* the cell number.

2.2.7. Saturation Binding - K_d and B_{max} Determination

Radioligand saturation cell binding experiments were carried out for determination of the dissociation constant K_d for ^{99m}Tc -mAbK1, ^{99m}Tc -fabK1 and ^{99m}Tc -f(ab')₂K1 and maximum number of binding sites (B_{max}) for NCI-H226 [236]. The average number of mesothelin receptors present on NCI-H226 cells was calculated by conversion of the B_{max} values. Briefly, about 50,000 NCI-H226 cells/well were plated overnight in a 24 well plate. Adherent cells were then incubated in serum-free culture media with increasing concentrations (0–80 nM) of ^{99m}Tc -mAbK1, ^{99m}Tc -fabK1 and ^{99m}Tc -f(ab')₂K1 in a total volume of 500 μl for 3 hours at 4°C. The cells were then washed twice with ice-cold PBS to remove unbound radioactivity, dissolved in 0.1 M NaOH and analyzed in a γ -counter. Prism[®] Version 5.0 software (GraphPad Software, San Diego, CA, USA) was used to fit the total binding values against the concentration of unbound radiolabelled antibodies, to a one-site saturation binding model. K_d and B_{max} were determined using this model by fitting only total binding, assuming that the amount of nonspecific binding was proportional to the concentration of radioligand.

2.2.8. Tumour Uptake and Biodistribution

Tumour uptake and biodistribution experiments were carried out in male C.B-17 SCID mice (Taconic, Germantown, New York, U.S.A.). ^{99m}Tc labelled mAbK1, fabK1 and f(ab')₂K1 were tested in 3 separate studies each consisting of 3 groups of 5 animals. Each mouse was injected with 10×10^6 NCI-H226 cells (mesothelin positive) in the upper back and 10×10^6 LCC6-HER2 cells (mesothelin negative) in the lower back. When tumours reached a size 0.5-1 cm in diameter, the mice were injected intravenously with 10-18 MBq of ^{99m}Tc -mAbK1, ^{99m}Tc -fabK1 or ^{99m}Tc -f(ab')₂K1. Five animals from each group were euthanized at 4 hours, 24 hours and 48 hours (or 4 hours, 8h and 24 hours for ^{99m}Tc -fab and ^{99m}Tc -f(ab')₂) after injection and major

organs were harvested. The radioactivity associated with each organ was analyzed on a γ -counter to obtain the biodistribution data. To compare the specific localization of the radioactivity in the tumours to that in blood or normal tissues, the ratio of radioactivity in the tumour or normal tissue to that in blood was determined by dividing the activity concentration of tissue by activity concentration of total blood. Animal experiments were carried out in accordance with the guidelines of the University of British Columbia Animal Care Committee.

2.2.9. Western Blotting

The verification of mesothelin protein expression in the harvested tumours was performed by Western blot using the anti mesothelin antibody mAbMB (Rockland Immunochemicals, Gilbertsville, Pennsylvania, U.S.A.). NCI-H226 cells in culture dishes were washed with phosphate-buffered saline (PBS) and lysed in 1 ml of RIPA buffer [150 mM NaCl, 1% nonyl phenoxy polyethoxy ethanol, 0.5% Na deoxycholate, 0.1% Na dodecyl sulfate, 50 mM Tris-HCl (pH 7.5), 1% protease inhibitor cocktail (Sigma)]. The cell lysates were centrifuged at 8,000 rpm (5223 g) for 10 min at 4°C and the supernatant was collected. Tumour lysates were prepared by homogenizing frozen tumour (H1-H6: Six NCI-H226 tumours, L1-L6: Six LCC6-HER2 tumours) and samples in 1 ml of ice-cold homogenization buffer [10 mM EGTA, 2 mM EDTA, 25 mM sucrose, Tris-HCl 20 mM (pH 7.5), 1% protease inhibitor cocktail], followed by sonication for 10 seconds. The tumour lysates were centrifuged at 11,000 rpm (9875 g) for 10 min at 4°C and the supernatant was collected. Samples were prepared for electrophoresis in Laemmli sample buffer (Bio-Rad) containing, 5% v/v of 2-mercaptoethanol (Bio-Rad). The samples were heated at 99°C for 5 min and fractionated using SDS-polyacrylamide gel (12% gel) and then transferred onto a nitrocellulose Hy-Bond ECL membrane (Amersham Ltd. Oakdale, Ontario, Canada). The membrane was then washed with 5% milk in Tris-Buffered Saline Tween-20 (TBST) for 1 hour at room temperature (RT) followed by incubation with the

primary antibody 5% BSA in TBST at 1:1000 dilution overnight at 4°C. Secondary antibody 1:5000 (horseshoe peroxidase-labelled goat antimouse IgG; Jackson ImmunoResearch Laboratories) was incubated for 1 hour at RT followed by chemiluminescence detection using the ECL Western blotting detection kit (Amersham) according to the manufacturer's suggested protocol. Images were captured using an Alpha Innotech FluorChem 8800 gel box imager (Alpha Innotech Co., San Leandro, California, U.S.A.). The bands were quantified by densitometric analysis using FluorChem software (Alpha Innotech). As a loading control, the membrane was stripped and reprobed with monoclonal anti- β -actin antibody (Sigma).

2.3. Results

2.3.1. ^{99m}Tc Labelling and Stability of mAbK1 Antibody and its fab and f(ab')₂ Fragments

In the current study, a radiochemical yield of >90% (92.6±1.6%) (**Figure 2.3**) was obtained for direct labelling of mAbK1 using the “pretinning” method. The impurities were mainly present in the form of hydrolysed ^{99m}Tc colloid (<10%), which was quantified by ITLC. Radiochemical purity of >95% was achieved by further purification of the radiolabelled antibody using centrifugal filters. The average number of SH groups generated on the mAbK1 antibody molecule after reduction with the ‘pretinning method’ was three, as determined using Ellman’s assay.

Non-reducing western blot confirmed formation of 50 kDa fabK1 fragment and 100 kDa f(ab')₂K1 fragment after digestion with ficin (**Figure 2.4**). For the indirectly labelled fabK1 and f(ab')₂ fragments, a radiochemical yield of 91.6±9.1% and 80.7±8.5% was achieved, respectively (**Figure 2.5**). Similar to ^{99m}Tc-mAbK1, rapid purification with centrifugal filters resulted in a radiochemical purity of >95% for these fragments. Control experiments carried out to directly label fabK1 fragments with [^{99m}Tc(CO)₃]⁺ resulted in < 20% radiochemical purity.

The antibody mAbK1 showed very good stability to cysteine challenge, with 95.1±0.9% of radioactivity still bound to the antibody after 1 hour. After 24 hours, 85.1±0.7% of the radioactivity was present on the antibody. For the fabK1 fragment, 79.5±1.7% of radioactivity was antibody-bound after 1 hour, which decreased to 66.7±4.9% after 24 hours. A cysteine challenge of f(ab')₂K1 showed that 72.5±2.8% of radioactivity was antibody-bound after 1 hour, which decreased to 63.4±0.5% after 24 hours (**Figure 2.6**). Control studies in 0.9% saline indicated that both antibody and fragments retained >90% of the ^{99m}Tc label after 24 hours.

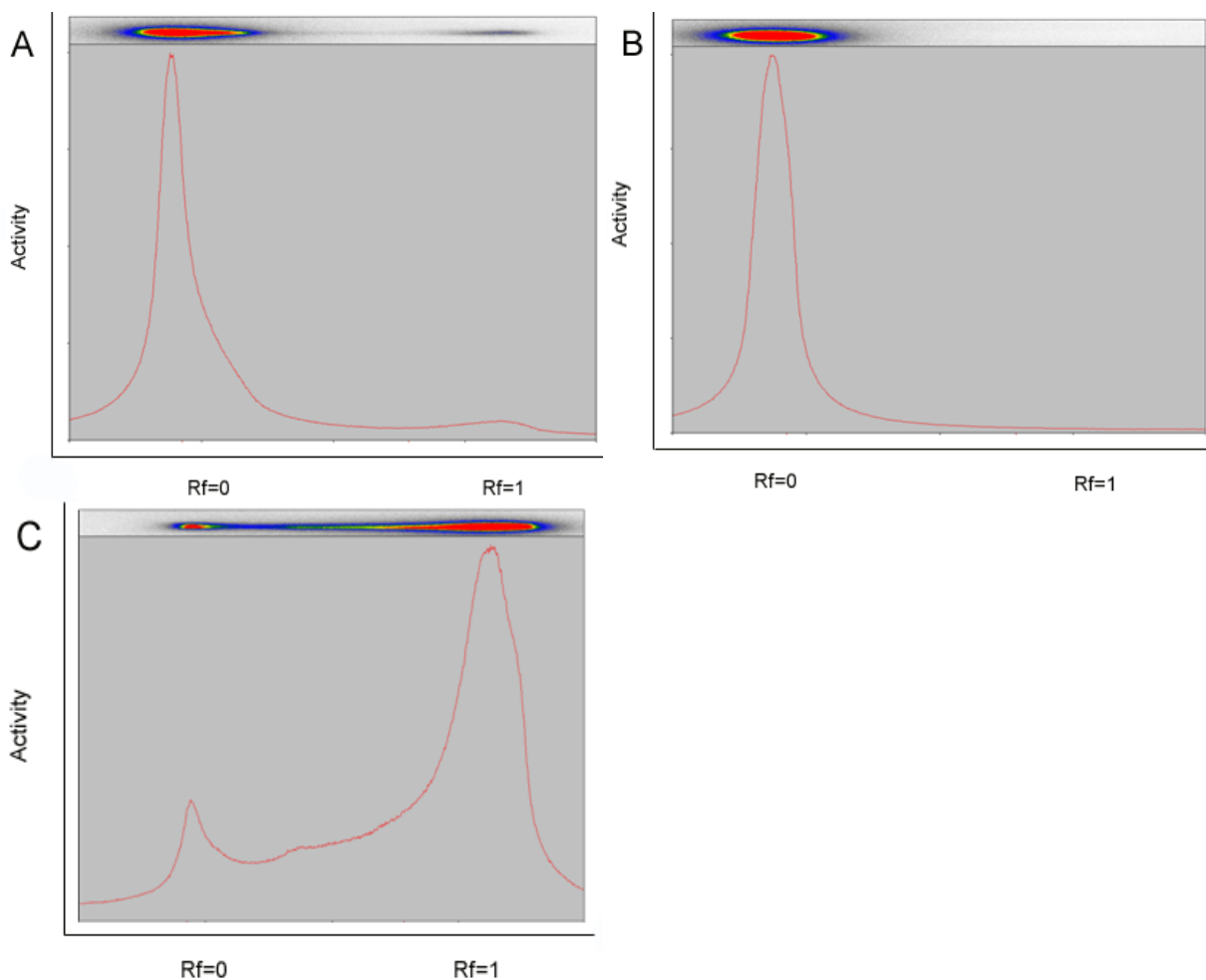


Figure 2.3. Representative autoradiographic images of ITLC strips used for the determination of the radiolabelling yield of ^{99m}Tc labelled mAbK1. ^{99m}Tc was conjugated to the antibody by a direct labelling method. Radiochemical purity was determined by ITLC using three different solvent systems to separate hydrolysed ^{99m}Tc colloid, and free ^{99m}Tc -pertechnetate. System I (ITLC-SG plates in saline): $R_f([\text{}^{99m}\text{Tc}]\text{pertechnetate}) = 1$, $R_f(^{99m}\text{Tc}\text{-mAbK1 and } ^{99m}\text{Tc}\text{-colloid}) = 0$ (A), System II (Whatman 3 MM chromatography strips in acetone): $R_f([\text{}^{99m}\text{Tc}]\text{pertechnetate}) = 1$, $R_f(^{99m}\text{Tc}\text{-mAbK1, } ^{99m}\text{Tc}\text{-colloid}) = 0$ (B), System III (ITLC-SG strips / 5 mg/ml HSA in ethanol: ammonium hydroxide: water = 2:1:5): $R_f(^{99m}\text{Tc}\text{-colloid}) = 0$, $R_f(^{99m}\text{Tc}\text{-mAbK1 and } [\text{}^{99m}\text{Tc}]\text{pertechnetate}) = 1$ (C). The radiochemical yield obtained was $92.6 \pm 1.6\%$.

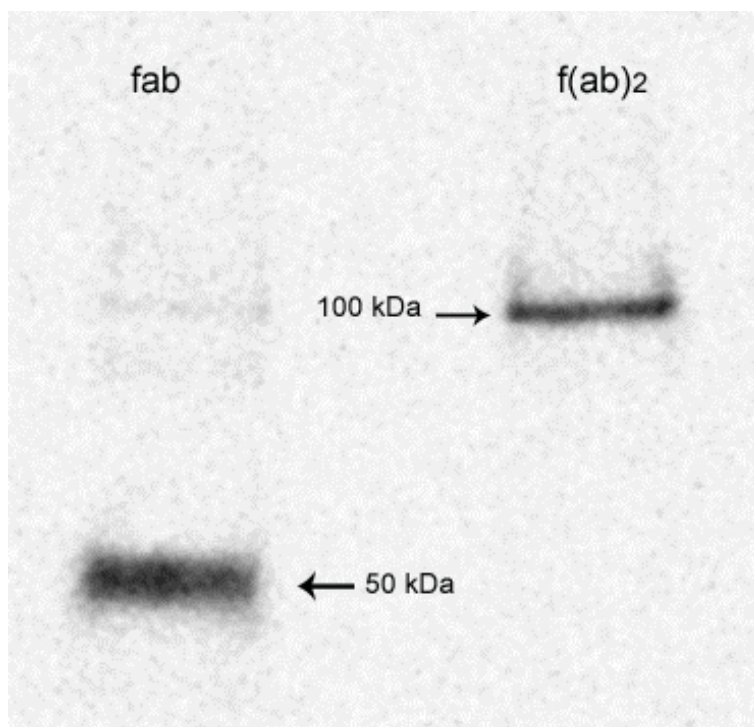


Figure 2.4. Western blot showing the molecular weights of fab and f(ab)₂ fragments of mAbK1. A non-reducing western blot was carried out for fab and f(ab)₂ fragments obtained after digestion with ficin. The western blot confirm the formation of 50 kDa fab and 100 kDa f(ab)₂ fragments.

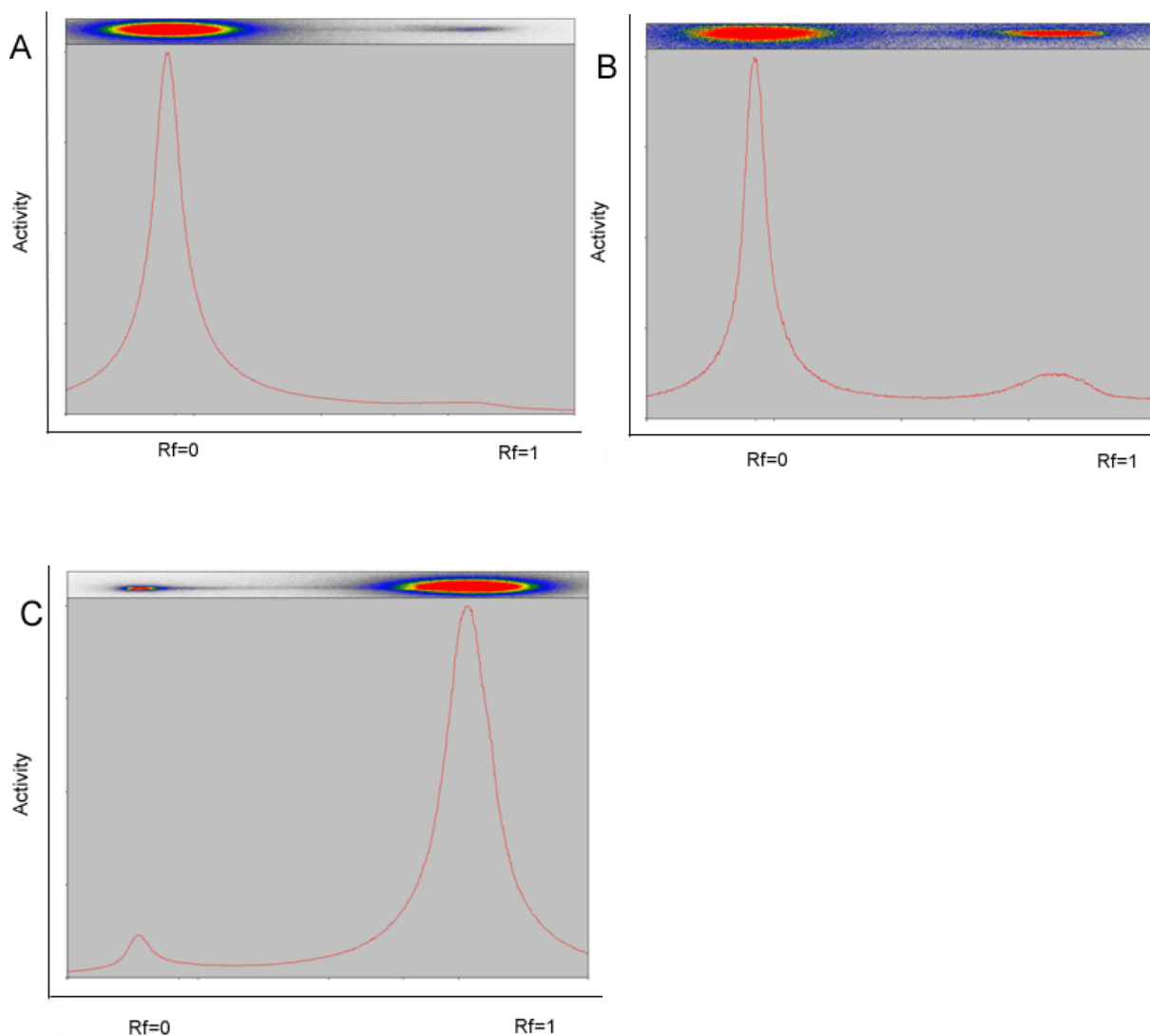


Figure 2.5. Representative autoradiographic images of ITLC strips used for determination of radiolabelling yield for ^{99m}Tc labelled fabK1 and f(ab) $\hat{\prime}$ $_2$ K1 fragments. ^{99m}Tc from the precursor, $[\text{}^{99m}\text{Tc}(\text{CO})_3]^+$ was conjugated to the antibody by means of a bifunctional tridentate ligand. The activity at $R_f = 0$ corresponds to ^{99m}Tc -fabK1 (A and C) or ^{99m}Tc -f(ab) $\hat{\prime}$ $_2$ K1 (B). The peak at $R_f = 0.6 - 1$ corresponds to unbound ^{99m}Tc impurities. The radiochemical yield obtained was $91.6 \pm 9.1\%$ and $80.7 \pm 8.5\%$ for ^{99m}Tc -fabK1 and ^{99m}Tc -f(ab) $\hat{\prime}$ $_2$ K1, respectively. Control experiments (C) carried out to directly label fab fragments with $[\text{}^{99m}\text{Tc}(\text{CO})_3]^+$ yielded $<20\%$ radiochemical purity.

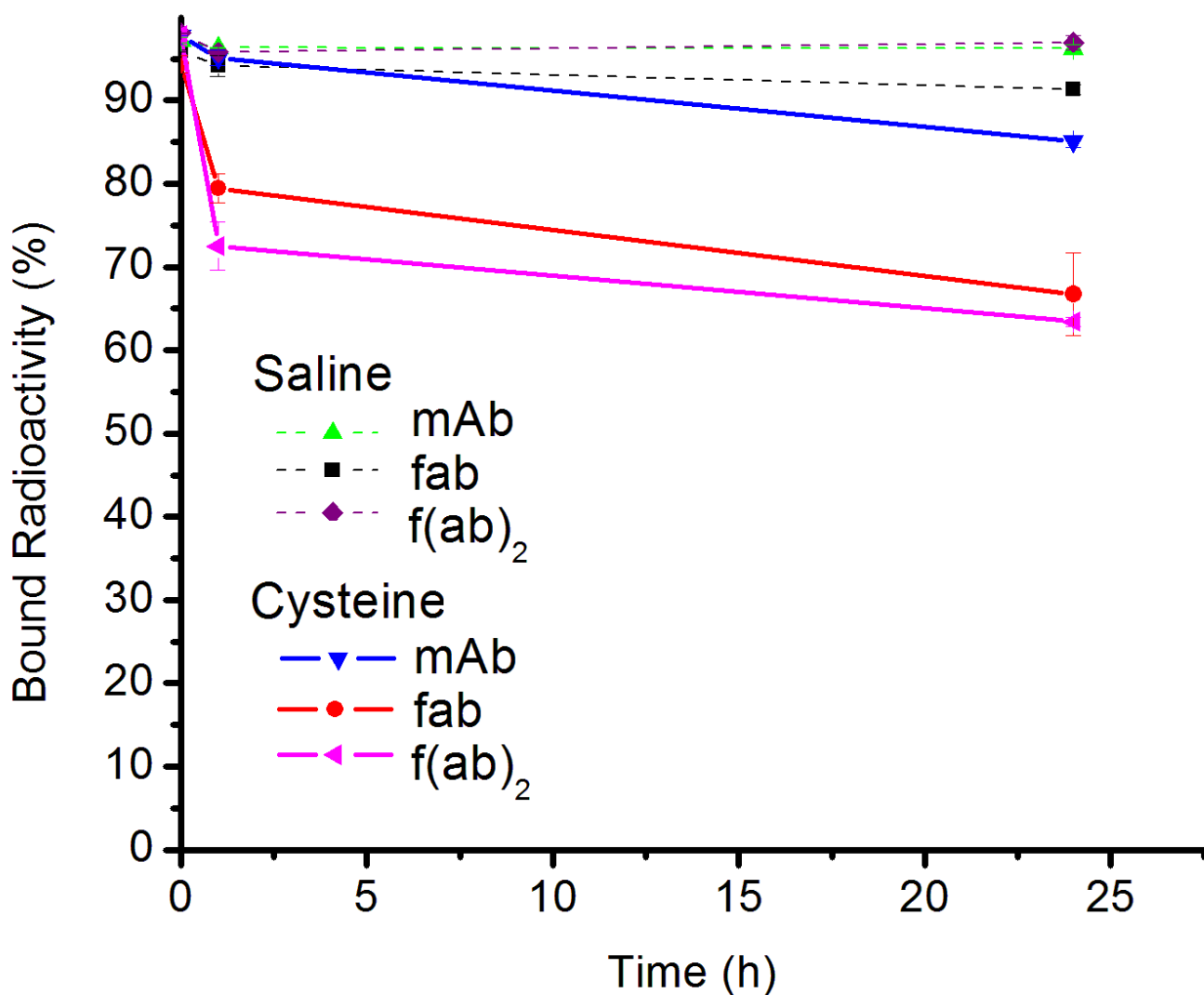


Figure 2.6. Stability of ^{99m}Tc labelled mAbK1, fabK1, f(ab)₂K1 in 1 mM cysteine after incubation for 1 hour and 24 hours at 37°C. After 1 hour, 95.1±0.9% of radioactivity was bound to mAbK1, while after 24 hours, 85.1±0.7% of the radioactivity was present on the antibody. For the fabK1 fragment, 79.5±1.7% of radioactivity was antibody-bound after 1 hour, which decreased to 66.7±4.9% after 24 hours. For f(ab)₂K1 72.5±2.8% of radioactivity was antibody-bound after 1 hour, which decreased to 63.4±0.5% after 24 hours. Control studies carried out in 0.9% saline for 1 hour and 24 hours at 37°C, indicated that the antibody and fragments retained >90% of the radiolabel for 24 hours.

2.3.2. Immunoreactivity of ^{99m}Tc Labelled Antibodies and Fragments

The immunoreactivity determined from the cell binding assay was 88%, 82%, and 80% for ^{99m}Tc -mAbK1 antibody, ^{99m}Tc -fabK1, and ^{99m}Tc -f(ab')₂K1, respectively. The good immunoreactivity of ^{99m}Tc -mAbK1 was also confirmed by immunofluorescence studies using mesothelin expressing NCI-H226 cells. In these studies, the ^{99m}Tc labelled mAbK1 antibody was observed to bind to surface mesothelin receptors of the NCI-H226 cells just as well as the non-radiolabelled antibody (**Figure 2.7**).

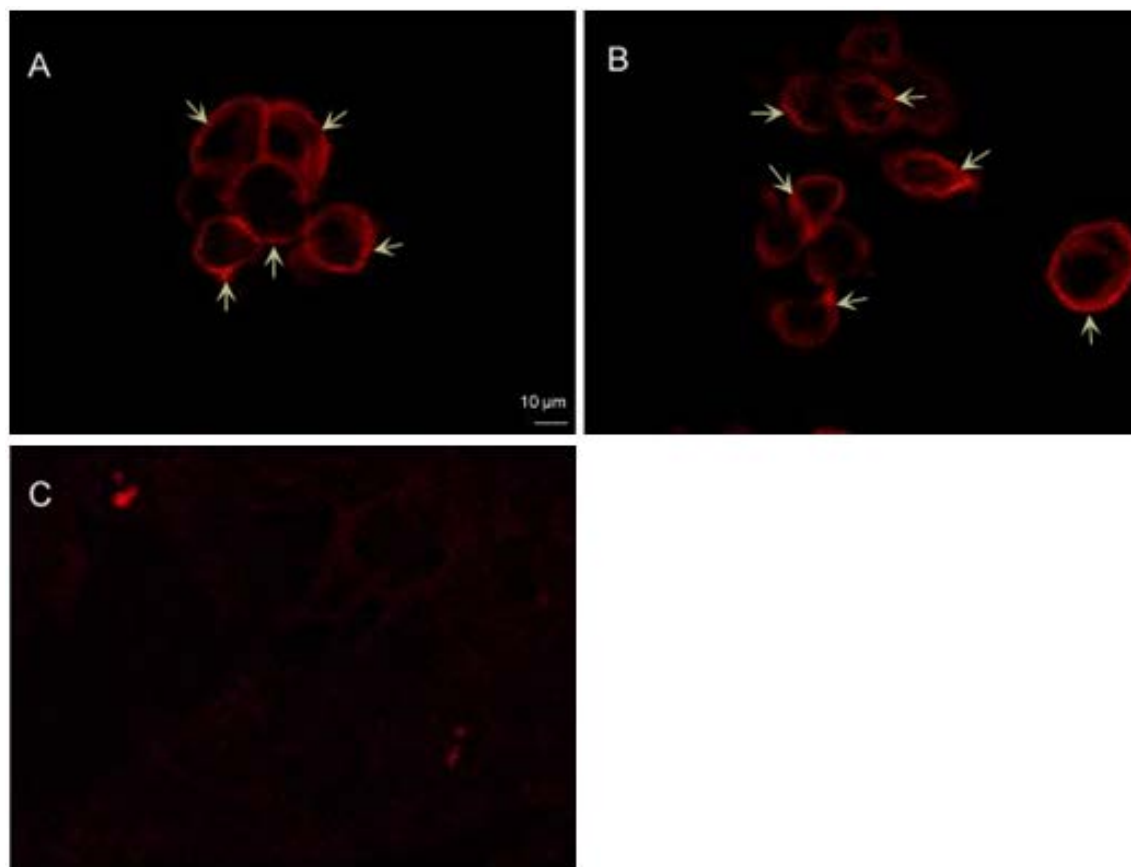


Figure 2.7. Representative photomicrographs illustrating immunohistochemical staining of mesothelin in NCI-H226 cells with (A) the unlabelled mAbK1 antibody and (B) the ^{99m}Tc -radiolabelled antibody. (C) is a control without the primary antibody. Arrows point to the cell surface expression of mesothelin.

2.3.3. K_d and B_{max} of Radioimmunoconjugates

The K_d values obtained from saturation binding experiments (**Figure 2.8**) were 21.5 ± 2.8 nM, 22.7 ± 6.4 nM and 25.0 ± 1.3 nM for ^{99m}Tc -mAbK1, ^{99m}Tc -fabK1 and ^{99m}Tc -f(ab')₂K1, respectively. The number of mesothelin receptors on NCI-H226 cells, calculated from the B_{max} values were $9.1 \times 10^4 \pm 1.0 \times 10^4$ / cell.

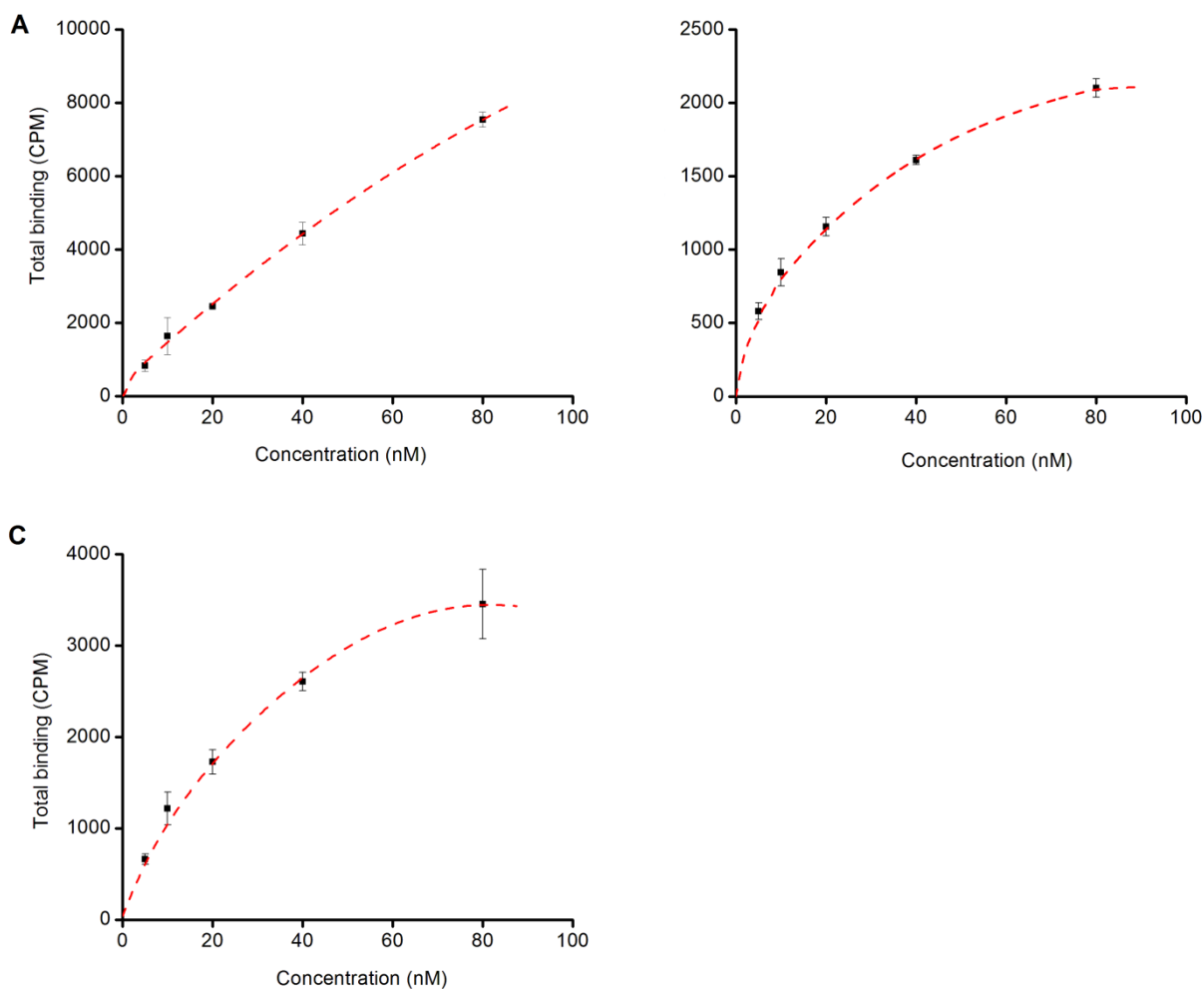


Figure 2.8. Representative total binding curves for (A) ^{99m}Tc -mAbK1, (B) ^{99m}Tc -fabK1, (C) ^{99m}Tc -f(ab')₂K1. Adherent NCI-H226 cells were incubated in serum-free culture media with increasing concentrations (0–80 nM) of ^{99m}Tc -mAbK1, ^{99m}Tc -fabK1 and ^{99m}Tc -f(ab')₂K1 for 3 hours at 4°C. After removal of unbound radioactivity, the cells bound activity, was determined and. Prism[®] Version 5.0 software used calculate the K_d and B_{max} values. The K_d values obtained from saturation binding experiments were 21.5 ± 2.8 nM, 22.7 ± 6.4 nM and 25.0 ± 1.3 nM for ^{99m}Tc -mAbK1, ^{99m}Tc -fabK1 and ^{99m}Tc -f(ab')₂K1, respectively. The number of mesothelin receptors on NCI-H226 cells, calculated from the B_{max} values were $9.1 \times 10^4 \pm 1.0 \times 10^4$ / cell.

2.3.4. Biodistribution and Tumour Uptake of ^{99m}Tc Labelled mAbK1 and its fab/ f(ab) 2 Fragments

Biodistribution of ^{99m}Tc -mAbK1, ^{99m}Tc -fabK1 and ^{99m}Tc - f(ab) 2 K1 was assessed in SCID mice bearing NCI-H226 and LCC6-HER2 tumours. Both NCI-H226 and LCC6-HER2 cells formed tumours following subcutaneous injection. Western blotting confirmed that mesothelin was expressed in NCI-H226 tumours but not in LCC6-HER2 tumours (**Figure 2.11**). The peak uptake of ^{99m}Tc -mAbK1 in mesothelin positive NCI-H226 tumours was $0.80\pm 0.39\%$ ID/g at 8 hours, showing a decrease thereafter to $0.42\pm 0.25\%$ ID/g at 24 hours and $0.38\pm 0.16\%$ ID/g at 48 hours (**Figure 2.9**). The corresponding uptake into mesothelin negative LCC6-HER2 tumours was $0.50\pm 0.40\%$ ID/g, $0.24\pm 0.26\%$ ID/g, and $0.19\pm 0.09\%$ ID/g at 8 hours, 24 hours and 48 hours, respectively. The major organs showing activity uptake were the liver and kidneys. After 8 hours, $6.25\pm 2.20\%$ ID/g was found localized in the liver, decreasing to $2.75\pm 1.45\%$ ID/g and $3.64\pm 1.53\%$ ID/g after 24 hours and 48 hours, respectively. Kidney uptake was $3.79\pm 0.65\%$ ID/g, $0.53\pm 0.64\%$ ID/g and $0.67\pm 0.25\%$ ID/g, at 8 hours, 24 hours and 48 hours, respectively. ^{99m}Tc -mAbK1 showed fast blood clearance with activity decreasing from $4.05\pm 1.33\%$ ID/g at 8 hours to $0.46\pm 0.14\%$ ID/g and $0.35\pm 0.10\%$ ID/g after 24 hours and 48 hours, respectively. The receding blood activities also led to an increase in tumour to blood ratios over time (**Table 1**).

^{99m}Tc -f(ab) 2 K1 showed slightly better uptake into NCI-H226 tumours compared to ^{99m}Tc -mAbK1 (**Figure 2.10 A**), with peak uptake of $1.22\pm 0.19\%$ ID/g, which was significantly higher ($P < 0.05$) than uptake into LCC6-HER2 tumours; $0.41\pm 0.29\%$ ID/g obtained after 8 hours. After 4 hours and 24 hours the uptake in NCI-H226 was only $0.89\pm 0.32\%$ ID/g and $0.68\pm 0.32\%$ ID/g, respectively. As observed with ^{99m}Tc -mAbK1, liver and kidneys were the other major organs showing activity localization. The activity in the liver declined from $7.43\pm 1.84\%$ ID/g at 4 hours to $5.69\pm 1.17\%$ ID/g and $0.51\pm 0.24\%$ ID/g, after 8 hours and 24 hours, respectively. Kidney

uptake was $13.34 \pm 2.36\%$ ID/g, $8.67 \pm 1.63\%$ ID/g and $5.28 \pm 1.11\%$ ID/g at 4 hours, 8 hours and 24 hours, respectively, indicating renal uptake. The tumour to blood ratios increased over time, but the ratios were always less than 1, indicating low tumour uptake as well as slow blood clearance (**Table 1**). ^{99m}Tc -fabK1 had better uptake into NCI-H226 tumours, compared to both ^{99m}Tc -f(ab')₂K1 and ^{99m}Tc -mAbK1 (**Figure 2.10 B**). The peak uptake of $1.36 \pm 0.23\%$ ID/g into NCI-H226 tumours was obtained at 8 hours, which was significantly higher than LCC6-HER2 tumour uptake of $0.34 \pm 0.10\%$ ID/g. At 4 hours and 24 hours, ^{99m}Tc -fabK1 showed similar uptake as seen for ^{99m}Tc -f(ab')₂K1 with NCI-H226 tumour uptake being $0.91 \pm 0.32\%$ ID/g and $0.77 \pm 0.32\%$ ID/g, respectively. The activity localized in the liver remained consistent over time, with $5.15 \pm 1.30\%$ ID/g, $6.00 \pm 0.65\%$ ID/g, $4.29 \pm 0.31\%$ ID/g found in the liver at 4 hours, 8 hours and 24 hours, indicating retention of activity in liver. While blood clearance of ^{99m}Tc -fabK1 was faster than ^{99m}Tc -f(ab')₂K1, the uptake into the kidneys at 4 hours was lower than ^{99m}Tc -f(ab')₂K1 with uptake value of $8.41 \pm 1.77\%$ ID/g. Thereafter, the kidney uptake values were similar to ^{99m}Tc -f(ab')₂K1, with $7.55 \pm 1.60\%$ ID/g and $5.44 \pm 0.70\%$ ID/g localized in the kidneys at 8 hours and 24 hours, respectively. The tumour to blood ratios increased as the activity from the blood pool receded, however, the ratios were always less than 1 (**Table 1**).

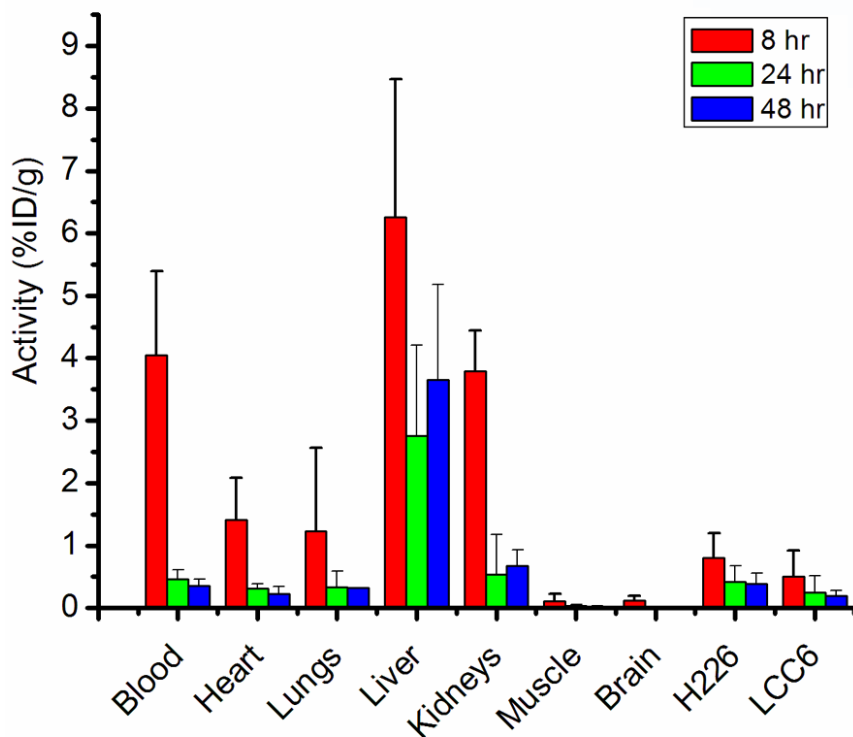


Figure 2.9. Biodistribution of ^{99m}Tc -mAbK1 (10-18 MBq), injected in SCID mice (n=5) bearing NCI-H226 (mesothelin positive) and LCC6-HER2 (mesothelin negative) subcutaneous xenografts. Percentage of the injected dose/gram (Activity %ID/g) was determined in the tumours and all major organs after 8, 24 and 48 hours, post-injection. ^{99m}Tc -mAbK1 showed fast blood clearance and peak uptake into NCI-H226 tumours was $0.80\pm 0.39\%$ ID/g at 8 hours. Data is presented as mean \pm SD.

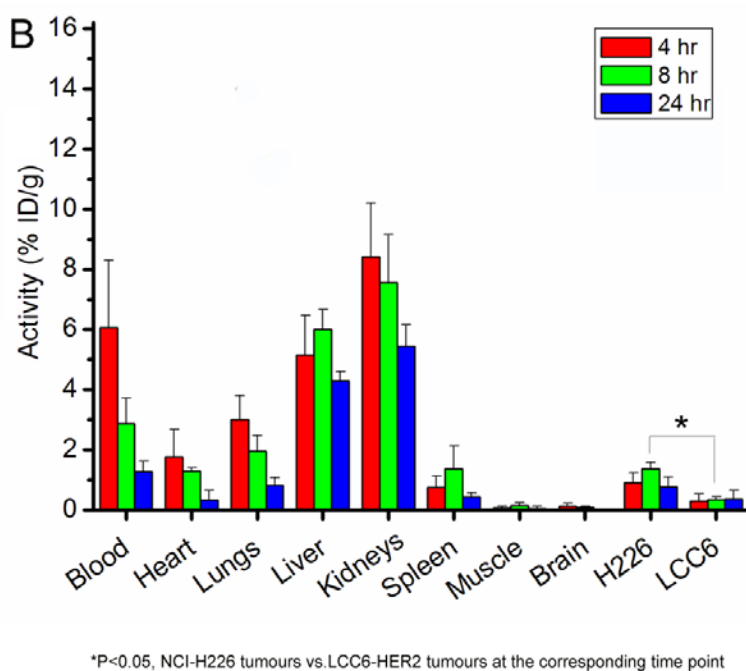
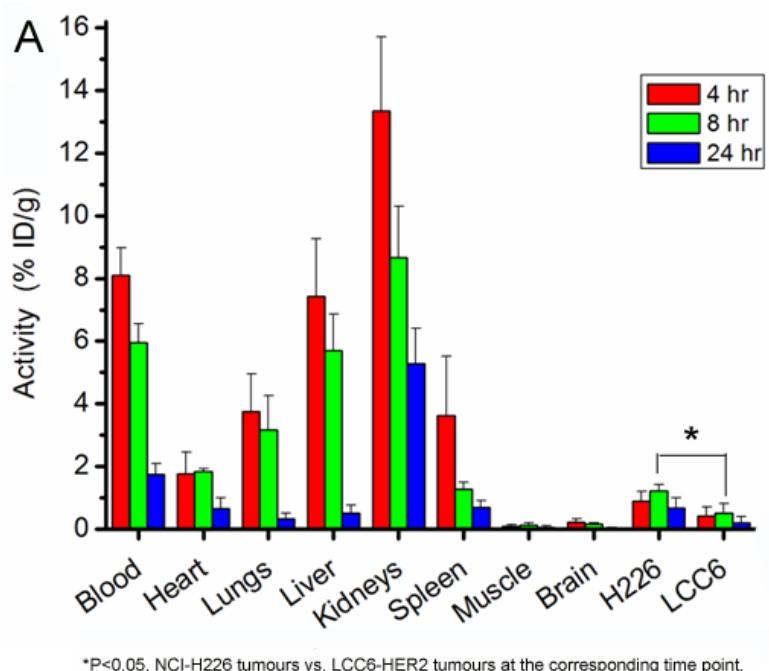


Figure 2.10. Biodistribution of ^{99m}Tc -labelled $f(ab)_2$ and fab fragments of mAbK1. Biodistribution was determined after injecting 10-18 MBq of ^{99m}Tc - $f(ab)_2$ (A) and ^{99m}Tc -fab (B), in SCID mice (n=5) bearing NCI-H226 (mesothelin positive) and (mesothelin negative) subcutaneous xenografts. Percentage of the injected dose/gram (Activity %ID/g) was determined in the tumours and all major organs after 4, 8, 24 hours, post-injection. Both ^{99m}Tc - $f(ab)_2$ K1 and ^{99m}Tc -fabK1 showed significantly higher uptake into NCI-H226 tumours than LCC6-HER2 tumours at 8 hours. Data is presented as mean \pm SD.

Table 2.1. Organ to blood ratios of ^{99m}Tc labelled mAbK1 and its fab and f(ab')₂ fragments in SCID mice (n=5) bearing NCI-H226 (mesothelin positive) and LCC6-HER2 (mesothelin negative).

	^{99m} Tc - mAbK1			^{99m} Tc - f(ab') ₂ K1			^{99m} Tc - fabK1		
	4 hrs	24 hrs	48 hrs	4 hrs	8 hrs	24 hrs	4 hrs	8 hrs	24 hrs
Heart	0.33±0.15	0.70±0.17	0.63±0.38	0.21±0.08	0.3±0.02	0.47±0.23	0.24±0.02	0.41±0.16	0.27±0.29
Brain	0.03±0.01	0.03±0.02	0.02±0.02	0.03±0.02	0.03±0.01	0.03±0.01	0.02±0.01	0.03±0.01	0.02±0.02
Liver	1.46±0.79	7.44±2.12	8.73±2.34	0.94±0.32	0.95±0.13	0.64±0.76	0.78±0.3	1.87±0.62	3.12±0.87
Kidneys	1.12±0.29	1.03±1.17	1.91±0.66	1.65±0.43	1.48±0.18	3.19±1.26	1.48±0.37	3.06±0.88	3.73±0.68
Muscle	0.02±0.02	0.08±0.05	0.06±0.05	0.01±0.01	0.02±0.01	0.04±0.02	0.01±0.01	0.05±0.03	0.04±0.04
H226	0.18±0.07	0.99±0.68	1.16±0.67	0.11±0.04	0.21±0.02	0.46±0.19	0.14±0.06	0.46±0.26	0.55±0.23
LCC6	0.12±0.08	0.60±0.80	0.55±0.29	0.05±0.03	0.08±0.05	0.12±0.10	0.05±0.04	0.11±0.05	0.27±0.26
Lungs	0.21±0.12	0.83±0.64	0.90±0.14	0.46±0.15	0.52±0.16	0.28±0.18	0.57±0.27	0.64±0.53	0.57±0.11

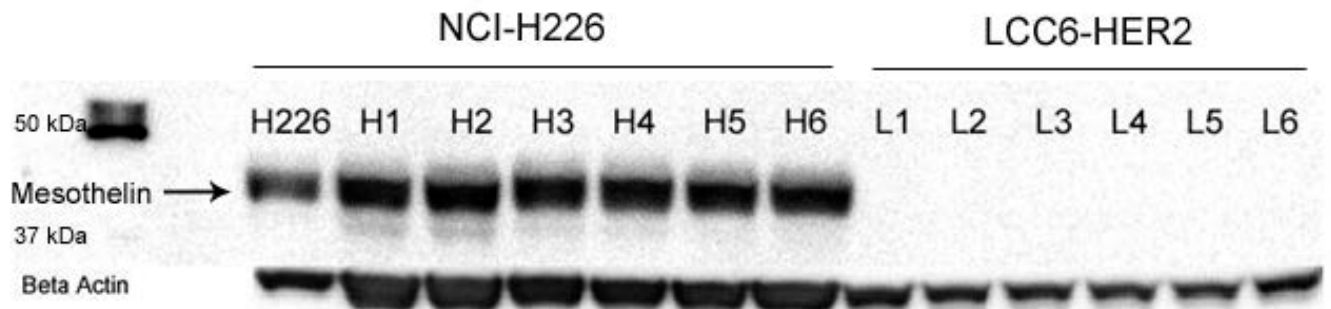


Figure 2.11. Western blot of mesothelin positive NCI-H226 (H1-H6) and mesothelin negative LCC6-HER2 (L1-L6) tumour lysates. *In vivo* expression of 40 kDa mesothelin was confirmed in NCI-H226 tumours, while LCC6-HER2 tumours did not express mesothelin. The cell lysate from NCI-H226 was used as a positive control, while beta actin was used as a loading control.

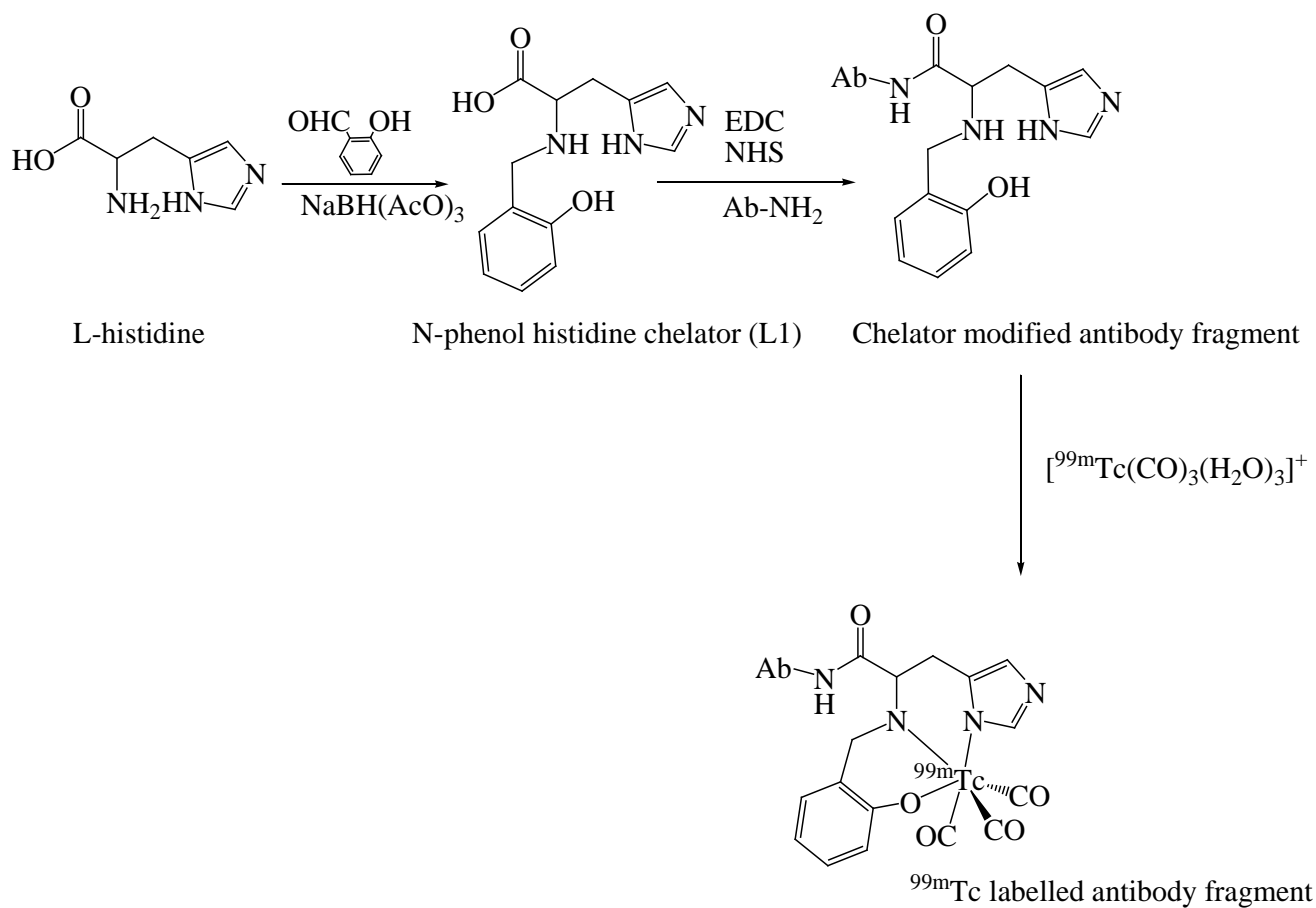


Figure 2.12. Synthetic scheme for preparing $^{99\text{m}}\text{Tc}$ labelled antibody fragments starting from L-histidine. The tridentate ligand L1 is obtained by reductive amination and binds to Ab through a stable amide bond. Ab in the figure represents $f(ab')_2$ fragment or fab fragment.

2.4. Discussion

An effective radiolabelled antibody-based imaging agent for mesothelin expressing cancers must achieve high tumour penetration as well as high tumour to blood ratios. In the current study, we radiolabelled antimesothelin antibody mAbK1 and its fab and f(ab')₂ fragments with ^{99m}Tc and tested their biodistribution in mice using an NCI-H226 tumour xenograft model. Although the biodistribution data revealed mesothelin mediated uptake in mesothelin expressing tumour xenografts (**Figures 2.9 and 2.10; Table 1**), the accumulation of ^{99m}Tc labelled radioimmunoconjugates was not high enough to allow imaging of tumours.

Direct labelling (without any intermediate bifunctional group) of mAbK1 antibody was accomplished by the 'pretinning method' developed by Rhodes *et al.* [237]. This method utilizes stannous ions (Sn²⁺) from SnCl₂ to reduce the disulfide bridges (S-S) on the antibody to thiol (SH) groups, which are required to bind ^{99m}Tc. These disulfides are present in the native protein as part of the cysteine (amino acid), which is present in the majority of protein backbones. In this labelling method, Sn²⁺ fulfills three essential roles: reduction of disulfides, co-ordination with –S⁻ groups and reduction of pertechnetate. Previous studies have shown that ^{99m}Tc labelling via –S⁻ groups produces radiochemically stable tracers [238]. Although ^{99m}Tc labelling by 'pretinning reaction' may involve several reactions taking place simultaneously or serially, the labelling can still be accomplished in a single reaction vial [230]. The tartrate in the reaction acts as a transfer ligand, by complexing the ^{99m}Tc formed after reduction of pertechnetate and then transferring it to the binding sites (thiol groups) on the antibody. The pH of the reaction is kept slightly acidic to prevent the oxidation of the thiol groups back to the disulfides [230]. Radiochemical purities of above 90% (92.6±1.6%) were consistently obtained using the 'pretinning' method for ^{99m}Tc labelling of mAbK1. The impurities, mainly in the form of reduced, hydrolysed ^{99m}Tc and free pertechnetate were quantified using ITLC.

Radiolabelling reaction can cause alterations in the immunoreactivity of the antibody, based on the number and location of the reduced disulfide groups. Although the disulfide groups in the antibody are located distal to the antigen binding site, the reduction reaction may cause structural alterations or fragmentation of light and heavy chains resulting in disruption of the antigen binding site. To preserve the immunoreactivity of the antibody, it is critical that the reduction procedure works optimally to form SH residues to bind to ^{99m}Tc . The maximum number of SH groups that can be generated in the IgG antibody is 36 [239], due to the presence of 6 inter chain and 12 intra chain disulfide bonds. From Ellman's assay the average number of SH groups generated on the mAbK1 antibody molecule after reduction with the 'pretinning method' was calculated to be three.

Although the 'pretinning method' was successfully used for the radiolabelling of whole IgG antibodies, it was not successful with the mAbK1 fragments, as radiochemical purities of less than 20% were obtained (data not shown). One possible explanation is that the number of SH groups available on the antibody fragments after reduction with SnCl_2 , is much lower than on the whole IgG [238,240]. It is also critical to modify only the exterior disulfide bridges that are not responsible for maintenance of the overall structure of the antibody, since the modification of the exterior disulfides can affect the immunoreactivity of the antibody [230]. This distinction may be difficult to achieve in case of the antibody fragments due to limited availability of the disulfide groups compared to the whole antibody molecule. Studies have also shown that reduction of $\text{f(ab}')_2$ with tin chloride leads to the formation of a mixture of $\text{f(ab}')_2$, fab, and peptides. The resulting fab fragments preferentially bind ^{99m}Tc and the radiolabelling reaction itself increases the relative amount of the monomeric fab fragments [241]. The above mentioned potential adverse effects of direct radiolabelling method on antibody fragments contributed to

their unsuccessful radiolabelling, and the bifunctional chelate approach was thus used to radiolabel the fragments.

In order to bind ^{99m}Tc to the antibody fragments, we used an indirect labelling approach by introducing a bifunctional chelator. For synthesis of the bifunctional chelator we chose the single amino acid L-histidine, a natural amino acid, and modified it with an additional phenol group to obtain after reductive amination the bifunctional tridentate ligand (**L1**) (**Figure 2.12**). Bioconjugation was based on the carbodiimide activation of the carboxylate of **L1** and further reaction with the amine groups present on the antibody fragments. Antibody fragments bear both ϵ amines (lysine residues) and α amines (N-terminus). While ϵ amines are good nucleophiles above pH 8.0, α amine groups react well at neutral pHs [242]. Therefore, by maintaining the pH of the reaction mixture at 7.0, selective labelling of N-terminus α amine groups of the antibody fragments is achieved. In this reaction the COOH group of **L1** binds to the biological molecule whereas the rest of the molecule (imidazole N, amine N and phenolate O) forms a tridentate chelator. Radiolabelling of the **L1**-containing fragments was then done by replacing the three aqua ligands of the complex precursor $[\text{}^{99m}\text{Tc}(\text{CO})_3(\text{H}_2\text{O})_3]^+$ with the tridentate chelator. The tridentate chelator binding to $[\text{}^{99m}\text{Tc}(\text{CO})_3]^+$ resulted in a neutral complex. The $^{99m}\text{Tc}(\text{I})$ tricarbonyl core has been commonly used in recent years [218,243,244] because of its relatively small size, kinetic inertness, and thermodynamic stability.

The use of a tridentate chelator such as **L1**, is favoured due to faster reaction rates and ability of the tridentate ligand to shield the $[\text{}^{99m}\text{Tc}(\text{CO})_3]^+$ core from *in vivo* crossreactivity to serum proteins [245]. The bifunctional chelator **L1** holds ^{99m}Tc securely attached to the radiopharmaceutical, while also providing the side arm for attachment of antibody fragment. To our knowledge, no specific chelators such as **L1** or any other bifunctional chelator for $[\text{}^{99m}\text{Tc}(\text{CO})_3]^+$ have been covalently bound to antibodies and their fragments. Previously, Chen

et al. have reported direct ^{99m}Tc labelling of the inherent histidine groups on the antibody Herceptin (trastuzumab) by simply incubating the antibody with $[\text{}^{99m}\text{Tc}(\text{CO})_3(\text{H}_2\text{O})_3]^+$ ion in saline [246]. Our control experiments, using a similar strategy, to directly label fab fragments with $[\text{}^{99m}\text{Tc}(\text{CO})_3]^+$ resulted in <20% radiochemical yield. Newer work with the $[\text{}^{99m}\text{Tc}(\text{CO})_3]^+$ labelling, uses hexa-histidine end groups on affibodies [247], which target the HER2 antigen, and nanobodies, which target the EGF receptor [226]. Labelling efficiencies and stabilities in their work are similar to ours. For example, Orlova *et al.* reported a 1 hour cysteine challenge result of 84% when a 5000-fold molar excess of cysteine was used, while our result was 79% with a 20,000-fold molar excess [228]. These results suggest that $[\text{}^{99m}\text{Tc}(\text{CO})_3]^+$ labelling using hexa-histidine end groups is comparable to the bifunctional chelator **L1** mediated labelling strategy used in our studies. Other strategies employed to date for labelling of $[\text{}^{99m}\text{Tc}(\text{CO})_3]^+$ to biomolecules have relied on using histidine-tags which are often genetically expressed for ease of purification of proteins, and specifically of different single chain antibody fragments (scFvs), as reviewed by Schibli and Schubiger [218].

Both ^{99m}Tc -fabK1 and ^{99m}Tc -f(ab')₂K1 retained their reactivity to the mesothelin antigen, suggesting that the bioconjugation of N-terminus amines did not cause any significant functional modification of the antigen binding site. Previous studies by Scheck *et al.* have also reported that epitope recognition and antigen binding capabilities of antibody and fab fragments remain unaffected after selective modification of their N-terminus amines [248].

In our biodistribution studies, the uptake of the injected dose correlated inversely with the molecular weight of the radiopharmaceutical. The 50 kDa fab fragment showed the highest uptake, followed by the 100 kDa f(ab')₂ fragment and then the 150 kDa IgG antibody. The peak uptake of ^{99m}Tc -mAbK1 in mesothelin positive NCI-H226 tumours was only about 0.80% at 8 hours, about two-fold higher than that in mesothelin negative LCC6-HER2 tumours at 4 hours,

24 hours and 48 hours (**Figure 2.9**). The tumour uptake of $^{99m}\text{Tc-f(ab')}_2\text{K1}$ (**Figure 2.10 A**) was higher than $^{99m}\text{Tc-mAbK1}$ with peak uptake of 1.2% ID/g of tissue at 8 hours. $^{99m}\text{Tc-fabK1}$ had the highest tumour uptake with peak uptake of 1.4% ID/g at 8 hours (**Figure 2.10 B**). In previous studies, Hassan *et al.* reported much higher tumour uptake of up to 50% ID/g at 72 hours for ^{111}In labelled mAbK1 in mice bearing mesothelin expressing A431K5 tumours. The authors also reported that the affinity of their ^{125}I labelled mAbK1 was very high ($K_d = 0.92$ nM). Our studies with the commercially obtained mAbK1 showed a much lower affinity ($K_d = 21.5 \pm 2.8$ nM, 22.7 ± 6.4 nM and 25.0 ± 1.3 nM for $^{99m}\text{Tc-mAbK1}$, $^{99m}\text{Tc-fabK1}$ and $^{99m}\text{Tc-f(ab')}_2\text{K1}$, respectively).

A tumour model with higher and clinically relevant mesothelin expression levels is critical for achieving sufficient accumulation of radiolabelled antimesothelin antibodies to allow imaging of tumours. In a recently reported study, Yoshida *et al.* observed a tumour uptake of 2.0 to 3.1% ID/g in NCI-H226 tumours for ^{64}Cu labelled anti-mesothelin fab and 1.6 to 2.1% ID/g for ^{111}In labelled fab. Their ^{111}In labelled IgG accumulated in the tumours at 5.3% ID/g after 24 h; but the corresponding tumour uptake of ^{125}I labelled IgG was only 2.5% ID/g. It is noteworthy that their radiolabelled antibodies and fragments had good affinity with K_d values ranging between 4.3 nM to 8 nM. The authors concluded that a more clinically relevant tumour model expressing higher mesothelin levels would be required to evaluate the potential of their anti-mesothelin radioimmunoconjugates. Our findings are in agreement with the observations made by Yoshida *et al.* regarding low localization of mesothelin targeted radioimmunoconjugates in NCI-H226 tumours. While the mesothelin expression levels of NCI-H226 cells are highest amongst established cell lines [157], it is evident that the expression levels are not enough to allow accumulation of mesothelin targeted agents. Therefore the utility of NCI-H226 cell line in pre-clinical development of mesothelin targeted agents is limited. It is also known that for an

antibody to be useful for development of a targeting agent against tumour associated antigens, it must possess good affinity (K_d value between 10 pM to 10 nM) [186]. Based on our studies the commercially obtained mAbK1 has a very low affinity and therefore is not useful as a mesothelin targeting agent. The low affinity of mAbK1 and low expression of mesothelin by NCI-H226 tumours are the main reasons for low tumour accumulation of ^{99m}Tc labelled radioimmunoconjugates.

Kidneys and liver were the major organs showing localization of radioimmunoconjugates. Liver uptake of antibodies and fragments can be attributed to the phagocytotic entrapment of antibody immunoprecipitates from the blood stream [249], Fc-receptor mediated binding to the liver macrophages (predominantly seen for whole IgG antibodies) [250] or complement receptor (CRIg) mediated binding to Kupffer cells followed by transport into the liver cells [251,252]. Incorporation of the $[\text{}^{99m}\text{Tc}(\text{CO})_3]^+$ moiety is known to decrease hydrophilicity and might thus lead to increased hepatobiliary clearance [253]. The kidney uptake was especially prevalent for ^{99m}Tc -f(ab')₂K1 and ^{99m}Tc -fabK1 due to rapid filtration of the antibody fragments and reabsorption by the kidney tubules. A similar phenomenon also explains the kidney uptake of lower molecular weight breakdown products of ^{99m}Tc -mAbK1. Kidneys are a major site of catabolism of low molecular weight proteins, which further leads to retention of the metabolic products in the lysosomal compartment of renal cells [187,188]. Previous studies have shown that radiolabelled antibodies attached to the bifunctional chelator via amine residues undergo complete degradation in kidneys leaving the non-metabolizable radionuclide bound chelate-amine derivative as the final product [254,255]. All of the above contribute to kidney localization of antibody fragments, which can lead to high activity (>50% ID/g) in the kidneys as reported in many studies [256-258]. In comparison, the kidney uptake values of ^{99m}Tc -f(ab')₂K1 and ^{99m}Tc -fabK1 are favourably lower.

After intravenous injection the radiolabelled antibody undergoes a phase of relatively rapid distribution during which it equilibrates with the extracellular fluid, therefore showing high blood pool activity [259]. Typically, whole IgG antibodies take 1-3 days to clear from the blood pool allowing achievement of target to blood ratios suitable for imaging. The fast blood clearance as observed for ^{99m}Tc -mAbK1, can severely limit the ability of antibodies to penetrate the tumours and therefore is partly responsible for low ^{99m}Tc -mAbK1 uptake in NCI-H226 tumours. While ^{99m}Tc -mAbK1 is cleared from the blood; it also appears to undergo elimination through the kidneys at the same rate. Although, ^{99m}Tc -mAbK1 showed good stability to cysteine challenge (**Figure 2.6**), the unexpected fast blood clearance suggests that ^{99m}Tc -mAbK1 was unstable *in vivo* [260]. In previously reported studies by Pimm *et al.* and Sakahara *et al.*, the authors have made similar observations for reduction mediated ^{99m}Tc labelled antibodies. The authors suggested two main mechanisms of *in vivo* instability: 1) Degradation of the antibody to low molecular weight products; and 2) release of ^{99m}Tc or small fragments containing ^{99m}Tc from the antibody. In our experiments, the instability of ^{99m}Tc -mAbK1 can be attributed to formation of smaller ^{99m}Tc labelled fragments, either due to fragmentation or degradation *in vivo*.

2.5. Conclusion

For the first time, bioconjugates between the fab and f(ab')₂ fragments of the anti-mesothelin antibody mAbK1 and a histidine-modified tridentate ligand were made and radiolabelled with [$^{99m}\text{Tc}(\text{CO})_3$]⁺. Our studies demonstrate that antibody fragments labelled using N-(*o*-phenol)-histidine chelator retain their antigen binding ability and immunoreactivity, and have stabilities comparable to previously reported antibody fragments labelled via genetically expressed histidine tags. Although the localization of the radioimmunoconjugates in the NCI-H226 tumours (mesothelin positive) was significantly higher than in LCC6-HER2 tumours (mesothelin

negative), the tumour accumulation in NCI-H226 tumours was not sufficient to allow SPECT imaging of tumours. Additionally, the *in vivo* instability of directly labelled ^{99m}Tc -mAbK1 resulted in lower accumulation in NCI-H226 tumours. The data presented in this chapter identified the main factors responsible for low tumour uptake of anti-mesothelin antibodies and provides direction to further research for successful pre-clinical development of mesothelin targeted radiotracers. From our findings it can be concluded that, in addition to designing stable radiolabelled probes, two main problem areas need to be addressed for pre-clinical development of mesothelin targeted radioimmunoimaging agent. Firstly, an antibody with higher affinity to mesothelin is required; secondly, a tumour xenograft model expressing higher and clinically relevant levels of mesothelin needs to be used for pre-clinical studies. Experiments addressing these issues are described in Chapter 3.

Chapter 3: SPECT/CT Imaging of Mesothelin Expressing Tumours with ^{111}In -Labelled Antibodies

3.1. Introduction

3.1.1. Imaging Mesothelin Expression with ^{111}In Labelled mAbMB Antibody

Mesothelin is over-expressed in some of the most difficult to treat cancers such as mesothelioma, pancreatic cancer and ovarian cancer [21,42,261]. This provides an opportunity to improve clinical outcomes in a significant number of patients by designing molecular bioprobes or therapies targeted towards mesothelin. The purpose of our research is to develop molecular bioprobes for immunoscintigraphic imaging (radioimmunodetection) of mesothelin expressing cancers. Immunoscintigraphic imaging for diagnosis of mesothelin expressing cancers requires efficient targeting of radiolabelled anti-mesothelin antibodies or fragments to tumour associated antigens with minimal background uptake. For this purpose we evaluated $^{99\text{m}}\text{Tc}$ labelled mAbK1 and its fab and f(ab) $^{\prime}$ $_2$ fragments in mice bearing mesothelin expressing NCI-H226 tumours, as described in Chapter 2. Results from these studies demonstrated the need for (1) higher mesothelin expressing tumour model to study the feasibility of imaging tumours with radiolabelled antibody (2) an antibody with higher affinity to mesothelin. The studies in this chapter focused on addressing these issues for improving the tumour uptake of radiolabelled antibodies, with the aim of imaging tumours using single photon emission computed tomography (SPECT). For the studies described in this chapter, we used A431K5 cell line as a model for mesothelin expressing tumours. A431K5 cell line was developed at NIH, by transfecting A431 cells with mesothelin encoding plasmid. The same cell line was also used previously by Hassan *et al.* to demonstrate high tumour uptake of ^{111}In -labelled mAbK1 antibody [164]. To address issues related to low mesothelin affinity of mAbK1 observed in Chapter 2, we considered the use of an alternative antibody with better affinity to mesothelin. In this respect, we chose mAbMB, which has better anti-mesothelin affinity characteristics compared to other available anti-mesothelin antibodies, including mAbK1, as reported by Onda *et al.* [160]. For the studies described in this chapter we used whole antibodies (mAbMB and mAbK1), which are taken up

by tumours slowly, compared to antibody fragments [262]. Whole antibodies are also cleared slowly from normal tissues, thus often requiring 1-2 days to attain maximal tumour to background ratios. Although ^{99m}Tc is the "ideal" isotope from the standpoints of efficiency and radiation dose, it has a short 6-hour half-life, which limits its usefulness for imaging with whole IgG's [263]. ^{111}In has a favourable half-life of 2.8 days for delayed imaging and therefore was chosen in our study as a suitable γ -emitting isotope. ^{111}In emits two γ - photons with energies of 173 keV and 247 keV, which are compatible with most SPECT imaging systems used in the clinic [185]. Besides ^{99m}Tc , ^{111}In is the only other radioisotope clinically approved for imaging with monoclonal antibody based imaging agents [264].

3.1.2. Current Study Outline

The purpose of study presented in this chapter was to evaluate the potential of the ^{111}In -labelled anti-mesothelin antibody mAbMB to selectively accumulate at a tumour site and to be imaged by SPECT/CT. We also compared the characteristics of ^{111}In -mAbMB to those of previously reported ^{111}In -mAbK1 in order to find the optimal one for imaging. Herein, we describe the radiolabelling of the mesothelin antibodies mAbMB and mAbK1 and report their immunoreactivity, affinity, internalization characteristics, biodistribution, and SPECT/CT imaging properties in tumour-bearing mice. The experiments presented in this chapter are outlined in the schematic shown in **Figure 3.1**.

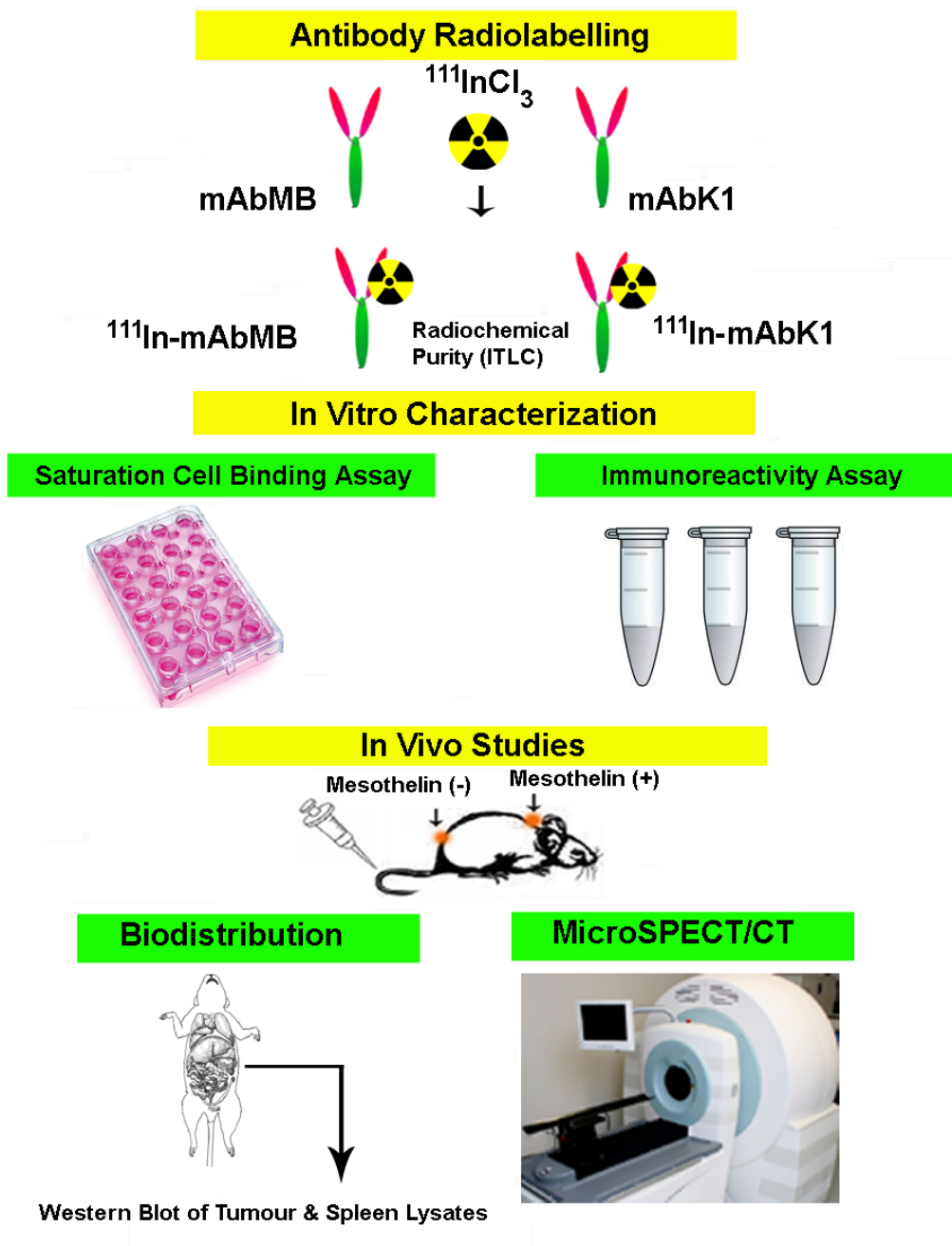


Figure 3.1. Experimental overview of chapter 3.

Both mAbK1 and mAbMB antibodies were radiolabelled with ^{111}In . Affinity and immunoreactivity properties of the radiolabelled antibodies were determined on A431K5 cells using cell based assays. Biodistribution studies were carried out in SCID mice bearing subcutaneous xenografts of A431K5 (mesothelin positive; neck) and A431 (mesothelin negative; lower back). Radioimmunoconjugates were injected through the tail vein and biodistribution determined at different time points for $^{111}\text{In-mAbMB}$ (at two doses) as well as $^{111}\text{In-mAbK1}$. Mesothelin expression of excised tumours was verified by Western blot.

3.2. Materials

All chemicals and reagents were purchased from Sigma-Aldrich (Oakville, Ontario, Canada). The mAbMB antibody was purchased from Rockland Immunochemicals (Gilbertsville, Pennsylvania, U.S.A.) and mAbK1 from Abcam (Cambridge, Massachusetts, U.S.A.). ITLC strips were obtained from Biodex (Cat# 150-771; Shirley, New York, U.S.A.). The cell culture media and supplements were obtained from Invitrogen (Burlington, Ontario, Canada). $^{111}\text{InCl}_3$ was obtained from MDS Nordion (Vancouver, British Columbia, Canada) and p-SCN-bn-DTPA from Macrocyclics (Dallas, Texas, U.S.A.). Ultracel 100K centrifugal filters were purchased from Millipore Corporation (Billerica, Massachusetts, U.S.A.). Reagents for electrophoresis were purchased from BIO-RAD Laboratories (Mississauga, Ontario, Canada). Activity measurements were carried out using a Packard Cobra II gamma counter (Perkin-Elmer, Waltham, Massachusetts, U.S.A.).

3.3. Methods

3.3.1. Radiolabelling

Antimesothelin antibodies mAbMB and mAbK1 were purified and buffer-exchanged into 0.1 M sodium bicarbonate, pH 8.5 using 100 kDa cut-off Ultracel centrifugal filters, and incubated on an Eppendorf shaker for 21 hours at room temperature with p-SCN-bn-DTPA in 0.1 M sodium bicarbonate at a molar ratio of 1:5. After 21 hours, unreacted DTPA (diethylene triamine pentaacetic acid) was removed by centrifugation through the centrifugal filters and antibody buffer-exchanged into 0.15 M ammonium acetate buffer, pH 5.5. For ^{111}In -labelling, $^{111}\text{InCl}_3$ (3.7 MBq/20 μg of antibody) was added to mAbMB and mAbK1 antibody, respectively, and incubated for 30 minutes on an Eppendorf shaker at room temperature. The radiolabelled antibodies were purified using the centrifugal filters and buffer-exchanged into phosphate buffered saline, pH 7.4 (PBS) for injection into mice or *in vitro* testing. Radiochemical purity was determined using ITLC-SG plates after DTPA challenge (0.05 M). Saline was used as the mobile phase. In this ITLC system, ^{111}In -DTPA moves to $R_f = 1$ and ^{111}In -mAb to $R_f = 0$. The number of DTPA molecules conjugated to the antibody was determined by trace labelling with $^{111}\text{InCl}_3$ [265]. Using this method a trace amount of $^{111}\text{InCl}_3$ is added to a small aliquot of antibody-DTPA reaction mixture. The free and conjugated DTPA molecules in the reaction mixture compete equally with the free ^{111}In . The number of DTPA molecules bound to antibody is then determined from the percentage of ^{111}In bound to the antibody and the molar ratio between DTPA and the antibody.

3.3.2. Cell Culture

A431K5 and A431 cell lines were generously provided by Dr. Ira Pastan (NCI, Bethesda, Maryland, U.S.A.) and Dr. Marcel Bally (Advanced Therapeutics, British Columbia Cancer

Agency, Vancouver, Canada), respectively. Both cell lines were cultured in Dulbecco's Modified Eagle medium supplemented with 10% fetal bovine serum, at 37°C in a humidified atmosphere in presence of 5% CO₂ as reported previously [164].

3.3.3. Determination of Immunoreactivity

A cell binding assay was carried out to determine the immunoreactivity of ¹¹¹In-mAbK1 and ¹¹¹In-mAbMB by a similar method as described in section 2.3.4 [235]. Briefly, different concentrations (2×10⁶ cells/ml to 10×10⁶ cells/ml) of mesothelin expressing A431K5 cells were incubated with 5 ng of ¹¹¹In-mAbK1 or ¹¹¹In-mAbMB on a rocker at 4°C for 2 hours. Following incubation, the cells were centrifuged for 5 minutes at 500 g, the supernatant was removed and the cells were washed 3 times with PBS containing 1% BSA and counted in a γ -counter to determine the total binding of ¹¹¹In-labelled antibody to A431K5 cells. Non-specific binding was determined in presence of excess unlabelled antibody (10 μ g). Specific binding was calculated as the difference between total and non-specific binding to A431K5 cells. The immunoreactivities were calculated from the Y-intercept of the double reciprocal plot of fraction of the radioactivity specifically bound *vs.* the cell number.

3.3.4. Saturation Binding - K_d and B_{max} Determination

Cell binding experiments were carried out by a similar method as described in section 2.3.7, for determination of the dissociation constant (K_d) for ¹¹¹In-mAbMB and ¹¹¹In-mAbK1 and maximum number of binding sites (B_{max}) for A431K5 cells [236]. Briefly, about 50,000 A431K5 cells/well were plated overnight in a 24 well plate. Adherent cells were then incubated in serum-free culture media with increasing concentrations (0–80 nM) of ¹¹¹In-antibody (mAbMB and mAbK1) in a total volume of 500 μ l for 3 hours at 4°C. The cells were then washed twice with

ice-cold PBS to remove unbound radioactivity, dissolved in 0.1 M NaOH and analyzed in a γ -counter. Prism[®] Version 5.0 software (GraphPad Software, San Diego, CA, USA) was used to fit the total binding values against the concentration of unbound radiolabelled antibodies, to a one-site saturation binding model. K_d and B_{max} were determined using this model by fitting only total binding, assuming that the amount of nonspecific binding was proportional to the concentration of radioligand. The average number of mesothelin receptors present on A431K5 cells was calculated by conversion of the B_{max} values.

3.3.5. Internalization of ¹¹¹In-labelled Antibodies by A431K5 Cells

To determine and compare the rate of internalization of ¹¹¹In-mAbMB and ¹¹¹In-mAbK1 by A431K5 cells, an internalization assay was carried out [158]. Briefly, 1×10^6 A431K5 cells were incubated in 1 ml medium with 5 ng of ¹¹¹In-labelled antibody for 1 hour at 4°C in culture tubes. Centrifugation for 5 minutes at 200 g was carried out to remove the unbound antibody, followed by one wash with ice-cold PBS. The cells were then re-cultured with 1 ml of medium or counted on the γ -counter for determination of internalization at time 0. At 3, 6 and 18 hours, the internalized fraction was separated by treating with 1 ml acidic buffer (0.1 M acetic acid in 0.01 M PBS, pH 2.85) and pelletized by centrifuging for 5 minutes at 200 g. The supernatant comprising the membrane-bound fraction (acid labile) was separated and both fractions counted in a γ - counter.

3.3.6. Tumour Uptake and Biodistribution

Tumour uptake and biodistribution experiments were carried out in male C.B-17 SCID mice (Taconic, Germantown, New York, U.S.A.). Mice were injected with 8×10^6 A431K5 (mesothelin positive) cells in the nape of the neck and the same number of A431 cells

(mesothelin negative) in the lower back. When tumours exceeded a size of 0.5 cm in diameter, four groups of mice (n=5) were injected intravenously with about 4 µg/740 kBq of ¹¹¹In-mAbMB and euthanized 24, 48, 72 and 96 hours later, all major organs removed and analyzed. Biodistribution of ¹¹¹In-mAbMB was similarly evaluated at 24 hours in one group of mice (n=3) not bearing any tumours.

Biodistribution of ¹¹¹In-mAbK1 was evaluated in 2 groups of mice (n=5) after injecting 740 kBq of ¹¹¹In-mAbK1 intravenously followed by euthanasia at 24 and 72 hours for collection of major organs. Additionally, biodistribution of ¹¹¹In-mAbMB antibody was also studied at a higher dose of between 7.4 to 10.1 MBq (50 µg/9.25 MBq) in two groups of mice (n=3) at 24 and 72 hours. To compare the extent of radioactivity localization in different organs and tumour, the ratio of radioactivity in different tissues and total blood (for the same weight) was determined. Animal experiments were carried out in accordance with the guidelines of the University of British Columbia's Animal Care Committee.

3.3.7. MicroSPECT/CT Imaging

MicroSPECT/CT imaging of mice bearing A431K5 and A431 tumours was performed after injection of ¹¹¹In-mAbMB at 24 (n=6), 48 (n=6) and 72 hours (n=3). In a parallel study, tumour-bearing mice (n=2) were injected with ¹¹¹In-mAbK1 and imaging was performed at 24, 48 and 72 hours. After injecting 7.4 to 10.1 MBq of activity, acquisitions were performed on a GammaMedica Ideas X-SPECT system (North Ridge, California, U.S.A.). CT acquisitions consisted of 1024 projections acquired over 360° with a 70 kVp, 205 µA cone beam x-ray. Cobra Exxim software (Feldkamp filtered back projection cone beam software) was used to reconstruct the image at an isotropic voxel size of 0.155 mm. The SPECT images were acquired using a dual head system fitted with 1 mm aperture medium energy pinhole collimators set at an ROR of 77

mm. Energy windows (10%) were set over the 173 keV and 247 keV peaks. The total counts/scan for 24, 48 and 72 hour acquisitions were 60,000-90,000, 45,000-65,000 and 40,000-50,000, respectively. GammaMedica-Ideas FLEX-SPECT software was used to reconstruct the data at an isotropic 1.17033 mm voxel size. After fusion of the SPECT and CT data, region of interest (ROI) analysis was carried out using AMIDE software (version 0.9.1) [266] to determine the target to non-target ratios (T/NT) for both A431K5 and A431 tumours and statistical significance calculated by student's t-test. Due to small sample size (n=2), statistical analysis was not carried out for ROI data of images obtained with ^{111}In -mAbK1.

3.3.8. Mesothelin Expression in Tumours

The verification of mesothelin protein expression in the harvested tumours was performed by Western blot using the anti mesothelin antibody mAbMB by a similar method as described in section 2.3.9. A431K5 cells in culture flasks were washed with PBS and lysed in 1 ml of RIPA buffer [150 mM NaCl, 1% nonyl phenoxy polyethoxy ethanol, 0.5% Na deoxycholate, 0.1% Na dodecylsulfate, 50 mM Tris-HCl (pH 7.5), 1% protease inhibitor cocktail (Sigma)]. The cell lysates were centrifuged at 8,000 rpm (5223 g) for 10 min at 4°C and the supernatant was collected. Tumour lysates were prepared by homogenizing frozen tumour (five A431K5 tumours K1-K5; five A431 tumours A1-A5) samples in 1 ml of ice-cold homogenization buffer [10 mM EGTA, 2 mM EDTA, 25 mM sucrose, Tris-HCl 20 mM (pH 7.5), 1% protease inhibitor cocktail], followed by sonication for 10 seconds. A spleen lysate (S) was also prepared to check for any cross reactivity by western blot analysis. A431K5 cell lysates were prepared and used as a positive control. The lysates were centrifuged at 11,000 rpm (9875 g) for 10 min at 4°C and the supernatant was collected. Samples were prepared for electrophoresis in Laemmli sample buffer (Bio-Rad) containing 5% v/v of 2-mercaptoethanol (Bio-Rad). The samples were heated at 99°C for 5 min, and loaded onto the SDS-polyacrylamide gel (12% gel) at a protein concentration of

10 µg/ per well, and fractionated, followed by transfer onto a nitrocellulose Hy-Bond ECL membrane (Amersham Ltd. Oakdale, Ontario, Canada). The membrane was then processed for washing with 5% milk in Tris-Buffered Saline Tween-20 (TBST) for 1 hour at room temperature (RT) followed by incubation with the anti-mesothelin antibody mAbMB in 5% BSA in TBST at 1:1000 dilution overnight at 4°C. Secondary antibody 1:5000 (horseshoe peroxidase-labelled goat antimouse IgG; Jackson ImmunoResearch Laboratories) was incubated for 1 hour at RT followed by chemiluminescence detection using the ECL Western blotting detection kit (Amersham) according to the manufacturer's suggested protocol. Images were captured using an Alpha Innotech FluorChem 8800 gel box imager (Alpha Innotech Co., San Leandro, California, U.S.A.). The bands were quantified by densitometric analysis using FluorChem software (Alpha Innotech). As a loading control, the membrane was stripped and reprobed with monoclonal anti-β-actin antibody (Sigma).

3.4. Results

3.4.1. Radiolabelling

¹¹¹In-labelling of both mAbK1 and mAbMB using the p-SCN-bn-DTPA chelator was consistently accomplished with labelling efficiencies of about 95% (94.78±0.63% for ¹¹¹In-mAbMB and 95.44±0.25% for ¹¹¹In-mAbK1). The average number of bound DTPA molecules was 2.6 per molecule of mAbK1 and 2.4 per molecule of mAbMB.

3.4.2. Immunoreactivity and Saturation Cell Binding Studies

The results of the immunoreactivity assay and saturation cell binding studies are summarized in **Table 3.1**. Both ¹¹¹In-labelled antibodies retained their reactivity to the mesothelin antigen, suggesting that the radiolabelling procedure did not cause any major modification to the structure of the antigen-binding site. Saturation cell binding studies indicate that ¹¹¹In-mAbMB has a lower K_d and therefore a higher affinity for the mesothelin receptors as compared to ¹¹¹In-mAbK1 (**Table 3.1**). The number of mesothelin receptors on A431K5 cells, calculated from the B_{max} values was $6.3 \times 10^5 \pm 1.9 \times 10^5$ / cell.

Table 3.1. Immunoreactivity of ¹¹¹In-mAbMB and ¹¹¹In-mAbK1 determined by a cell-binding assay using A431K5 cells. Total binding of ¹¹¹In-mAbMB and ¹¹¹In-mAbK1 to A431K5 cells was used to calculate K_d . Data is presented as mean±SD.

	Immunoreactivity (%)	K_d (nM)
¹¹¹ In-mAbMB	78.5±3.5	3.6±1.7
¹¹¹ In-mAbK1	76.3±3.8	29.3±2.3

3.4.3. Internalization by A431K5 cells

We studied internalization of ^{111}In -mAbMB and ^{111}In -mAbK1 from the cell membrane using A431K5 cells (**Figure 3.2**). After a 1 hour pre-incubation at 4°C (time 0 hours) $21.6\pm 6.5\%$ of total bound ^{111}In -mAbMB was present in the internalized acid resistant fraction, whereas for ^{111}In -mAbK1, the internalized fraction was only $6.0\pm 2.5\%$. After 3 hours at 37°C , internalized fractions increased to $46.2\pm 6.9\%$ and $32.8\pm 1.2\%$ for ^{111}In -mAbMB and ^{111}In -mAbK1, respectively. After 6 hours, the internalized fractions were $52.1\pm 3.7\%$ and $41.5\pm 7.6\%$, respectively. At 18 hours, the internalization of ^{111}In -mAbMB was significantly different ($P<0.05$) at $76.4\pm 6.8\%$ compared to $59\pm 0.6\%$ for ^{111}In -mAbK1. Control studies carried out at 4°C showed that the internalized fraction increased slowly over time; at 18 hours maximal internalization of $29.9\pm 10.0\%$ and $26.9\pm 3.6\%$ was obtained for ^{111}In -mAbMB and ^{111}In -mAbK1, respectively.

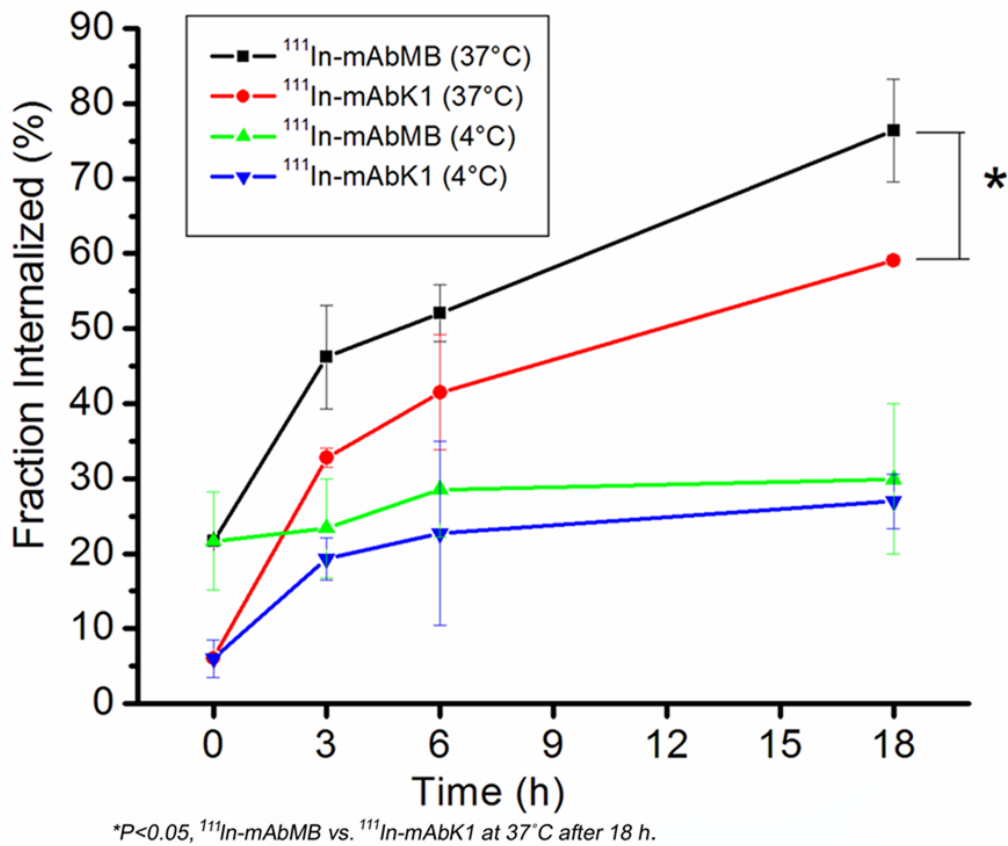


Figure 3.2. Time and temperature dependent cellular internalization of $^{111}\text{In-mAbMB}$ and $^{111}\text{In-mAbK1}$ by A431K5 cells. $^{111}\text{In-mAbMB}$ has greater cellular internalization than $^{111}\text{In-mAbK1}$ throughout the time course of the study, with significantly higher values ($P < 0.05$) achieved at 18 hours. Data is presented as mean \pm SD.

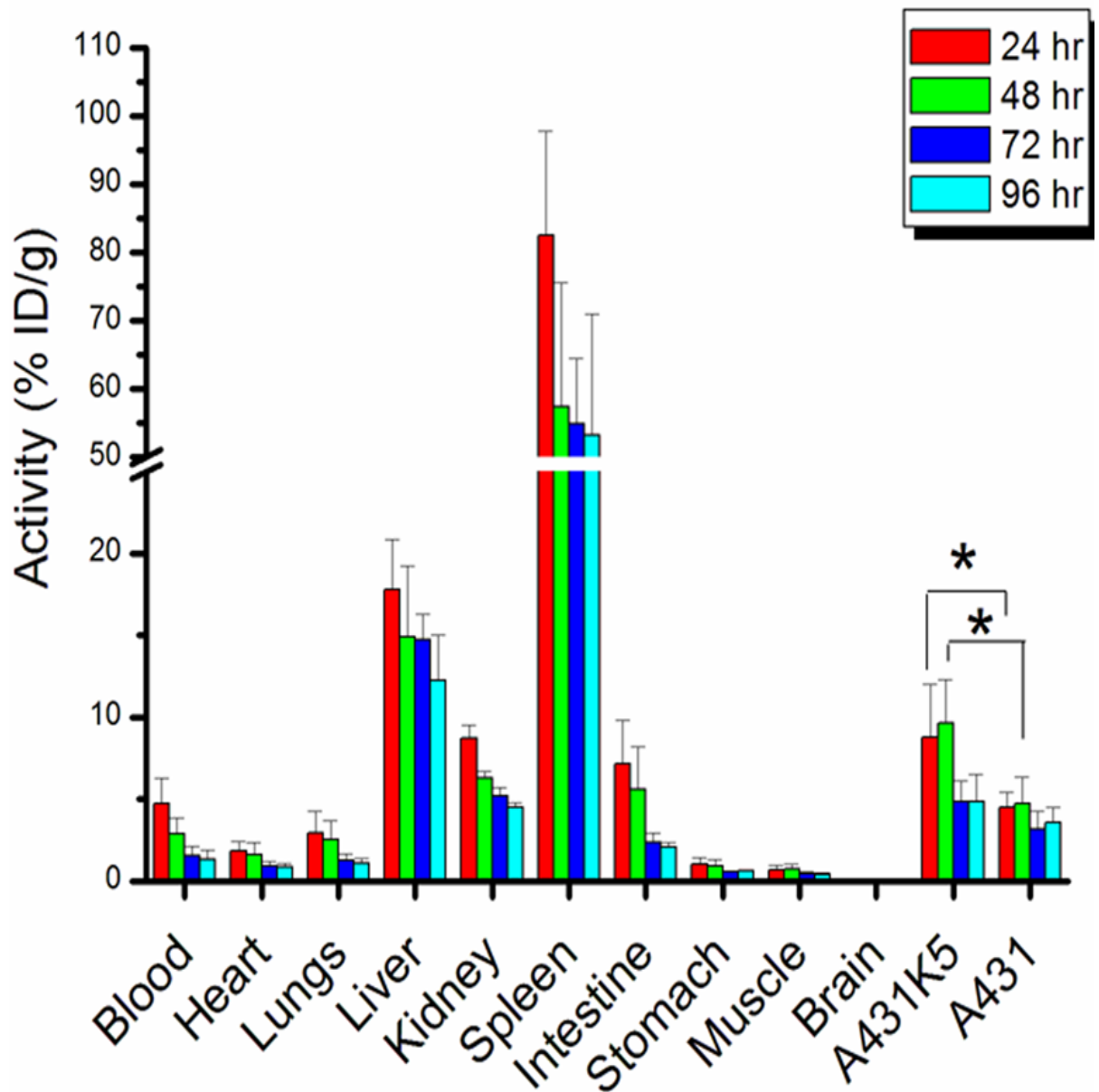
3.4.4. Biodistribution Studies

Biodistribution studies for ^{111}In -mAbMB were performed in SCID mice at two different doses. At the dose of 740 kBq (**Figure 3.3**), after 24 hours, $8.74\pm 3.25\%$ ID/g was localized in the A431K5 tumours, whereas $4.5\pm 0.91\%$ ID/g was present in A431 tumours. Maximal A431K5 tumour uptake of $9.65\pm 2.65\%$ ID/g was obtained at 48 hours, which was significantly different ($P<0.05$) from the corresponding uptake for A431 tumours, $4.7\pm 1.65\%$ ID/g. Thereafter, the tumour localization declined to $<5\%$ for A431K5 tumours and $<3.5\%$ for A431 tumours at 72 hours and remained steady until 96 hours. In addition to the tumours, ^{111}In -mAbMB showed uptake in the spleen, liver and kidneys. Spleen uptake was $82.4\pm 15.3\%$ ID/g after 24 hours and declined to $57.32\pm 18.19\%$ ID/g at 48 hours. Maximal uptake of ^{111}In -mAbMB into liver ($17.79\pm 3.04\%$ ID/g) as well as kidneys ($8.7\pm 0.82\%$ ID/g) was obtained at 24 hours. Blood activity remained relatively low at all time points and showed a steady decline from $4.71\pm 1.58\%$ ID/g at 24 hours to $1.29\pm 0.58\%$ ID/g at 96 hours. The tumour to blood ratio was >1 at all time points, and increased over time from 24 to 96 hours (**Table 3.2**). Biodistribution studies in mice without any tumours indicated low uptake of ^{111}In -mAbMB in spleen ($8.06\pm 0.70\%$ ID/g) and $6.13\pm 0.60\%$ ID/g in liver, while rest of organs showed similar activity uptake as the tumour bearing mice (**Figure 3.5**).

When 7.4 to 10.1 MBq of ^{111}In -mAbMB was injected, $13.15\pm 6.37\%$ ID/g had localized in A431K5 tumours at 48 hours, whereas, at the same time A431 tumours accumulated $3.71\pm 1.79\%$ ID/g (**Figure 3.4**). At 72 hours, $14.29\pm 6.18\%$ ID/g and $4.93\pm 2.84\%$ ID/g was found localized in A431K5 and A431 tumours, respectively. Kidney uptake at 48 hours ($11.60\pm 2.10\%$ ID/g) was higher than the uptake with the lower dose (740 kBq) of ^{111}In -mAbMB, but at 72 hours the kidney uptake at both doses was similar. The overall spleen uptake of ^{111}In -mAbMB expressed in terms of %ID/organ at the higher dose was lower than that observed at the lower dose for both

48 and 72 hour time points (**Figure 3.6 A**). The spleen weights showed a decrease of about 60% compared to the spleen weights obtained at lower dose (**Figure 3.6 B**). As a result, the spleen activity in terms of % ID/g at the higher dose was greater than that observed at the lower dose for both 48 and 72 hour time points (**Figure 3.6 C**). Activity taken up by the liver was similar at both doses. Blood activity was $5.26 \pm 2.04\%$ ID/g at 48 hours and further declined to $3.57 \pm 1.64\%$ ID/g at 72 hours. The maximal tumour to blood ratio of 4.02 ± 0.72 was obtained for A431K5 tumours at 72 hours, while the corresponding tumour to blood ratio for A431 tumours was only 1.43 ± 0.80 (**Table 3.3**).

For ^{111}In -mAbK1, biodistribution studies were carried out only at the dose of 740 kBq (**Figure 3.7**). At 24 hours, $3.04 \pm 0.68\%$ ID/g was taken up in the A431K5 tumours, while $2.22 \pm 0.41\%$ ID/g was found in the A431 tumours. After 72 hours, tumour localization declined to $2.32 \pm 0.11\%$ ID/g for A431K5 tumours and to $1.64 \pm 0.46\%$ ID/g for A431 tumours. At both time points the activity uptake in the A431K5 tumours was significantly higher ($P < 0.05$) than in the A431 tumours. Liver uptake was $23.00 \pm 2.86\%$ ID/g and $17.02 \pm 2.17\%$ ID/g at 24 and 72 hours, respectively. Although the liver uptake was higher for ^{111}In -mAbK1 than ^{111}In -mAbMB, spleen showed much less uptake at both 24 ($8.05 \pm 1.13\%$ ID/g) and 72 hours ($6.0 \pm 1.96\%$ ID/g). ^{111}In -mAbK1 localization in the kidneys was 4.87 ± 0.33 and $3.28 \pm 1.17\%$ ID/g at 24 and 72 hours, respectively, which was again lower than that of ^{111}In -mAbMB. Blood activity was also lower ($2.8 \pm 0.67\%$ ID/g and $1.13 \pm 1.6\%$ ID/g at 24 and 72 hours, respectively) indicating faster clearance of ^{111}In -mAbK1. At 24 hours, tumour to blood ratio for A431K5 tumours was 1.20 ± 0.26 , which increased to 5.29 ± 0.88 after 72 hours (**Table 3.4**).

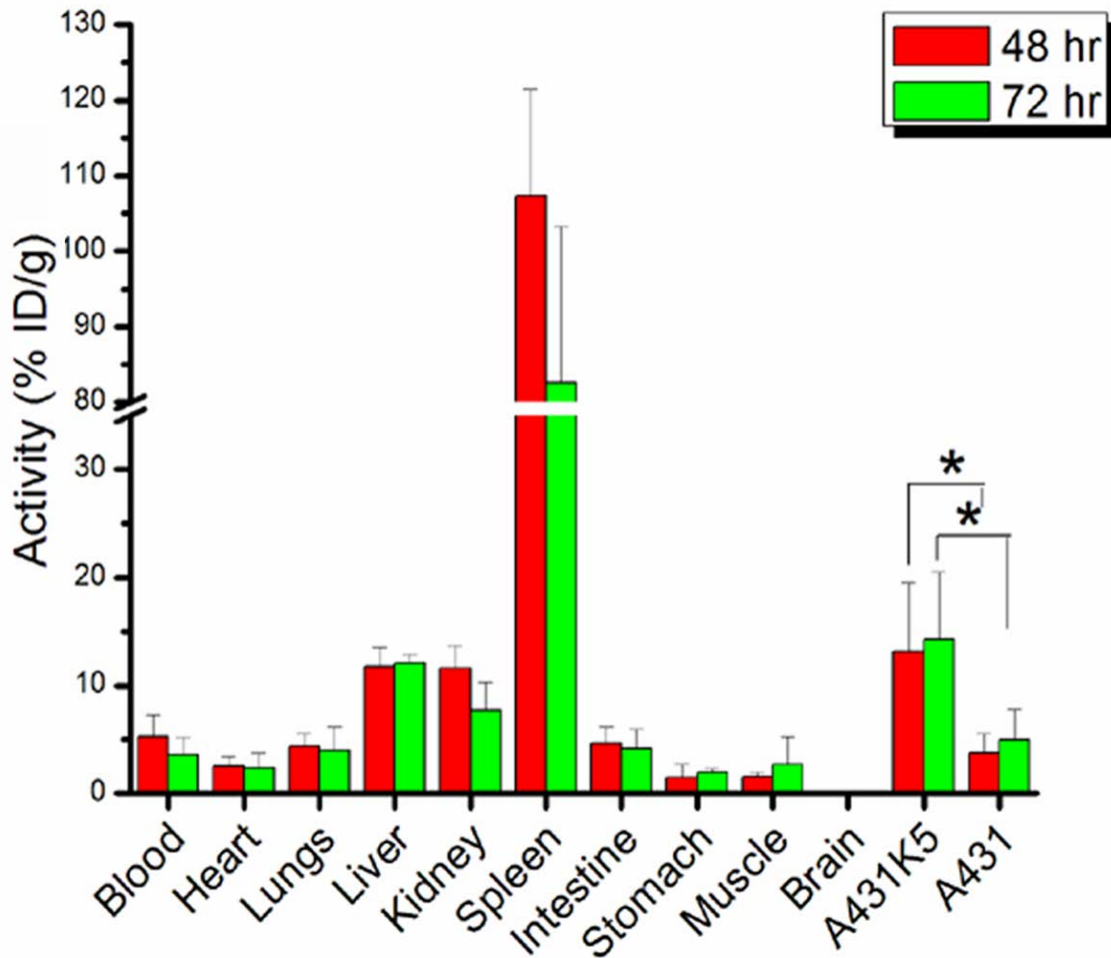


* $P < 0.05$, A431K5 tumours vs. A431 tumours at the corresponding time point

Figure 3.3. Biodistribution of ^{111}In -mAbMB (740 kBq) injected into SCID mice (n=5) bearing A431K5 (mesothelin positive) and A431 (mesothelin negative) subcutaneous xenografts. Percentage of the injected dose/gram (Activity % ID/g) was determined in the tumours and all major organs after 24, 48, 72 and 96 hours. Data is presented as mean \pm SD.

Table 3.2. Organ to blood ratios of ¹¹¹In-mAbMB (740 kBq), injected in SCID mice (n=5) bearing A431K5 (mesothelin positive) and A431 (mesothelin negative) subcutaneous xenografts. Biodistribution was determined after 24, 48, 72 and 96 hours. Data is presented as mean±SD.

Organ	24 h	48 h	72 h	96 h
Blood	1	1	1	1
Heart	0.41±0.05	0.54±0.13	0.61±0.12	0.68±0.12
Lungs	0.64±0.15	0.83±0.19	0.82±0.11	0.89±0.19
Liver	4.52±2.27	5.73±2.87	10.94±4.60	10.70±4.30
Kidneys	2.15±0.85	2.36±0.76	3.86±0.05	3.91±1.26
Spleen	19.79±5.99	20.74±8.28	39.33±15.12	44.67±18.71
Intestine	1.58±0.32	1.88±0.60	1.66±0.68	1.72±0.44
Stomach	0.23±0.05	0.31±0.05	0.38±0.10	0.49±0.12
Muscle	0.15±0.01	0.25±0.04	0.30±0.04	0.33±0.08
Brain	0.03±0.01	0.04±0.01	0.04±0.05	0.05±0.01
A431K5 (meso +ve)	1.89±0.36	3.23±0.66	3.27±0.51	3.83±0.38
A431 (meso -ve)	1.03±0.28	1.52±0.27	2.14±0.46	2.95±0.58



* $P < 0.08$, A431K5 tumours vs. A431 tumours at the corresponding time point.

Figure 3.4. Biodistribution of ^{111}In -mAbMB (7.4 to 10.1 MBq), injected in SCID mice (n=3) bearing A431K5 (mesothelin positive) and A431 (mesothelin negative) subcutaneous xenografts. Percentage of the injected dose/gram (Activity %ID/g) was determined in the tumours and all major organs after 48 and 72 hours. Data is presented as mean \pm SD.

Table 3.3. Organ to blood ratios of ¹¹¹In-mAbMB (7.4 to 10.1 MBq), injected in SCID mice (n=3) bearing A431K5 and A431 subcutaneous xenografts. Biodistribution was determined after 48 and 72 hours. Data is presented as mean±SD.

Organ	48 h	72 h
Blood	1	1
Heart	0.49±0.12	0.64±0.09
Lungs	0.86±0.11	1.08±0.12
Liver	2.42±4.60	3.84±1.52
Kidneys	2.37±0.05	2.25±0.30
Spleen	23.57±15.12	24.74±5.65
Intestine	0.90±0.68	1.18±0.26
Stomach	0.23±0.10	0.59±0.16
Muscle	0.31±0.04	0.64±0.37
Brain	0.03±0.05	0.06±0.02
A431K5 (meso +ve)	2.42±0.51	4.02±0.72
A431 (meso -ve)	0.68±0.46	1.43±0.80

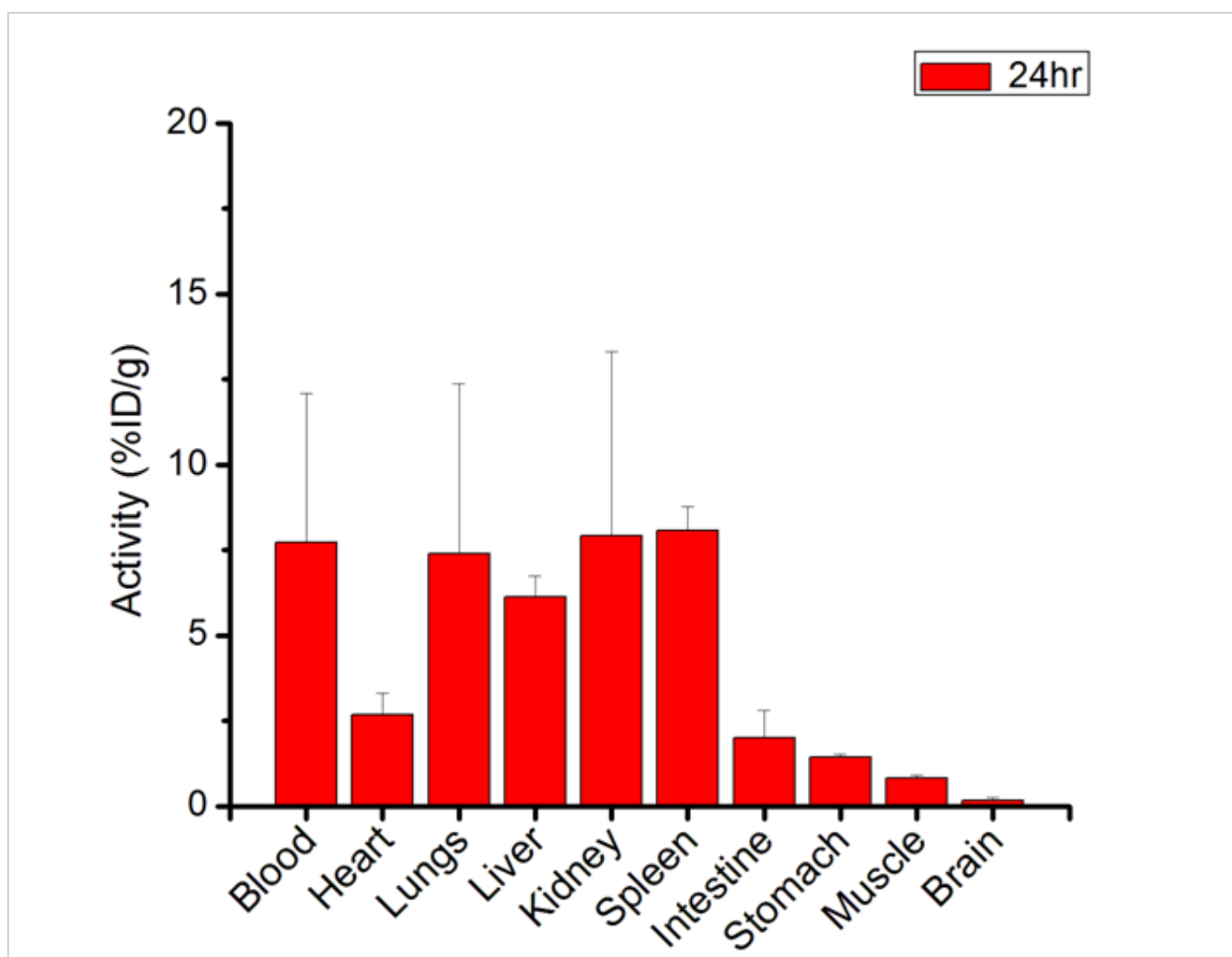


Figure 3.5. Biodistribution of ^{111}In -mAbMB in SCID mice (n=3) without tumours. Percentage of the injected dose/gram (Activity %ID/g) was determined in all major organs after 24 hours. Data is presented as mean \pm SD.

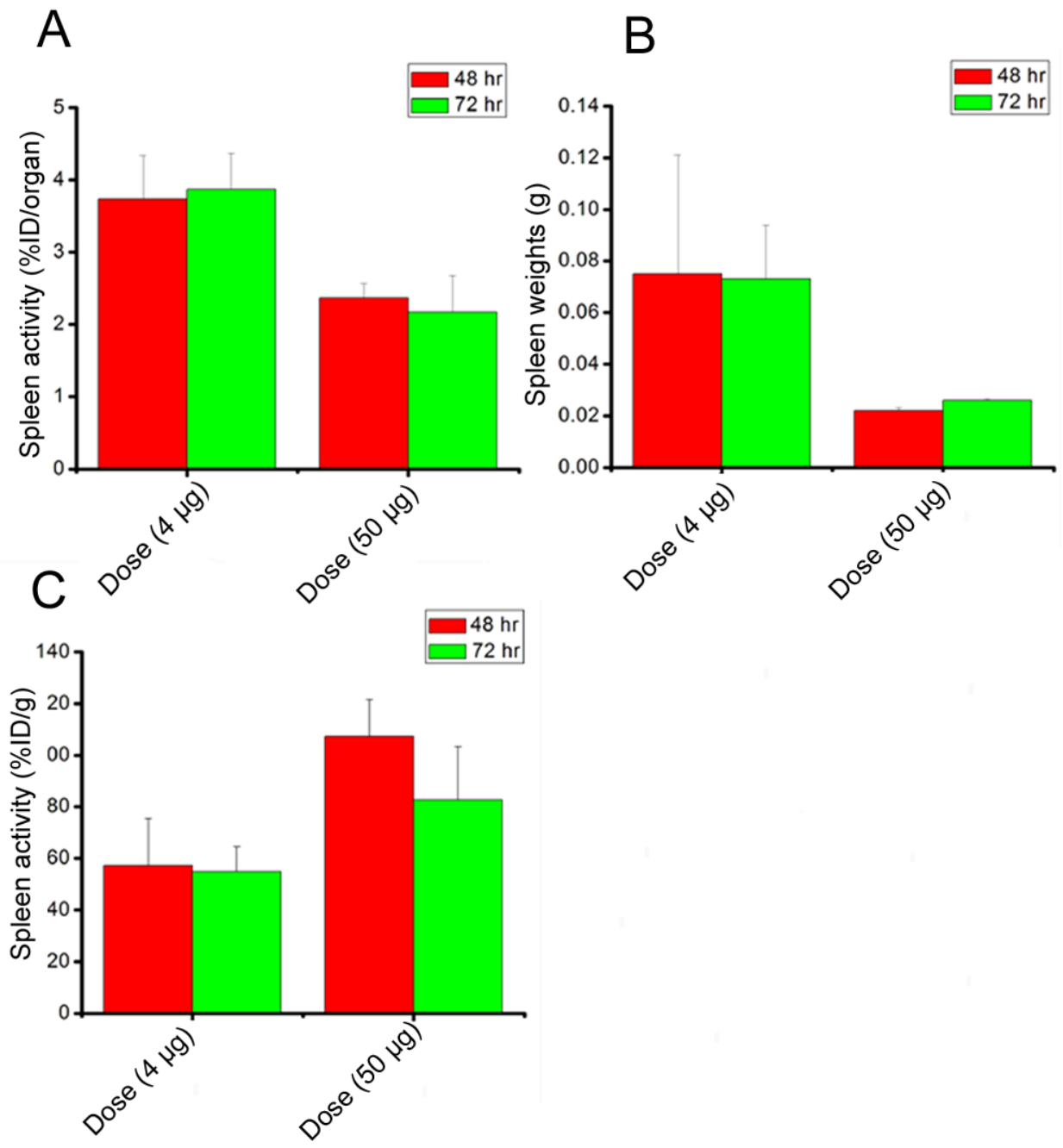


Figure 3.6. A comparison of spleen activity uptake and spleen weights at 48 and 72 hours after injection of ¹¹¹In-mAbMB at low dose (4 µg) or high dose (50 µg). The spleen activity in terms of %ID/organ (A) decreases at the higher dose accompanied by decrease in the spleen weights (B), which results in an increased activity on per weight basis (%ID/g) in spleen (C). Data is presented as mean±SD.

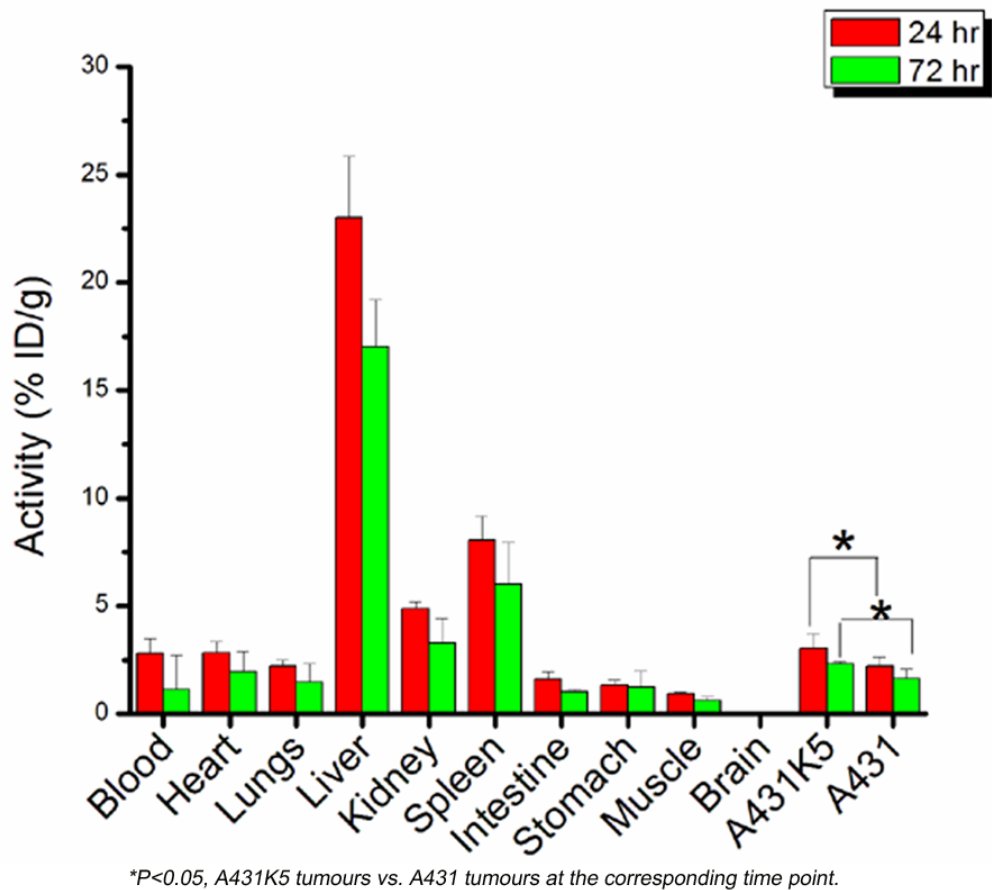


Figure 3.7. Biodistribution of ^{111}In -mAbK1 (740 kBq), injected in SCID mice (n=5) bearing A431K5 (mesothelin positive) and A431 (mesothelin negative) subcutaneous xenografts. Percentage of the injected dose/gram (Activity %ID/g) was determined in the tumours and all major organs after 24 and 72 hours. Data is presented as mean \pm SD.

Table 3.4. Organ to blood ratios of ¹¹¹In-mAbK1 (740 kBq) in SCID mice (n=3) bearing A431K5 (mesothelin positive) and A431 (mesothelin negative) subcutaneous xenografts. Biodistribution were determined after 24 and 72 hours. Data is presented as mean±SD.

Organ	24 h	72 h
Blood	1	1
Heart	1.08±0.14	3.39±0.61
Lungs	0.91±0.12	2.73±1.59
Liver	9.78±1.12	36.94±4.73
Kidneys	1.96±0.13	3.86±0.05
Spleen	3.26±0.47	11.80±1.60
Intestine	0.70±0.09	2.23±0.45
Stomach	0.55±0.09	2.53±1.44
Muscle	0.41±0.02	1.34±0.34
Brain	0.03±0.00	0.08±0.01
A431K5 (meso +ve)	1.20±0.26	5.29±0.88
A431 (meso -ve)	0.88±0.18	3.40±0.64

3.4.5. MicroSPECT/CT Imaging

^{111}In -mAbMB was clearly visualized in A431K5 tumours 24, 48 and 72 hours after injection (**Figure 3.8 A**). The activity distribution in spleen and liver was also evident, confirming the findings of biodistribution studies. T/NT ratios for A431K5 and A431 tumours obtained by ROI analysis of the images showed that ^{111}In -mAbMB was targeted better to A431K5 tumours than to A431 tumours. The difference in T/NT ratios was significant at all the three time points (**Figure 3.9 A**). Although mice injected with ^{111}In -mAbK1 showed lower tumour uptake, the tumours were still visualized (**Figure 3.8 B**). ^{111}In -mAbK1 activity was also observed in the bladder indicating clearance through the organ. ROI analysis showed that A431K5 tumours had better uptake than A431 tumours, with T/NT ratios increasing over time (**Figure 3.9 B**), however statistical analysis was not carried out due to the small sample size. Better T/NT ratios and image contrast of A431K5 tumours was obtained for ^{111}In -mAbMB, compared to ^{111}In -mAbK1.

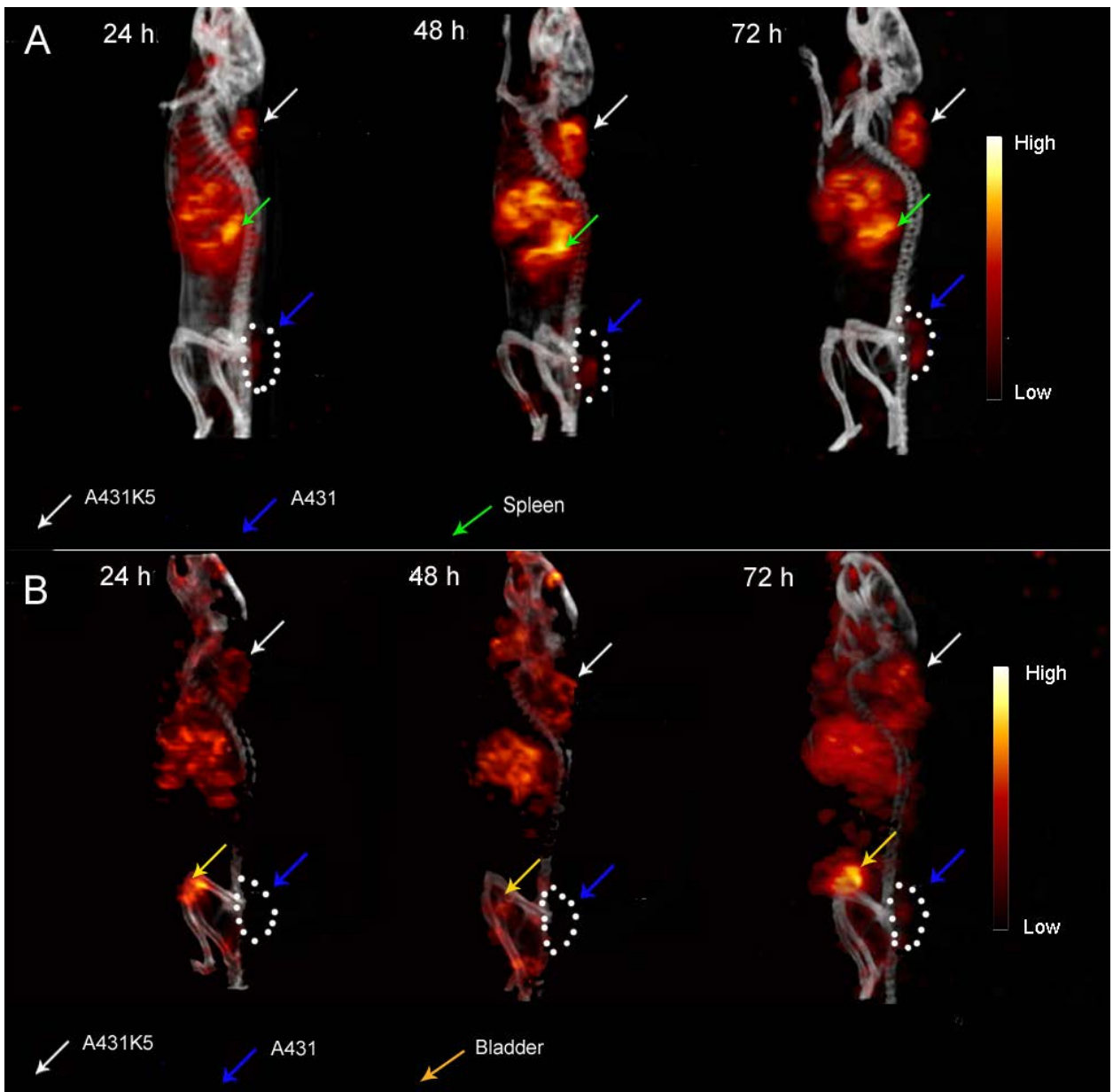


Figure 3.8. MicroSPECT/CT images of SCID mice bearing A431K5 (mesothelin positive) and A431 (mesothelin negative) tumours. SCID mice were injected with 7.4 to 10.1 MBq of (A) ^{111}In -mAbMB and (B) ^{111}In -mAbK1 and images were acquired after 24, 48 and 72 hours (h).

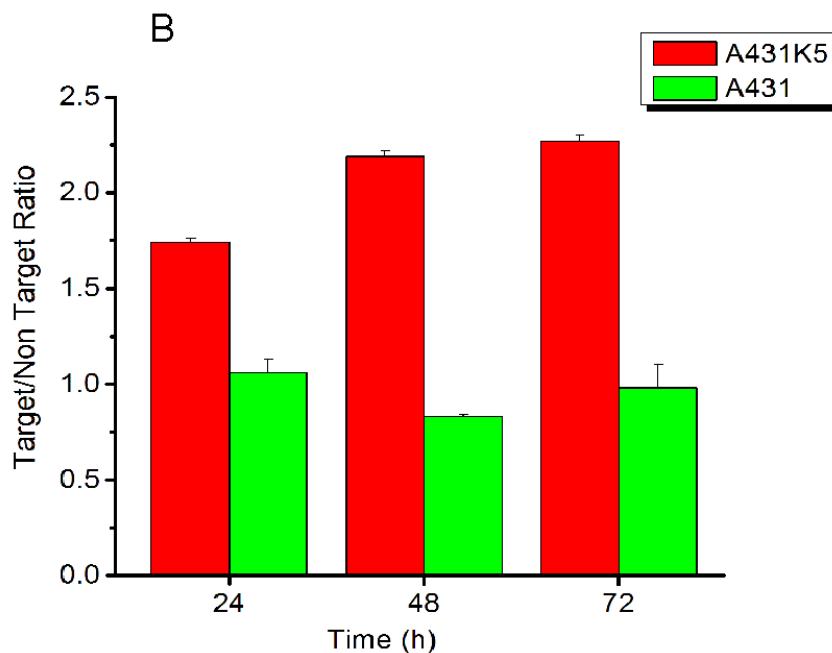
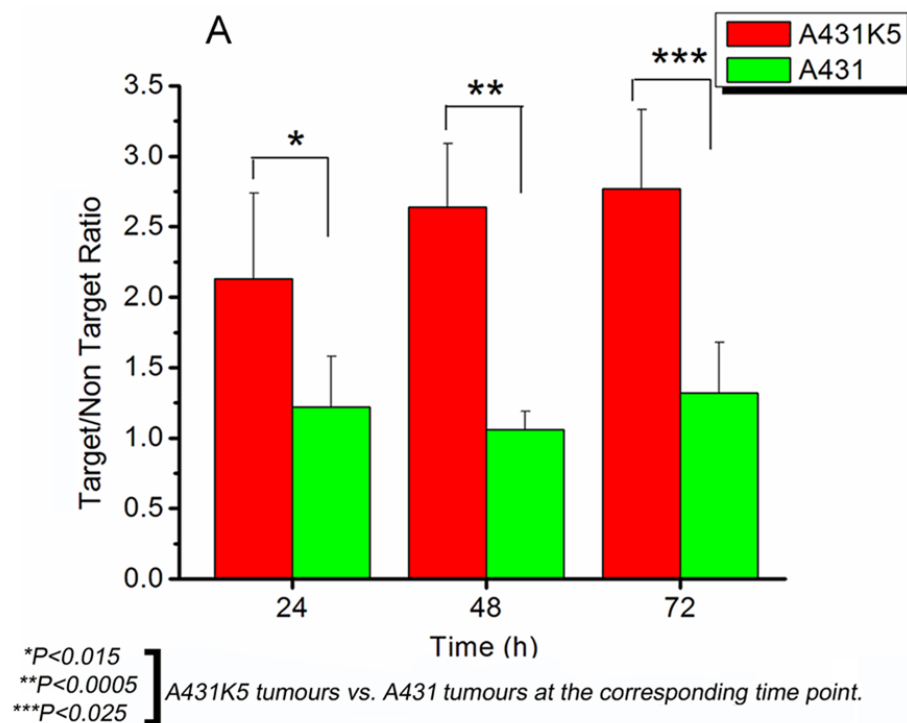


Figure 3.9. Target to Non-Target (T/NT) ratios calculated from ROI analysis of microSPECT/CT images of SCID mice bearing A431K5 and A431 subcutaneous xenografts. Images were acquired (A) at 24 (n=6), 48 (n=6) and 72 (n=3) hours after injection with 7.4 to 10.1 MBq of ^{111}In -mAbMB and (B) at 24, 48 and 72 hours of mice (n=2) injected with 7.4 to 10.1 MBq of ^{111}In -mAbK1. Data is presented as mean \pm SD.

3.4.6. Mesothelin Expression in Tumours

Both A431K5 and A431 cells formed tumours following subcutaneous injection. Western blotting confirmed that mesothelin was expressed in the A431K5 tumours but not in the A431 tumours nor in the spleen (**Figure 3.10**). Both the precursor (71 kDa) and mature mesothelin (40 kDa) bands as reported previously by Ho *et al.* [267], were visualized on the Western blots.

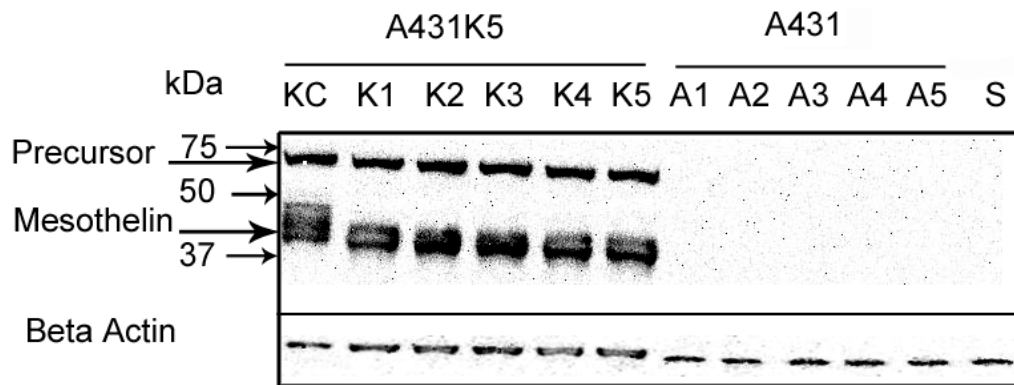


Figure 3.10. Western blot confirming the mesothelin expression in A431K5 (K1-K5) tumours. The spleen (S) and A431 (A1-A5) tumours showed no expression of mesothelin. The cell lysate from A431K5 (KC) was used as a positive control, while beta actin was used as a loading control.

3.5. Discussion

In the present study the preclinical SPECT imaging of mesothelin-expressing tumours using radiolabelled anti-mesothelin antibodies was successfully demonstrated. Although the tumour uptake with ^{111}In -mAbK1 was again significantly lower than reported by Hassan *et al.*, it was possible to image the mesothelin-expressing tumours. The superior uptake of ^{111}In -mAbK1 into A431K5 tumours, compared to previously observed uptake of $^{99\text{m}}\text{Tc}$ labelled fab and $\text{f(ab}')_2$ of mAbK1, in NCI-H226 tumours (Chapter 2) can be attributed to the 7 times higher mesothelin expression by A431K5 cells (6.3×10^5 receptors/cell) than NCI-H226 tumours (9.1×10^4 receptors/cell). The newly available mAbMB was clearly superior in the form of the ^{111}In -mAbMB radioimmunoimaging bioprobe. *In vitro* studies also confirmed the specific binding and internalization of ^{111}In -mAbMB in mesothelin-expressing A431K5 cells. In addition, comparative studies to ^{111}In -mAbK1 revealed that ^{111}In -mAbMB has superior mesothelin targeting properties. Such a radiolabelled antibody might be considered in patients, after applying recent strategies towards developing chimeric or fully humanized forms of this antibody [268].

Established cell lines such as NCI-H226 express low levels of mesothelin. For this reason, we used A431K5 cells which express mesothelin at levels similar to those seen on immunohistochemical examination of patient tumour specimens [156]. A431K5 cells are human, epidermoid A431 cells stably transfected with pcD3CAK1-9, a plasmid encoding the mesothelin gene [269]. Our studies indicate that A431K5 cells express about 6.3×10^5 mesothelin receptors per cell.

A requirement for a radiolabelled antibody is that it be able to bind a specific antigen with high affinity (low K_d). Under *in vitro* conditions, a K_d value between 10 pM (higher affinity) and 10

nM (lower affinity), is considered ideal [186]. We demonstrated that the affinity of ^{111}In -mAbMB ($K_d = 3.6$ nM) for mesothelin receptors is about 8 times higher than that of ^{111}In -mAbK1 ($K_d = 29.3$ nM). Onda *et al.* reported the same order of affinities using a surface plasmon resonance assay; they determined a K_d value of 0.6 nM for mAbMB whereas the K_d value was 12 nM for mAbK1. It is not clear why an earlier reported K_d value of 0.92 nM by the same group was many times lower, but it might explain why they saw such a high activity uptake (~53% ID/g) of ^{111}In -mAbK1 in mesothelin expressing tumours in their studies [164]. Our studies showed that the commercially obtainable mAbK1 has a much lower affinity.

Previous studies with A431K5 cells have demonstrated that mesothelin targeted immunoconjugates undergo internalization after binding to the cell surface [158,269]. Antibodies labelled with ^{111}In by means of a DTPA chelator can have an additional advantage in imaging if they become internalized by cells. Post internalization, ^{111}In is often trapped in the lysosomes of cells after catabolism of the antibody (residualization), thus leading to longer and higher retention inside the cells [270], which can help achieve higher target to non-target ratios. Our results showed that both ^{111}In -mAbMB and ^{111}In -mAbK1 are internalized by A431K5 cells. After 1 hour pre-incubation at 4°C, cellular internalization of ^{111}In -mAbMB was greater than that of ^{111}In -mAbK1, which further resulted in higher accumulation of ^{111}In -mAbMB in the cells over time. Imaging with ^{111}In -mAbMB, therefore, may be advantageous as its internalization was higher at all time points (**Figure 3.2**). These results also indicate that mAbMB may be useful for radiotherapy when radiolabelled with a therapeutic radionuclide.

For unambiguous imaging, the radiolabelled antibody must accumulate at high levels within the tumours and be cleared from the blood within a time frame compatible with the radionuclide's half-life. Biodistribution studies at a dose of 4 $\mu\text{g}/740$ kBq of ^{111}In -mAbMB suggested that 24 to

72 hours is a good window for microSPECT/CT imaging (**Figure 3.3**). While maximum uptake of ^{111}In -mAbMB into A431K5 cells was obtained at 48 hours, the uptake into A431K5 was significantly higher than A431 tumours at both 24 and 48 hours. The non-specific uptake of the radioactivity in A431 tumours is presumably a result of high vascular permeability, which leads to retention of activity by the Enhanced Permeation and Retention (EPR) effect [271]. ^{111}In -mAbMB was cleared from the blood at a fast rate resulting in steadily increasing tumour to blood ratios over time, which may also partially be an effect of residualization of ^{111}In in the tumours.

Since previous studies revealed that biodistribution and kinetics of radiolabelled antibodies can be dose dependent [262,272], we also investigated the post-imaging biodistribution at a higher antibody dose of 50 $\mu\text{g}/9.25$ MBq. Increasing the dose resulted in higher uptake at both 48 and 72 hours (**Figure 3.4**). This increased accumulation in A431K5 tumours can partly be attributed to the availability of a higher dose of ^{111}In -mAbMB in the bloodstream due to about 30% lower non-specific accumulation (% ID/organ) in major sites such as liver and spleen.

Small amounts of mesothelin are expressed on the mesothelial lining of the lung and the peritoneal wall in normal mice with an expression pattern similar to that of humans [105]. Our biodistribution and imaging studies did not show any major uptake (cross-reactivity) by the lungs, as ^{111}In -mAbMB was cleared from the lungs at a similar rate as from blood. Also, little activity uptake was observed at these sites during imaging. At both doses activity was mainly localized in spleen and liver. Liver uptake is mostly a result of nonspecific dose contribution, as immunoglobulins from the bloodstream are trapped and processed there [272,273]. The observed high activity uptake by the spleen at the higher dose of ^{111}In -mAbMB was associated with decreases in spleen weights, which can be attributed to the depletion of hematopoietic cells

resulting from higher radiation dose. Spleen being composed of lymphatic tissue is highly radiosensitive [274] and a loss of spleen weight in mice on exposure to radiation has been reported previously [275,276]. ^{111}In emits auger electrons in addition to the gamma radiation, which can cause toxic effects if taken up intracellularly due to local high density electron irradiation [277]. While it is known that the toxic auger effects depend on location of the radionuclide within the cell, the subcellular localization of ^{111}In -mAbMB in spleen needs further investigation. The percentage of injected dose in spleen when calculated on a per organ basis was lower at the 50 μg dose of ^{111}In -mAbMB compared to the 4 μg dose (**Figure 3.6 A**). However, the decrease in spleen weight (**Figure 3.6 B**) resulted in an apparent increase in percentage of injected dose on per gram basis in spleen (**Figure 3.6 C**). According to Bera *et al.* some expression of mesothelin may be expected in spleen [105], although we did not detect any using Western blotting (**Figure 3.10**). Also, no cross reactivity of the mAbMB antibody towards proteins expressed by spleen was observed in the Western blot studies. Antibodies are positively charged molecules, while DTPA substitution imparts a negative charge that might influence their organ uptake. However, based on previous reports, the level of DTPA substitution (2.4 per molecule of mAbMB) achieved in our studies is optimal for imaging [189,190]. Furthermore, the same DTPA substitution in the mAbK1 antibody resulted in much lower spleen uptake in the same animal model. Previously, Sato *et al.* have also reported high spleen uptake of their mesothelin targeted ^{111}In labelled tetravalent single-chain Fv-streptavidin fusion protein (SS1scFvSA), in mice bearing A431K5 tumours [158]. Although, the authors did not explain the reasons for the high spleen uptake, their results suggest a role of circulating mesothelin antigen in forming immune complexes with ^{111}In labelled SS1scFvSA, which then undergo phagocytic uptake by spleen. We believe that the spleen uptake of ^{111}In -mAbMB is mediated by a similar mechanism. Such a phenomenon is not predominant with ^{111}In -mAbK1 due to its lower affinity for mesothelin. We further investigated the possible role of circulating mesothelin antigen, by

carrying out a biodistribution study in mice not bearing any tumours (**Figure 3.5**). The low spleen and liver uptake of ^{111}In -mAbMB observed in these mice compared to tumour-bearing mice, clearly points to the role played by the shed tumour antigens in promoting spleen and liver uptake.

Although, we did not measure the amount of shed mesothelin in A431K5 tumour bearing mice, prior studies by Zhang *et al.* have shown that the amount of mesothelin shed into the blood circulation can range between 0.7 nM to 10 nM depending on the size of the A431K5 tumours. Ho *et al.* have also demonstrated the shedding of mesothelin in A431K5 tumour model [146,278], while prior studies by Hellstorm *et al.* have shown that mesothelin is extensively shed by the tumour cells and finds its way into the blood circulation [279]. Although the presence of serum mesothelin has also been observed in mesothelioma and pancreatic cancer patients [141,280], it remains to be seen whether it will lead to spleen uptake of ^{111}In -mAbMB in human patients. Prior studies in human patients injected with radiolabelled antibodies against carcinoembryonic antigen (CEA) have shown that although there is formation of immune complexes with the circulating antigens, the localization of activity into the tumours remains unaffected and there is no marked clearance of the radiolabel in the liver or the spleen. As a result tumour detection by γ -immunoscintigraphy remained unaffected [281].

Our studies showed that the uptake of ^{111}In -mAbK1 into A431K5 tumours is much lower than that of ^{111}In -mAbMB, and is also very low compared to the high uptake reported by Hassan *et al.* [164]. We believe the main reason for this disparity is the lower affinity of mAbK1 used in our studies. In a recent paper, Yoshida *et al.* reported a peak accumulation of about 5.8% ID/g for their ^{111}In -DTPA-IgG radioimmunoconjugate used to target mesothelin expressing NCI-H226 tumours at 48 hours, whereas their ^{111}In -DTPA-Fab accumulation peaked with 2.1% ID/g at 6

hours. While the authors did not report any SPECT/CT imaging with the above conjugates, they were successful in visualizing NCI-H226 tumours with ^{64}Cu -DOTA-Fab using PET. However, it was suggested that with a peak tumour uptake of 3.1% ID/g at 6 hours, the tumour uptake of ^{64}Cu -DOTA-Fab was “insufficient” for clinical imaging [166].

For tumour visualization, it is important to achieve a high tumour to surrounding tissue ratio together with high absolute activity uptake in the tumours. As seen in our SPECT/CT images, significant uptake of ^{111}In -mAbMB was detected in A431K5 tumours at all time points, which was much higher than that observed in A431 tumours and was consistent with the findings of the biodistribution studies (**Figure 3.8**). The locations of high activity uptake were consistent over time and radiolocalization in the liver and spleen was also clearly resolved. As evident from the ROI analysis significantly higher T/NT ratios of ^{111}In -mAbMB were obtained for A431K5 tumours than A431 tumours at all time points (**Figure 3.9 A**). Although A431K5 tumours were visualized with ^{111}In -mAbK1, superior image contrast was obtained with ^{111}In -mAbMB.

3.6. Conclusion

We demonstrated that mesothelin expression can be imaged with SPECT in tumour-bearing mice using ^{111}In -labelled anti-mesothelin antibodies. The biodistribution and imaging characteristics of ^{111}In -mAbMB make it a better choice than ^{111}In -mAbK1 for imaging mesothelin expression in tumours, although its non-specific uptake in spleen needs to be better understood and addressed. When fully optimized, such mesothelin-specific imaging agent will be useful in the diagnosis of mesothelioma, pancreatic cancer and ovarian cancer. Moreover, mesothelin targeting with therapeutic radioisotopes such as ^{90}Y , ^{188}Re , and ^{131}I or even the recently tested alpha-emitters ^{211}At and ^{213}Bi [272] can potentially be useful for radioimmunotherapy of tumours and their metastases [282].

Chapter 4: Development and Evaluation of Dual-Modality (MRI/SPECT) Molecular Imaging Bioprobe for Mesothelin Expressing Cancers

4.1. Introduction

4.1.1. Dual Modality Imaging of Mesothelin Expressing Cancers

Combining two or more different imaging modalities in the same agent can be of considerable value in molecular imaging, especially for cancers that are difficult to diagnose and treat. Many such agents have been previously reported that combine optical imaging with MRI (Magnetic Resonance Imaging) [283-285]. However, the limited resolution and penetration depth of optical imaging considerably limits their clinical application. Compared to this, the higher sensitivity and resolution of the two radionuclide imaging modalities SPECT (Single Photon Emission Computed Tomography) and PET (Positron Emission Tomography) makes them an ideal choice for selective functional imaging with molecular targeted agents.

Considerable focus has been given to evaluating the best imaging modality for mesotheliomas, pancreatic and ovarian cancers [35-37,286-290]. An imaging modality with the potential to distinguish accurately between benign and malignant lesions and to define the extent of disease would be invaluable in the management of these cancers [38]. Better imaging of the tumour sites will facilitate TNM (Tumour Node Metastasis) staging, permit more accurate, targeted drug or radiation delivery as well as provide better assessment of the response to chemotherapy, all of which will result in improved patient outcome.

Mesothelin over-expression in mesotheliomas, pancreatic and ovarian cancers presents an opportunity to selectively target and image these difficult to diagnose tumours. By designing mesothelin specific radiolabelled SPECT imaging bioprobes, clinically useful functional information about these cancers can be obtained. However, SPECT images have limited spatial resolution and lack anatomical details for reference, rendering the precise localization of lesions difficult. Co-registration of SPECT with anatomic images of the same animal, from either CT

(Computed Tomography) or MRI has been commonly used in the clinic to address this problem. The use of MRI presents specific advantages compared with CT, including lack of ionizing radiation, high soft-tissue contrast, and sensitivity to tissue alterations [197,291]. Although MRI can also be used alone to assess total tumour burden in the course of treatment, the identification of residual viable tumour based only on anatomical changes remains difficult especially after therapy, when active tumour tissue cannot be distinguished from reparative changes or scars [38]. The above limitations of SPECT and MRI can be circumvented by combining the two modalities. With the recent availability of semiconductor detectors for SPECT (and PET), which are insensitive to magnetic fields, it has become possible to develop co-axial multi-modality nuclear medicine/magnetic resonance instrumentation, thus paving way to the development of dual modality SPECT/MRI scanners [197].

4.1.2. Iron Oxide Nanoparticles for MR Imaging

Tumour specific MRI contrast agents can be prepared by coating iron oxide nanoparticles with monoclonal antibodies directed against tumour antigens [292-294]. Studies have shown that such preparations retain their ability to bind tumour antigens as well as their relaxometric properties. Using these antibody-coated iron oxide nanoparticles MRI image contrast can be easily induced in a concentration range of 1-10 nM by spin-echo methods [9]. The important properties of iron oxide nanoparticles for MR imaging applications are biocompatibility, injectability, high relaxivity, lack of toxicity, and high level accumulation in the target tissue and organ [295].

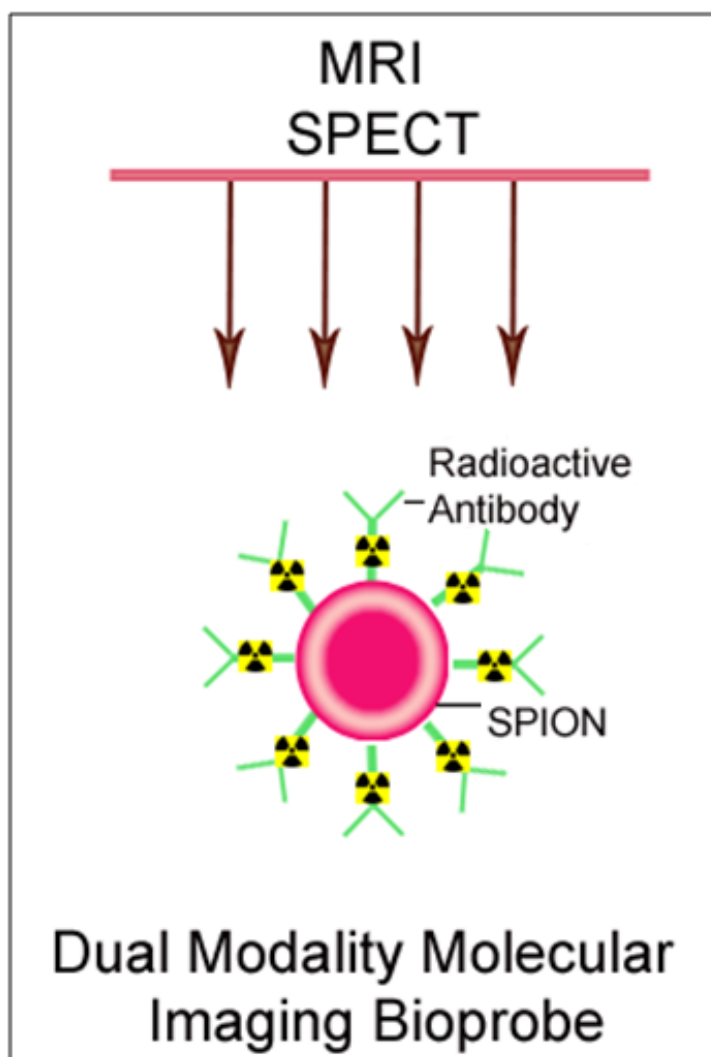


Figure 4.1. Schematic of the proposed dual modality MRI/SPECT imaging bioprobe.

4.1.3. Current Study Outline

In chapter 3 we developed ^{111}In labelled anti mesothelin antibody mAbMB (^{111}In -mAbMB) and used it to specifically image mesothelin expressing cancers using SPECT. The purpose of the current study is to develop a dual-modality molecular imaging bioprobe by conjugating ^{111}In -mAbMB to superparamagnetic iron oxide nanoparticles (SPIONs), which would allow combined SPECT/MR imaging of mesothelin expressing cancers. The experiments presented in this chapter are outlined in the schematic shown in **Figure 4.2**. This study mainly focuses on the

evaluation of dual-modality nano bioprobe for MR imaging. Additionally, autoradiography and biodistribution studies were carried out to provide proof of principle for their suitability for simultaneous γ -imaging by SPECT. The iron oxide nanoparticles were first characterized by Transmission Electron Microscopy (TEM) and Dynamic Light Scattering (DLS) and then conjugated with ^{111}In -mAbMB using the carbodiimide coupling reaction. ^{111}In -mAbMB conjugated SPIONs (^{111}In -mAbMB-SPIONs) were characterized for reactivity and specific binding by *in vitro* cell binding assays and confocal microscopy. MR relaxation properties of these nano bioprobes were studied using *in vitro* MRI. Finally, SCID mice bearing A431K5 tumours (mesothelin positive) and A431 tumours (mesothelin negative), were intravenously injected with ^{111}In -mAbMB-SPIONs and biodistribution and MR imaging studies were carried out at different time intervals post-injection.

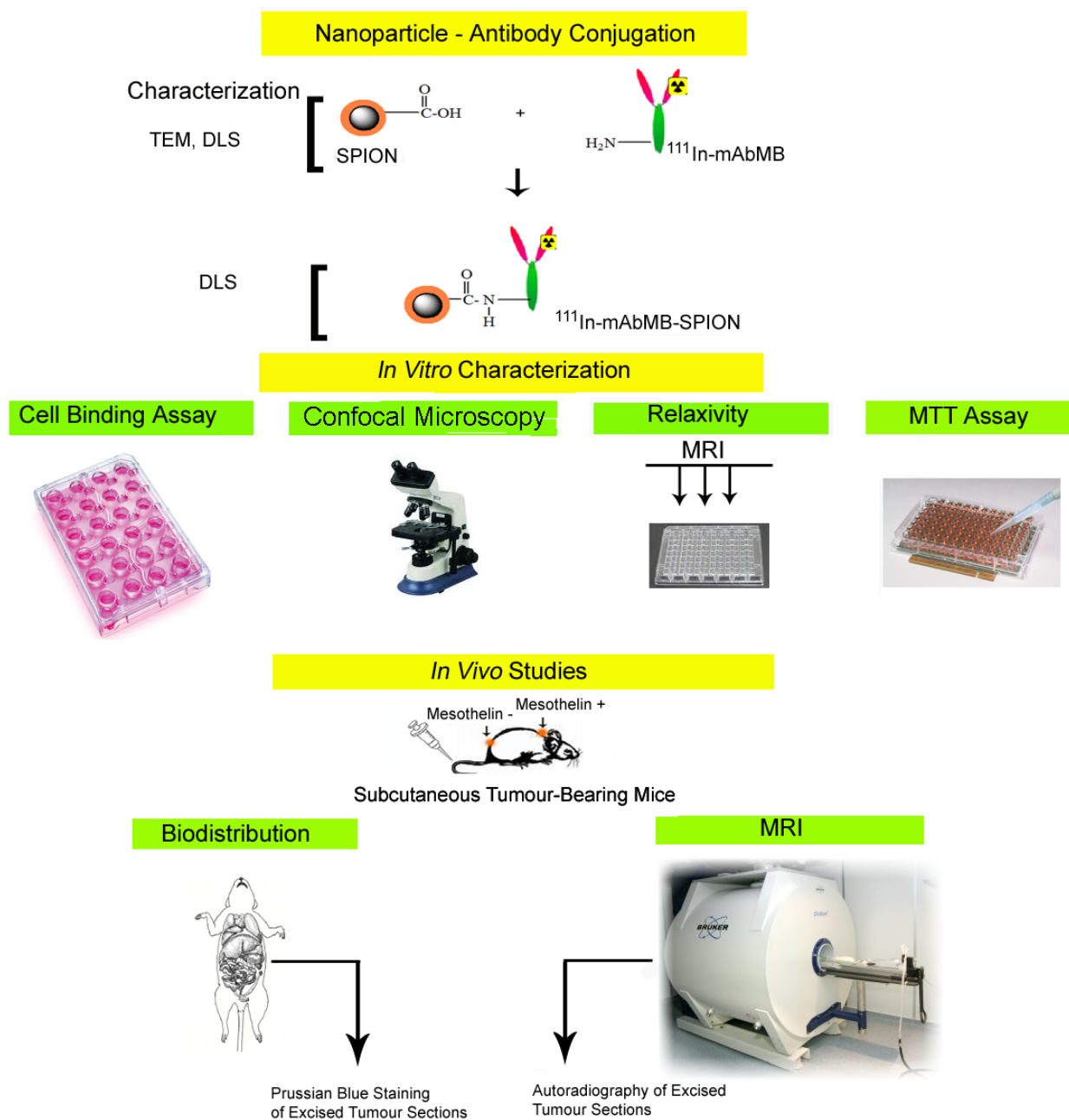


Figure 4.2. Experimental overview of chapter 4.

SPIONs were first characterized by TEM and DLS and then conjugated with $^{111}\text{In-mAbMB}$ by carbodiimide coupling reaction. The reactivity and specificity of $^{111}\text{In-mAbMB-SPIONs}$ was ascertained by cell binding assays and confocal microscopy. Relaxivity was determined by carrying out *in vitro* MRI of phantoms containing different iron concentrations of $^{111}\text{In-mAbMB-SPIONs}$. MTT assay was performed to determine cytotoxicity. Biodistribution and MRI studies were carried out in SCID mice bearing subcutaneous xenografts of A431K5 cells (mesothelin +) A431 cells (mesothelin -). Excised tumours were sectioned and Prussian blue staining and autoradiography studies were carried out.

4.2. Materials

All chemicals and reagents were purchased from Sigma, Aldrich (Oakville, Ontario, Canada). The cell culture media and supplements were obtained from Invitrogen (Invitrogen, Burlington, Ontario, Canada). The mAbMB antibody was purchased from Rockland Immunochemicals (Gilbertsville, Pennsylvania, U.S.A.). $^{111}\text{InCl}_3$ was obtained from MDS Nordion (Vancouver, British Columbia, Canada) and p-SCN-bn-DTPA from Macrocyclics (Dallas, Texas, U.S.A.). SPIONs (Fluidmax CMX) were received as a generous gift from Chemicell (Berlin, Germany). Activity measurements were carried out using a Packard Cobra II gamma counter (Perkin-Elmer, Waltham, Massachusetts, U.S.A.). For in vitro and in vivo studies the iron concentrations were based on iron content of SPIONs determined by Inductively Coupled Plasma Mass Spectrometry (ICP-MS) at Exova Laboratory Testing Services, BC, Canada.

4.3. Methods

4.3.1. Particle Characterization by TEM and Zetasizer

SPIONs (Fluidmag-CMX, <100 nm) obtained from Chemicell have a magnetic core and are coated with carboxy methyl dextran, which provides the carboxylic acid groups for antibody conjugation. The core structure of SPIONs was determined by transmission electron microscopy (TEM) to understand the general morphology of the magnetic core as well as to determine the particle size distribution. A drop of diluted solution of the SPIONs in water was placed in carbon-coated copper TEM grid (150 mesh, Ted Pella Inc, Redding, CA) and was allowed to air-dry. The samples were imaged at 200 kV using a FEI Tecnai G2 transmission electron microscope (Hillsboro, Oregon, USA). The hydrodynamic diameter of nanoparticles was determined by DLS measurements carried out on a Malvern 3000HS Zetasizer (Malvern Instruments Ltd, Malvern, UK) with a He–Ne laser (532 nm) and 90° collecting optics. Data was analyzed using CONTIN algorithms provided by Malvern Zetasizer software.

4.3.2. Conjugation of ¹¹¹In-mAbMB Antibody with SPIONs

The carbodiimide coupling reaction (**Figure 4.5**) was used to conjugate the ¹¹¹In-mAbMB antibody to the SPIO nanoparticles [296]. SPIO nanoparticles (5 mg) were washed 3 times with 1 ml of 0.1M MES (2-(*N*-morpholino) ethanesulfonic acid) buffer, pH 4.5. The particles were then suspended in a freshly prepared EDC (1-ethyl-3-(3-dimethylaminopropyl)-carbodiimide) solution containing 10 mg EDC in 0.25 ml MES solution and shaken in an Eppendorf thermomixer at 800 rpm for 10 minutes at room temperature, followed by magnetically washing 3 times with 1 ml PBS (phosphate buffered saline, pH 7.4). After resuspending the particles in 0.25 ml of PBS, about 50 µg of ¹¹¹In-mAbMB (9.25 MBq) solution was mixed with the activated particles for 2 hours at RT. The antibody-conjugated nanoparticles (¹¹¹In-mAbMB-SPIONs)

were collected and magnetically washed three times with PBS. Amount of conjugated antibody was determined by measuring the activity in the washes and the nanoparticle suspension.

4.3.3. *In Vitro* Cell Binding and Specificity

A431K5 and A431 cells were cultured in Dulbecco's Modified Eagle medium supplemented with 10% fetal bovine serum at 37°C in a humidified atmosphere in the presence of 5% CO₂ as reported previously [164]. About 50,000 A431K5 and A431 cells/well were plated overnight in 24-well plates and then incubated with 0.2 ml of a suspension containing 0.05 mg/ml [Fe] equivalent of ¹¹¹In-mAbMB-SPIONs at 37°C. After 3, 6 and 24 hours, cell supernatants were collected, the adherent cells washed twice with PBS and lysed with 0.1 M NaOH. Unbound activity present in supernatant and washes was counted along with bound activity present on the cells to determine the percent uptake of ¹¹¹In-mAbMB-SPIONs by cells. In a separate experiment, two sets of A431K5 cells were plated overnight in 24-well plates at a concentration of 50,000 cells /well. One set was incubated with 0.2 ml of a suspension containing 0.05 mg/ml [Fe] equivalent of ¹¹¹In-mAbMB-SPIONs for 3 hours, while the second set was incubated with the same quantity of ¹¹¹In-mAbMB-SPIONs in presence of unlabelled mAbMB and the cell bound activity was determined by the above described procedure. For confocal microscopy studies about 50,000 A431K5 were plated overnight on cover slips in 24-well plate followed by incubation with 0.05 mg/ml (Fe) of ¹¹¹In-mAbMB-SPIONs at 37°C. Following incubation, the cover slips were washed 3 times with ice cold PBS and incubated with acetone at -20°C for 5 minutes to permeabilize the cells. The cover slips were then equilibrated with saline-sodium citrate buffer (SSC buffer: 0.3M NaCl and 0.03M sodium citrate in distilled water at pH 7.0) for 10 minutes, followed by incubation with propidium iodide staining solution (working solution 1:3000 in SSC buffer prepared from 1 mg/ml propidium iodide in sterile water) for 10 minutes. The cover slips were then washed 3 times with SSC buffer and mounted on the microscopic

slides using mounting medium. The slides were then observed using a Leica DM 2500 confocal microscope. The dye was excited at a wavelength of 533 nm, and the emission wavelength was 617 nm. Similarly, two other control sets of experiments were carried out with SPIONs (without antibody) at 37°C and ^{111}In -mAbMB-SPIONs at 4°C. The images were processed with ImageJ software (NIH, Bethesda, USA) and colour analysis was performed using the 'RGB Measure' plugin.

4.3.4. Relaxivity Measurement and *In Vitro* MR Imaging

Phantoms for *in vitro* MR imaging were prepared by combining appropriate quantities of SPIONs and ^{111}In -mAbMB-SPIONs (concentration range 0 to 0.55 mM) with 2.5% agarose gel at 60° C and then mixing them on the vortex mixer. An aliquot of 100 μl of this mixture was transferred quickly to a 96-well plate and allowed to cool down on an ice bath. An MRI image was taken for the 96-well plate and signal intensity was obtained by summing up the pixel intensities of a specific region of interest (ROI). Paravision version 4.0 was used as the software for data acquisition, reconstruction and visualization/analysis of the images. For the r_1 relaxivity calculation, 8 inversion recovery RARE (Rapid Acquisition with Refocused Echoes) images were used to measure the relaxation rate, R1 ($= 1/T_1$) of each sample in the well plate. The individual images had different inversion times (TI=36, 100, 500, 1000, 1500, 2000, 3000, 5000 milli seconds), which varied with the amount of T_1 -weighting, experienced by each image. For a particular sample, the mean signal intensity from a ROI was plotted with respect to inversion time, and was then fitted to an exponential regrowth relationship. The time constant (T_1) of this fitted exponential equals the reciprocal of R1. The R1 of each sample was plotted with respect to concentration and the slope was determined for calculation of r_1 relaxivity.

For r_2 relaxivity calculation, a spin-echo Carr-Purcell-Meiboom-Gill (CPMG) sequence was used to measure relaxation rate, R_2 ($=1/T_2$) of each sample in the well plate. The CPMG sequence generated 32 echo images within the same acquisition. The signal intensity at each echo image reflects the transverse magnetization remaining at a certain time (echo time) after the initial spin excitation. The signal intensity decays with respect to echo time according to the T_2 decay process. The relationship of signal intensity versus echo time (e.g., mean intensity from ROI) was fitted to an exponential decay plot. The fitted time constant obtained was T_2 ($=1/R_2$). Finally, the R_2 of each sample was plotted with respect to concentration, and the slope was determined for calculation of r_2 relaxivity.

4.3.5. Tumour Uptake and Biodistribution

Biodistribution of ^{111}In -mAbMB-SPIONs was evaluated in male C.B-17 SCID mice (Taconic, Germantown, New York, U.S.A.). Mice were subcutaneously injected with 5×10^6 A431K5 cells (mesothelin positive) in the upper back and 5×10^6 A431 cells (mesothelin negative) in the lower back. When tumours exceeded a size of 0.5 cm in diameter, the mice were injected intravenously with ^{111}In -mAbMB-SPIONs at a dose of 15 mg/kg body weight equivalent of Fe (740 kBq), based on previously reported studies [297,298]. Animals were euthanized at 24 hours and 72 hours post-injection and major organs harvested. The radioactivity associated with each organ was analyzed on a γ -counter to obtain the biodistribution data. The ratio of radioactivity in the tumour or normal tissue to that in blood was determined by dividing the activity per weight of tissue by activity per weight of total blood.

4.3.6. Prussian Blue Staining of Tissue Specimens

Tissue specimens were frozen in OCT compound (Sakura Finetek Inc., Torrance, CA) with liquid nitrogen and 10 μm sections were made using a cryotome (CM1850; Leica Microsystems GmbH). At the time of staining, sections were washed with 5% formaldehyde in PBS, and then washed twice with PBS before applying *Pearl's Prussian Blue* staining for 20 min. *Pearl's Prussian Blue* solution is obtained by mixing equal volumes of 4% potassium ferrocyanide solution and 4% HCl. Slides were then counterstained for 10 minutes with neutral red stain. Slides were examined by optical microscopy using a Leica DMLB microscope (Leica Microsystems Inc, Bannockburn, Illinois, U.S.A.) with attached Retiga 2000R camera and processed using Image J software.

4.3.7. *In Vivo* MRI Studies

SCID mice ($n = 3$) bearing A431K5 and A431 tumour xenografts implanted at their neck and lower back, respectively, were injected via tail vein with ^{111}In -mAbMB-SPIONs, 15 mg/kg body weight equivalent of Fe (740 kBq). At 24 hours and 72 hours post-injection, the mice were anesthetized using isoflurane and subjected to *in vivo* MR imaging using a 7 Tesla Bruker Biospec 70/30 USR. For image acquisition, a quadrature birdcage volume coil: 7 cm inner diameter, manufactured by Bruker Biospin (Ettlingen, Germany) was used. Coronal images were taken with the following parameters: FOV = $5 \times 5 \text{ cm}^2$; matrix size = 256×256 ; slice thickness = 1 mm; TE = 6 milliseconds; TR = 700 milliseconds. Axial images were taken using the same method with FOV = $4 \times 4 \text{ cm}^2$. For image analysis of A431K5 tumours, the freely downloadable 3D Slicer program version 3.6 (www.slicer.org) was used. To quantitatively determine the change in MR contrast in A431K5 tumours, intensity histograms were constructed by selecting tumour ROIs which remained anatomically consistent (no volume change) throughout the study,

as shown in **Figure 4.16**. The ROIs within the tumours were manually segmented and the image intensity within each ROI was transformed into a colour-plot (**Figure 4.16**). To get better sensitivity only one slice and not the entire 3D tumour was chosen. The total area of each curve sums up to 1 (probability density). Mean and standard deviation were determined assuming Gaussian distribution, and served as a model for position and width of histograms for all time points.

4.3.8. Autoradiography

Ex-vivo autoradiography of major organs was carried out after biodistribution studies by exposing a 20×25 cm² phosphor screen (Perkin-Elmer Waltham, MA, U.S.A.) to the excised organs followed by visualization using a phosphor imager (Cyclone storage phosphor imager; Perkin-Elmer) with OptiQuant software. To verify the distribution of ¹¹¹In-mAbMB-SPIONs in the tumours, 20 µm sections of A431K5 tumours were made using a cryotome (CM1850; Leica Microsystems GmbH) and a phosphor screen was exposed to the sections for 24 hours followed by phosphor imaging.

4.3.9. Cellular Toxicity Determination by MTT Assay

The MTT (3-[4,5-dimethylthiazol-2yl]-2,5-diphenyltetrazolium bromide) assay is a colourimetric assay, where viable cells take up the yellow MTT dye into their mitochondria and metabolize it there producing blue colour formazan crystals, which are then dissolved and read spectrophotometrically. About 8000 A431K5 tumour cells were plated, in 100 µL of media, into each well of a 96-well plate and incubated for 24 hours. A total of 100 µL of a suspension containing 0.1 and 0.5 [Fe] mg/mL of, ¹¹¹In-mAbMB-SPIONs, SPIONs and Feridex IV (Advanced Magnetics, Inc. Lexington, MA, USA), in DMEM media were added and incubated

for another 48 hours. A total of 20 μL of a 5 mg/mL MTT solution was added and incubated for three more hours. As a control, 150 μL of PBS at pH 7.4 was added to cells in eight of the wells. The supernatant in each well was removed followed by addition of 150 μL of dimethyl sulfoxide to solubilize the cells and MTT crystals. The plate was then placed on a shaker for 30 minutes to dissolve all crystals. The blue colour produced in each well was then read at 570 nm on a multiwell UV spectrophotometer. The cell survival was determined by comparing the absorption of each sample with that of the control cell, which by definition had a cell survival of 100%. The samples of magnetic nanoparticles were considered toxic if the difference between the percentage of cell survival of control and treated cells was statistically significant at the 5% level, as determined by a students *t*-test.

4.4. Results

4.4.1. Particle Characterization and Antibody Conjugation

The average hydrodynamic size of SPIO nanoparticles measured using a DLS method was 69.6 nm (**Figure 4.3**), while the average magnetic core size determined using TEM was 15.6 nm (**Figure 4.4**). The DLS measurements carried out on ^{111}In -mAbMB-SPIONs showed that the size increased to 76.6 nm and the polydispersity index increased from 0.16 to 0.18. By measuring the radioactivity associated with the nanoparticles, we determined that about $76.5\pm 4.9\%$ of ^{111}In -mAbMB was conjugated to the SPIONs after the carbodiimide coupling reaction.

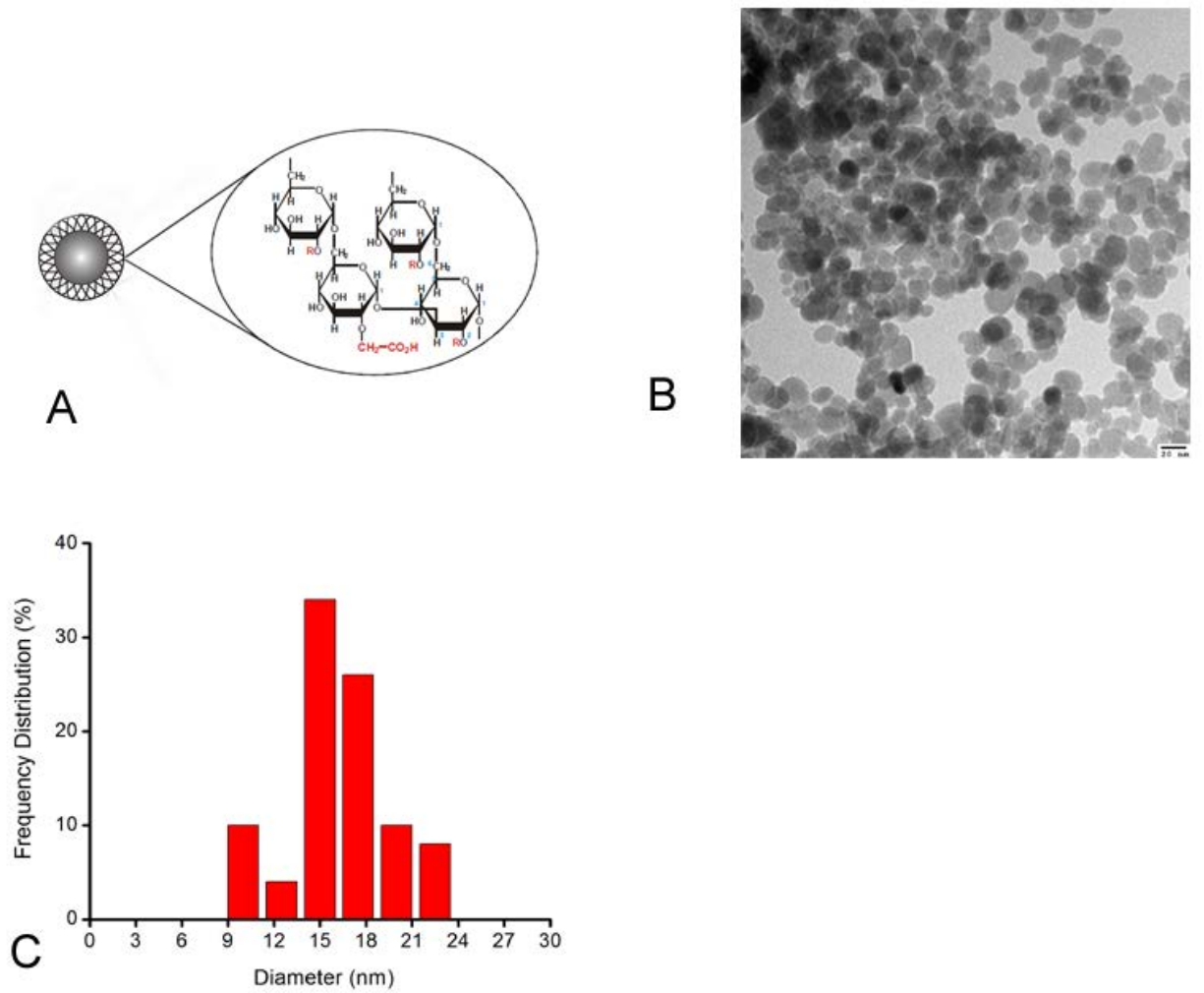


Figure 4.3. Characterization of SPIONs. (A) Schematic of the carboxy methyl dextran coated SPIONs. (B) TEM micrograph of the SPIONs. (C) Frequency distribution (n=50) of the magnetic core size of SPIONs obtained from TEM. Scale bar is 20 μm.

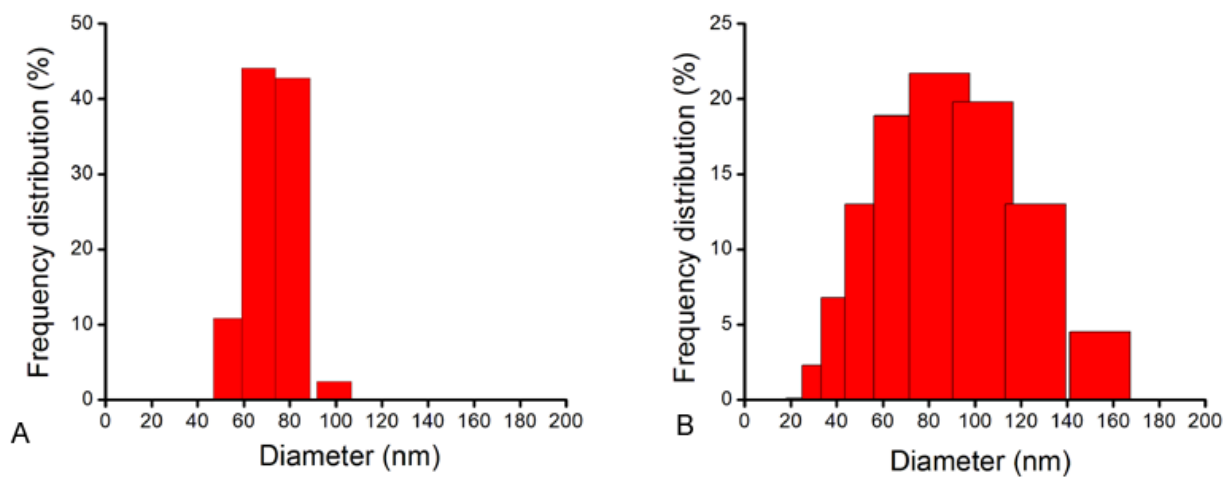


Figure 4.4. Particle size of SPIONs before and after antibody conjugation. Frequency distribution of the hydrodynamic diameter of SPIONs (A) and ¹¹¹In-mAbMB-SPIONs (B) obtained from DLS method.

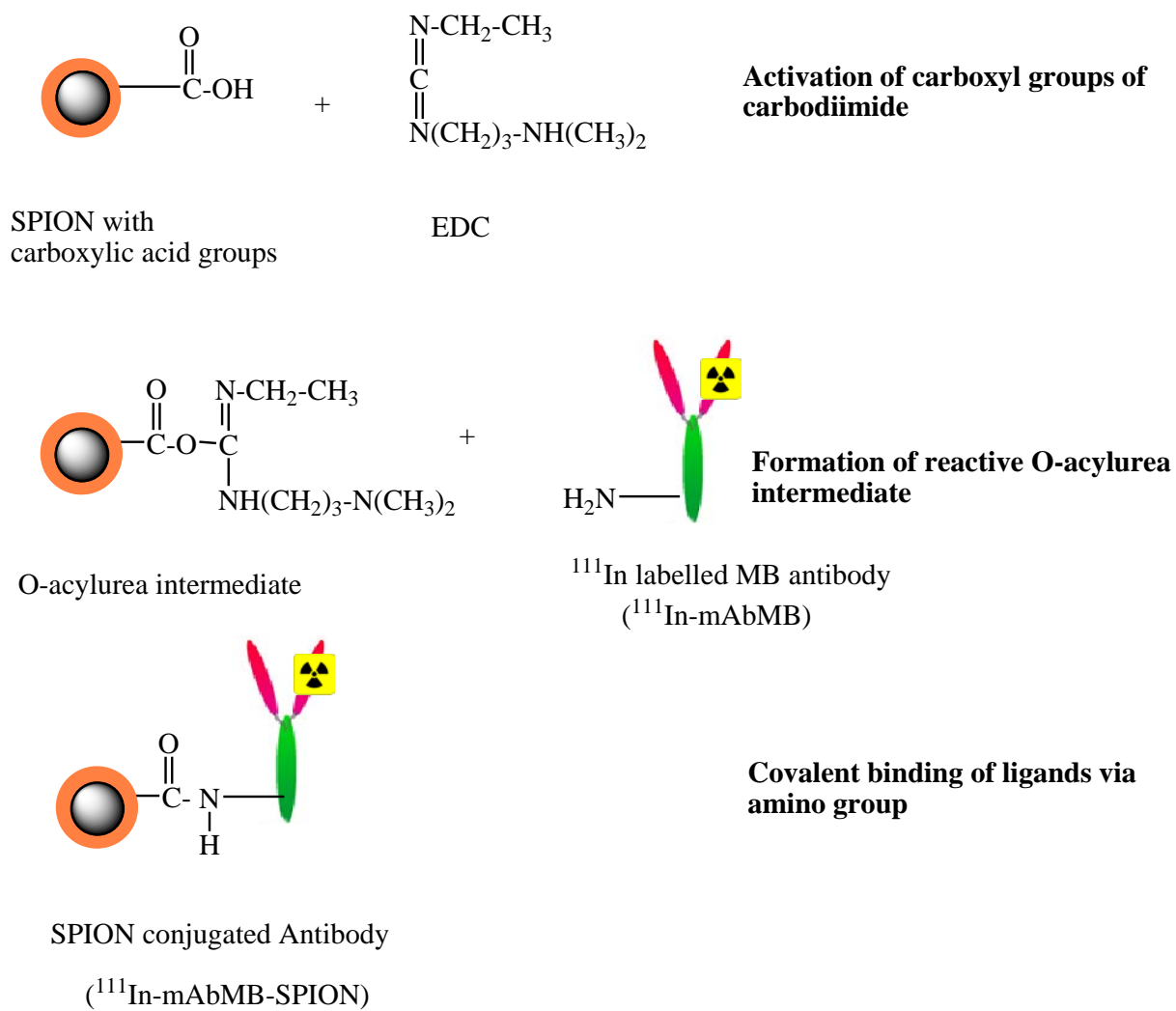


Figure 4.5. Overview of antibody conjugation to SPIONs by carbodiimide coupling reaction. EDC reacts with the carboxylic acid groups on the particle surface to form an active ester intermediate (O-acylisourea). In the presence of an antibody, a peptide bond is formed, releasing an isourea byproduct.

4.4.2. *In Vitro* Cell Binding and Specificity

The cell uptake of ^{111}In -mAbMB-SPIONs by A431K5 cells was significantly higher than that of A431 cells at all the time points, indicating the immunoconjugates' ability to bind specifically to mesothelin expressing cells (**Figure 4.6**). The use of EDC coupling enabled the covalent attachment of the ^{111}In -mAbMB to the SPIONs without substantially damaging the active binding site of the antibodies. The ratios of specific uptake to non-specific uptake at 3, 6 and 24 hours post incubation were 4.5, 3.4 and 8.0, respectively. As shown in **Figure 4.7**, the binding of ^{111}In -mAbMB-SPIONs to A431K5 cells was inhibited by mAbMB, which demonstrated that cellular uptake of ^{111}In -mAbMB-SPIONs was mediated by antibody binding. The cell uptake of ^{111}In -mAbMB-SPIONs by A431K5 cells was 4.5 times higher than the cell uptake in presence of excess of unlabelled mAbMB (**Figure 4.7**). The cellular uptake of the ^{111}In -mAbMB-SPIONs in A431K5 cells was studied qualitatively by confocal microscopy (**Figure 4.8**). Confocal microscopy pictures of A431K5 cells were obtained 3 hours after incubation with 0.05 mg/ml Fe/ml concentration of ^{111}In -mAbMB-SPIONs or SPIONs. **Figure 4.8 A** shows the interaction between the cells and the ^{111}In -mAbMB-SPIONs at the incubation temperature of 4°C where no endocytosis takes place. As a result, the particles do not get internalized into the cells and remain bound to the cell wall. At the incubation temperature of 37°C , however, particles are clearly visualized inside the cells (**Figure 4.8 B**). It can also be seen from **Figure 4.8 C** that unlabelled SPIONs are not extensively bound or internalized by the A431K5 cells. Color analysis indicated that ^{111}In -mAbMB-SPIONs showed 2.3 times higher cell binding and uptake in A431K5 cells compared to SPIONs. Evidence from all three cell binding studies confirms the specific binding ability of ^{111}In -mAbMB-SPIONs to mesothelin expressing cells.

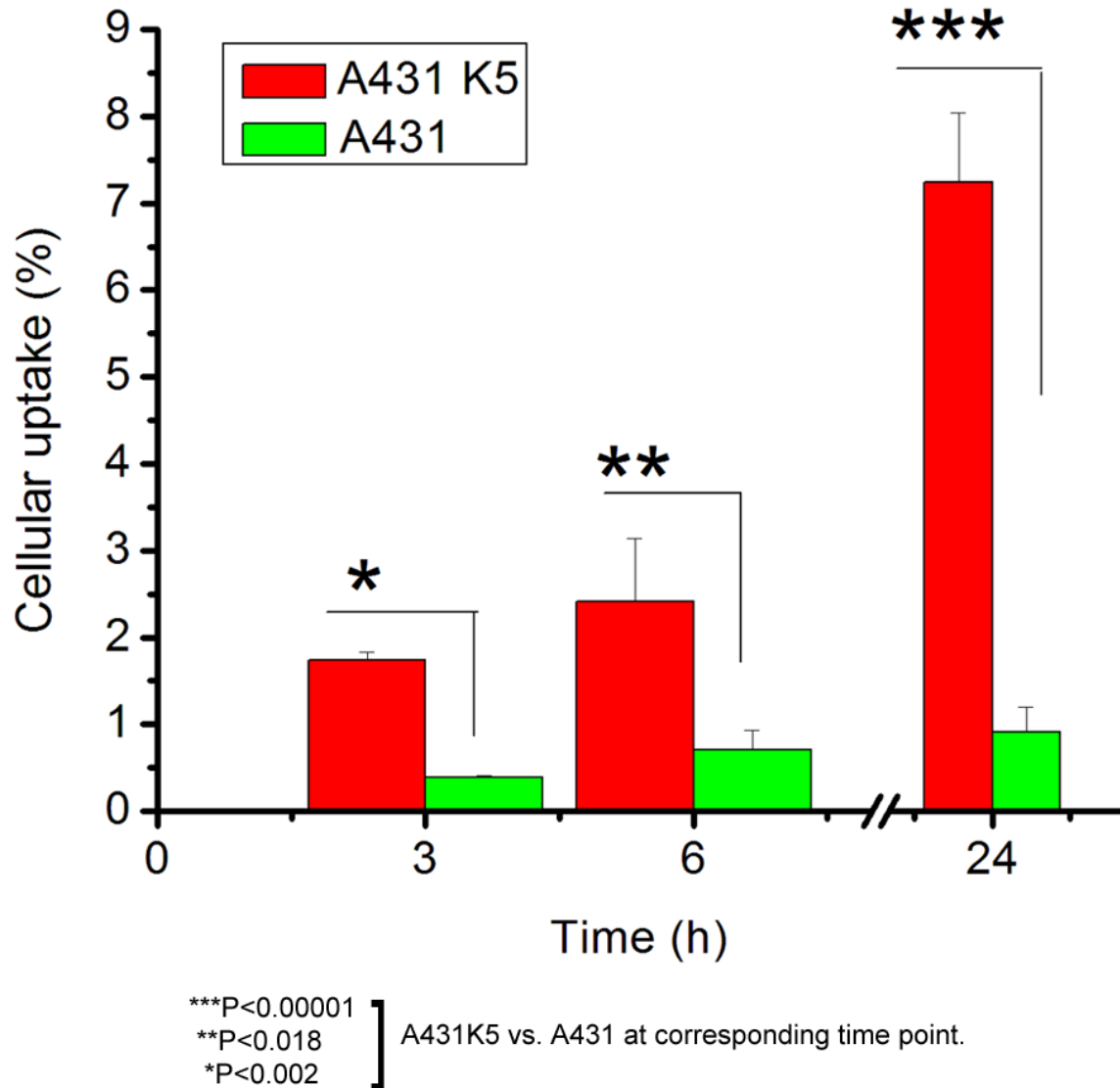


Figure 4.6. Cellular uptake of ¹¹¹In-mAbMB-SPIONs by A431K5 and A431 cells. The cells were incubated with 0.05 mg/ml Fe equivalent of ¹¹¹In-mAbMB-SPIONs at 37°C and cellular uptake determined after 3 hours, 6 hours and 24 hours. Significantly higher uptake was observed in A431K5 cells compared to A431 cells. Data is presented as mean±SD.

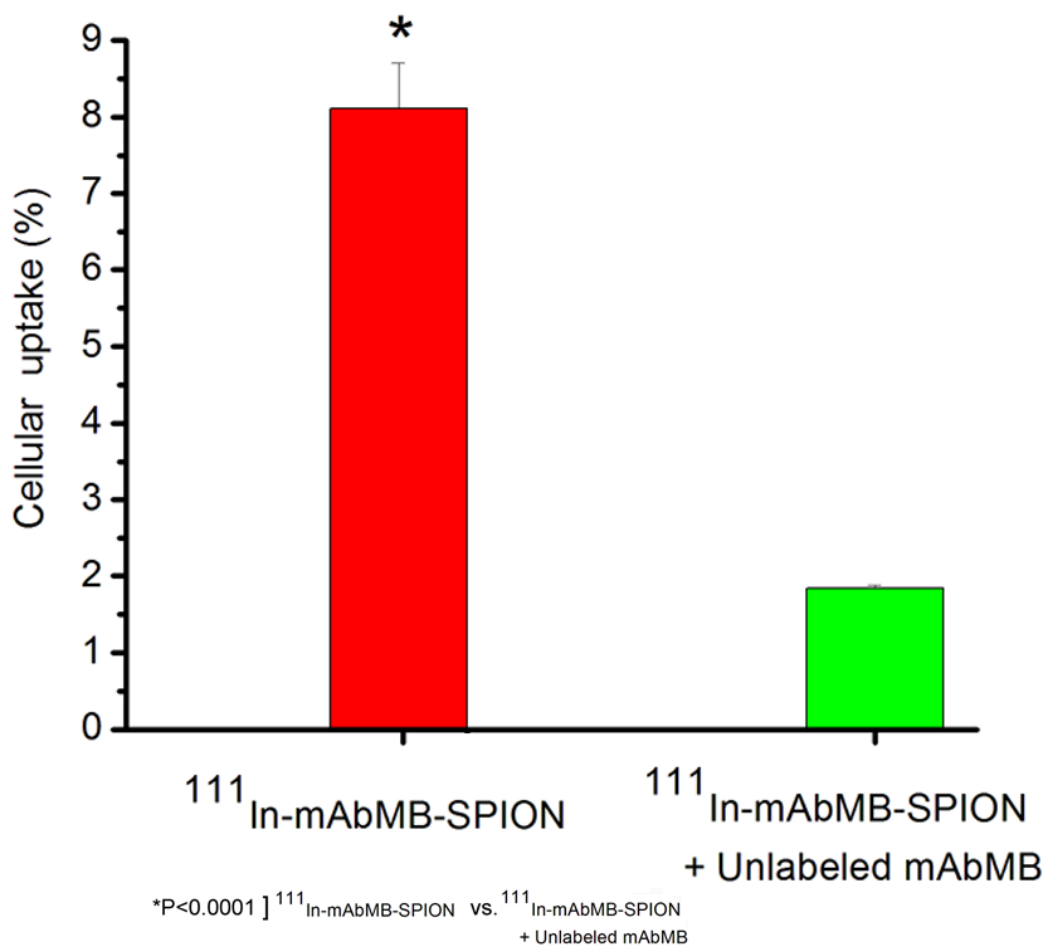


Figure 4.7. Competitive binding assay of $^{111}\text{In-mAbMB-SPIONs}$ to A431K5 cells. A431K5 cells were incubated with 0.05 mg/ml Fe equivalent of $^{111}\text{In-mAbMB-SPIONs}$ at 37°C and cellular uptake determined after 24 hours. About 4.5 times higher uptake of $^{111}\text{In-mAbMB-SPIONs}$ was observed in A431K5 cells compared to that observed in presence of excess unlabelled mAbMB. Data is presented as mean±SD.

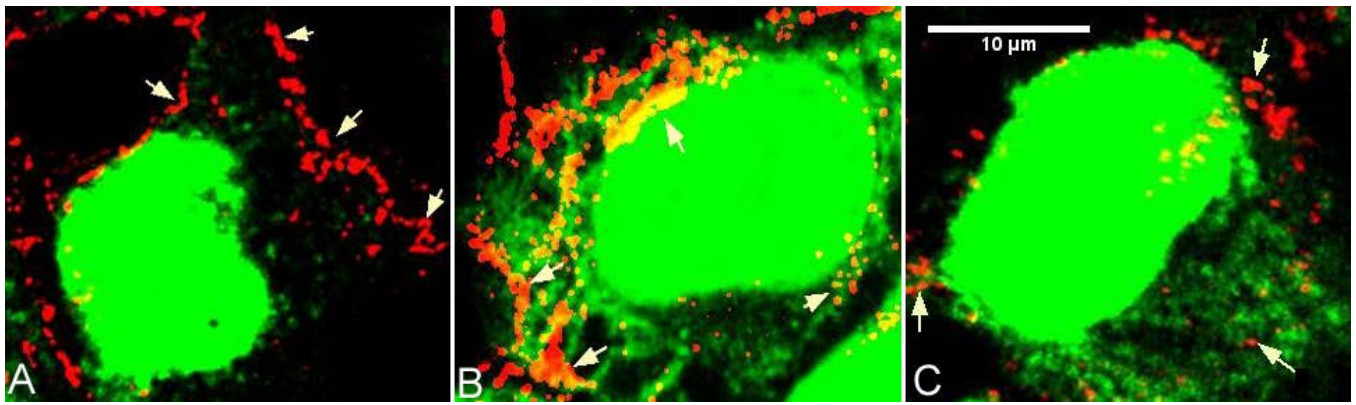


Figure 4.8. Confocal microscopy images of cellular uptake of ^{111}In -mAbMB-SPIONs and SPIONs by A431K5 cells. A431K5 cells were incubated for 3 hours with 0.05 mg/ml Fe equivalent of ^{111}In -mAbMB-SPIONs at 4°C showed binding to the cell membrane while cellular internalization was inhibited (A) and at 37°C , ^{111}In -mAbMB-SPIONs was mainly internalized by the cells (B). When A431K5 cells were incubated with 0.05 mg/ml Fe equivalent of SPIONs, decreased binding and internalization was observed (C). Arrows in the figure point to the ^{111}In -mAbMB-SPIONs and SPIONs, respectively.

4.4.3. Relaxivity Measurement and *In Vitro* MR Imaging

The ^{111}In -mAbMB-SPIONs had a relaxivity of $r_2 = 469.57 \text{ mM}^{-1}\text{s}^{-1}$ and $r_1 = 0.59 \text{ mM}^{-1}\text{s}^{-1}$. In comparison the unconjugated SPIONs had $r_2 = 397.33 \text{ mM}^{-1}\text{s}^{-1}$ and $r_1 = 0.54 \text{ mM}^{-1}\text{s}^{-1}$ (**Figure 4.10 A & B**). The higher T_2 relaxation indicated that ^{111}In -mAbMB-SPIONs could be used for T_2 -weighted MRI imaging. Iron oxide cores in ^{111}In -mAbMB-SPIONs produced a characteristic darkening at increasing iron concentrations, as seen in **Figure 4.9**. Qualitatively, equivalent contrast between ^{111}In -mAbMB-SPIONs and SPIONs could be observed from the signal intensity images at different concentrations (0 to 0.55 mM) (**Figure 4.9**).

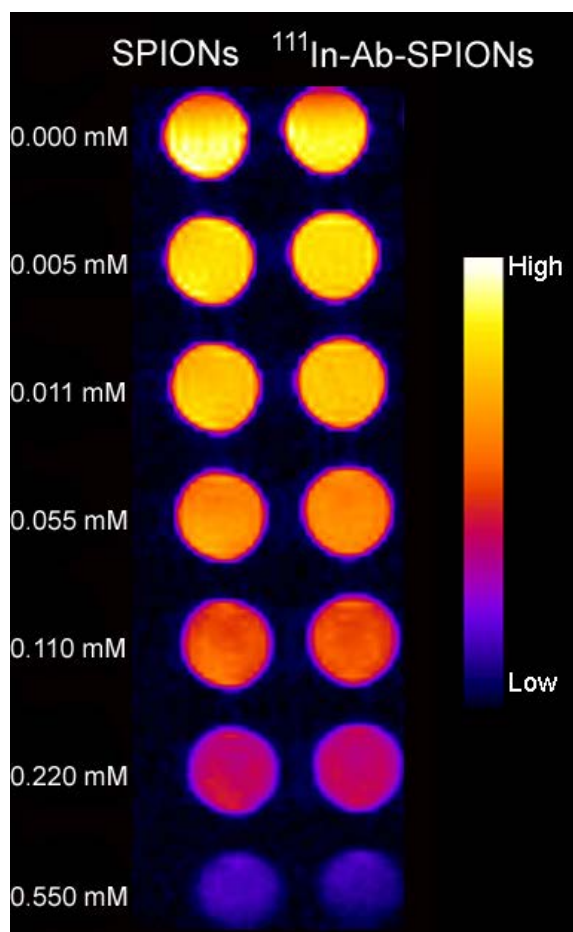
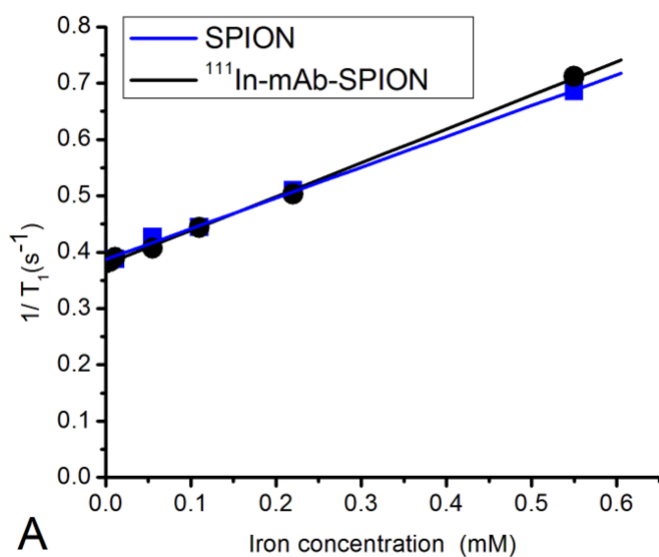
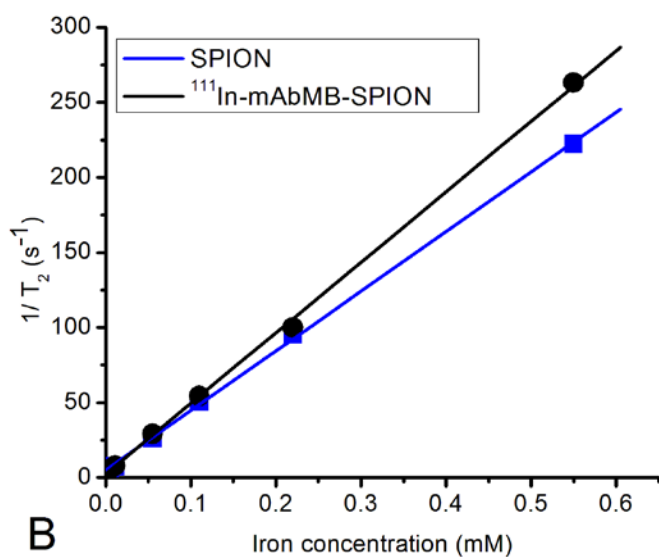


Figure 4.9. Signal intensity weighted MR image of phantom agar gel at different Fe concentrations for SPIONs and ^{111}In -mAbMB-SPIONs.



A

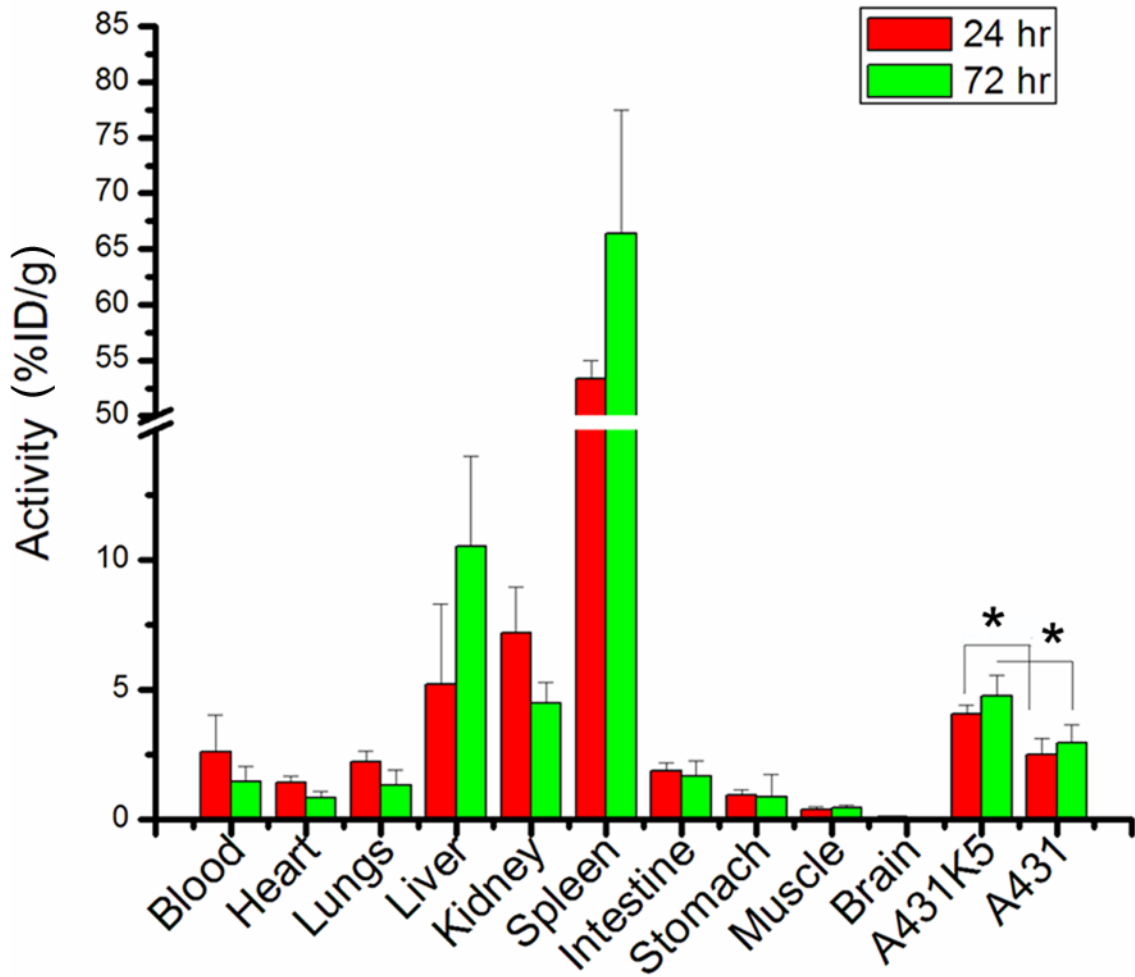


B

Figure 4.10. Relaxivity determination of SPIONs and ^{111}In -mAbMB-SPIONs using T1 and T2 weighted MR image. Phantoms containing different Fe concentration of SPIONs and ^{111}In -mAbMB-SPIONs were made in agar gel. T₁ and T₂ weighted images were obtained by using inversion recovery pulse and CPMG sequence, respectively. Signal intensity was used to obtain fitted T₁ (A) and T₂ (B) time constants, which were plotted against the respective concentrations. Relaxivity values r_1 and r_2 were obtained from slopes of linear fits of experimental data.

4.4.4. Tumour Uptake and Biodistribution

¹¹¹In-mAbMB-SPIONs exhibited significantly higher ($P < 0.05$) localization in the A431K5 tumours compared to A431 tumours at 24 hours and 72 hours post-injection (**Figure 4.11**). The uptake into the A431K5 tumours increased from $4.05 \pm 0.34\%$ ID/g to $4.76 \pm 0.79\%$ ID/g, at 24 and 72 hours, respectively. In comparison, A431 showed an uptake of $2.48 \pm 0.62\%$ ID/g and $2.94 \pm 0.70\%$ ID/g, at 24 and 72 hours, respectively. Blood pool levels of ¹¹¹In-mAbMB-SPIONs decreased from $2.59 \pm 1.42\%$ ID/g at 24 hours to 1.47 ± 0.568 at 72 hours. Accumulation in lungs was quite similar to blood pool levels with $2.23 \pm 0.39\%$ ID/g and $1.32 \pm 0.59\%$ ID/g at 24 and 72 hours, respectively. Heart showed lower accumulation than blood and lungs with $1.42 \pm 0.23\%$ ID/g and $0.83 \pm 0.22\%$ ID/g localized at 24 and 72 hours, respectively. Liver experienced a relatively low nanoparticle uptake of $5.19 \pm 3.10\%$ ID/g and $10.50 \pm 3.48\%$ ID/g at 24 and 72 hours, respectively, while the uptake into the spleen was quite high. The spleen activity increased from $53.34 \pm 1.65\%$ ID/g at 24 hours to $66.37 \pm 11.06\%$ ID/g at 72 hours. Kidney uptake decreased from $7.19 \pm 1.75\%$ ID/g at 24 hours to $4.47 \pm 0.80\%$ ID/g at 72 hours. The activity uptake into the other evaluated organs (intestine, stomach, muscle, brain) was relatively low and constant at both time points. As seen in **Table 4.1**, the tumour to blood ratios were greater than 1 at both 24 and 72 hours time points. Ratio of activity localization in A431K5 tumours compared to blood was 2.18 ± 1.68 at 24 hours and 3.81 ± 0.87 at 72 hours, while for A431 tumours it was 1.41 ± 1.23 at 24 hours and 2.13 ± 0.20 at 72 hours. These results correlated well with the autoradiographic images of the organs where spleen, liver, kidney and A431K5 tumours showed the highest uptake (**Figure 4.12**).



*P<0.05, A431K5 tumours vs. A431 tumours as the corresponding time point.

Figure 4.11. Biodistribution of ^{111}In -mAbMB-SPIONs injected into SCID mice (n=5) bearing A431K5 (mesothelin positive) and A431 (mesothelin negative) subcutaneous xenografts. Percentage of the injected dose/gram (Activity %ID/g) was determined in the tumours and all major organs after 24 and 72 hours. Data is presented as mean \pm SD.

Table 4.1. Organ to blood ratios determined from biodistribution of ¹¹¹In-mAbMB-SPIONs (15 mg/kg body weight Fe), injected in SCID mice (n=3) bearing A431K5 and A431 subcutaneous xenografts. Organ to blood ratios were determined after 24 and 72 hours. Data is presented as mean±SD.

Organ	24 h	72 h
Blood	1	1
Heart	0.80±0.71	0.58±0.08
Lungs	1.18±0.89	0.93±0.15
Liver	2.07±0.46	8.14±5.12
Kidneys	4.28±4.20	3.16±0.71
Spleen	28.62±21.97	48.38±20.75
Intestine	0.94±0.59	1.14±0.21
Stomach	0.21±0.17	0.31±0.11
Brain	0.05±0.03	0.05±0.01
A431K5 (meso +ve)	2.18±1.68	3.81±0.87
A431 (meso -ve)	1.41±1.23	2.13±0.20

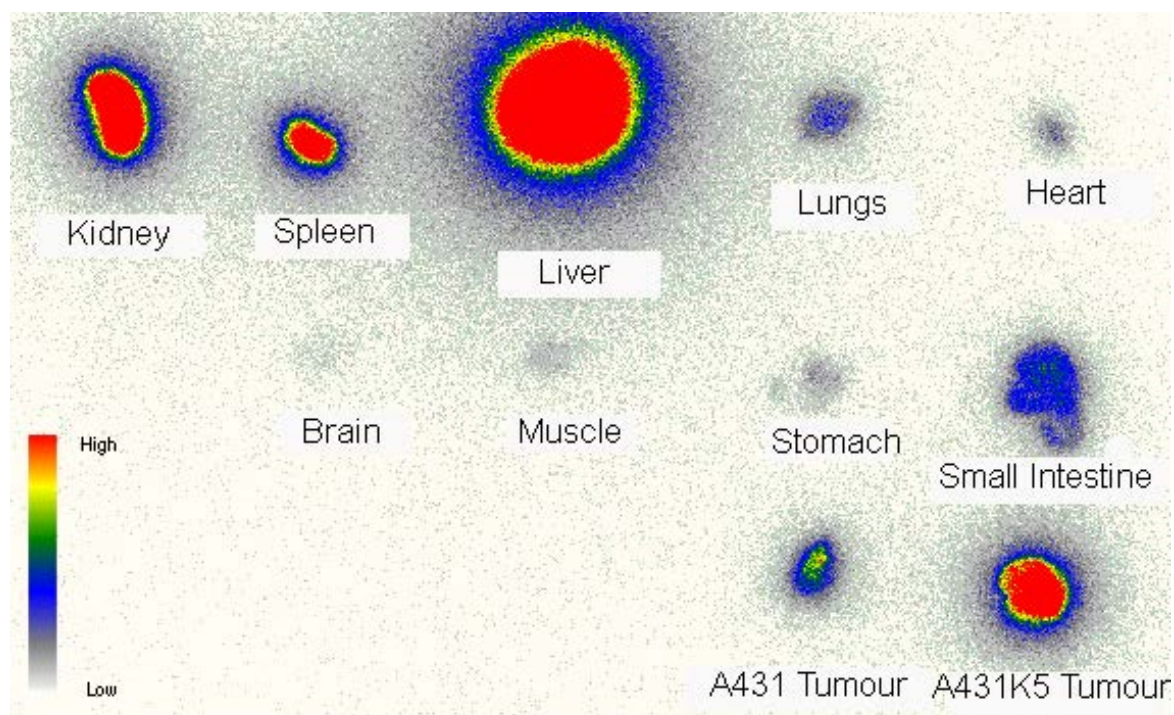


Figure 4.12. A representative autoradiographic image of excised organs. At 72 hours post-injection of ^{111}In -mAbMB-SPIONs major organs were excised and ex-vivo autoradiography of major organs was carried out by exposing a $20 \times 25 \text{ cm}^2$ phosphor screen to the excised organs followed by visualization using a phosphor imager. High activity uptake can be visualized mainly in liver, spleen, kidney and A431K5 tumour.

4.4.5. Prussian Blue Staining

Microscopic examination of tumour sections stained with Prussian blue showed the presence of iron nanoparticles in A431K5 tumour tissue. In the **Figure 4.13**, the red colour indicates nuclei, and the pink is cytoplasm, whereas the SPIONs are stained blue. Strong blue colour can be seen in the cytoplasm of the tumour cells. A431 tumours, though to a lesser extent, also showed (**Figure 4.13**) the presence of iron oxide, which indicates non-specific uptake due to the EPR effect [271]. As expected on the basis of biodistribution data, higher iron oxide staining was observed in the spleen of mice (**Figure 4.13 C**).

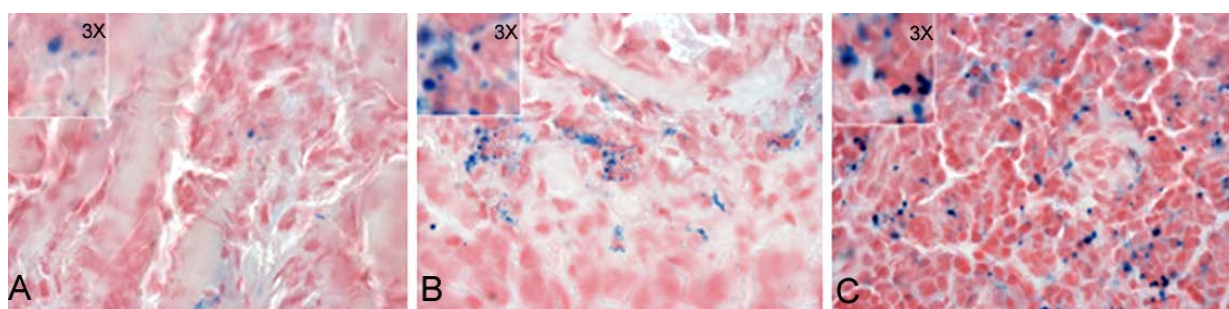


Figure 4.13. Iron oxide staining of tissue specimens of A431 tumour (A), A431K5 tumour (B) and spleen (C), by Prussian blue staining method. While spleen shows the highest presence of iron oxide, the presence of iron oxide in A431K5 tumour is greater than A431 tumour. The insets provide a 3 times magnified view of the tissue.

4.4.6. *In Vivo* MRI Studies

The potential of the ^{111}In -mAbMB-SPIONs for MR imaging was investigated in a mouse xenograft model. Coronal as well as axial images were acquired at pre-injection and 24 hours and 72 hours post-injection time points. The volumes of A431K5 tumours increased by about 28% at 24 hours and 38% at 72 hours, compared to the pre-injection time point as shown in **Figure 4.15**. From coronal MRI images (**Figure 4.14**), the change in contrast can be observed between pre-injection time point, which is more pronounced at the 24 hour time point and can be

said to be an effect of accumulated ^{111}In -mAbMB-SPIONs. For the corresponding A431 tumours the signal intensity of MR T_2 -weighted images was reduced mainly at the margin of A431 tumours as seen in **Figure 4.14**. The change in MR signal for A431K5 tumours is also apparent in axial images especially in the region pointed out by the arrows in the **Figure 4.15**. Confirmation of ^{111}In -mAbMB-SPIONs uptake in this region was obtained from autoradiography of the excised tumour sections (**Figure 4.15**). The intensity histograms (**Figure 4.16**) show the frequency of occurrence of particular image intensity within the ROI, indicated by the colour-plots. The suppression of tumour signal by ^{111}In -mAbMB-SPIONs is mainly seen in the post 24 hours scan and is represented by the shift in the curve towards the lower intensity region on the x-axis. By determining the mean image intensities from the intensity histograms, 33% and 9% decrease in image intensities compared to pre-injection time point, was observed for 24 hours and 72 hours time points, respectively. While axial images of A431 tumours also showed suppression of signal intensity (**Figure 4.17**), but due to lower resolution of the images, image intensity analysis was not carried out.

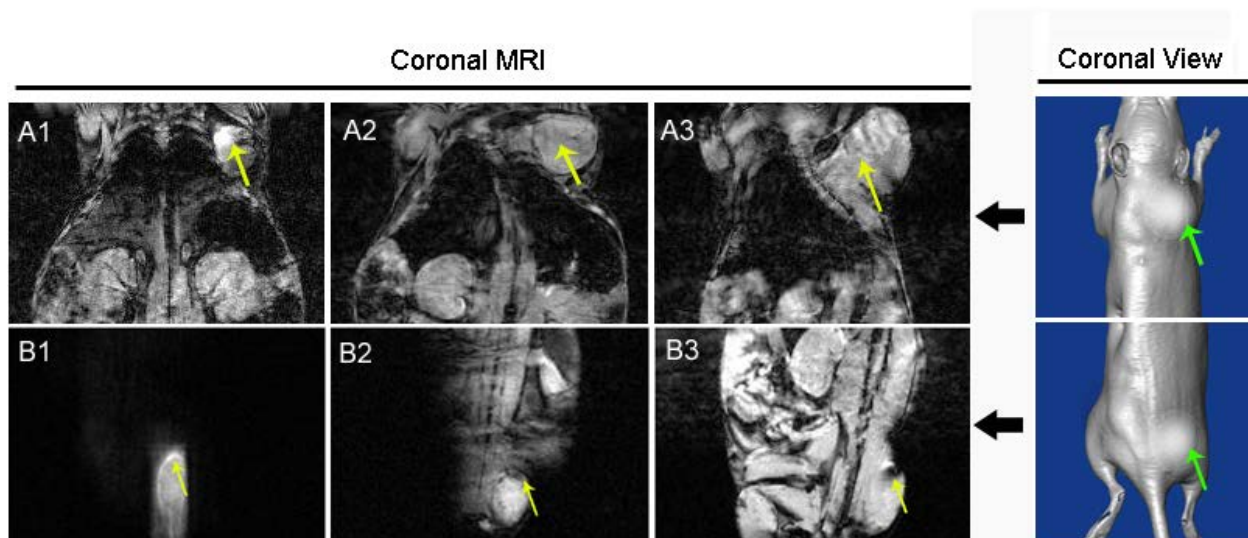


Figure 4.14. T₂ weighted coronal gradient echo MR images of SCID mice bearing xenograft tumours, injected intravenously with 15 mg/kg body weight Fe equivalent of ¹¹¹In-mAbMB-SPIONs. Images A1, A2 and A3 represent A431K5 tumour at pre-injection and 24 hours and 72 hours post-injection time points, respectively, while images B1, B2 and B3 are corresponding images for the A431 tumour from the same mouse. The mice were imaged using a 7 T MRI Bruker scanner. The yellow arrows in the images point to the regions in the tumours, where a change in MR signal can be observed. The insets to the right are a representation of the coronal view of the mouse with green arrows indicating the locations of tumours (neck-A431K5, lower back A431).

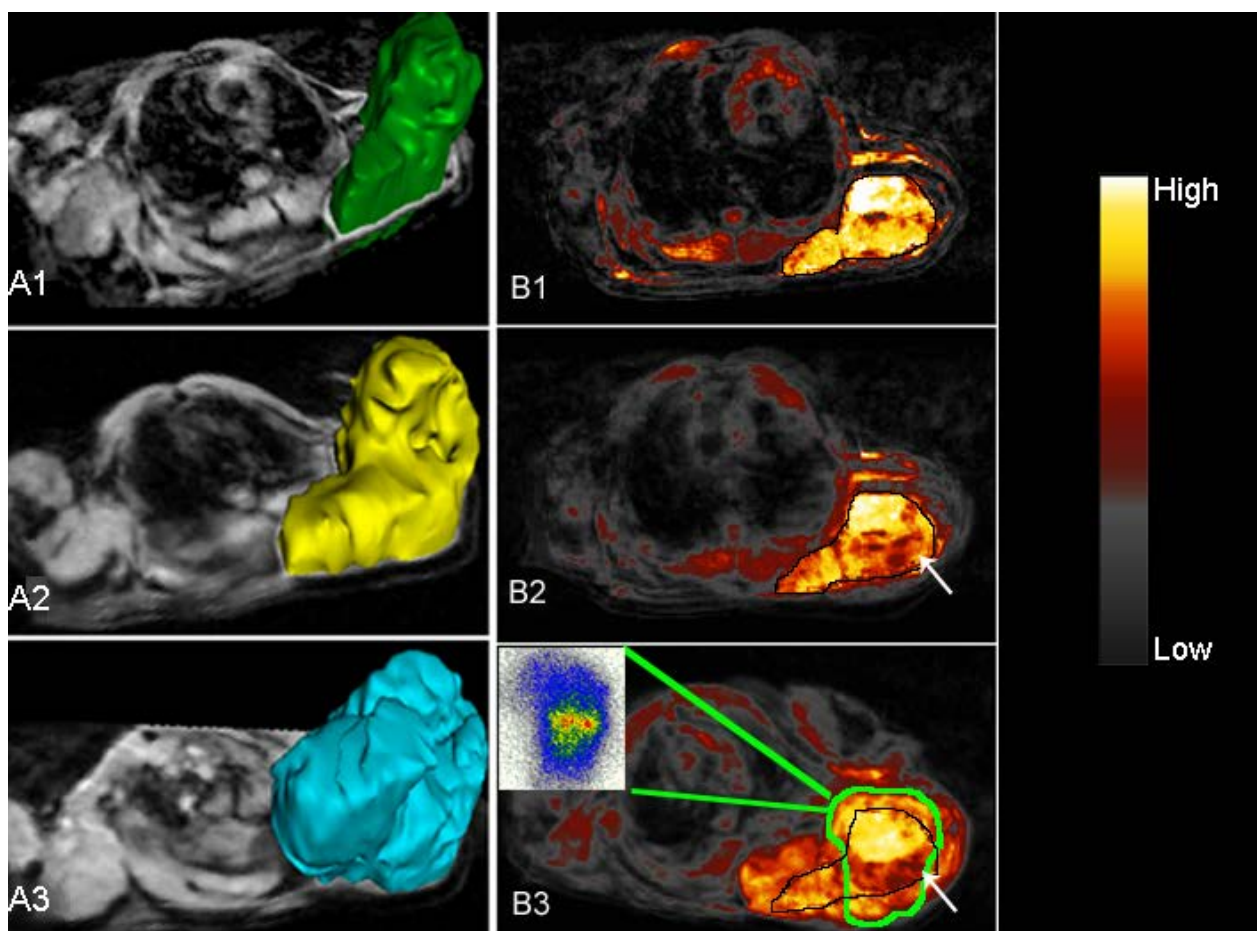


Figure 4.15. T_2 weighted axial gradient echo MR images and tumour volume maps for A431K5 tumours of SCID mice bearing xenograft tumours, injected intravenously with 15 mg/kg body weight Fe equivalent of ^{111}In -mAbMB-SPIONs. Image analysis was performed using the 3D Slicer program. Images A1, A2 and A3 represent A431K5 tumour volumes obtained at pre-injection and 24 and 72 post-injection time points, respectively. Images B1, B2 and B3 are the MR images of A431K5 tumour at pre-injection and 24 and 72 hours post-injection time points, respectively. The inset in image B3 represents the autoradiographic image of a 20 μm tumour section obtained from the corresponding tumour. The region of MR signal change observed in the B3 image correlates with the region of activity uptake as observed in the autoradiographic image. The mice were imaged using a 7 T MRI Bruker scanner.

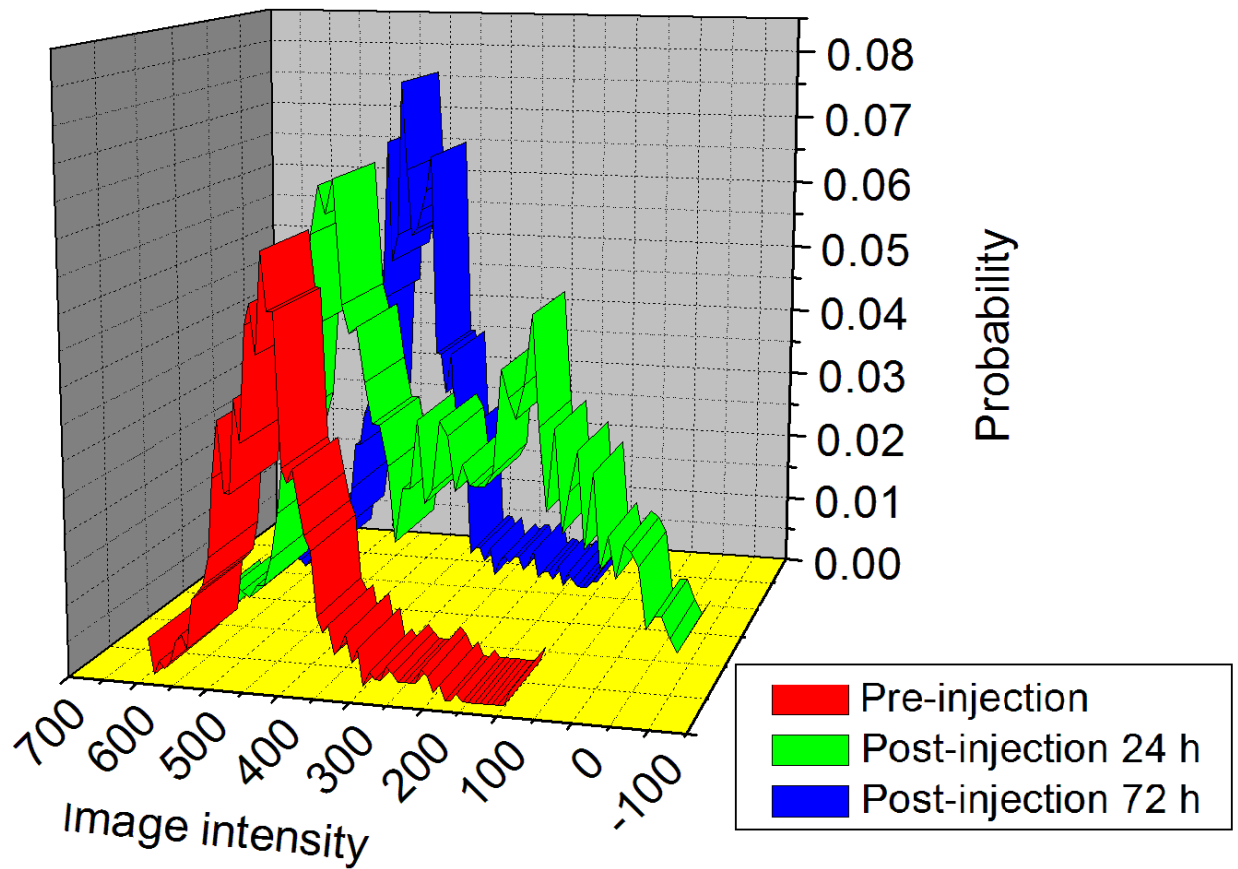


Figure 4.16. ROI intensity histograms for T2 weighted axial gradient echo MR images of A431K5 tumours. SCID mice bearing A431K5 tumours were, injected intravenously with 15 mg/kg body weight Fe equivalent of ^{111}In -mAbMB-SPIONs. The suppression of the signal intensity is mainly observed for the 24 hours image, represented by a shift in the green curve towards lower intensity region on the x-axis.

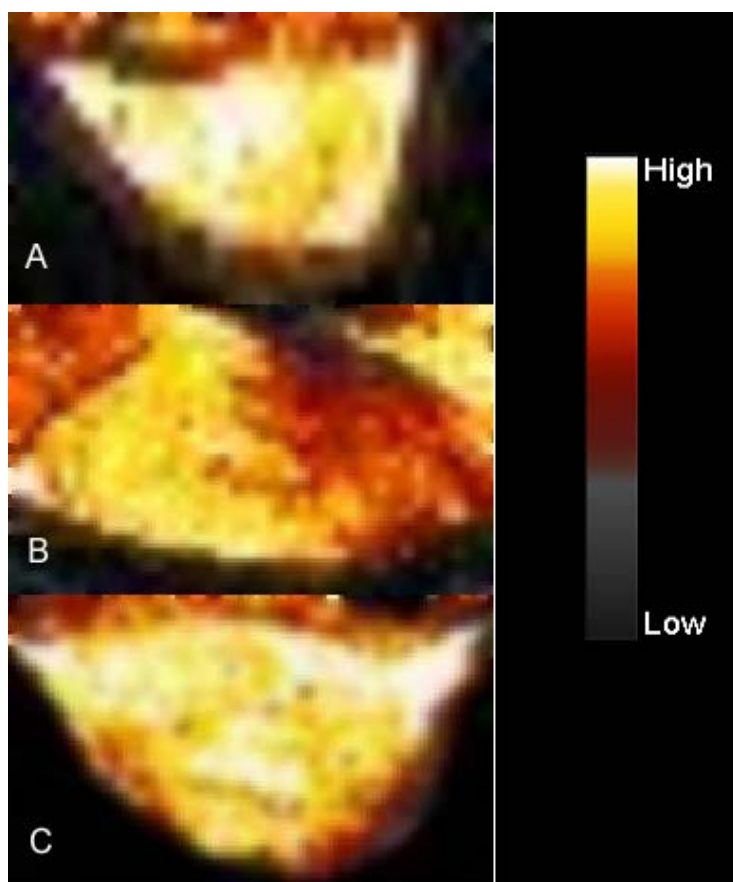


Figure 4.17. T₂ weighted axial gradient echo MR images for A431 tumours of SCID mice bearing xenograft tumours, injected intravenously with 15 mg/kg body weight Fe equivalent of ¹¹¹In-mAbMB-SPIONs at pre-injection (A), 24 hours (B) and 72 hours (C) post-injection.

4.4.7. MTT Assay

Cell viability in the presence of ¹¹¹In-mAbMB-SPIONs was evaluated by MTT assay, 24 hours after incubation with A431 cells at an equivalent concentration of 0.1 and 0.5 mg [Fe]/ml and compared with unconjugated SPIONs and Feridex IV at the same iron concentration. The p value obtained by student's t-test comparing the cell viabilities of untreated cells (control) with the respective samples indicates that all the samples tested show low toxicity on A431 cells, in the concentration range tested (**Figure 4.18**).

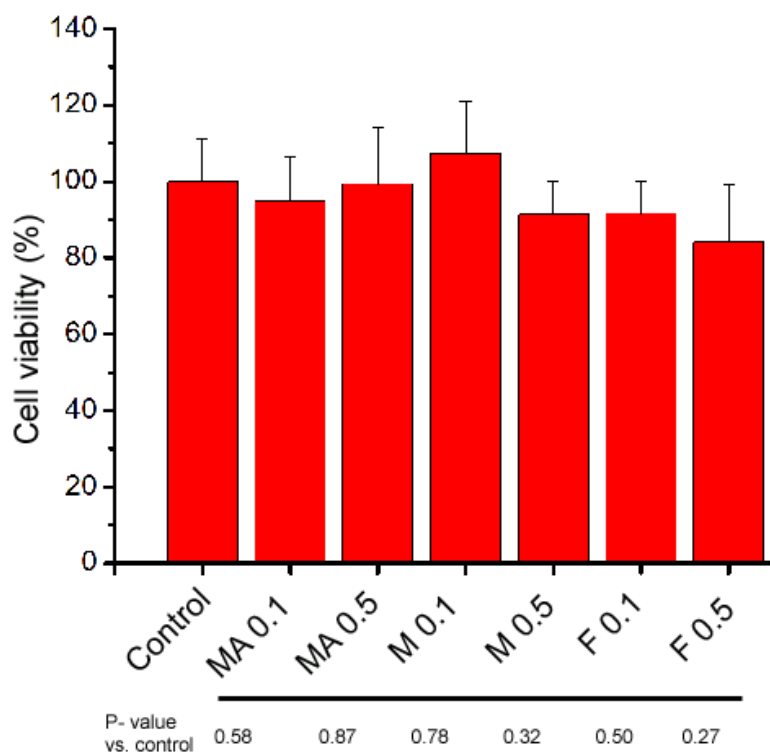


Figure 4.18. MTT assay on A431 cells. Cell viability of the ^{111}In -mAbMB-SPIONs (MA) was determined by the MTT assay, 24 hours after incubation with A431 cells and compared with SPIONs (M) and Feridex IV (F) at the equivalent concentration of 0.1, 0.5 [Fe] mg/ml, respectively ($n = 8$). Untreated cells were used as control to determine 100% cell viability.

4.5. Discussion

In chapter 3, we demonstrated that ^{111}In -mAbMB can specifically target mesothelin expressing tumours allowing us to image them using SPECT. In an attempt to further improve imaging outcomes in a few of the most challenging cancers, pancreatic, ovarian and mesothelioma, we designed a dual-modality MRI/SPECT imaging bioprobe by conjugating ^{111}In -mAbMB with SPIONs. The resultant ^{111}In -mAbMB-SPIONs showed specific uptake into A431K5 tumours and produced a change in the MR signal when tested in MRI experiments. There are only a few reported studies on the development of such dual-modality imaging bioprobes combining radionuclide imaging (SPECT or PET) with MRI [202,299,300]. Using ^{125}I -labelled antibody-magnetic nanoparticle conjugates, Otsuji *et al.* showed significantly higher uptake in colorectal tumours than in normal tissue and also observed reduced MR signal intensity in the treated tumours [301]. In another study, Liu *et al.* demonstrated the specific tumour uptake of their ^{125}I -labelled antibody-magnetic nanoparticles by SPECT and MRI imaging [292]. In comparison, we used ^{111}In as a SPECT motif to develop dual modality bioprobes for imaging mesothelin expressing tumours.

SPIO nanoparticles consist of numerous iron oxide crystals coated with dextran or carboxydextran. The useful superparamagnetic iron oxide (SPIO) nanoparticles for MRI have high molar relaxivities and are nontoxic due to their dextran coating [302,303]. Weissleder *et al.* first presented the concept of small superparamagnetic probes conjugated to an antibody where they attached iron oxide nanoparticles to antimyosin fab for immunospecific MR imaging of cardiac infarcts. Specific binding of the immunoconjugate to infarcted, but not to normal myocardium, was confirmed [211]. For tumour-specific imaging, monoclonal antibodies specific for CEA [304], epidermal growth factor receptors [305], and human glioma cell-surface antigen

[306] have been attached to iron oxide nanoparticles. Their efficacies have been established in ex-vivo and animal studies.

For our studies we used SPIONs (Fluidmax-CMX), which were first characterized by TEM and DLS to ensure that the SPIONs were present as stable colloidal dispersions, without aggregation (**Figure 4.3**). Post antibody conjugation, the hydrodynamic diameter of the particles, expectedly, increased from 69.6 nm to 76.6 nm. This was also accompanied by a change in the size distribution profile (**Figure 4.4**) leading to increase in the polydispersity index from 0.16 to 0.18, which can be attributed to slight aggregation during the coupling reaction. In comparison, the mean size of most clinically approved SPION formulations like Feridex IV, Endorem and Resovist, approximately ranges between 60 to 250 nm [200,201], while the polydispersity index can be as high as 0.29 [201]. The conjugation yields obtained from the carbodiimide coupling reaction between ^{111}In -mAbMB and the SPIONs revealed that ^{111}In -mAbMB was effectively coupled to the SPIONs. A comparison of cell binding to mesothelin expressing A431K5 and non-mesothelin expressing A431 cells, over a period of 24 hours suggested that ^{111}In -mAbMB-SPIONs retained their mesothelin reactivity and binding specificity (**Figure 4.6**). The competition binding assay performed with excess free mAbMB again demonstrated the specificity of the interaction of ^{111}In -mAbMB-SPIONs with A431K5 cells (**Figure 4.7**). Qualitatively, confocal microscopy confirmed the specific interaction between ^{111}In -mAbMB-SPIONs and A431K5 cells (**Figure 4.8**).

Higher molar relaxivity of a contrast agent implies that lower concentrations are required for achieving the characteristic darkening associated with MR imaging. Higher molar relaxivity is especially important for applications requiring extravasation of the contrast agent (tumour imaging), because of typically lower accumulation of the contrast agent. For such applications,

SPIONs are especially suitable as they possess high transverse relaxivity due to each particle being composed of many thousands of iron atoms. Additionally, coupling with specific molecular targeted ligands (like antibodies and peptides) provides them an ability to accumulate in extra vascular tissue (tumours) at appropriate concentrations to produce an optimum MR effect [307]. Several groups have successfully developed high relaxivity contrast agents with r_2 values ranging between 281 mMs^{-1} to 453 mMs^{-1} [308-310]. In our *in vitro* relaxivity studies, we observed a signal hypointensity gradient in proportion to the increasing iron concentrations for ^{111}In -mAbMB-SPIONs, as shown in **Figures 4.9 and 4.10**. Qualitatively, the signal hypointensity of unconjugated SPIONs and ^{111}In -mAbMB-SPIONs was equivalent indicating that the conjugation did not affect the relaxation properties of the SPIONs. The r_2 relaxivity values of SPIONs (397.33 mMs^{-1}) as well as ^{111}In -mAbMB-SPIONs (469.57 mMs^{-1}) were higher than those reported for Feridex IV (268 mMs^{-1} at 0.47 T). In our previously done studies we obtained r_2 relaxivity values of 224 mMs^{-1} using the 7 T MR imaging system (data not shown). These results provide evidence about the uniform and high crystalline nature of the SPIONs and making them an excellent choice for MRI probe development [311].

The use of radiolabelled MR probes, in addition to being useful for the SPECT imaging, also allows determination of the biodistribution and *in vivo* characteristics of the imaging bioprobes, which is difficult to achieve solely by MRI. The main purpose of our biodistribution study was to evaluate specific tumour uptake of ^{111}In -mAbMB-SPIONs in A431K5 tumours and compare it to non-specific uptake in A431 tumours. Since the peak uptake of ^{111}In -mAbMB was obtained between 24 and 72 hours in our previous studies (Chapter 3), we chose to evaluate the biodistribution of ^{111}In -mAbMB-SPIONs, at 24 and 72 hours post-injection. To achieve high tumour penetration of molecular probes, it is necessary to achieve longer circulation times in the blood, but the rapid sequestration of intravenously injected colloidal particles from the blood by

the reticuloendothelial system (liver and spleen) poses a major barrier [312]. In our studies, ^{111}In -mAbMB-SPIONs showed high localization in spleen, similar to that seen for ^{111}In -mAbMB (Chapter 3). This spleen uptake (**Figure 4.11**) can be attributed to the binding of ^{111}In -mAbMB-SPIONs to shed mesothelin antigen from A431K5 tumours, forming immune complexes that are sequestered by the spleen [130,278]. When compared to spleen, the liver uptake was much lower at 24 hours, but increase in activity accumulation was observed by 72 hours, indicating that blood clearance mediated by hepatic midzonal and periportal Kupffer cells, increased over time [312]. The sequestered SPIO particles are metabolized and transferred to the body iron stores and incorporated into erythrocyte haemoglobin [313]. Despite high spleen uptake, the blood retention of ^{111}In -mAbMB-SPIONs was $2.59 \pm 1.42\%$ ID/g at 24 hours. In comparison, Glaus *et al.* reported about $1.0 \pm 0.05\%$ ID/g in the blood at 24 hours post-injection for their ^{64}Cu labelled iron oxide nanoparticles (without any specific ligands) for dual modality imaging (MRI/PET) [202]. The authors also reported $31.33 \pm 2.33\%$ ID/g and $18.05 \pm 1.27\%$ ID/g in liver and spleen at 24 hours, respectively. While blood levels of ^{111}In -mAbMB-SPIONs decreased between 24 hours and 72 hours, the corresponding activity levels in A431K5 tumours increased slightly from $4.05 \pm 0.34\%$ ID/g at 24 hours to $4.76 \pm 0.79\%$ ID/g at 72 hours. Based on tumour blood volume calculations [314] the contribution of blood to the activity values in A431K5 tumours was negligible ($<0.0001\%$ ID/g). The activities in A431 tumours were significantly lower ($P < 0.05$) than A431K5 tumours, which points to specific uptake of ^{111}In -mAbMB-SPIONs in A431K5 tumours, which was also confirmed by Prussian blue staining (**Figure 4.13**). In comparison, Otsuji *et al.* reported about 7.5% ID/g in receptor targeted tumours compared to about 1.5% ID/g in control tumours at 24 hours, while the values at 72 hours decreased to about 6.5% ID/g and 1.0% ID/g, respectively. When compared to ^{111}In -mAbMB (Chapter 3), the A431K5 tumour uptake of ^{111}In -mAbMB-SPIONs was lower at 24 hour time point (8.74% ID/g vs. 4.05% ID/g), while at 72 hours, A431K5 tumour uptake of both ^{111}In -mAbMB and ^{111}In -mAbMB-SPIONs

was similar (4.82% ID/g vs. 4.76% ID/g). The reduced uptake of ^{111}In -mAbMB-SPIONs at 24 hours can be attributed to their larger size compared to ^{111}In -mAbMB, which poses an additional challenge to overcome the vascular and interstitial barriers within the tumor [315].

In general, MR imaging correlated well with biodistribution findings. The MR signal change was clearly visible in A431K5 tumours between, pre-injection and post-injection time points in both coronal as well as axial MR images indicating presence of iron oxide particles in the tumours (**Figures 4.14 and 4.15**). The regions of signal hyposensitivity correlated well with tumour distribution of the probe as evident from autoradiography (**Figure 4.15**). Further quantitative analysis showed that the signal specifically obtained from A431K5 tumours was reduced, especially at 24 hours time point (**Figures 4.16**). This was also observed in the MR pictures as regions of signal hyposensitivity. However, at 72 hours the hypointensive signal although higher compared to pre-injection time point, was reduced compared to 24 hours time point. This can partly be attributed to the decline in blood pool reservoir of ^{111}In -mAbMB-SPIONs during 24 hours and 72 hours period, thus resulting in reduced incremental uptake as indicated by the biodistribution studies. In comparison, the MR signals of A431 tumours were less hypointensive and were mostly prevalent along the margins of the tumours as seen in **Figure 4.14**.

Despite high expression of mesothelin by A431K5 tumours, the shed mesothelin creates a major impediment to mesothelin directed delivery of the ^{111}In -mAbMB-SPIONs. Although, we observed this phenomenon in previous studies with ^{111}In -mAbMB (Chapter 2), the unavailability of a relevant mesothelin expressing tumour model, which does not shed mesothelin, limited our choice to A431K5 cells for these studies. The other cell lines, like NCI-H226 cells (Chapter 2) express even lower amounts of mesothelin and are therefore not useful. We demonstrated the potential of ^{111}In -mAbMB-SPIONs for simultaneous γ -imaging by carrying out biodistribution

and autoradiographic studies (**Figure 4.12**). Further validation of their usefulness as γ -imaging bioprobes is required and can be obtained by SPECT.

Receptor-directed agents such as MIONs sized less than 40 nm are most capable of passing through capillary fenestra and inter-endothelial junctions to reach the extra-vascular space. This passage is a prerequisite for targeted imaging and would help in achieving higher tumour concentrations, but none of such agents are yet clinically approved [210,211]. The use of surface modified SPIONs with larger size is therefore a reasonable choice as they possess larger magnetization values, thus making them capable of faster spin-spin relaxation processes of surrounding water molecules [316]. The T_2 enhancing effects observed in MRI images as well as the higher A431K5 tumour uptake provide evidence of the ability of ^{111}In -mAbMB-SPIONs to specifically target mesothelin expressed by tumours. In addition, ^{111}In -mAbMB-SPIONs have suitable relaxation rates as well as biocompatibility characteristics, which make them suitable for MR imaging. With the progress made recently in development of combined PET/MRI and SPECT/MRI scanners, dual modality imaging agents such as the ones developed in the current study, have enormous potential of being used in the clinic within the next few years [192,194,317-319].

4.6. Conclusion

We successfully developed and tested a novel dual-modality molecular imaging probe for *in vivo* detection of mesothelin expressing tumours by both MRI and SPECT. This imaging bioprobe comprises the ^{111}In labelled antimesothelin antibody mAbMB chemically conjugated to carboxy methyl dextran coated iron oxide nanoparticles. The high relaxivity and specific targeting of the bioprobes resulted in enhanced MR contrast effect in mesothelin positive tumours compared to mesothelin negative tumours. Covalently bound ^{111}In acted as a SPECT detection motif and was

used to provide proof of principle by autoradiography and biodistribution studies. It is anticipated that combining MRI and SPECT imaging modalities will enable characterization of tumours based on both functional and anatomical information and will provide a powerful diagnostic tool for early diagnosis and monitoring of mesothelin expressing cancers.

Chapter 5: Summary and Conclusion

5.1. Research Rationale

Mesothelin is highly expressed in mesotheliomas, pancreatic adenocarcinomas and ovarian cancers. Its potential as a target for cancer therapy is very well recognized due to the limited expression of mesothelin on normal human tissues and high expression in cancer cells. Many groups have designed immunotherapeutic agents that either target cell surface mesothelin or elicit an immune response against mesothelin. Some of these agents are already in the clinic or about to enter clinical trials which include CAT-5001 (recombinant immunotoxin against mesothelin), MORAb-009 (cytotoxic chimeric anti-mesothelin monoclonal antibody) and CRS-207 (*Listeria monocytogene*-mesothelin vaccine). For a detailed review on the mesothelin directed immunotherapy please refer to the review by Hassan *et al.*, 2008 [102]. In light of the progress made in the field of immunotherapeutic targeting of mesothelin, it is surprising that there are only two reported studies exploring the pre-clinical development of mesothelin targeted imaging agents, while none of these agents has progressed into clinical testing [164,166]. The potential of mesothelin as an imaging target for early detection and management of mesothelin positive malignancies, can only be fully realized by developing and evaluating new mesothelin targeted imaging agents. The research described in this dissertation was carried out with the goal of exploiting the potential of mesothelin as a target for imaging mesothelin expressing cancers. The main objective of this research is to develop and evaluate molecular imaging bioprobes targeting mesothelin (**Figure 5.1**). This work utilizes the antibody targeting approach for selective delivery of radionuclides and MRI contrast agents for visualization of tumours. Since these cancers are best treated when diagnosed early this approach is highly significant for management of these cancers. Through this work we evaluated the features of different antibodies, antibody fragments, radionuclides, nanoparticles and cell models for development of a mesothelin specific molecular imaging bioprobe. We followed two approaches for the

development of a mesothelin specific imaging bioprobe. In the first approach, antimethelin antibodies were radiolabelled using different methods and tested for SPECT imaging of mesothelin expressing cancers. In the second approach, we coupled these radiolabelled antibodies with iron oxide nanoparticles (MRI contrast agent) to develop a novel mesothelin targeted dual-modality SPECT/MRI imaging agent. The work in this dissertation describes the evaluation of these imaging bioprobes using *in vitro* and *in vivo* methods. Strategies to achieve high tumour accumulation of imaging bioprobes were also assessed. The specific targeting ability of the molecular imaging bioprobes was evaluated using biodistribution and imaging studies in mesothelin expressing tumour xenograft mouse model and compared with non-mesothelin expressing control tumours.

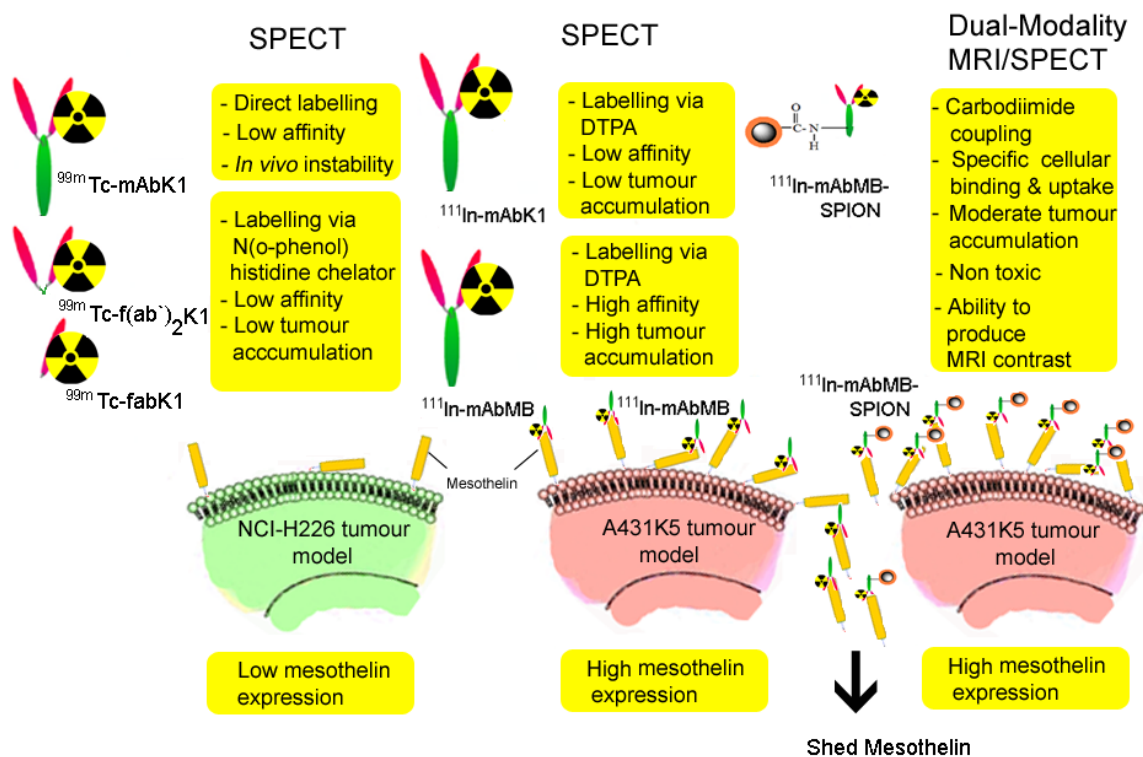


Figure 5.1. Overview of research findings.

5.2. Assessing Suitability of ^{99m}Tc Labelled mAbK1 Antibody and its Fragments in NCI-H226 Tumour Model

^{99m}Tc is the radionuclide of choice for scintigraphic imaging, but radiolabelling of antibodies with ^{99m}Tc is challenging and has been a subject of considerable research [216,320-322]. Both direct and indirect labelling methods of ^{99m}Tc have been explored by researchers in the past; for a review see Reilly-, 1993 [215]. Additionally, Alberto *et al.* described a new indirect method [218] for ^{99m}Tc labelling using $^{99m}\text{Tc}(\text{I})$ tricarbonyl core, which has been commonly used in recent years [218,243,244]. In the current work we used both direct as well as indirect labelling methods. While mAbK1 antibody was radiolabelled with ^{99m}Tc using the direct labelling method after reduction with SnCl_2 , the fab and f(ab')_2 fragments of mAbK1 were radiolabelled with $^{99m}\text{Tc}(\text{I})$ tricarbonyl core using an N-(*o*-phenol)-histidine chelator, synthesized in our lab. In contrast, prior studies have mainly focused on using genetically expressed histidine-tags on the proteins for radiolabelling with $^{99m}\text{Tc}(\text{I})$ tricarbonyl core [218].

Achievement of high tumour to background ratios is critical for imaging tumours with radiotracers. Whole IgG antibodies take 1-3 days to clear from blood due to their high molecular weight (150 kDa), while ^{99m}Tc has a half-life of only 6 hours, thus permitting imaging only within the first 24 hours of administration. To address this potential incompatibility, we considered the use of fab (~50 kDa) and f(ab')_2 (~100 kDa) fragments of mAbK1 as an alternative strategy for achieving sufficient tumour uptake and background clearance for imaging within the time frame compatible with the half life of ^{99m}Tc .

Successful antigen targeted tumour imaging requires high and stable antigen expression levels in tumour cells as well as low or absent expression in normal tissues. Additionally, the radiolabelled antibody must bind to the antigen with high binding affinity [323]. NCI-H226 cells

express the highest amount of mesothelin amongst the established cell lines [157] and therefore were used in our studies for *in vitro* studies as well as for development of tumour xenografts in mice for biodistribution studies. Assessment of the immunoreactivity and affinity properties was done using *in vitro* radioligand binding assays. While all three ^{99m}Tc labelled radioimmunoconjugates retained their reactivity to mesothelin, their affinity properties were less than optimal ($K_d = 21 - 25 \text{ nM}$). The binding assay also revealed the low expression of mesothelin on NCI-H226 cells ($9.1 \pm 1.0 \times 10^4$ receptors/cell). The low affinity of mAbK1 and its fragments to mesothelin was an unexpected finding, since the previous studies have indicated high affinity ($K_d = 0.92 \text{ nM}$) for the same antibody [164]. In comparison, the clinically approved monoclonal antibody trastuzumab (Herceptin) targeting HER2 receptors for treatment of breast cancers has a much higher affinity ($K_d = 5 \text{ nM}$), while the HER2 expressing cell lines such as SK-BR-3 also express much higher levels of HER2 receptors ($2.0 \pm 0.23 \times 10^6$ receptors/cell) [256,324]. Another clinically used monoclonal antibody rituximab has a K_d value of 8 nM, again indicating high affinity binding to CD20 receptors of normal and neoplastic B cells [324]. The low expression of mesothelin by NCI-H226 tumours and low binding affinity of the mAbK1 antibody contributed to insufficient tumour uptake of the ^{99m}Tc labelled radioimmunoconjugates as revealed by the biodistribution studies. Similar findings were reported by Yoshida *et al.* in a recent study using ^{64}Cu labelled antimesothelin fab fragments for targeting mesothelin expressing NCI-H226 tumours. In our studies, although the tumour uptake was low, the blood clearance and peak uptake time point of 8 hours for both fab and f(ab)_2 fragments indicated their compatibility for ^{99m}Tc based radioimmunoimaging. Another interesting finding was the fast blood clearance of ^{99m}Tc -mAbK1, which can be attributed to *in vivo* instability of the directly labelled ^{99m}Tc -mAbK1. This finding was unexpected since our cysteine challenge results of ^{99m}Tc -mAbK1 did not predict instability due to transchelation of ^{99m}Tc from the antibody. Thus, in this case, the instability can be attributed to the fragmentation of antibody as also observed in

earlier studies with directly labelled antibodies by Pimm *et al.* and Sakahara *et al.* [325,326]. This instability of ^{99m}Tc -mAbK1 prevented us from determining its real pharmacokinetic behaviour and also contributed to low tumour uptake. Based on the findings of this study we identified the critical factors for preclinical development of mesothelin targeted probes. It is evident from our studies that the NCI-H226 cell model does not express sufficient levels of mesothelin to allow sufficient accumulation of the anti-mesothelin imaging probes in tumour xenografts developed in mice. Further the K_d values suggest that mAbK1 has a low binding affinity for mesothelin. We adapted our study design to address these issues as explained in Chapter 3 by choosing an alternative antibody with high affinity to mesothelin as well using a cell model with higher mesothelin expression levels.

5.3. Designing Mesothelin Targeted SPECT Imaging Probes with ^{111}In Labelled mAbMB Antibody and Comparison of its Properties with ^{111}In Labelled mAbK1

In continuation of our work towards development of mesothelin directed molecular imaging bioprobes, we focused on using alternative strategies to resolve the issues related to low uptake of anti-mesothelin probes by mesothelin expressing tumours as observed in chapter 2. Due to increasing research interest in mesothelin targeting, new and improved anti-mesothelin antibodies have recently become available. Onda *et al.* developed two new anti mesothelin antibodies, mAbMB and mAbMN, and reported that mAbMB has the best affinity towards mesothelin amongst all available antibodies [160]. In their studies, mAbMB has a K_d value of 0.62 nM, while for mAbK1 the K_d value is 12 nM. Based on its higher affinity to mesothelin we selected mAbMB for the development of mesothelin targeted imaging probes. We also replaced ^{99m}Tc with another γ -emitting isotope, ^{111}In , which is more suitable for imaging with whole IgG's and their slower blood clearance and longer tumour penetration time because of its half-life of 2.8 days. Since ^{111}In -mAbK1 had shown excellent mesothelin targeting potential in

previous studies by Hassan *et al.* [164], we chose to compare the imaging characteristics of ^{111}In -mAbMB with ^{111}In -mAbK1. This work also provided evidence for pharmacokinetic and biodistribution behaviour of mAbK1, which we were unable to obtain in chapter 2, due to *in vivo* instability. ^{111}In labelling of both mAbMB and mAbK1 was accomplished with high efficiency using the bifunctional chelator p-SCN-bn-DTPA [327].

To address the drawbacks of low mesothelin expression levels by established cell lines, Dr. Ira Pastan's laboratory (NIH, USA) has developed an alternative mesothelin expressing cell line by transfecting epidermoid A431 cells with pcD3CAK1-9, a plasmid encoding mesothelin gene [269]. The resulting A431K5 cells have mesothelin expression similar to that seen on immunohistochemical examination of patient tumour specimens [156]. This cell line was used by Hassan *et al.* for their biodistribution study of ^{111}In labelled mAbK1 [164] and also has been used for mesothelin related investigations by many other groups [143,145,158,159]. Dr. Ira Pastan generously provided the A431K5 cell line for our work. Our studies indicate that A431K5 cells express about 7 times higher mesothelin receptors per cell than NCI-H226 cells. Through *in vitro* cell binding assays it was determined that ^{111}In -mAbMB ($K_d = 3.6$ nM) has about 8 fold higher affinity than ^{111}In -mAbK1 ($K_d = 29.3$ nM). The lower affinity observed for ^{111}In -mAbK1 is not consistent with the affinity results reported by Hassan *et al.* ($K_d = 0.92$ nM). It should however be acknowledged that, for our studies we used the commercially available mAbK1, while Hassan *et al.* used the antibodies produced in their laboratory for their experiments. It is also noteworthy that, despite the excellent results obtained in the biodistribution study, no further development or studies have been reported on ^{111}In labelled mAbK1 by Hassan *et al.* The affinity results for ^{111}In -mAbK1 are similar to those obtained for $^{99\text{m}}\text{Tc}$ -mAbK1 in chapter 2 and also explain the low tumour uptake of ^{111}In -mAbK1 by A431K5 tumours compared to that of ^{111}In -mAbMB.

For *in vivo* studies, our tumour model comprised of subcutaneous xenografts of both A431K5 tumour (mesothelin positive) and A431 tumour (mesothelin negative) grown on the same mouse. The main advantage of this model is that it allows determination of specific tumour uptake as well as the non-specific uptake related to the non specific binding and EPR effect. Additionally, this model also allows reduction in the number of animals as each mouse functions as its 'own control', which is a significant advantage with respect to cost and ethical considerations. A caveat to using such a model is that it works on the assumption that the control and test tumours have a similar microenvironment. Alternatively, the effect of non-specific binding and EPR can be evaluated by using a non-specific antibody control in A431K5 tumour bearing mice. However, such a control radiolabelled non-specific antibody must be equivalent to the specific antibody with respect to its *in vivo* pharmacokinetics; otherwise differences in the blood concentrations of radioactivity may lead to incorrect estimation of non specific binding and EPR effect on tumour uptake [236]. In the biodistribution studies, carried out in subcutaneous tumour xenograft bearing SCID mice, we observed significantly higher uptake into the mesothelin expressing A431K5 tumours compared to control A431 tumours, at both high and low dose of ^{111}In -mAbMB, indicating specific targeting ability of ^{111}In -mAbMB. At low dose of ^{111}In -mAbMB, peak activity uptake was observed at 48 hours after injection, while at the high dose the peak uptake of the tumour was slightly higher at 72 hours than at 48 hours. One of the limitations of the high dose study was that biodistribution of only three mice (n= 3) was obtained, although the results are still statistically significant.

SPECT imaging and the ROI analysis thereof provided further confirmation of specific localization of ^{111}In -mAbMB in mesothelin expressing A431K5 tumours. One of the interesting findings of the biodistribution studies was the preferential uptake of ^{111}In -mAbMB by the spleen, which was also confirmed by the SPECT images. At the high dose of ^{111}In -mAbMB, spleen

uptake also caused decrease in spleen weights possibly due to depletion of the hematopoietic cells in the spleen as a result of the local high density electron irradiation from auger electron emission of ^{111}In [275,276]. In our western blot studies no cross reactivity of mAbMB with spleen antigens was observed. Previously, Sato *et al.* have also reported high spleen uptake of their mesothelin targeted ^{111}In labelled tetravalent single-chain Fv-streptavidin fusion protein (SS1scFvSA), in mice bearing A431K5 tumours. In the same study, the spleen uptake was blocked by administration of unlabelled SS1scFvSA, which suggests a role of circulating mesothelin antigen in forming immune complexes with ^{111}In labelled SS1scFvSA, which undergoes phagocytic uptake by spleen. We believe that the spleen uptake of ^{111}In -mAbMB is mediated by a similar mechanism. Low spleen and liver uptake of ^{111}In -mAbMB observed in non-tumour bearing mice compared to tumour-bearing mice clearly points to the role played by the shed tumour antigens in promoting spleen and liver uptake. Prior studies by Hellstorm *et al.* have shown that mesothelin extensively shed by the tumour cells finds way into the blood circulation. Studies by Ho *et al.* and Zhang *et al.* have specifically used the A431K5 tumour model to further demonstrate the shedding of mesothelin antigen [146,278]. Additionally, Zhang *et al.* determined that the amount of mesothelin shed into the blood circulation can range between 0.7 nM to 10 nM depending on the size of the A431K5 tumours. Prior studies have extensively focused on evaluating the effect of circulating antigen in case of carcinoembryonic antigen producing xenografts in mice. For a detailed review about the effect of circulating antigen on immunoscintigraphy please refer to the review by Pimm [281].

It is noteworthy that high affinity antibodies form more immune complexes and therefore are effectively cleared from the circulation by either liver or spleen [328]. This provides an explanation for low spleen uptake of ^{111}In -mAbK1 (low affinity) in our studies. In addition, it is also possible for different xenograft types to secrete different levels of the antigen into the

circulation, due to different rate of antigen production in tumours as well as different size of the tumours [329,330]. The low spleen uptake of ^{111}In labelled mAbK1 in the studies by Hassan *et al.* can perhaps be attributed to this phenomenon. Due to immune complex formation, the blood circulation of shed mesothelin antigen can restrict the effective uptake of radiolabelled antibodies into human tumour xenografts in mice and have an impact on immunoscintigraphy [281]. Hagan *et al.* have shown up to 3-fold higher tumour localization of anti-CEA antibodies in mice bearing colon carcinoma xenografts that produce low levels (20 ng/g/h) of CEA, compared to mice having xenografts with high production levels (1000 ng/g/h) of CEA. Nonetheless, in our studies, despite the presence of circulating antigen we were clearly able to visualize specific activity localization in A431K5 tumours.

In human patients injected with radiolabelled anti-CEA antibodies, the formation of immune complexes with circulating CEA, rather surprisingly does not affect the localization of activity into the tumours and there is no marked clearance of the radiolabel in liver or spleen. As a result tumour detection by γ -immunoscintigraphy remains unaffected [331,332]. It is therefore possible that the spleen uptake of ^{111}In -mAbMB observed in the mouse model in our studies may not be prevalent in the human patients.

There is no conclusive evidence in previous literature that explains this difference between mouse models and human patients, although a number of possibilities have been explained in the review by Pimm [281]. From a future perspective a more detailed investigation of the effects of circulating mesothelin antigen on tumour imaging with ^{111}In -mAbMB is required. For such studies one might also consider the use of an alternative mesothelin expressing tumour model which does not shed mesothelin. In this regard H9 cell line reported recently by Feng *et al.* might be promising, after prior evaluation of its mesothelin shedding properties [154]. If necessary pre-

administration of the cold antibody can be used as a strategy to successfully avoid spleen uptake of ^{111}In -mAbMB due to circulating mesothelin antigen.

For clinical imaging, the sensitivity of the radiopharmaceutical is critical especially for detecting small lesions. The sensitivity of imaging depends not just on the radiopharmaceutical, but also on factors related to the tumour, surrounding tissue as well as the imaging system [333]. Our investigation revealed preferential localization of ^{111}In -mAbMB into the mesothelin expressing tumours. The blood clearance and lower normal tissue distribution of ^{111}In -mAbMB also resulted in higher T/NT ratios. While both these findings have a favourable influence on the sensitivity of tumour detection, the non-specific uptake into spleen adversely affects the sensitivity. Imaging sensitivity also depends on factors such as tumour vascularity, heterogeneity of receptor expression, lesion size and location, collimator resolution, efficiency of detection systems and the display of final image [333], however, the current study was not designed to evaluate these factors.

5.4. Designing Dual-Modality MRI/SPECT Imaging Probes with ^{111}In Labelled mAbMB and SPIONs

In chapter 3 we established that ^{111}In -mAbMB specifically targets mesothelin expressing tumours and can be used for SPECT/CT imaging of mesothelin expressing tumours. To fully realize the potential of this specific interaction of ^{111}In -mAbMB and mesothelin for imaging, we attempted to design a dual-modality SPECT/MR imaging bioprobe. A combination of two or more detection techniques, made possible by multi-modal imaging agents ensures enhanced visualisation of biological materials and better reliability of collected data, thus enabling improved diagnostic accuracy and radiotherapy planning. SPECT when combined with MRI can produce images with high sensitivity, resolution and soft tissue contrast, overall providing

anatomical as well as functional information. The field of dual-modality imaging with SPECT/MRI, although very promising is only at a nascent stage, with relatively few studies reported so far [192,292,317,334].

In this work, we conjugated ^{111}In -mAbMB to carboxymethyl dextran coated SPIONs and determined their biodistribution and targeting efficacy in mice bearing mesothelin positive A431K5 tumour and control A431 tumour. Significantly higher uptake of ^{111}In -mAbMB-SPIONs into A431K5 tumours confirmed their specific targeting ability. However, spleen uptake as seen in chapter 3 for ^{111}In -mAbMB was also prevalent for ^{111}In -mAbMB-SPIONs, which can be attributed to the role played by circulating mesothelin antigen, as explained in the previous section. Additionally, the SPION diameter also greatly affects the biodistribution since the particles from 60 to 150 nm are taken up by the reticuloendothelial system leading to accumulation in the liver and spleen. Although the concentration of ^{111}In -mAbMB-SPIONs was not very high in A431K5 tumours ($4.05 \pm 0.34\%$ ID/g at 24 hours and $4.76 \pm 0.79\%$ ID/g at 72 h), their high molar relaxivity ($469.57 \text{ mM}^{-1}\text{s}^{-1}$) contributed to signal hypointensity in A431K5 tumours which was greater than A431 tumours (**Figure 4.14**). By combining the information gathered from biodistribution studies, Prussian blue staining, autoradiography and MRI imaging, we confirmed that ^{111}In -mAbMB-SPIONs not only extravasate but are also retained in the tumours. The tumour uptake into the A431K5 tumours can be mainly attributed to mesothelin specific targeting of ^{111}In -mAbMB-SPIONs, while some of the tumour uptake and retention is also due to the more permeable vasculature environment at the tumour site, i.e., the EPR (enhanced permeation and retention) effect [271]. The tumour uptake determination in the control A431 tumours helps to delineate the effect of EPR due the absence of mesothelin receptors on these tumours. These results also indicate a reasonable circulation half-life of the particles which is sufficient to allow tumour uptake.

All of the above observations are encouraging, for the development of a SPECT/MRI molecular imaging probe for mesothelin expressing cancers. However these findings can only be considered as preliminary evidence, primarily due to unavailability of SPECT data for ^{111}In -mAbMB-SPIONs. The logistical problems associated with simultaneous SPECT and MRI imaging prevented us from incorporating *in vivo* dual-modality imaging in our study design. Instead, we used autoradiography and biodistribution studies to examine activity uptake in the tumours and major organs. Although both these methods are useful indicators of the suitability of ^{111}In -mAbMB-SPIONs for SPECT imaging, they do not provide direct evidence of γ -scintigraphy. Also the amount of activity administered (740 kBq) was much less than would be required for SPECT imaging. By further optimizing the amount of ^{111}In -mAbMB conjugated to SPIONs, it is possible to attain activity amounts suitable for imaging without increasing the administered dose of Fe. In addition, strategies for achieving a higher concentration of the dual modality probe also need to be considered. Promising in this regard are particles with diameters of 10–40 nm, including ultra-small SPIO or monocrystalline SPIO, due to their prolonged blood circulation time and ability to cross capillary walls [211,305].

5.5. Conclusions

The work in this dissertation demonstrates for the first time successful SPECT imaging of mesothelin expressing cancers using radiolabelled antibodies. We evaluated the characteristics of the two anti-mesothelin antibodies mAbMB and mAbK1 using *in vitro* and *in vivo* methods for use as imaging probes for mesothelin expressing cancers. Our studies provide evidence that ^{111}In -mAbMB is a better choice than ^{111}In -mAbK1 for imaging mesothelin expression in tumours. However, we also observed high localization of ^{111}In -mAbMB in the spleen, which suggests a role of circulating mesothelin antigen in forming immune complexes with ^{111}In -mAbMB. While ^{111}In -mAbMB due to its molecular specificity is promising for the detection of

mesothelin expressing cancers, its non-specific uptake in spleen needs to be better understood and addressed. When fully optimized, ^{111}In -mAbMB will be useful as a γ -emitting radiopharmaceutical for detection, treatment planning and monitoring of mesothelioma, pancreatic and ovarian cancers. Moreover, mesothelin targeting with therapeutic radioisotopes such as ^{90}Y , ^{188}Re , and ^{131}I can potentially be useful for radioimmunotherapy [282]. Studies with NCI-H226 cell line as a mesothelin expressing cell model revealed insufficient expression of mesothelin and therefore it can be concluded that NCI-H226 cells are not useful for pre-clinical developmental research of mesothelin targeted agents. Moreover, we observed that anti-mesothelin mAbK1 has a low affinity towards mesothelin and therefore is not an appropriate choice for the development as an imaging bioprobe for mesothelin expressing cancers. We also demonstrated for the first time the $^{99\text{m}}\text{Tc}$ ($[\text{}^{99\text{m}}\text{Tc}(\text{CO})_3]^+$) labelling of fab and f(ab)_2 fragments of the anti-mesothelin antibody mAbK1 using a histidine-modified tridentate ligand. However, these bioconjugates also had low affinity towards mesothelin (due to low affinity mAbK1). The dual-modality imaging bioprobe developed by conjugating ^{111}In -mAbMB with SPIONs demonstrated specific targeting and imaging capability in A431K5 tumour bearing mice. The high relaxivity and specific targeting of the bioprobes resulted in enhanced MR contrast effect in mesothelin positive tumours compared to mesothelin negative tumours. Covalently bound ^{111}In , acted as a SPECT detection motif and was used to provide proof of principle by autoradiography and biodistribution studies.

The data presented in this dissertation contributes significantly to our knowledge of the cell lines and antibodies required for pre-clinical development of molecular bioprobes for imaging mesothelin. The prototype radiopharmaceutical ^{111}In -mAbMB developed in this work especially holds promise to be developed into an imaging bioprobe for clinical use. In addition, the developed dual-modality imaging bioprobe may be beneficial in improving the imaging

outcomes of these difficult to treat tumours. In conclusion, molecular imaging agents targeting mesothelin certainly have a role to play for detection and monitoring of mesothelin expressing cancers.

BIBLIOGRAPHY

- [1] Goldenberg DM, DeLand F, et al. (1978). *Use of radiolabeled antibodies to carcinoembryonic antigen for the detection and localization of diverse cancers by external photoscanning*. N Engl J Med **298**, 1384-1386.
- [2] Goldenberg DM, Griffiths GL (1992). *Editorial: Radioimmunotherapy of cancer: Arming the missiles*. J Nucl Med **33(6)**, 1110-1112.
- [3] Goldenberg DM (2002). *Targeted therapy of cancer with radiolabeled antibodies*. J Nucl Med **43**, 693-713.
- [4] Baio G, Fabbi M, et al. (2010). *Two-step in vivo tumor targeting by biotin-conjugated antibodies and superparamagnetic nanoparticles assessed by magnetic resonance imaging at 1.5 T*. Mol Imaging Biol **12**, 305-15.
- [5] Gao X, Cui Y, et al. (2004). *In vivo cancer targeting and imaging with semiconductor quantum dots*. Nat Biotechnol **22**, 969-76.
- [6] Sharkey RM, Goldenberg DM (2005). *Perspectives on cancer therapy with radiolabeled monoclonal antibodies*. J Nucl Med **46 Suppl 1**, 115S-27S.
- [7] Moffat FL, Jr., Pinsky CM, et al. (1996). *Clinical utility of external immunoscintigraphy with the IMMU-4 technetium-99m Fab' antibody fragment in patients undergoing surgery for carcinoma of the colon and rectum: results of a pivotal, phase III trial. The Immunomedics Study Group*. J Clin Oncol **14**, 2295-305.
- [8] Sodee DB, Ellis RJ, et al. (1998). *Prostate cancer and prostate bed SPECT imaging with ProstaScint: semiquantitative correlation with prostatic biopsy results*. Prostate **37**, 140-8.
- [9] Cerdan S, Lotscher HR, et al. (1989). *Monoclonal antibody-coated magnetite particles as contrast agents in magnetic resonance imaging of tumors*. Magn Reson Med **12**, 151-63.
- [10] Artemov D, Mori N, et al. (2003). *MR molecular imaging of the Her-2/neu receptor in breast cancer cells using targeted iron oxide nanoparticles*. Magn Reson Med **49**, 403-8.
- [11] Argani P, Iacobuzio-Donahue C, et al. (2001). *Mesothelin is overexpressed in the vast majority of ductal adenocarcinomas of the pancreas: identification of a new pancreatic cancer marker by serial analysis of gene expression (SAGE)*. Clin Cancer Res **7**, 3862-3868.

- [12] Muminova ZE, Strong TV, Shaw DR (2004). *Characterization of human mesothelin transcripts in ovarian and pancreatic cancer*. BMC Cancer **4**, 19.
- [13] Swierczynski SL, Maitra A, et al. (2004). *Analysis of novel tumor markers in pancreatic and biliary carcinomas using tissue microarrays*. Hum Pathol **35**, 357-366.
- [14] Yokokawa J, Palena C, et al. (2005). *Identification of novel human CTL epitopes and their agonist epitopes of mesothelin*. Clin Cancer Res **11**, 6342-6351.
- [15] Watanabe H, Okada G, et al. (2005). *Expression of mesothelin mRNA in pure pancreatic juice from patients with pancreatic carcinoma, intraductal papillary mucinous neoplasm of the pancreas, and chronic pancreatitis*. Pancreas **30**, 349-354.
- [16] Hassan R, Laszik ZG, et al. (2005). *Mesothelin is overexpressed in pancreaticobiliary adenocarcinomas but not in normal pancreas and chronic pancreatitis*. Am J Clin Pathol **124**, 838-845.
- [17] Ordonez NG (2003). *Value of mesothelin immunostaining in the diagnosis of mesothelioma*. Mod Pathol **16**, 192-197.
- [18] Hassan R, Kreitman RJ, et al. (2005). *Localization of mesothelin in epithelial ovarian cancer*. Appl Immunohistochem Mol Morphol **13**, 243-247.
- [19] Robinson BW, Lake RA (2005). *Advances in malignant mesothelioma*. N Engl J Med **353**, 1591-603.
- [20] Robinson BW, Musk AW, Lake RA (2005). *Malignant mesothelioma*. Lancet **366**, 397-408.
- [21] Moore RG, Maclaughlan S (2010). *Current clinical use of biomarkers for epithelial ovarian cancer*. Curr Opin Oncol **22**, 492-7.
- [22] Kazan-Allen L (2005). *Asbestos and mesothelioma: worldwide trends*. Lung Cancer **49 Suppl 1**, S3-8.
- [23] Marrett LD, Ellison LF, Dryer D (2008). *Canadian cancer statistics at a glance: mesothelioma*. Canadian Medical Association Journal **178**, 677-678.
- [24] Lee CW, Martin J, et al. (2008). *Malignant mesothelioma: Canadian perspective and research directions*. Current Oncology **15**, 104-111.

- [25] Antman K, Hassan R, et al. (2005). *Update on malignant mesothelioma*. *Oncology (Williston Park)* **19**, 1301-9; discussion 1309-10, 1313-6.
- [26] Gold DV, Modrak DE, et al. (2004). *Combined ⁹⁰Yttrium-DOTA-labeled PAM4 antibody radioimmunotherapy and gemcitabine radiosensitization for the treatment of a human pancreatic cancer xenograft*. *Int J Cancer* **109**, 618-626.
- [27] Goel A, Batra SK (2001). *Antibody constructs for radioimmunodiagnosis and treatment of human pancreatic cancer*. *Teratog Carcinog Mutagen* **21**, 45-57.
- [28] Patz EF, Jr., Rusch VW, Heelan R (1996). *The proposed new international TNM staging system for malignant pleural mesothelioma: application to imaging*. *AJR Am J Roentgenol* **166**, 323-7.
- [29] Benamore RE, O'Doherty M J, Entwisle JJ (2005). *Use of imaging in the management of malignant pleural mesothelioma*. *Clin Radiol* **60**, 1237-1247.
- [30] West SD, Lee YC (2006). *Management of malignant pleural mesothelioma*. *Clin Chest Med* **27**, 335-54.
- [31] Renshaw AA, Dean BR, et al. (1997). *The role of cytologic evaluation of pleural fluid in the diagnosis of malignant mesothelioma*. *Chest* **111**, 106-9.
- [32] Boutin C, Rey F, et al. (1993). *Thoracoscopy in pleural malignant mesothelioma: a prospective study of 188 consecutive patients. Part 2: Prognosis and staging*. *Cancer* **72**, 394-404.
- [33] Belli C, Anand S, et al. (2010). *Translational therapies for malignant pleural mesothelioma*. *Expert Rev Respir Med* **4**, 249-60.
- [34] Martino D, Pass HI (2004). *Integration of multimodality approaches in the management of malignant pleural mesothelioma*. *Clin Lung Cancer* **5**, 290-8.
- [35] Stermann DH, Albelda SM (2005). *Advances in the diagnosis, evaluation, and management of malignant pleural mesothelioma*. *Respirology* **10**, 266-83.
- [36] Byrne M, Hillerdal G (2005). *Imaging, staging and response evaluation*. *Lung Cancer* **49 Suppl 1**, S25-6.

- [37] Truong MT, Marom EM, Erasmus JJ (2006). *Preoperative evaluation of patients with malignant pleural mesothelioma: role of integrated CT-PET imaging*. J Thorac Imaging **21**, 146-53.
- [38] Steinert HC, Santos Dellea MM, et al. (2005). *Therapy response evaluation in malignant pleural mesothelioma with integrated PET-CT imaging*. Lung Cancer **49 Suppl 1**, S33-5.
- [39] Boiselle PM, Patz EF, Jr., et al. (1998). *Imaging of mediastinal lymph nodes: CT, MR, and FDG PET*. Radiographics **18**, 1061-9.
- [40] Evans AL, Gleeson FV (2004). *Radiology in pleural disease: state of the art*. Respirology **9**, 300-12.
- [41] Jemal A, Siegel R, et al. (2010). *Cancer statistics, 2010*. CA Cancer J Clin **60**, 277-300.
- [42] New Drug Combo Improves Outcome of Advanced Pancreatic Cancer (http://www.cancer.org/docroot/NWS/content/NWS_1_1x_New_Drug_Combos_Improve_Outcome_of_Advanced_Pancreatic_Cancer.asp); (accessed August 2006).
- [43] Yeo CJ, Cameron JL, et al. (1997). *Six hundred fifty consecutive pancreaticoduodenectomies in the 1990s: pathology, complications, and outcomes*. Ann Surg **226**, 248-57; discussion 257-60.
- [44] Decker GA, Batheja MJ, et al. *Risk factors for pancreatic adenocarcinoma and prospects for screening*. Gastroenterol Hepatol (N Y) **6**, 246-54.
- [45] Korner M, Hayes GM, et al. (2005). *Secretin receptors in normal and diseased human pancreas: marked reduction of receptor binding in ductal neoplasia*. Am J Pathol **167**, 959-68.
- [46] Jensen RT, Wank SA, et al. (1989). *Interaction of CCK with pancreatic acinar cells*. Trends Pharmacol Sci **10**, 418-23.
- [47] Nock B, Nikolopoulou A, et al. (2003). *[^{99m}Tc]Demobesin 1, a novel potent bombesin analogue for GRP receptor-targeted tumour imaging*. Eur J Nucl Med Mol Imaging **30**, 247-258.
- [48] Pakzad F, Groves AM, Ell PJ (2006). *The role of positron emission tomography in the management of pancreatic cancer*. Semin Nucl Med **36**, 248-56.

- [49] Elsayes KM, Narra VR, et al. (2006). *Pancreatic tumors: diagnostic patterns by 3D gradient-echo post contrast magnetic resonance imaging with pathologic correlation*. *Curr Probl Diagn Radiol* **35**, 125-39.
- [50] Bast RC, Jr., Hennessy B, Mills GB (2009). *The biology of ovarian cancer: new opportunities for translation*. *Nat Rev Cancer* **9**, 415-28.
- [51] Bjorge T, Engeland A, et al. (1998). *Prognosis of 2,800 patients with epithelial ovarian cancer diagnosed during 1975-94 and treated at the Norwegian Radium Hospital*. *Acta Obstet Gynecol Scand* **77**, 777-81.
- [52] Brun JL, Feyler A, et al. (2000). *Long-term results and prognostic factors in patients with epithelial ovarian cancer*. *Gynecol Oncol* **78**, 21-7.
- [53] Ozols RF (2005). *Treatment goals in ovarian cancer*. *Int J Gynecol Cancer* **15 Suppl 1**, 3-11.
- [54] Holschneider CH, Berek JS (2000). *Ovarian cancer: epidemiology, biology, and prognostic factors*. *Semin Surg Oncol* **19**, 3-10.
- [55] Shaaban A, Rezvani M (2009). *Ovarian cancer: detection and radiologic staging*. *Clin Obstet Gynecol* **52**, 73-93.
- [56] Amendola MA, Walsh JW, et al. (1981). *Computed tomography in the evaluation of carcinoma of the ovary*. *J Comput Assist Tomogr* **5**, 179-86.
- [57] Buy JN, Ghossain MA, et al. (1991). *Epithelial tumors of the ovary: CT findings and correlation with US*. *Radiology* **178**, 811-8.
- [58] Buy JN, Moss AA, et al. (1988). *Peritoneal implants from ovarian tumors: CT findings*. *Radiology* **169**, 691-4.
- [59] Javitt MC (2007). *ACR Appropriateness Criteria on staging and follow-up of ovarian cancer*. *J Am Coll Radiol* **4**, 586-9.
- [60] Belmar C, So PW, et al. (2007). *Non-invasive genetic imaging for molecular and cell therapies of cancer*. *Clin Transl Oncol* **9**, 703-14.
- [61] Manning HC, Goebel T, et al. (2004). *Targeted molecular imaging agents for cellular-scale bimodal imaging*. *Bioconjug Chem* **15**, 1488-95.

- [62] Piwnica-Worms DR (2004). *Introduction to molecular imaging*. J Am Coll Radiol **1**, 2-3.
- [63] Riedel C, Dohan O, et al. (2001). *Journey of the iodide transporter NIS: from its molecular identification to its clinical role in cancer*. Trends Biochem Sci **26**, 490-6.
- [64] Kubota K, Yamada S, et al. (1996). *PET imaging of primary mediastinal tumours*. Br J Cancer **73**, 882-6.
- [65] Thakur ML (2009). *Genomic biomarkers for molecular imaging: predicting the future*. Semin Nucl Med **39**, 236-46.
- [66] Mishani E, Hagooley A (2009). *Strategies for molecular imaging of epidermal growth factor receptor tyrosine kinase in cancer*. J Nucl Med **50**, 1199-202.
- [67] Dobrucki LW, de Muinck ED, et al. (2010). *Approaches to multimodality imaging of angiogenesis*. J Nucl Med **51 Suppl 1**, 66S-79S.
- [68] Dunn BK, Wagner PD, et al. (2010). *Molecular markers for early detection*. Semin Oncol **37**, 224-42.
- [69] van Persijn van Meerten EL, Gelderblom H, Bloem JL (2010). *RECIST revised: implications for the radiologist. A review article on the modified RECIST guideline*. Eur Radiol **20**, 1456-67.
- [70] Borsook D, Beccera LR, et al. (2009). *Molecular Imaging: Basic Approaches*. Imaging in CNS Drug Discovery and Development. Springer New York, 105-119.
- [71] Wagner S, Breyholz HJ, et al. (2006). *Molecular imaging of matrix metalloproteinases in vivo using small molecule inhibitors for SPECT and PET*. Curr Med Chem **13**, 2819-38.
- [72] Dobrucki LW, Sinusas AJ (2010). *PET and SPECT in cardiovascular molecular imaging*. Nat Rev Cardiol **7**, 38-47.
- [73] Sharkey RM, Karacay H, et al. (2008). *Metastatic human colonic carcinoma: molecular imaging with pretargeted SPECT and PET in a mouse model*. Radiology **246**, 497-507.
- [74] Gerasimou GP, Aggelopoulou TC, et al. (2006). *Molecular imaging (SPECT and PET) in the evaluation of patients with movement disorders*. Nucl Med Rev Cent East Eur **9**, 147-53.

- [75] Cook GJ (2003). *Oncological molecular imaging: nuclear medicine techniques*. Br J Radiol **76 Spec No 2**, S152-8.
- [76] Jia F, Figueroa SD, et al. (2008). *Molecular imaging of bcl-2 expression in small lymphocytic lymphoma using ¹¹¹In-labeled PNA-peptide conjugates*. J Nucl Med **49**, 430-8.
- [77] Gabriel M, Decristoforo C, et al. (2007). *⁶⁸Ga-DOTA-Tyr3-octreotide PET in neuroendocrine tumors: comparison with somatostatin receptor scintigraphy and CT*. J Nucl Med **48**, 508-18.
- [78] Ilovich O, Jacobson O, et al. (2008). *Formation of fluorine-18 labeled diaryl ureas--labeled VEGFR-2/PDGFR dual inhibitors as molecular imaging agents for angiogenesis*. Bioorg Med Chem **16**, 4242-51.
- [79] Luker GD, Fracasso PM, et al. (1997). *Modulation of the multidrug resistance P-glycoprotein: detection with technetium-99m-sestamibi in vivo*. J Nucl Med **38**, 369-72.
- [80] Marriott CJ, Cadorette JE, et al. (1994). *High-resolution PET imaging and quantitation of pharmaceutical biodistributions in a small animal using avalanche photodiode detectors*. J Nucl Med **35**, 1390-6.
- [81] Grigsby PW, Malyapa RS, et al. (2007). *Comparison of molecular markers of hypoxia and imaging with (60)Cu-ATSM in cancer of the uterine cervix*. Mol Imaging Biol **9**, 278-83.
- [82] Bowen ML, Orvig C (2008). *^{99m}Technetium carbohydrate conjugates as potential agents in molecular imaging*. Chem Commun (Camb), 5077-91.
- [83] Shapiro EM, Skrtic S, et al. (2004). *MRI detection of single particles for cellular imaging*. Proc Natl Acad Sci U S A **101**, 10901-6.
- [84] Gallagher FA (2010). *An introduction to functional and molecular imaging with MRI*. Clin Radiol **65**, 557-66.
- [85] Dafni H, Landsman L, et al. (2002). *MRI and fluorescence microscopy of the acute vascular response to VEGF165: vasodilation, hyper-permeability and lymphatic uptake, followed by rapid inactivation of the growth factor*. NMR Biomed **15**, 120-31.
- [86] Weissleder R, Moore A, et al. (2000). *In vivo magnetic resonance imaging of transgene expression*. Nat Med **6**, 351-5.

- [87] Dodd SJ, Williams M, et al. (1999). *Detection of single mammalian cells by high-resolution magnetic resonance imaging*. *Biophys J* **76**, 103-9.
- [88] Shah K, Weissleder R (2005). *Molecular optical imaging: applications leading to the development of present day therapeutics*. *NeuroRx* **2**, 215-25.
- [89] Sheth RA, Mahmood U (2010). *Optical Molecular Imaging and its Emerging Role in Colorectal Cancer*. *Am J Physiol Gastrointest Liver Physiol*
- [90] Chernomordik V, Hassan M, et al. (2010). *Quantitative Analysis Of Her2 Receptor Expression In Vivo By Near-infrared Optical Imaging*. *Mol Imaging* **9**, 192-200.
- [91] van Zanten TS, Lopez-Bosque MJ, Garcia-Parajo MF (2010). *Imaging individual proteins and nanodomains on intact cell membranes with a probe-based optical antenna*. *Small* **6**, 270-5.
- [92] Umezawa Y (2005). *Genetically encoded optical probes for imaging cellular signaling pathways*. *Biosens Bioelectron* **20**, 2504-11.
- [93] Douma K, Prinzen L, et al. (2009). *Nanoparticles for optical molecular imaging of atherosclerosis*. *Small* **5**, 544-57.
- [94] Qin C, Zhu S, Tian J (2010). *New Optical Molecular Imaging Systems*. *Curr Pharm Biotechnol*
- [95] Jennings LE, Long NJ (2009). *'Two is better than one'--probes for dual-modality molecular imaging*. *Chem Commun (Camb)*, 3511-24.
- [96] Zhou SA, Brahme A (2010). *Development of high-resolution molecular phase-contrast stereoscopic X-ray imaging for accurate cancer diagnostics*. *Radiat Prot Dosimetry* **139**, 334-8.
- [97] Chang K, Pastan I (1996). *Molecular cloning of mesothelin, a differentiation antigen present on mesothelium, mesotheliomas, and ovarian cancers*. *Proc Natl Acad Sci U S A* **93**, 136-40.
- [98] Hassan R, Bera T, Pastan I (2004). *Mesothelin: a new target for immunotherapy*. *Clin Cancer Res* **10**, 3937-3942.

- [99] Onda M, Nagata S, et al. (2006). *Megakaryocyte potentiation factor cleaved from mesothelin precursor is a useful tumor marker in the serum of patients with mesothelioma*. Clin Cancer Res **12**, 4225-31.
- [100] Scholler N, Fu N, et al. (1999). *Soluble member(s) of the mesothelin/megakaryocyte potentiating factor family are detectable in sera from patients with ovarian carcinoma*. Proc Natl Acad Sci U S A **96**, 11531-6.
- [101] Robinson BW, Creaney J, et al. (2003). *Mesothelin-family proteins and diagnosis of mesothelioma*. Lancet **362**, 1612-6.
- [102] Hassan R, Ho M (2008). *Mesothelin targeted cancer immunotherapy*. European Journal of Cancer **44**, 46-53.
- [103] Shaw DR, Muminova ZE, Strong TV (2004). *Mesothelin: a new target for immunotherapy*. Clin Cancer Res **10**, 8751; author reply 8752.
- [104] Kojima T, Oh-eda M, et al. (1995). *Molecular cloning and expression of megakaryocyte potentiating factor cDNA*. J Biol Chem **270**, 21984-90.
- [105] Bera TK, Pastan I (2000). *Mesothelin is not required for normal mouse development or reproduction*. Mol Cell Biol **20**, 2902-2906.
- [106] Rump A, Morikawa Y, et al. (2004). *Binding of ovarian cancer antigen CA125/MUC16 to mesothelin mediates cell adhesion*. J Biol Chem **279**, 9190-8.
- [107] Scholler N, Garvik B, et al. (2007). *Development of a CA125-mesothelin cell adhesion assay as a screening tool for biologics discovery*. Cancer Lett **247**, 130-136.
- [108] Gubbels JA, Belisle J, et al. (2006). *Mesothelin-MUC16 binding is a high affinity, N-glycan dependent interaction that facilitates peritoneal metastasis of ovarian tumors*. Mol Cancer **5**, 50.
- [109] Kaneko O, Gong L, et al. (2009). *A binding domain on mesothelin for CA125/MUC16*. J Biol Chem **284**, 3739-49.
- [110] Hassan R, Schweizer C, et al. (2010). *Inhibition of mesothelin-CA-125 interaction in patients with mesothelioma by the anti-mesothelin monoclonal antibody MORAb-009: Implications for cancer therapy*. Lung Cancer **68**, 455-9.

- [111] Cheng WF, Huang CY, et al. (2009). *High mesothelin correlates with chemoresistance and poor survival in epithelial ovarian carcinoma*. Br J Cancer **100**, 1144-53.
- [112] Bharadwaj U, Li M, et al. (2008). *Mesothelin-induced pancreatic cancer cell proliferation involves alteration of cyclin E via activation of signal transducer and activator of transcription protein 3*. Mol Cancer Res **6**, 1755-65.
- [113] Chang MC, Chen CA, et al. (2009). *Mesothelin inhibits paclitaxel-induced apoptosis through the PI3K pathway*. Biochem J **424**, 449-58.
- [114] Uehara N, Matsuoka Y, Tsubura A (2008). *Mesothelin promotes anchorage-independent growth and prevents anoikis via extracellular signal-regulated kinase signaling pathway in human breast cancer cells*. Mol Cancer Res **6**, 186-93.
- [115] Mesothelioma diagnosis questions (<http://www.mesotheliomaweb.org/doctor-patient.htm>); (accessed July 2006).
- [116] Miettinen M, Sarlomo-Rikala M (2003). *Expression of calretinin, thrombomodulin, keratin 5, and mesothelin in lung carcinomas of different types: an immunohistochemical analysis of 596 tumors in comparison with epithelioid mesotheliomas of the pleura*. Am J Surg Pathol **27**, 150-158.
- [117] Yaziji H, Battifora H, et al. (2006). *Evaluation of 12 antibodies for distinguishing epithelioid mesothelioma from adenocarcinoma: identification of a three-antibody immunohistochemical panel with maximal sensitivity and specificity*. Mod Pathol **19**, 514-23.
- [118] Kachali C, Eltoum I, et al. (2006). *Use of mesothelin as a marker for mesothelial cells in cytologic specimens*. Semin Diagn Pathol **23**, 20-4.
- [119] Jhala N, Jhala D, et al. (2006). *Biomarkers in Diagnosis of pancreatic carcinoma in fine-needle aspirates*. Am J Clin Pathol **126**, 572-9.
- [120] Chen Y, Zheng B, et al. (2007). *Accurate discrimination of pancreatic ductal adenocarcinoma and chronic pancreatitis using multimarker expression data and samples obtained by minimally invasive fine needle aspiration*. Int J Cancer **120**, 1511-7.
- [121] Baruch AC, Wang H, et al. (2007). *Immunocytochemical study of the expression of mesothelin in fine-needle aspiration biopsy specimens of pancreatic adenocarcinoma*. Diagn Cytopathol **35**, 143-7.

- [122] Li M, Bharadwaj U, et al. (2008). *Mesothelin is a malignant factor and therapeutic vaccine target for pancreatic cancer*. *Mol Cancer Ther* **7**, 286-96.
- [123] Showalter SL, Huang YH, et al. (2008). *Nanoparticulate delivery of diphtheria toxin DNA effectively kills Mesothelin expressing pancreatic cancer cells*. *Cancer Biol Ther* **7**, 1584-90.
- [124] Frierson HF, Jr., Moskaluk CA, et al. (2003). *Large-scale molecular and tissue microarray analysis of mesothelin expression in common human carcinomas*. *Hum Pathol* **34**, 605-609.
- [125] Chang K, Pastan I, Willingham MC (1992). *Isolation and characterization of a monoclonal antibody, K1, reactive with ovarian cancers and normal mesothelium*. *Int J Cancer* **50**, 373-381.
- [126] Ordonez NG (2003). *Application of mesothelin immunostaining in tumor diagnosis*. *Am J Surg Pathol* **27**, 1418-1428.
- [127] Huang CY, Cheng WF, et al. (2006). *Serum mesothelin in epithelial ovarian carcinoma: a new screening marker and prognostic factor*. *Anticancer Res* **26**, 4721-8.
- [128] Abdel-Azeez HA, Labib HA, et al. (2010). *HE4 and mesothelin: novel biomarkers of ovarian carcinoma in patients with pelvic masses*. *Asian Pac J Cancer Prev* **11**, 111-6.
- [129] Linkov F, Lisovich A, et al. (2007). *Early detection of head and neck cancer: development of a novel screening tool using multiplexed immunobead-based biomarker profiling*. *Cancer Epidemiol Biomarkers Prev* **16**, 102-7.
- [130] Hellstrom I, Raycraft J, et al. (2006). *Mesothelin variant 1 is released from tumor cells as a diagnostic marker*. *Cancer Epidemiol Biomarkers Prev* **15**, 1014-1020.
- [131] Robinson BW, Creaney J, et al. (2005). *Soluble mesothelin-related protein--a blood test for mesothelioma*. *Lung Cancer* **49 Suppl 1**, S109-11.
- [132] Creaney J, Robinson BW (2005). *Detection of malignant mesothelioma in asbestos-exposed individuals: the potential role of soluble mesothelin-related protein*. *Hematol Oncol Clin North Am* **19**, 1025-40, v.
- [133] Weber DG, Taeger D, et al. (2007). *Soluble mesothelin-related peptides (SMRP) - high stability of a potential tumor marker for mesothelioma*. *Cancer Biomark* **3**, 287-92.

- [134] Azim HA, Jr., Gaafar R, et al. (2008). *Soluble mesothelin-related protein in malignant pleural mesothelioma*. J Egypt Natl Canc Inst **20**, 224-9.
- [135] Schneider J, Hoffmann H, et al. (2008). *Diagnostic and prognostic value of soluble mesothelin-related proteins in patients with malignant pleural mesothelioma in comparison with benign asbestosis and lung cancer*. J Thorac Oncol **3**, 1317-24.
- [136] Hellstrom I, Hellstrom KE (2008). *SMRP and HE4 as biomarkers for ovarian carcinoma when used alone and in combination with CA125 and/or each other*. Adv Exp Med Biol **622**, 15-21.
- [137] Rodriguez JA, Li M, et al. (2005). *Gene overexpression in pancreatic adenocarcinoma: diagnostic and therapeutic implications*. World J Surg **29**, 297-305.
- [138] Scherpereel A, Lee YC (2007). *Biomarkers for mesothelioma*. Curr Opin Pulm Med **13**, 339-443.
- [139] Beyer HL, Geschwindt RD, et al. (2007). *MESOMARK: a potential test for malignant pleural mesothelioma*. Clin Chem **53**, 666-72.
- [140] Roe OD, Creaney J, et al. (2008). *Mesothelin-related predictive and prognostic factors in malignant mesothelioma: a nested case-control study*. Lung Cancer **61**, 235-43.
- [141] Tajima K, Hiramama M, et al. (2008). *ERC/mesothelin as a marker for chemotherapeutic response in patients with mesothelioma*. Anticancer Res **28**, 3933-6.
- [142] Hassan R, Bullock S, et al. (2007). *Phase I study of SS1P, a recombinant anti-mesothelin immunotoxin given as a bolus I.V. infusion to patients with mesothelin-expressing mesothelioma, ovarian, and pancreatic cancers*. Clin Cancer Res **13**, 5144-9.
- [143] Hassan R, Ebel W, et al. (2007). *Preclinical evaluation of MORAb-009, a chimeric antibody targeting tumor-associated mesothelin*. Cancer Immun **7**, 20.
- [144] Brockstedt DG, Leong M, et al. (2005). *Recombinant listeria monocytogenes-based immunotherapy targeting mesothelin for the treatment of pancreatic and ovarian cancer*. AACR Meeting Abstracts **2005**, 1418-.
- [145] Zhang Y, Xiang L, et al. (2006). *Synergistic antitumor activity of taxol and immunotoxin SS1P in tumor-bearing mice*. Clin Cancer Res **12**, 4695-701.

- [146] Zhang Y, Xiang L, et al. (2007). *Immunotoxin and Taxol synergy results from a decrease in shed mesothelin levels in the extracellular space of tumors*. Proc Natl Acad Sci U S A **104**, 17099-104.
- [147] Thomas AM, Santarsiero LM, et al. (2004). *Mesothelin-specific CD8(+) T cell responses provide evidence of in vivo cross-priming by antigen-presenting cells in vaccinated pancreatic cancer patients*. J Exp Med **200**, 297-306.
- [148] Huang YH, Zugates GT, et al. (2009). *Nanoparticle-delivered suicide gene therapy effectively reduces ovarian tumor burden in mice*. Cancer Res **69**, 6184-91.
- [149] Hung CF, Calizo R, et al. (2007). *A DNA vaccine encoding a single-chain trimer of HLA-A2 linked to human mesothelin peptide generates anti-tumor effects against human mesothelin-expressing tumors*. Vaccine **25**, 127-35.
- [150] Chang CL, Wu TC, Hung CF (2007). *Control of human mesothelin-expressing tumors by DNA vaccines*. Gene Ther **14**, 1189-98.
- [151] Breidenbach M, Rein DT, et al. (2005). *Mesothelin-mediated targeting of adenoviral vectors for ovarian cancer gene therapy*. Gene Ther **12**, 187-93.
- [152] Ho M, Feng M, et al. (2010). *A novel high affinity human monoclonal antibody to mesothelin*. Int J Cancer
- [153] Inami K, Abe M, et al. (2009). *Antitumor activity of anti-C-ERC/mesothelin monoclonal antibody in vivo*. Cancer Sci
- [154] Feng Y, Xiao X, et al. (2009). *A novel human monoclonal antibody that binds with high affinity to mesothelin-expressing cells and kills them by antibody-dependent cell-mediated cytotoxicity*. Mol Cancer Ther
- [155] Li Q, Verschraegen CF, et al. (2004). *Cytotoxic activity of the recombinant anti-mesothelin immunotoxin, SS1(dsFv)PE38, towards tumor cell lines established from ascites of patients with peritoneal mesotheliomas*. Anticancer Res **24**, 1327-35.
- [156] Hassan R, Lerner MR, et al. (2002). *Antitumor activity of SS(dsFv)PE38 and SS1(dsFv)PE38, recombinant antimmesothelin immunotoxins against human gynecologic cancers grown in organotypic culture in vitro*. Clin Cancer Res **8**, 3520-3526.

- [157] Fan D, Yano S, et al. (2002). *Targeted therapy against human lung cancer in nude mice by high-affinity recombinant antimesothelin single-chain Fv immunotoxin*. *Mol Cancer Ther* **1**, 595-600.
- [158] Sato N, Hassan R, et al. (2005). *Pretargeted radioimmunotherapy of mesothelin-expressing cancer using a tetravalent single-chain Fv-streptavidin fusion protein*. *J Nucl Med* **46**, 1201-1209.
- [159] Hassan R, Viner JL, et al. (2000). *Anti-tumor activity of K1-LysPE38QQR, an immunotoxin targeting mesothelin, a cell-surface antigen overexpressed in ovarian cancer and malignant mesothelioma*. *J Immunother* **23**, 473-479.
- [160] Onda M, Willingham M, et al. (2005). *New monoclonal antibodies to mesothelin useful for immunohistochemistry, fluorescence-activated cell sorting, Western blotting, and ELISA*. *Clin Cancer Res* **11**, 5840-5846.
- [161] Chang K, Pastan I (1994). *Molecular cloning and expression of a cDNA encoding a protein detected by the K1 antibody from an ovarian carcinoma (OVCA-3) cell line*. *Int J Cancer* **57**, 90-7.
- [162] Brinkmann U, Webber K, et al. (1997). *Cloning and expression of the recombinant FAb fragment of monoclonal antibody K1 that reacts with mesothelin present on mesotheliomas and ovarian cancers*. *Int J Cancer* **71**, 638-44.
- [163] Chowdhury PS, Vasmatzis G, et al. (1998). *Improved stability and yield of a Fv-toxin fusion protein by computer design and protein engineering of the Fv*. *J Mol Biol* **281**, 917-28.
- [164] Hassan R, Wu C, et al. (1999). *¹¹¹Indium-labeled monoclonal antibody K1: biodistribution study in nude mice bearing a human carcinoma xenograft expressing mesothelin*. *Int J Cancer* **80**, 559-563.
- [165] Adsay NV, Basturk O, et al. (2005). *Ductal neoplasia of the pancreas: nosologic, clinicopathologic, and biologic aspects*. *Semin Radiat Oncol* **15**, 254-64.
- [166] Yoshida C, Sogawa C, et al. (2010). *Development of positron emission tomography imaging by ⁶⁴Cu-labeled Fab for detecting ERC/mesothelin in a mesothelioma mouse model*. *Nucl Med Commun* **31**, 380-388.
- [167] Pressman D, Keighley G (1948). *The zone of activity of antibodies as determined by the use of radioactive tracers; the zone of activity of nephritoxic ant kidney serum*. *J Immunol* **59**, 141-6.

- [168] Pressman D, Hill RF, Foote FW (1949). *The Zone of Localization of Anti-Mouse-Kidney Serum as Determined by Radioautographs*. Science **109**, 65-6.
- [169] Pressman D, Korngold L (1953). *The in vivo localization of anti-Wagner-osteogenic-sarcoma antibodies*. Cancer **6**, 619-23.
- [170] Mach JP, Carrel S, et al. (1974). *In vivo localisation of radiolabelled antibodies to carcinoembryonic antigen in human colon carcinoma grafted into nude mice*. Nature **248**, 704-6.
- [171] Goldenberg DM, Preston DF, et al. (1974). *Photoscan localization of GW-39 tumors in hamsters using radiolabeled anticarcinoembryonic antigen immunoglobulin G*. Cancer Res **34**, 1-9.
- [172] Dykes PW, Hine KR, et al. (1980). *Localisation of tumour deposits by external scanning after injection of radiolabelled anti-carcinoembryonic antigen*. Br Med J **280**, 220-2.
- [173] Kim EE, DeLand FH, et al. (1980). *Radioimmunodetection of cancer with radiolabeled antibodies to alpha-fetoprotein*. Cancer Res **40**, 3008-12.
- [174] Goldenberg DM, Kim EE, DeLand FH (1981). *Human chorionic gonadotropin radioantibodies in the radioimmunodetection of cancer and for disclosure of occult metastases*. Proc Natl Acad Sci U S A **78**, 7754-8.
- [175] Kohler G, Milstein C (1975). *Continuous cultures of fused cells secreting antibody of predefined specificity*. Nature **256**, 495-7.
- [176] Larson SM (1987). *Lymphoma, melanoma, colon cancer: diagnosis and treatment with radiolabeled monoclonal antibodies*. The 1986 Eugene P. Pendergrass New Horizons Lecture. Radiology **165**, 297-304.
- [177] Gasparini M, Bombardieri E, et al. (1995). *Clinical utility of radioimmunosintigraphy of non-Hodgkin's lymphoma with radiolabelled LL2 monoclonal antibody, LymphoSCAN: preliminary results*. Tumori **81**, 173-8.
- [178] Patt YZ, Podoloff DA, et al. (1994). *Technetium 99m-labeled IMMU-4, a monoclonal antibody against carcinoembryonic antigen, for imaging of occult recurrent colorectal cancer in patients with rising serum carcinoembryonic antigen levels*. J Clin Oncol **12**, 489-95.

- [179] Kelloff GJ, Krohn KA, et al. (2005). *The progress and promise of molecular imaging probes in oncologic drug development*. Clin Cancer Res **11**, 7967-7985.
- [180] Sodee DB, Nelson AD, et al. (2005). *Update on fused capromab pendetide imaging of prostate cancer*. Clin Prostate Cancer **3**, 230-8.
- [181] Petronis JD, Regan F, Lin K (1998). *Indium-111 capromab pendetide (ProstaScint) imaging to detect recurrent and metastatic prostate cancer*. Clin Nucl Med **23**, 672-7.
- [182] Breitz HB, Tyler A, et al. (1997). *Clinical experience with Tc-99m nofetumomab merpentan (Verluma) radioimmunoscinigraphy*. Clin Nucl Med **22**, 615-20.
- [183] Liu Y, Wu C (1991). *Radiolabeling of monoclonal antibodies with metal chelates*. Pure Appl Chem **63**, 427-463.
- [184] Mahmood A, Jones AG (2003). *Technetium radiopharmaceuticals*. In: Welch MJ, Redvanly CS (eds) Handbook of radiopharmaceuticals: radiochemistry and applications. John Wiley & Sons, West Sussex, 323-362.
- [185] Halpern SE (1986). *The advantages and limits of Indium-111 labeling of antibodies. Experimental studies and clinical applications*. Int J Rad Appl Instrum B **13**, 195-201.
- [186] Eckelman WC, Kilbourn MR, Mathis CA (2006). *Discussion of targeting proteins in vivo: in vitro guidelines*. Nucl Med Biol **33**, 449-451.
- [187] Behr TM, Becker WS, et al. (1995). *Comparison of complete versus fragmented technetium-99m-labeled anti-CEA monoclonal antibodies for immunoscintigraphy in colorectal cancer*. J Nucl Med **36**, 430-41.
- [188] Li L, Olafsen T, et al. (2002). *Reduction of kidney uptake in radiometal labeled peptide linkers conjugated to recombinant antibody fragments. Site-specific conjugation of DOTA-peptides to a Cys-diabody*. Bioconjug Chem **13**, 985-95.
- [189] Gangopadhyay A, Petrick AT, Thomas P (1996). *Modification of antibody isoelectric point affects biodistribution of ¹¹¹Indium-labeled antibody*. Nucl Med Biol **23**, 257-261.
- [190] ten Kate CI, Fischman AJ, et al. (1990). *Effect of isoelectric point on biodistribution and inflammation: imaging with indium-111-labelled IgG*. Eur J Nucl Med **17**, 305-309.

- [191] Carrasquillo JA, Abrams PG, et al. (1988). *Effect of antibody dose on the imaging and biodistribution of indium-111 9.2.27 anti-melanoma monoclonal antibody*. J Nucl Med **29**, 39-47.
- [192] Hamamura MJ, Ha S, et al. (2010). *Development of an MR-compatible SPECT system (MRSPECT) for simultaneous data acquisition*. Phys Med Biol **55**, 1563-75.
- [193] Catana C, Procissi D, et al. (2008). *Simultaneous in vivo positron emission tomography and magnetic resonance imaging*. Proc Natl Acad Sci U S A **105**, 3705-10.
- [194] Wehrl HF, Judenhofer MS, et al. (2009). *Pre-clinical PET/MR: technological advances and new perspectives in biomedical research*. Eur J Nucl Med Mol Imaging **36 Suppl 1**, S56-68.
- [195] Judenhofer MS, Wehrl HF, et al. (2008). *Simultaneous PET-MRI: a new approach for functional and morphological imaging*. Nat Med **14**, 459-65.
- [196] Boss A, Bisdas S, et al. (2010). *Hybrid PET/MRI of Intracranial Masses: Initial Experiences and Comparison to PET/CT*. J Nucl Med **51**, 1198-205.
- [197] Wagenaar DJ, Kapusta M, et al. (2006). *Rationale for the combination of nuclear medicine with magnetic resonance for pre-clinical imaging*. Technol Cancer Res Treat **5**, 343-50.
- [198] Laurent S, Forge D, et al. (2008). *Magnetic iron oxide nanoparticles: synthesis, stabilization, vectorization, physicochemical characterizations, and biological applications*. Chem Rev **108**, 2064-110.
- [199] Aime S, Nano R, Grandi M (1988). *A new class of contrast agents for magnetic resonance imaging based on selective reduction of water-T2 by chemical exchange*. Invest Radiol **23 Suppl 1**, S267-70.
- [200] Tanimoto A, Kuribayashi S (2006). *Application of superparamagnetic iron oxide to imaging of hepatocellular carcinoma*. Eur J Radiol **58**, 200-16.
- [201] Jain TK, Foy SP, et al. (2009). *Magnetic resonance imaging of multifunctional pluronic stabilized iron-oxide nanoparticles in tumor-bearing mice*. Biomaterials **30**, 6748-56.
- [202] Glaus C, Rossin R, et al. (2010). *In vivo evaluation of (64)Cu-labeled magnetic nanoparticles as a dual-modality PET/MR imaging agent*. Bioconjug Chem **21**, 715-22.

- [203] Kobukai S, Baheza R, et al. (2010). *Magnetic nanoparticles for imaging dendritic cells*. *Magn Reson Med* **63**, 1383-90.
- [204] Lind K, Kresse M, et al. (2002). *A novel formulation for superparamagnetic iron oxide (SPIO) particles enhancing MR lymphography: comparison of physicochemical properties and the in vivo behaviour*. *J Drug Target* **10**, 221-30.
- [205] Guardia P, Perez N, et al. (2010). *Controlled synthesis of iron oxide nanoparticles over a wide size range*. *Langmuir* **26**, 5843-7.
- [206] Wen G, Zhang XL, et al. (2002). *Superparamagnetic iron oxide (Feridex)-enhanced MRI in diagnosis of focal hepatic lesions*. *Di Yi Jun Yi Da Xue Xue Bao* **22**, 451-2.
- [207] Wang YX, Hussain SM, Krestin GP (2001). *Superparamagnetic iron oxide contrast agents: physicochemical characteristics and applications in MR imaging*. *Eur Radiol* **11**, 2319-31.
- [208] Kinoshita M, Yoshioka Y, et al. (2010). *MR molecular imaging of HER-2 in a murine tumor xenograft by SPIO labeling of anti-HER-2 affibody*. *Contrast Media Mol Imaging* **5**, 18-22.
- [209] Weissleder R, Kelly K, et al. (2005). *Cell-specific targeting of nanoparticles by multivalent attachment of small molecules*. *Nat Biotechnol* **23**, 1418-23.
- [210] Weissleder R, Lee AS, et al. (1991). *Polyclonal human immunoglobulin G labeled with polymeric iron oxide: antibody MR imaging*. *Radiology* **181**, 245-9.
- [211] Weissleder R, Lee AS, et al. (1992). *Antimyosin-labeled monocrystalline iron oxide allows detection of myocardial infarct: MR antibody imaging*. *Radiology* **182**, 381-5.
- [212] Lee JH, Sherlock SP, et al. (2009). *High-contrast in vivo visualization of microvessels using novel FeCo/GC magnetic nanocrystals*. *Magn Reson Med* **62**, 1497-509.
- [213] Yang H, Zhang C, et al. (2010). *Water-soluble superparamagnetic manganese ferrite nanoparticles for magnetic resonance imaging*. *Biomaterials* **31**, 3667-73.
- [214] Tromsdorf UI, Bigall NC, et al. (2007). *Size and surface effects on the MRI relaxivity of manganese ferrite nanoparticle contrast agents*. *Nano Lett* **7**, 2422-7.

- [215] Reilly RM (1993). *Immunoscintigraphy of tumours using ^{99m}Tc -labelled monoclonal antibodies: a review*. Nucl Med Commun **14**, 347-59.
- [216] Rhodes BA, Martinez-Duncker C (1990). *Direct labeling of antibodies with ^{99m}Tc* . Am Biotechnol Lab **8**, 50-3.
- [217] Franz J, Volkert WA, et al. (1987). *The production of ^{99m}Tc -labeled conjugated antibodies using a cyclam-based bifunctional chelating agent*. Int J Rad Appl Instrum B **14**, 569-72.
- [218] Alberto R, Schibli R, Egli A (2002). *Method for the preparation of facial metal tricarbonyl compounds and their use in the labelling of biologically active substrates*. U.S. Patent No. 6,344,178 B1
- [219] Bowen ML, Chen Z-F, et al. (2009). *Long-chain rhenium and technetium glucosamine conjugates*. Dalton Trans, 9228-9236.
- [220] Bowen ML, Lim NC, et al. (2009). *Glucosamine conjugates bearing N,N,O-donors: potential imaging agents utilizing the $[M(\text{CO})_3]^+$ core ($M = \text{Re}, \text{Tc}$)*. Dalton Trans, 9216-9227.
- [221] Stichelberger A, Waibel R, et al. (2003). *Versatile synthetic approach to new bifunctional chelating agents tailor made for labeling with the fac- $[M(\text{CO})_3]^+$ core ($M = \text{Tc}, ^{99m}\text{Tc}, \text{Re}$): synthesis, in vitro, and in vivo behavior of the model complex $[M(\text{APPA})(\text{CO})_3]$ (APPA = [(5-amino-pentyl)-pyridin-2-yl-methyl-amino]-acetic acid)*. Nucl Med Biol **30**, 465-70.
- [222] Maresca KP, Marquis JC, et al. (2010). *Novel polar single amino acid chelates for technetium-99m tricarbonyl-based radiopharmaceuticals with enhanced renal clearance: application to octreotide*. Bioconjug Chem **21**, 1032-42.
- [223] Chan C, Cai Z, et al. (2010). *^{111}In - or ^{99m}Tc -labeled recombinant VEGF bioconjugates: in vitro evaluation of their cytotoxicity on porcine aortic endothelial cells overexpressing Flt-1 receptors*. Nucl Med Biol **37**, 105-15.
- [224] Zobi F, Spingler B, et al. (2003). *Toward novel DNA binding metal complexes: structure and basic kinetic data of $[M(9\text{MeG})_2(\text{CH}_3\text{OH})(\text{CO})_3]^+$ ($M = ^{99m}\text{Tc}, \text{Re}$)*. Inorg Chem **42**, 2818-20.
- [225] Waibel R, Alberto R, et al. (1999). *Stable one-step technetium-99m labeling of His-tagged recombinant proteins with a novel Tc(I)-carbonyl complex*. Nat Biotechnol **17**, 897-901.

- [226] Huang L, Gainkam LO, et al. (2008). *SPECT imaging with ^{99m}Tc -labeled EGFR-specific nanobody for in vivo monitoring of EGFR expression*. *Mol Imaging Biol* **10**, 167-75.
- [227] Willuda J, Kubetzko S, et al. (2001). *Tumor targeting of mono-, di-, and tetravalent anti-p185(HER-2) miniantibodies multimerized by self-associating peptides*. *J Biol Chem* **276**, 14385-92.
- [228] Orlova A, Nilsson FY, et al. (2006). *Comparative in vivo evaluation of technetium and iodine labels on an anti-HER2 affibody for single-photon imaging of HER2 expression in tumors*. *J Nucl Med* **47**, 512-519.
- [229] Boucher Y, Baxter LT, Jain RK (1990). *Interstitial pressure gradients in tissue-isolated and subcutaneous tumors: implications for therapy*. *Cancer Res* **50**, 4478-84.
- [230] Rhodes BA (1991). *Direct labeling of proteins with ^{99m}Tc* . *Int J Rad Appl Instrum B* **18**, 667-676.
- [231] Mishra P, Singh AK, et al. (1994). *A novel method for labelling human immunoglobulin-G with ^{99m}Tc suitable for inflammation scintigraphy*. *Nucl Med Commun* **15**, 723-729.
- [232] Qi P, Muddukrishna SN, et al. (1996). *Direct ^{99m}Tc -labeling of antibodies by sodium dithionite reduction, and role of ascorbate as a stabilizer in cysteine challenge*. *Nucl Med Biol* **23**, 827-35.
- [233] Stopar TG, Mlinaric-Rascan I, et al. (2006). *^{99m}Tc -rituximab radiolabelled by photo-activation: a new non-Hodgkin's lymphoma imaging agent*. *Eur J Nucl Med Mol Imaging* **33**, 53-9.
- [234] Abramoff MD, Magelhaes PJ, Ram SJ (2004). *Image Processing with ImageJ*. *Biophotonics Int* **7**, 36-42.
- [235] Lindmo T, Boven E, et al. (1984). *Determination of the immunoreactive fraction of radiolabeled monoclonal antibodies by linear extrapolation to binding at infinite antigen excess*. *J Immunol Methods* **72**, 77-89.
- [236] McLarty K, Cornelissen B, et al. (2009). *Associations between the uptake of ^{111}In -DTPA-trastuzumab, HER2 density and response to trastuzumab (Herceptin) in athymic mice bearing subcutaneous human tumour xenografts*. *Eur J Nucl Med Mol Imaging* **36**, 81-93.

- [237] Rhodes BA, Torvestad DA, et al. (1982). *Tc-99m labeling and acceptance testing of radiolabeled antibodies and antibody fragments*. In: Burchiel SW, Rhodes BA (eds) *Tumor Imaging: The radiochemical detection of cancer*. Masson Publishing, New Mexico, 111-123.
- [238] Paik CH, Phan LN, et al. (1985). *The labeling of high affinity sites of antibodies with ^{99m}Tc* . *Int J Nucl Med Biol* **12**, 3-8.
- [239] Iznaga-Escobar N, Morales A, Nunez G (1996). *Micromethod for quantification of SH groups generated after reduction of monoclonal antibodies*. *Nucl Med Biol* **23**, 641-644.
- [240] Paik CH, Eckelman WC, Reba RC (1986). *Transchelation of ^{99m}Tc from low affinity sites to high affinity sites of antibody*. *Int J Rad Appl Instrum B* **13**, 359-62.
- [241] Rhodes BA, Zamora PO, et al. (1986). *Technetium-99m labeling of murine monoclonal antibody fragments*. *J Nucl Med* **27**, 685-693.
- [242] Elwell K, Howard CG (2001). *Chemically Modifying Antibodies*. In: G. HC, D. BR (eds) *Basic Methods in Antibody Production and Characterization*. CRC Press, Florida, 199-215.
- [243] Saatchi K, Hafeli UO (2009). *Radiolabeling of biodegradable polymeric microspheres with $[\text{}^{99m}\text{Tc}(\text{CO})_3]^+$ and in vivo biodistribution evaluation using MicroSPECT/CT imaging*. *Bioconjug Chem* **20**, 1209-17.
- [244] Saatchi K, Hafeli UO (2007). *One-pot syntheses, coordination, and characterization of application-specific biodegradable ligand-polymers*. *Dalton Trans*, 4439-45.
- [245] Schibli R (2007). *Technetium and Rhenium Tricarbonyl core*. In: Zolle I (ed) *Technetium-99m Pharmaceuticals: Preparation and Quality Control in Nuclear Medicine*. Springer Verlag, New York, 27-39.
- [246] Chen WJ, Yen CL, et al. (2008). *Direct ^{99m}Tc labeling of Herceptin (trastuzumab) by $^{99m}\text{Tc}(\text{I})$ tricarbonyl ion*. *Appl Radiat Isot* **66**, 340-345.
- [247] Orlova A, Nilsson FY, et al. (2006). *Comparative in vivo evaluation of technetium and iodine labels on an anti-HER2 antibody for single-photon imaging of HER2 expression in tumors*. *J Nucl Med* **47**, 512-519.
- [248] Scheck RA, Francis MB (2007). *Regioselective labeling of antibodies through N-terminal transamination*. *ACS Chem Biol* **2**, 247-251.

- [249] Reske SN, Vyska K, Feinendegen LE (1981). *In vivo assessment of phagocytic properties of Kupffer cells*. J Nucl Med **22**, 405-10.
- [250] Silverstein SC, Steinman RM, Cohn ZA (1977). *Endocytosis*. Annu Rev Biochem **46**, 669-722.
- [251] Helmy KY, Katschke KJ, Jr., et al. (2006). *CR1g: a macrophage complement receptor required for phagocytosis of circulating pathogens*. Cell **124**, 915-27.
- [252] Toth CA, Thomas P, et al. (1985). *Receptor-mediated endocytosis of carcinoembryonic antigen by rat liver Kupffer cells*. Cancer Res **45**, 392-7.
- [253] Orlova A, Magnusson M, et al. (2006). *Tumor imaging using a picomolar affinity HER2 binding affibody molecule*. Cancer Res **66**, 4339-48.
- [254] Rogers BE, Franano FN, et al. (1995). *Identification of metabolites of ¹¹¹In-diethylenetriaminepentaacetic acid-monoclonal antibodies and antibody fragments in vivo*. Cancer Res **55**, 5714s-5720s.
- [255] Tsai SW, Li L, et al. (2001). *Metabolism and renal clearance of ¹¹¹In-labeled DOTA-conjugated antibody fragments*. Bioconjug Chem **12**, 264-70.
- [256] Tang Y, Wang J, et al. (2005). *Imaging of HER2/neu-positive BT-474 human breast cancer xenografts in athymic mice using (111)In-trastuzumab (Herceptin) Fab fragments*. Nucl Med Biol **32**, 51-8.
- [257] Govindan SV, Goldenberg DM, et al. (1996). *Thiolations, ^{99m}Tc labelings, and animal in vivo biodistributions of divalent monoclonal antibody fragments*. Bioconjug Chem **7**, 290-7.
- [258] Griffiths GL, Goldenberg DM, et al. (1994). *Technetium-99m, Rhenium-186, and Rhenium-188 direct labeled antibodies*. Cancer **73**, 761-768.
- [259] Mather SJ (1990). *Radiolabelled antibodies and peptides*. In: Sampson CB (ed) Textbook of radiopharmacy theory and practice, 3 edn. Gordon and Breach Science Publishers, Amsterdam, 63-82.
- [260] Hnatowich DJ, Virzi F, et al. (1994). *Can a cysteine challenge assay predict the in vivo behavior of ^{99m}Tc-labeled antibodies?* Nucl Med Biol **21**, 1035-44.

- [261] Jemal A, Siegel R, et al. (2009). *Cancer statistics, 2009*. CA Cancer J Clin **59**, 225-49.
- [262] Dijkers EC, Kosterink JG, et al. (2009). *Development and characterization of clinical-grade ⁸⁹Zr-trastuzumab for HER2/neu immunoPET imaging*. J Nucl Med **50**, 974-981.
- [263] Harrison KA, Tempero MA (1995). *Diagnostic use of radiolabeled antibodies for cancer*. Oncology (Williston Park) **9**, 625-31 DISC 634, 636, 641.
- [264] Boswell CA, Brechbiel MW (2007). *Development of radioimmunotherapeutic and diagnostic antibodies: an inside-out view*. Nucl Med Biol **34**, 757-78.
- [265] Hnatowich DJ, Childs RL, et al. (1983). *The preparation of DTPA-coupled antibodies radiolabeled with metallic radionuclides: an improved method*. J Immunol Methods **65**, 147-157.
- [266] Loening AM, Gambhir SS (2003). *AMIDE: a free software tool for multimodality medical image analysis*. Mol Imaging **2**, 131-137
- [267] Ho M, Bera TK, et al. (2007). *Mesothelin expression in human lung cancer*. Clin Cancer Res **13**, 1571-5.
- [268] Pelat T, Hust M, Thullier P (2009). *Obtention and engineering of non-human primate (NHP) antibodies for therapeutics*. Mini Rev Med Chem **9**, 1633-8.
- [269] Chowdhury PS, Viner JL, et al. (1998). *Isolation of a high-affinity stable single-chain Fv specific for mesothelin from DNA-immunized mice by phage display and construction of a recombinant immunotoxin with anti-tumor activity*. Proc Natl Acad Sci U S A **95**, 669-674.
- [270] Press OW, Shan D, et al. (1996). *Comparative metabolism and retention of iodine-125, yttrium-90, and indium-111 radioimmunoconjugates by cancer cells*. Cancer Res **56**, 2123-2129.
- [271] Maeda H, Wu JC, et al. (2000). *Tumor vascular permeability and the EPR effect in macromolecular therapeutics: a review*. Journal of Controlled Release **65**, 271-284.
- [272] Nakamae H, Wilbur DS, et al. (2009). *Biodistributions, myelosuppression, and toxicities in mice treated with an anti-CD45 antibody labeled with the alpha-emitting radionuclides bismuth-213 or astatine-211*. Cancer Res **69**, 2408-2415.

- [273] Couturier O, Supiot S, et al. (2005). *Cancer radioimmunotherapy with alpha-emitting nuclides*. Eur J Nucl Med Mol Imaging **32**, 601-614.
- [274] Congdon CC (1966). *The destructive effect of radiation on lymphatic tissue*. Cancer Res **26**, 1211-20.
- [275] Kurnick NB, Nokay N (1962). *Changes induced in the mouse spleen by graded doses of total-body x-irradiation*. Radiat Res **17**, 140-4.
- [276] Cobb LM, Butler SA (1987). *Treatment of the murine lymphoma A31 with intravenous, sterilized, ^{114m}In-loaded A31 cells*. Radiother Oncol **10**, 217-30.
- [277] Hofer KG (2000). *Biophysical aspects of Auger processes*. Acta Oncol **39**, 651-7.
- [278] Ho M, Onda M, et al. (2006). *Mesothelin is shed from tumor cells*. Cancer Epidemiol Biomarkers Prev **15**, 1751.
- [279] Hellstrom I, Friedman E, et al. (2008). *Anti-mesothelin antibodies and circulating mesothelin relate to the clinical state in ovarian cancer patients*. Cancer Epidemiol Biomarkers Prev **17**, 1520-6.
- [280] Johnston FM, Tan MC, et al. (2009). *Circulating mesothelin protein and cellular antimesothelin immunity in patients with pancreatic cancer*. Clin Cancer Res **15**, 6511-8.
- [281] Pimm MV (1995). *Circulating antigen: bad or good for immunoscintigraphy?* Nucl Med Biol **22**, 137-145.
- [282] Waldmann T (2003). *ABCs of radioisotopes used for radioimmunotherapy: alpha- and beta-emitters*. Leuk Lymphoma **44 Suppl 3**, S107-S113.
- [283] Rosenberg JT, Kogot JM, et al. *Intracellular bimodal nanoparticles based on quantum dots for high-field MRI at 21.1 T*. Magn Reson Med
- [284] Oostendorp M, Douma K, et al. *Gadolinium-labeled quantum dots for molecular magnetic resonance imaging: R(1) versus R(2) mapping*. Magn Reson Med **64**, 291-298.
- [285] Koole R, Mulder WJ, et al. (2009). *Magnetic quantum dots for multimodal imaging*. Wiley Interdiscip Rev Nanomed Nanobiotechnol **1**, 475-91.

- [286] Armato SG, Entwisle J, et al. (2008). *Current state and future directions of pleural mesothelioma imaging*. Lung Cancer **59**, 411-420.
- [287] D'Onofrio M, Gallotti A, Pozzi Mucelli R (2010). *Imaging techniques in pancreatic tumors*. Expert Rev Med Devices **7**, 257-73.
- [288] Vachiranubhap B, Kim YH, et al. (2009). *Magnetic resonance imaging of adenocarcinoma of the pancreas*. Top Magn Reson Imaging **20**, 3-9.
- [289] Iyer VR, Lee SI (2010). *MRI, CT, and PET/CT for ovarian cancer detection and adnexal lesion characterization*. AJR Am J Roentgenol **194**, 311-21.
- [290] Mody VV, Nounou MI, Bikram M (2009). *Novel nanomedicine-based MRI contrast agents for gynecological malignancies*. Adv Drug Deliv Rev **61**, 795-807.
- [291] Marzola P, Osculati F, Sbarbati A (2003). *High field MRI in preclinical research*. Eur J Radiol **48**, 165-70.
- [292] Liu S, Jia B, et al. (2009). *A novel type of dual-modality molecular probe for MR and nuclear imaging of tumor: preparation, characterization and in vivo application*. Mol Pharm **6**, 1074-82.
- [293] Amstad E, Zurcher S, et al. (2009). *Surface functionalization of single superparamagnetic iron oxide nanoparticles for targeted magnetic resonance imaging*. Small **5**, 1334-42.
- [294] Chen TJ, Cheng TH, et al. (2009). *Targeted Herceptin-dextran iron oxide nanoparticles for noninvasive imaging of HER2/neu receptors using MRI*. J Biol Inorg Chem **14**, 253-60.
- [295] Ito A, Shinkai M, et al. (2005). *Medical application of functionalized magnetic nanoparticles*. J Biosci Bioeng **100**, 1-11.
- [296] Rudershausen S, Gruttner C, et al. (2002). *Multifunctional superparamagnetic nanoparticles for life sciences applications* European cells and materials **3**, 81-83.
- [297] Lee H, Lee E, et al. (2006). *Antibiofouling polymer-coated superparamagnetic iron oxide nanoparticles as potential magnetic resonance contrast agents for in vivo cancer imaging*. J Am Chem Soc **128**, 7383-9.

- [298] Lee CM, Jeong HJ, et al. (2009). *Superparamagnetic iron oxide nanoparticles as a dual imaging probe for targeting hepatocytes in vivo*. *Magn Reson Med* **62**, 1440-6.
- [299] Lee HY, Li Z, et al. (2008). *PET/MRI dual-modality tumor imaging using arginine-glycine-aspartic (RGD)-conjugated radiolabeled iron oxide nanoparticles*. *J Nucl Med* **49**, 1371-9.
- [300] Xie J, Chen K, et al. (2010). *PET/NIRF/MRI triple functional iron oxide nanoparticles*. *Biomaterials* **31**, 3016-22.
- [301] Otsuji E, Kuriu Y, et al. (2006). *Monoclonal antibody A7 coupled to magnetic particles as a contrast enhancing agent for magnetic resonance imaging of human colorectal carcinoma*. *Cancer Immunol Immunother* **55**, 728-33.
- [302] Saini S, Stark DD, et al. (1987). *Ferrite particles: a superparamagnetic MR contrast agent for the reticuloendothelial system*. *Radiology* **162**, 211-6.
- [303] Stark DD, Weissleder R, et al. (1988). *Superparamagnetic iron oxide: clinical application as a contrast agent for MR imaging of the liver*. *Radiology* **168**, 297-301.
- [304] Tiefenauer LX, Kuhne G, Andres RY (1993). *Antibody-magnetite nanoparticles: in vitro characterization of a potential tumor-specific contrast agent for magnetic resonance imaging*. *Bioconjug Chem* **4**, 347-52.
- [305] Suwa T, Ozawa S, et al. (1998). *Magnetic resonance imaging of esophageal squamous cell carcinoma using magnetite particles coated with anti-epidermal growth factor receptor antibody*. *Int J Cancer* **75**, 626-34.
- [306] Suzuki M, Honda H, et al. (1996). *Development of a target-directed magnetic resonance contrast agent using monoclonal antibody-conjugated magnetic particles*. *Noshuyo Byori* **13**, 127-32.
- [307] Gossuin Y, Gillis P, et al. (2009). *Magnetic resonance relaxation properties of superparamagnetic particles*. *Wiley Interdiscip Rev Nanomed Nanobiotechnol* **1**, 299-310.
- [308] Ma HL, Xu YF, et al. (2008). *Superparamagnetic iron oxide nanoparticles stabilized by alginate: pharmacokinetics, tissue distribution, and applications in detecting liver cancers*. *Int J Pharm* **354**, 217-26.

- [309] Barick KC, Aslam M, et al. (2009). *Nanoscale assembly of amine functionalized colloidal iron oxide*. *J Magn Magn Mater* **321**, 1529-1532.
- [310] Sung CK, Hong KA, et al. (2009). *Dual-modal nanoprobe for imaging of mesenchymal stem cell transplant by MRI and fluorescence imaging*. *Korean J Radiol* **10**, 613-22.
- [311] Roca AG, Veintemillas-Verdaguer S, et al. (2009). *Effect of nanoparticle and aggregate size on the relaxometric properties of MR contrast agents based on high quality magnetite nanoparticles*. *J Phys Chem B* **113**, 7033-9.
- [312] Moghimi SM, Hunter AC, Murray JC (2001). *Long-circulating and target-specific nanoparticles: theory to practice*. *Pharmacol Rev* **53**, 283-318.
- [313] Arbab AS, Bashaw LA, et al. (2003). *Characterization of biophysical and metabolic properties of cells labeled with superparamagnetic iron oxide nanoparticles and transfection agent for cellular MR imaging*. *Radiology* **229**, 838-46.
- [314] Bally MB, Mayer, D. L., Hope, J.M., Nayar, R. (1993). *Pharmacodynamics of liposomal drug carriers: methodological considerations*. In: Gregeriadis G (ed) *Liposome Technology*, 2nd edn, vol III. CRC Press, 27-41.
- [315] Ferrari M (2010). *Frontiers in cancer nanomedicine: directing mass transport through biological barriers*. *Trends Biotechnol* **28**, 181-8.
- [316] Jun YW, Huh YM, et al. (2005). *Nanoscale size effect of magnetic nanocrystals and their utilization for cancer diagnosis via magnetic resonance imaging*. *J Am Chem Soc* **127**, 5732-3.
- [317] Hamamura MJ, Ha S, et al. (2010). *Initial Investigation of preclinical integrated SPECT and MR imaging*. *Technol Cancer Res Treat* **9**, 21-8.
- [318] Yamamoto S, Imaizumi M, et al. (2010). *Design and performance from an integrated PET/MRI system for small animals*. *Ann Nucl Med*
- [319] Pichler BJ, Kolb A, et al. (2010). *PET/MRI: paving the way for the next generation of clinical multimodality imaging applications*. *J Nucl Med* **51**, 333-6.
- [320] Mishra P, Singh AK, et al. (1994). *A novel method for labelling human immunoglobulin-G with ⁹⁹Tcm suitable for inflammation scintigraphy*. *Nucl Med Commun* **15**, 723-9.

- [321] Thakur ML, DeFulvio JD (1991). *Technetium-99m-labeled monoclonal antibodies for immunoscintigraphy. Simplified preparation and evaluation*. J Immunol Methods **137**, 217-24.
- [322] Thakur ML, DeFulvio J, et al. (1991). *Technetium-99m labeled monoclonal antibodies: evaluation of reducing agents*. Int J Rad Appl Instrum B **18**, 227-33.
- [323] Mariani G (1999). *Imaging of pancreatic adenocarcinoma with radiolabeled monoclonal antibodies*. Ann Oncol **10 Suppl 4**, 37-40.
- [324] Longo DL, . (2008). *Monoclonal Antibodies in Cancer Treatment*. In: Bruce A. Chabner. TJI, Jr., Dan L. Longo (ed) Harrison's Manual of Oncology. The McGraw Hill Companies, 111-122.
- [325] Pimm MV, Rajput RS, et al. (1991). *Anomalies in reduction-mediated technetium-99m labelling of monoclonal antibodies*. Eur J Nucl Med **18**, 973-6.
- [326] Sakahara H, Saga T, et al. (1993). *In vivo instability of reduction-mediated 99mTc-labeled monoclonal antibody*. Nucl Med Biol **20**, 617-23.
- [327] Mirzadeh S, Brechbiel MW, et al. (1990). *Radiometal labeling of immunoproteins: covalent linkage of 2-(4-isothiocyanatobenzyl)diethylenetriaminepentaacetic acid ligands to immunoglobulin*. Bioconjug Chem **1**, 59-65.
- [328] Beatty BG, Beatty JD, et al. (1989). *Effect of specific antibody pretreatment on liver uptake of 111In-labeled anticarcinoembryonic antigen monoclonal antibody in nude mice bearing human colon cancer xenografts*. Cancer Res **49**, 1587-94.
- [329] Hagan PL, Halpern SE, et al. (1985). *In vivo kinetics of radiolabeled monoclonal anti-CEA antibodies in animal models*. J Nucl Med **26**, 1418-23.
- [330] Pedley RB, Boden JA, et al. (1989). *The effect of serum CEA on the distribution and clearance of anti-CEA antibody in a pancreatic tumour xenograft model*. Br J Cancer **60**, 549-54.
- [331] Abdel-Nabi HH, Schwartz AN, et al. (1987). *Colorectal carcinoma: detection with indium-111 anticarcinoembryonic-antigen monoclonal antibody ZCE-025*. Radiology **164**, 617-21.

- [332] Bosslet K, Steinstrasser A, et al. (1988). *Quantitative considerations supporting the irrelevance of circulating serum CEA for the immunoscintigraphic visualization of CEA expressing carcinomas*. Eur J Nucl Med **14**, 523-8.
- [333] Reilly RM, Gariepy J (1998). *Factors influencing the sensitivity of tumor imaging with a receptor-binding radiopharmaceutical*. J Nucl Med **39**, 1036-43.
- [334] Goetz C, Breton E, et al. (2008). *SPECT low-field MRI system for small-animal imaging*. J Nucl Med **49**, 88-93.
- [335] Ho M, Hassan R, et al. (2005). *Humoral immune response to mesothelin in mesothelioma and ovarian cancer patients*. Clin Cancer Res **11**, 3814-20.

APPENDIX

Appendix A

A.1. Mesothelin Expression in Patient Tumour Specimens

Mesothelin is a differentiation antigen that is expressed in epithelioid type of mesotheliomas which comprise 50 to 65% of malignant mesothelioma cases. The current immunohistological study was carried out to confirm the expression of mesothelin in clinical cases of epithelioid type mesothelioma.

A.2. Materials and Methods

We obtained 17 cases of paraffin embedded epithelioid mesothelioma tissue blocks from the tumor tissue bank at the Vancouver General Hospital, with the help of our collaborator and clinical pathologist, Dr. John English. Dr. John English also provided us with two cases of reactive fibrous pleurisy tissue blocks to be used as control non-mesothelin expressing lung tissue. The study was carried out as per a protocol approved by the UBC Research and Ethics Board. The tissue blocks were sectioned into 5 μm sections using a microtome, and then immersed into a 40°C water bath for 10 minutes. Afterwards, the sections were placed on glass slides and stored at 37°C overnight. The slides were then stored in the refrigerator at 4°C.

For immunostaining, slides from each sample (both mesothelioma and reactive fibrous pleurisy) were incubated at 57°C for 45 minutes. The slides were then washed twice with xylene for 3 minutes each, then with 70%, 90%, 100% ethanol and water for 10 minutes each, respectively, then with 100%, 90%, 70% ethanol and water for 10 minutes each, respectively. Next, each slide was incubated with 300 μl of 5% normal goat serum for 1 hour at room temperature to block non-specific binding of antibodies. The primary antibody (mAbK1) was diluted to 1:400 using

the antibody diluent (Dako, Burlington, Ontario, Canada). The slides were then incubated with antibodies in a humidity chamber at 4°C overnight.

The slides were washed three times each for 5 minutes with PBS and incubated with Texas red-conjugated goat anti-mouse secondary antibody (1:300; Jackson ImmunoResearch, West Grove, Pennsylvania, U.S.A.) at room temperature for 90 minutes in the dark and humidity conditions. Following subsequent washes with PBS, cover slips were mounted onto the slides. Control slides without primary and secondary antibodies were prepared in a similar manner. Images were captured on a Leica DMLB microscope (Leica Microsystems Inc, Bannockburn, Illinois, U.S.A.) with attached Retiga 2000R camera and processed using Image J software.

A.3. Results

Fifteen of the 17 patient samples tested (88%) expressed mesothelin. The membrane expression of mesothelin was clearly visualized in the tumour specimens (**Figure A.1**). Representative images of two negative cases of mesothelin expression in mesothelioma specimens are shown in **Figure A.2**. The reactive fibrous pleurisy tissue specimens also did not show mesothelin expression (**Figure A.3**). These results provided further confirmation of mesothelin expression in epithelioid mesothelioma as reported previously by many authors [17,118,335].

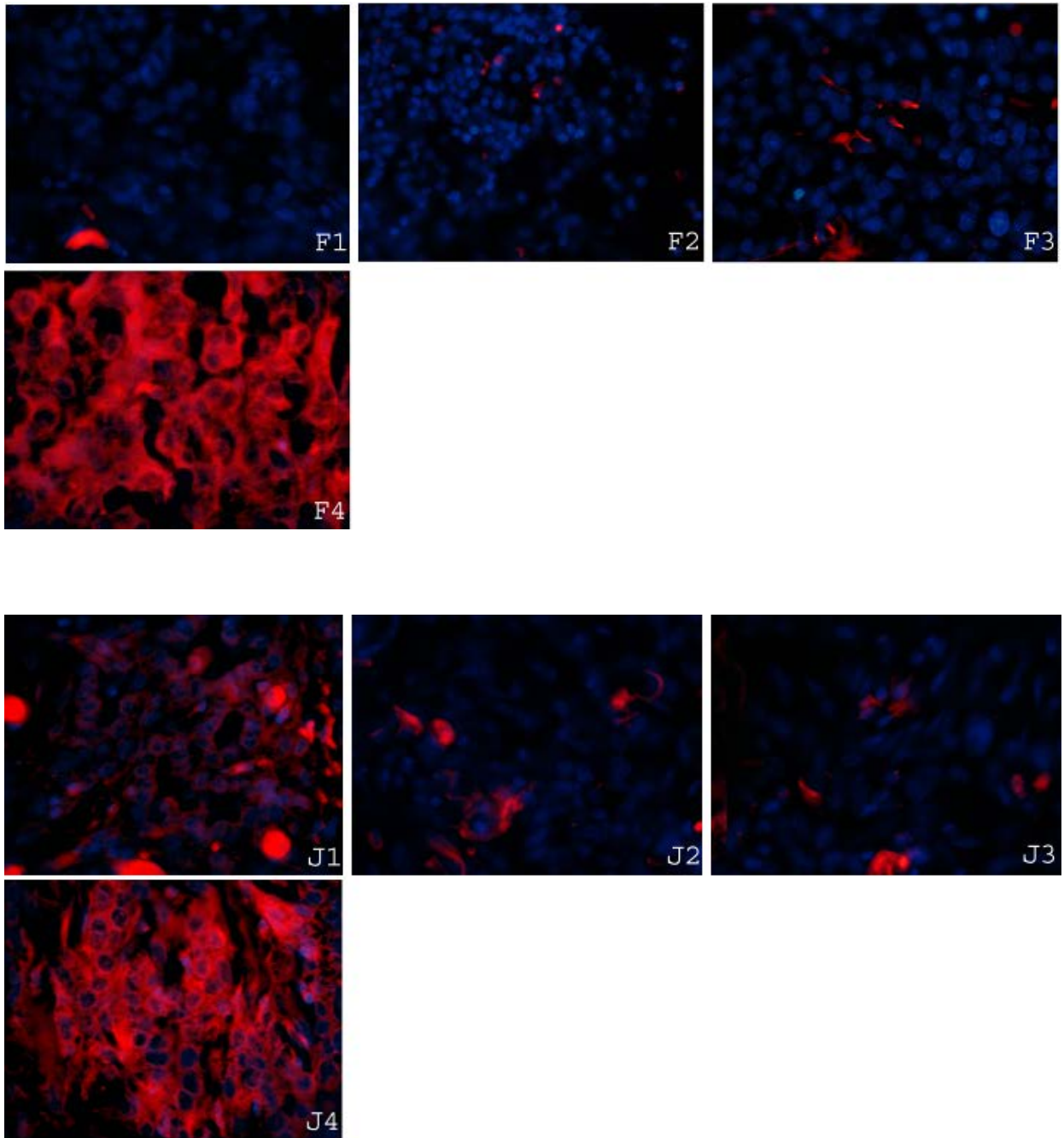


Figure A.1. Representative fluorescent microscopy images of two positive cases (F, J) of mesothelioma patient tumour samples from our post-mortem histology study. The cell nuclei were stained blue with DAPI. The control images were obtained without primary and secondary antibody (F1, J1), without primary antibody but with secondary antibody (F2, J2) and with primary antibody but no secondary antibody (F3, J3). The final picture (F4, J4) of the slide stained with both primary anti-mesothelin antibody and secondary antibody shows the mesothelin receptors stained red.

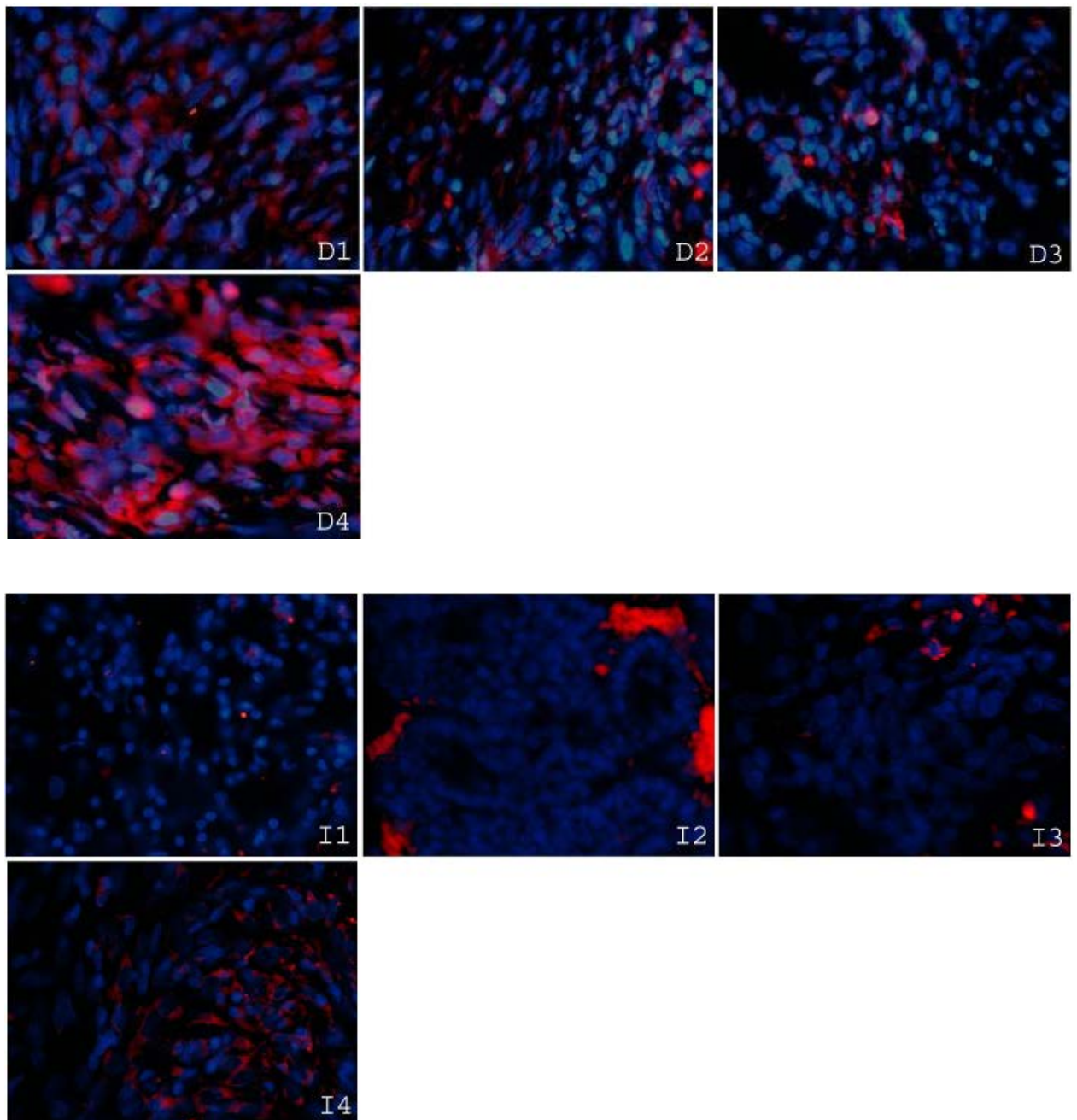


Figure A.2. Representative fluorescent microscopy images of two negative cases (D, I) of mesothelioma patient tumour samples from our post-mortem histology study. The cell nuclei were stained blue with DAPI. The control images were obtained without primary and secondary antibody (D1, I1), without primary antibody but with secondary antibody (D2, I2) and with primary antibody but no secondary antibody (D3, I3). The final picture (D4, I4) of the slide stained with both primary anti-mesothelin antibody and secondary antibody shows very low mesothelin staining.

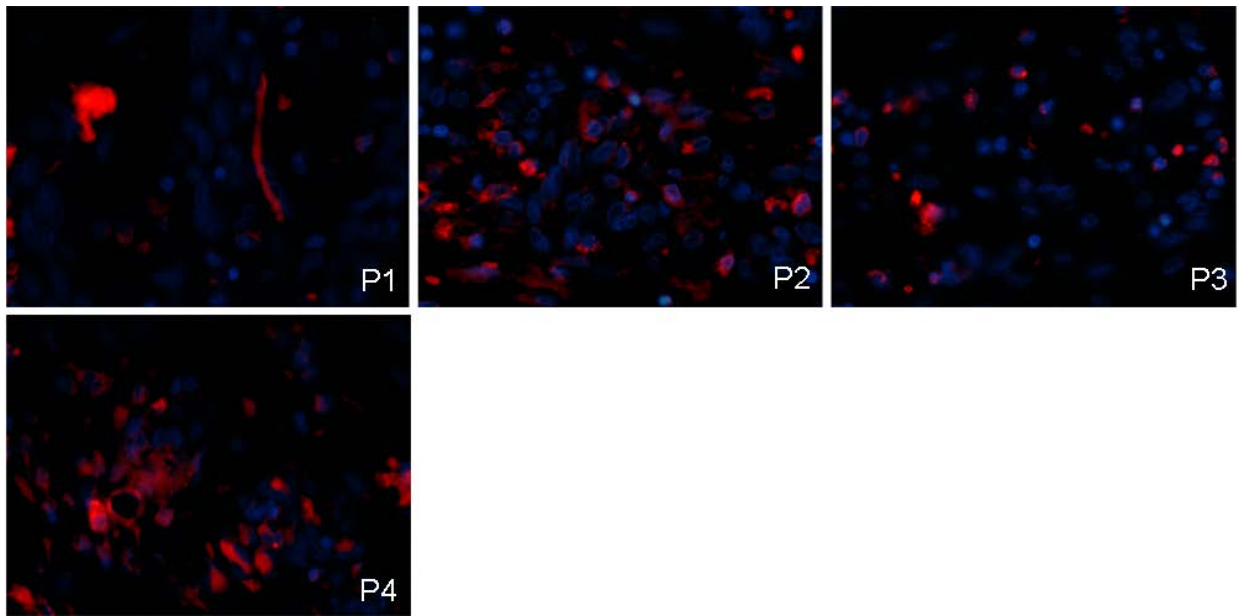


Figure A.3. Representative fluorescent microscopy images of a reactive fibrous pleurisy patient sample (P) from our post-mortem histology study. The cell nuclei were stained blue with DAPI. The control images were obtained without primary and secondary antibody (P1), without primary antibody but with secondary antibody (P2) and with primary antibody but no secondary antibody (P3). The final picture (P4) of the slide stained with both primary anti-mesothelin antibody and secondary antibody shows very low mesothelin staining.